Photoproduction of J/ψ Mesons at Medium and Low Elasticities at HERA

DISSERTATION

zur Erlangung des Doktorgrades
des Fachbereichs Physik
der Universität Hamburg

vorgelegt von

Fabrice Salvaire
aus Paris

Hamburg
2007

Gutachterin der Dissertation:	Prof. Dr. Beate Naroska
Gutachter der Dissertation:	Prof. Dr. Eckhard Elsen
Gutachterin der Disputation:	Prof. Dr. Beate Naroska
Gutachter der Disputation:	Prof. Dr. Achim Geiser
Datum der Disputation:	13.09.2007
Vorsitzender des Prüfungsausschusses:	Dr. Hans Dierk Rüter
Vorsitzender des Promotionsausschusses:	Dr. Günter Huber
Dekan des Departments Physik der MIN-Fakultät:	Dr. Arno Frühwald

À mes parents

Abstract

The first analysis of inelastic J/ψ mesons production in photoproduction ($Q^2 < 2.5\,\mathrm{GeV}^2$) of the H1 experiment for the second phase of HERA (HERA II) is presented. The analysis is carried out at low and medium elasticities. The production of heavy quarks (charm, or bottom) is of special interest since the mass of the quarks provides a hard scale for the application of perturbative QCD. The muonic decay channel is used to select the J/ψ mesons.

The data was collected by the H1 detector during the period 2003–2005, and corresponds to an integrated luminosity of $133\,\mathrm{pb}^{-1}$. However only a subset of this data could be analysed. At the start of HERA II the trigger system was affected by a sizeable background. Then a fault was introduced in the trigger software during the summer 2004 and was only discovered and solved in April 2006. This means that approximately 80 % of the triggered events at medium elasticities and 65 % at low elasticities was lost during this period. Moreover during the first half of 2005 the muon trigger was affected by faulty power supplies. Consequently two good data taking periods are analysed: a first period with an integrated luminosity of $23\,\mathrm{pb}^{-1}$ collected in 2004, and a second period of $60\,\mathrm{pb}^{-1}$ collected during the second half of 2005, which is however strongly affected by the malfunction of the trigger software.

In the medium elasticity region the total photoproduction cross section as a function of the photon-proton centre-of-mass energy $W_{\gamma\mathrm{p}}$ and the single differential cross sections as functions of the transverse momentum squared of the J/ψ meson $P^2_{t,\psi}$ and the elasticity z are extracted. The analysis covers the kinematic range $0.3 \leqslant z \leqslant 0.9$, $60 \leqslant W_{\gamma\mathrm{p}} \leqslant 240\,\mathrm{GeV}$ and $P^2_{t,\psi} > 1\,\mathrm{GeV}^2$. The same analysis is performed at low elasticity for the kinematic region $0.05 \leqslant z \leqslant 0.45$, $120 \leqslant W_{\gamma\mathrm{p}} \leqslant 260\,\mathrm{GeV}$ and $P^2_{t,\psi} > 1\,\mathrm{GeV}^2$.

The results are in agreement within the statistical uncertainties at one or two standard deviations with the previous H1 measurements using HERA I data. At this stage of the analysis of the HERA II data, the statistics do not permit an improvement to the previous measurements and thus do not provide an improved comparison with theoretical models.

Zusammenfassung

Die erste Analyse der unelastischen J/ψ Mesonproduktion in Photoproduktion ($Q^2 < 2.5\,\mathrm{GeV}^2$) für die zweite Phase des Experimentes H1 bei HERA (HERA II) wird vorgestellt. Die Analyse wird bei niedrigen und mittleren Elastizitäten durchgeführt. Die Produktion der schweren Quarks (Charm oder Bottom) ist von speziellem Interesse, da die Masse der Quarks als harte Skala für die Anwendung von perturbativer QCD dienen kann. Der myonische Zerfallskanal wird benutzt, um die J/ψ Mesonen zu selektieren.

Die Daten wurden mit dem Detektor H1 während der Periode 2003–2005 gesammelt und entsprechen einer integrierten Luminosität von $133\,\mathrm{pb}^{-1}$. Jedoch nur eine Teilmenge dieser Daten konnte analysiert werden. Am Anfang von HERA II wurde das Triggersystem durch hohen Untergrund beeinträchtigt. Dann wurde versehentlich ein Fehler in der Trigger-Software während des Sommers 2004 eingebaut und erst im April 2006 entdeckt und beseitigt. Dies heißt, dass ungefähr 80 % der getriggerten Ereignisse mittlerer Elastizität und 65 % niedriger Elastizität während dieser Periode verloren gegangen sind. Außerdem wurde während der ersten Hälfte von 2005 der Myon-Trigger durch fehlerhafte Spannungsversorgung beeinträchtigt. Infolgedessen werden nur zwei gute Datenperioden analysiert: in 2004, der ersten Periode, wurde eine integrierte Luminosität von $23\,\mathrm{pb}^{-1}$ gesammelt und in der zweiten Hälfte von 2005 eine integrierte Luminosität von $60\,\mathrm{pb}^{-1}$ erreicht. Diese zweite Periode wurde von Problemen mit der Trigger-Software beeinflusst.

In der mittleren Elastizitätsregion werden der totale Wirkungsquerschnitte in Photoproduktion als Funktion der Photon-Proton Schwerpunktenergie $W_{\gamma\mathrm{p}}$ und die differentiellen Wirkungsquerschnitte als Funktionen des quadrierten Transversalimpulses des J/ψ Mesons $P^2_{t,\psi}$ und der Elastizität z bestimmt. Die Analyse deckt den kinematischen Bereich $0.3 \leqslant z \leqslant 0.9$, $60 \leqslant W_{\gamma\mathrm{p}} \leqslant 240\,\mathrm{GeV}$ und $P^2_{t,\psi} > 1\,\mathrm{GeV}^2$ ab. Die gleiche Analyse wird bei niedriger Elastizität für die kinematische Region $0.05 \leqslant z \leqslant 0.45$, $120 \leqslant W_{\gamma\mathrm{p}} \leqslant 260\,\mathrm{GeV}$ und $P^2_{t,\psi} > 1\,\mathrm{GeV}^2$ durchgeführt.

Die Resultate stimmen innerhalb der statistischen Fehler von ein oder zwei Standardabweichungen mit den vorhergehenden Messwerten von H1 mit HERA I Daten überein. In diesem Stadium der Analyse der HERA II Daten ermöglicht die Statistik keine Verbesserung beim Vergleich mit theoretischen Modellen.

Résumé

Cette thèse présente la première analyse de la photo-production ($Q^2 < 2.5\,\mathrm{GeV}^2$) inélastique de mésons J/ψ de l'expérience H1 pour la seconde phase de HERA (HERA II). L'analyse est effectuée à basse et moyenne élasticité. La production de mésons lourds (charme, ou beauté) est particulièrement intéressante puisque la masse des quarks lourds procure une échelle de renormalisation pour la mise en application de méthodes perturbatives de QCD. Les mésons J/ψ sont sélectionnés via le canal de désintégration en muons.

Les données ont été collectées par le détecteur H1 durant les années 2003–2005, ce qui correspond à une luminosité intégrée de $133\,\mathrm{pb}^{-1}$. Toutefois, seulement une partie de ces données a pu être analysée. Au redémarrage de HERA II, le système de déclenchement a été affecté de façon non négligeable par le bruit de fond. Ensuite une erreur a été introduite dans le programme du système de déclenchement durant l'été 2004. Celle-ci fût seulement découverte et résolue en avril 2006. Il en résulte une perte sèche de 80 % des données enregistrées à moyenne élasticité et de 65 % à basse élasticité durant cette période. De plus durant la première moitié de l'année 2005, le système de déclenchement du détecteur de muons a été affecté pas des alimentations défectueuses. Par conséquent deux bonnes périodes de prise de données sont analysées : une première période avec une luminosité intégrée de $23\,\mathrm{pb}^{-1}$ collectée durant l'année 2004, et une deuxième période de $60\,\mathrm{pb}^{-1}$ collectée durant la seconde moitié de l'année 2005, et qui est sévèrement affectée par le dysfonctionnement du système de déclenchement.

À moyenne élasticité sont extraites la section efficace totale de photo-production en fonction de l'énergie du centre-de-masse photon-proton $W_{\gamma\mathrm{p}}$, ainsi que les sections efficaces différentielles en fonction du carré de l'impulsion transverse du méson J/ψ $P^2_{t,\psi}$, et de l'élasticité z. L'analyse couvre le domaine cinématique $0.3 \leqslant z \leqslant 0.9$, $60 \leqslant W_{\gamma\mathrm{p}} \leqslant 240\,\mathrm{GeV}$ et $P^2_{t,\psi} > 1\,\mathrm{GeV}^2$. La même analyse est effectuée à basse élasticité pour le domaine cinématique $0.05 \leqslant z \leqslant 0.45$, $120 \leqslant W_{\gamma\mathrm{p}} \leqslant 260\,\mathrm{GeV}$ et $P^2_{t,\psi} > 1\,\mathrm{GeV}^2$.

Les résultats sont compatibles à l'intérieur de la marge d'erreur à un ou deux écarts standards avec les précédentes mesures de H1 pour la période HERA I. À ce stade de l'analyse des données de HERA II, la statistique ne permet pas d'améliorer la précision des mesures et donc une meilleur discrimination entre les différents modèles théoriques.

Contents

Introduction **1**

1 Charmonium Production **3**
1.1 The HERA Microscope . . . 3
1.2 Kinematics in ep Scattering . . . 5
1.3 The Charmonium System . . . 6
1.4 J/ψ Meson Kinematics . . . 8
1.4.1 The Elasticity . . . 8
1.4.2 J/ψ Meson Polarisation . . . 9
1.5 Models for Inelastic Production of J/ψ Mesons . . . 10
1.5.1 Inelastic Production of Heavy Quark Pairs . . . 11
1.5.2 The Colour Evaporation Model . . . 12
1.5.3 The Colour Singlet Model . . . 12
1.5.4 The Factorisation Approach within Non-Relativistic QCD . . . 15
1.5.5 The Status at HERA . . . 17
1.5.5.1 Comparison of Cross Sections with the Colour Singlet Model . . . 17
1.5.5.2 Comparison of Cross Sections with NRQCD Calculations . . . 19
1.5.5.3 Conclusion of this Overview . . . 21
1.5.5.4 Preliminary Results of the ZEUS Collaboration . . . 22
1.6 The Diffractive Processes . . . 23

2 The H1 Detector at HERA **25**
2.1 The HERA Collider . . . 25
2.1.1 HERA Operation . . . 26
2.1.2 The Second Phase of HERA . . . 29
2.2 The H1 Detector . . . 30
2.2.1 The Tracking Systems . . . 33
2.2.1.1 The Central Tracking System . . . 33
2.2.1.2 The Forward Tracking System . . . 35
2.2.1.3 The Backward Tracking System . . . 35
2.2.2 The Calorimeters . . . 35
2.2.2.1 The Liquid Argon Calorimeter . . . 35
2.2.2.2 The Spaghetti Calorimeter (SpaCal) . . . 36
2.2.2.3 The Plug2k . . . 37
2.2.2.4 The Tail Catcher . . . 37
2.2.3 The Muon Detectors . . . 37
2.2.3.1 The Central Muon Detector . . . 37
2.2.3.2 The Forward Muon Detector . . . 38

2.2.4 The Time of Flight System . . . 38
2.2.5 The Measurement of the Luminosity . . . 39
2.2.6 Detectors Installed in the Ring . . . 40
2.3 The Trigger System . . . 40
2.3.1 Level 1 . . . 42
2.3.2 Level 2 . . . 43
2.3.3 Level 3 . . . 43
2.3.4 Level 4 . . . 43
2.3.5 Level 1 Triggers Elements . . . 44
2.3.5.1 CIP Trigger Elements . . . 44
2.3.5.2 DC$r\phi$ Trigger Elements . . . 44
2.3.5.3 FTT Trigger Elements . . . 44
2.3.5.4 Muon Trigger Elements . . . 45
2.3.5.5 SpaCal Trigger Elements . . . 45
2.3.5.6 Time of Flight Trigger Elements . . . 45
2.3.6 The Level 4 "Heavy Flavour Closed" Finder . . . 45

3 Monte Carlo Simulation and Reconstruction of the Kinematic Variables 47
3.1 Simulation Process . . . 47
3.2 Monte Carlo Programs . . . 48
3.2.1 EPJPSI . . . 48
3.2.2 DIFFVM . . . 49
3.3 Reconstruction of the Kinematic Variables . . . 50
3.3.1 Reconstruction of the Decay Muons . . . 50
3.3.2 Reconstruction of the J/ψ Mesons and the Transverse Momentum Squared of the J/ψ Meson $P^2_{t,\psi}$ . . . 52
3.3.3 Reconstruction of the Kinematic Variables $W_{\gamma\mathrm{p}}$ and z . . . 57
3.3.4 Reconstruction of the Polarisation Variables $\cos\theta^\star$ and $\phi^\star$ . . . 67
3.3.5 Purity and Stability . . . 76

4 Selection of J/ψ Mesons in Photoproduction 81
4.1 Preselection . . . 81
4.1.1 Run Selection . . . 82
4.1.2 Integrated Luminosity . . . 83
4.1.3 J/ψ Meson Finder . . . 84
4.1.3.1 J/ψ Meson Topology . . . 84
4.1.3.2 J/ψ Meson Selection . . . 84
4.1.4 Common Selection of the Inelastic J/ψ Mesons . . . 85
4.2 Acceptance and Selection of J/ψ Mesons at Medium z . . . 89
4.2.1 Acceptance . . . 89
4.2.2 Selection Cuts . . . 96
4.2.3 Minimum Number of Tracks and Rejection of Background Originating from Diffractive ψ(2S) . . . 97
4.2.4 Selection Efficiency . . . 99
4.3 Acceptance and Selection of J/ψ Mesons at Low z . . . 102
4.3.1 Acceptance . . . 102
4.3.2 Selection Cuts . . . 111
4.3.3 Selection Efficiency . . . 112

5 Data Taking Periods and Trigger Efficiency **115**
5.1 The 2003-2004 e^+ Data Taking Period . . . 116
5.2 The 2004-2005 e^- Data Taking Period . . . 121
5.3 Subtrigger Yield . . . 126
5.4 Trigger Efficiency . . . 129
5.4.1 Trigger Level One . . . 129
5.4.1.1 Trigger Element Efficiency . . . 131
5.4.1.2 Subtrigger Efficiency . . . 140
5.4.2 Trigger Level Four . . . 145
5.4.2.1 Origin of the Malfunction . . . 145
5.4.2.2 Impact and Treatment of the Malfunction . . . 146
5.5 Event Weights . . . 153

6 Muon Identification Efficiency **155**
6.1 LAr Muon Identification Efficiency . . . 157
6.2 Iron Muon Identification Efficiency . . . 159
6.3 Muon identification Efficiency Reweighting . . . 164

7 Cross Section Measurement **167**
7.1 Selected Data Samples . . . 167
7.2 Background Subtraction . . . 171
7.3 Comparison with the Simulation . . . 175
7.3.1 Reweighting of $P^2_{t,\psi}$ . . . 175
7.3.2 Normalisation of the Simulations . . . 176
7.3.3 Distributions of Observables . . . 178
7.4 Systematic Errors . . . 189
7.4.1 Track Reconstruction . . . 189
7.4.2 Muon Identification Efficiency . . . 189
7.4.3 Iron Trigger Efficiency . . . 190
7.4.4 Proton Parton Density Function . . . 190
7.4.5 Photon Parton Density Fusion . . . 190
7.4.6 Diffractive J/ψ and ψ(2S) Background . . . 190
7.4.7 Sources of Background for the Low z Selection . . . 190
7.4.8 Luminosity and Branching Ratio . . . 191
7.5 Cross Sections as Functions of $W_{\gamma p}$, z, $P^2_{t,\psi}$ . . . 191
7.5.1 Total Efficiency . . . 192
7.5.2 Photon Flux . . . 193
7.5.3 Bin Centre Determination . . . 194
7.5.4 Cross Sections for the Medium z Selection . . . 195
7.5.5 Cross Sections for the Low z Selection . . . 196
7.6 Tables for the Cross Sections . . . 199
7.6.1 Tables for the Low z Selection . . . 200
7.6.2 Tables for the Medium z Selection . . . 202
7.7 Invariant Mass Distributions . . . 204
7.7.1 Mass Distributions for the Low z Selection . . . 205
7.7.1.1 2003-2004 e^+ Data Taking Period . . . 205
7.7.1.2 2004-2005 e^- Data Taking Period . . . 206
7.7.2 Mass Distributions for the Medium z Selection . . . 207
7.7.2.1 2003-2004 e^+ Data Taking Period . . . 207

7.7.2.2 2004-2005 e^- Data Taking Period 210

Conclusions and Outlook **213**

A Subtrigger Definitions **215**

Introduction

The HERA storage ring is a unique accelerator to study high energy physics in electron-proton collisions. It is well suited to study accurately the structure functions of the proton, but permits also to study other physics aspects like tests of perturbative and non-perturbative quantum chromodynamics, study of diffractive phenomena, and physics beyond the standard model. After the first phase a second phase was started in 2001 with the aim to increase the specific luminosity and polarise longitudinally the electron beam around the two collider experiments H1 and ZEUS.

Quantum Flavour Dynamics (QFD) and Quantum Chromodynamics (QCD) are relativistic quantum field theories which describe the electromagnetism and the electro-weak interactions and, respectively, the strong interaction of quarks and gluons. The application of relativistic quantum field theories to physics problems uses perturbative computation techniques. For QED the coupling constant is small, $\alpha \approx 1/137$, and thus perturbative series as a function of α are convergent. On the other hand for QCD the running of the coupling constant α_s is larger. For this reason perturbative QCD computations require the presence of a "hard scale", then α_s is small and perturbative series converge. The production of heavy quarks (charm, bottom) is of special interest since the mass of the quarks provides a hard scale for the application of perturbative QCD. The dominant production mechanism for heavy quarks at HERA is direct photon-gluon fusion. The electron acts as a source of quasi-real photons which interact with a gluon from the proton via a pair of quarks. This process is directly sensitive to the gluon density inside the proton.

The cross section for the production of charm quarks is much higher than that for the bottom quarks due to its smaller mass and its larger electric charge and is thus the best choice for analyses. In order to distinguish the production of charm quarks from the large background originating from light quarks, (up, down and strange), charmed mesons like the $D^{\star\pm}$ ("open charm") or bound charm-anticharm states like the J/ψ meson are used. The J/ψ meson can be identified and triggered in the H1 detector via its muonic decay mode. There are several models which describe the production of $c\overline{c}$ pairs and the transition from the $c\overline{c}$ to the J/ψ meson.

Until 1992 the data on J/ψ meson production in lepton-hadron and hadron-hadron collisions were compatible with the "Colour Singlet Model" (CSM). The CSM is based on the idea that only $c\overline{c}$ states with the same quantum numbers as the J/ψ are allowed to evolve into a J/ψ meson. The analysis of the data collected in the 1992-93 run of the Tevatron, however, showed that the cross section of J/ψ and also ψ(2S) production in $p\overline{p}$ collisions is underestimated by the CSM by more than an order of magnitude.

A new approach, the "Colour Octet Model" (COM) based on an effective field theory called Non-Relativistic Quantum Chromodynamics (NRQCD), was introduced which can accommodate a larger production rate. It includes more intermediate $c\overline{c}$ states than the CSM which are allowed to evolve into a J/ψ meson. This also has consequences for J/ψ production in other processes, e.g. at HERA.

At HERA different production mechanisms are possible, such as direct production or by "resolved" photons. The elasticity z which corresponds to the relative photon energy transferred to the J/ψ meson is often used to distinguish regions where these are expected to dominate. In this

thesis the analysis is performed in two elasticity regions. In the medium z region, $0.3 \leqslant z \leqslant 0.9$, the direct photon-gluon fusion process is the dominating process. In the second elasticity region, $0.05 \leqslant z \leqslant 0.45$, processes with so-called "resolved" photons provided for previous measurements a good description of the cross section. In such processes the photon acts like a hadron and only a fraction of its energy takes part in the interaction with the gluon from the proton. The differences between the predictions of the CSM and the COM are more significant in the low z region than at medium z. However a non-negligible contribution of B mesons is also expected in this region.

The first chapter of this thesis will describe the kinematics of electron-proton scattering, and discusses different models for the production of J/ψ mesons. The second chapter gives an overview over the HERA storage ring and the H1 detector. The Monte Carlo simulations used to correct the data for detector effects are presented in the third chapter, which also contains a study of the resolution in the reconstruction of kinematic variables. Chapter four describes the data selection and investigates the efficiencies in the two elasticity regions. The 2003-2005 data taking period and the trigger efficiency is discussed in chapter five, in particular all the difficulties of this period. Then a study of the muon identification efficiency is given in chapter six. Finally the results of the analyses in the medium and the low elasticity region are presented in chapter seven. The Monte Carlo simulation used for the efficiency determination is compared with the data. The cross sections are extracted and compared to previous measurements. The results are summarised in the final chapter and an outlook is given.

«. . . on reconnaîtra, lorsque la physique expérimentale sera plus avancé, que toutes les phénomènes, ou de la pesanteur, ou de l'élasticité, ou de l'attraction, ou du magnétisme, ou de l'électricité, ne se sont que des faces différentes de la même affection.»
(Denis Diderot, De l'interprétation de la nature, 1753)

Chapter 1

Charmonium Production

In this chapter, firstly some key points necessary to understand the physics prospect at the HERA microscope will be given. Indeed we can find a lot of similarity between optics and high energy physics at HERA. Then the kinematics in electron-proton scattering will be described. Finally, a review of the present knowledge of the Charmonium and of related theoretical models and open questions on this field will be given.

1.1 The HERA Microscope

The "discovery" of the proton began with the research of Ernest Rutherford in 1919. These experiments at the beginning of the 20th century demonstrated that the matter, the elements of the Dimitri Ivanovich Mendeleïev classification in 1869, are the aggregation of *atoms*, and these atoms consist of *nucleons*, proton or neutron. The word *atoms* comes from the Greek, *atomos*, which means "what cannot be divided".

The discovery of the proton was the first evidence, that Nature played at "Matryoshka doll". This similitude brings Gell-Mann and Zweig to develop the quark model in 1964 and to postulate the existence of another sub-level of constituent, the *quarks*. The first evidence of the quarks was found in deep inelastic scattering experiments at SLAC in 1967. Consequently, a proton is not an indivisible, or a fundamental constituent, but is made of three quarks, uud. The following years, the quark theory was confirmed with the discovery of the J/ψ meson and its constituent c quark in 1974.

The first experiments to study the internal structure of the proton used fix targets probed by electron beams. In order to improve the measurements and to probe deeper into the proton, the proton super-microscope HERA was formally approved on April 6, 1984. This collider is the only electron-proton storage ring in the world.

The HERA storage ring was specially designed to study the proton. This machine is a kind of "magnifying glass" for protons. In order to tackle the subject, I will draw a parallel between this and a magnifying glass one uses to see objects too small for our visual acuity. The human eye is a detector sensitive to the visible light, a flux of photons, or its wave equivalent with a wave length of the order of 0.5 µm. The wave length is related to the resolution of the probe. That is why the human eye cannot see finer details less than 0.5 µm. Since the wave length λ is also related

to the momentum P of the corpuscle by the formula of "de Broglie" $\lambda = \frac{h}{P}$, the resolution can be improved by photons of higher energies.

Moreover waves have other interesting properties like diffraction and interferences. To exploit this, you have to use a coherent light source, like a laser. For example, you can measure the size of a hole from the diffraction pattern, and you can even deduce the shape of a piece of metal with holes in it. The mathematical framework of this phenomenon is called "Fourier optics". Since matter is mainly constituted of vacuum, a proton in "very first approximation" can be approximated to a metallic slice with three holes. The specific framework to describe the structure of the proton are the *structure functions*, which were studied accurately with HERA.

Since the radius of the proton is approximately 0.8 fm, it corresponds to the energy range of the *gamma rays*, of the order of 1 GeV. The solution to reach this scale is the HERA machine. This storage ring uses two rings, a ring to accelerate protons and another one to accelerate electrons or positrons in order to increase the energy available in the centre of mass.

The electron beam produces synchrotron radiation like standard electron machines. But at the interaction region with the proton beam, the Bethe-Heitler processes (figure 1.1) take place at large impact parameters, while at lower impact parameter and, in lowest order (Born approximation) ep scattering is described by the exchange of a gauge boson ($\gamma^\star, \mathrm{Z}^0, \mathrm{W}^+, \mathrm{W}^-$) between the electron and a parton of the proton (figure 1.2).

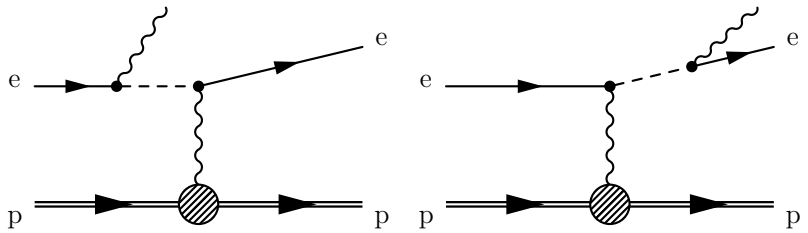

Figure 1.1: Bethe-Heitler process, ep $\longrightarrow$ epγ.

Processes with the exchange of the neutral boson $\gamma^\star$ and Z^0 are called "neutral current processes" and the exchange of charged bosons W^+ and W^- is called "charged current process". The possibility to have polarised electrons and positrons at HERA is important in order to study the charged current process. The exchange of the gauge bosons of the weak interaction Z^0, W^+, W^- is suppressed by a factor, related to the propagator of the interaction, $Q^2/(Q^2 + M^2_{\mathrm{Z}^0,\mathrm{W}})$ with respect to the exchange of photons, and therefore negligible at small virtuality Q^2.

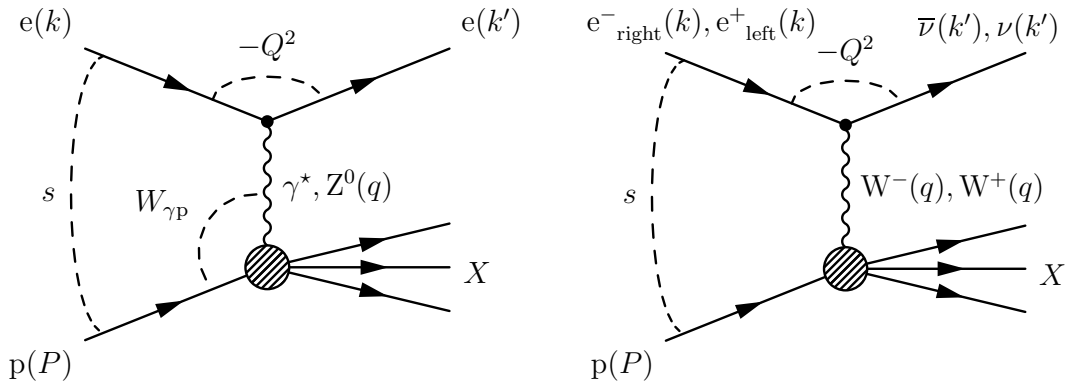

Figure 1.2: Neutral current processes and charged current processes

1.2 Kinematics in ep Scattering

Before explaining the kinematics in ep scattering, the H1 coordinate system will be defined, shown in figure 1.3. The $\overrightarrow{x}$ axis points towards the ring centre, $\overrightarrow{y}$ vertically upwards, and $\overrightarrow{z}$ in the proton direction. The azimuthal angle ϕ is defined as the magnitude of the rotation about the $\overrightarrow{z}$ axis. The polar angle θ is defined as the magnitude of the rotation about the $-\overrightarrow{x}$ axis. The polar angle θ is defined in the range $[0, \pi]$, and the azimuthal angle ϕ in the range $[-\pi, \pi]$.

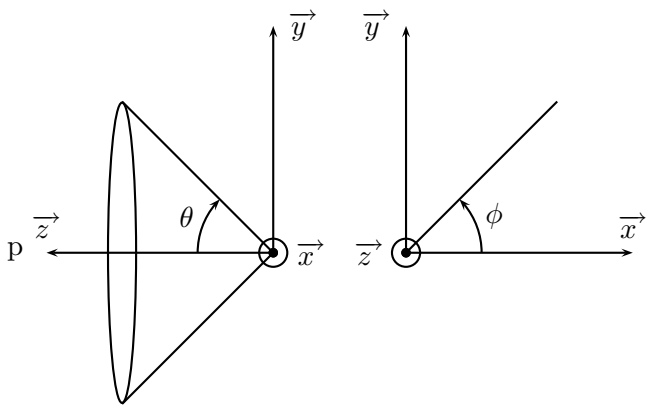

Figure 1.3: H1 coordinate system

In the two sketches, the third axis of the frame is perpendicular to the paper plane and points towards the reader. It is indicated by a dot surrounded by a circle.

The kinematic variables used to describe ep scattering are shown in figure 1.2. Let $k = \left(E_\mathrm{e}, -E_\mathrm{e}\overrightarrow{z}\right)$ [1] the four-momentum of the incoming electron, k' the four-momentum of the scattered electron, and $P = \left(E_\mathrm{p}, E_\mathrm{p}\overrightarrow{z}\right)$ the four-momentum of the incoming proton, where $E_\mathrm{e} = 27.6\,\mathrm{GeV}$ and $E_\mathrm{p} = 920\,\mathrm{GeV}$ are the beam energies of the electron, and the proton respectively. The following Lorentz invariant quantities are defined:

- The centre of mass energy squared is defined as:

$$s \mathrel{\widehat{=}} (k+P)^2 \approx 4E_\mathrm{e}E_\mathrm{p} \tag{1.1}$$
$$\approx 2k \cdot P \tag{1.2}$$

  Masses were neglected in this approximation. The centre of mass energy available at HERA is $\sqrt{s} \approx 318\,\mathrm{GeV}$.

- The four-momentum squared of the exchanged photon is defined as:

$$Q^2 \mathrel{\widehat{=}} -q^2 \mathrel{\widehat{=}} -(k'-k)^2 \tag{1.3}$$

  This quantity is commonly called virtuality. It corresponds to the resolution power of the probe. It is useful to distinguish two kinematic ranges. The threshold on Q^2 is defined as the minimum Q^2 to detect the scattered electron in the H1 detector, approximately $Q^2 \approx 1\,\mathrm{GeV}^2$. Thus we define the photoproduction domain ($Q^2 < 1\,\mathrm{GeV}^2$) where the electron is scattered in the beam pipe, and the Deep Inelastic Scattering (DIS) ($Q^2 > 1\,\mathrm{GeV}^2$) where the electron is scattered in the main detector.

[1] Masses are neglected.

- The energy in the photon proton centre of mass system is defined as:

$$W_{\gamma p}^2 \widehat{=} (P+q)^2 \tag{1.4}$$

Moreover the two following fractions are defined:

- In the rest system of the incoming proton the fraction of the electron energy which is transferred to the hadronic final state is given by:

$$y \widehat{=} \frac{q \cdot P}{k \cdot P} \tag{1.5}$$

- The fraction of the momentum of the scattered parton with respect to the proton momentum, is called "Bjorken scaling variable":

$$x_B \widehat{=} \frac{Q^2}{2P \cdot q} \tag{1.6}$$

From the previous definitions $W_{\gamma p}$ and y can be rewritten as follows

$$W_{\gamma p}^2 = y(s - m_e^2 - m_p^2) - Q^2 + m_p^2 \tag{1.7}$$

$$y = \frac{W_{\gamma p}^2 + Q^2 - m_p^2}{s - m_e^2 - m_p^2} \tag{1.8}$$

Which simplifies in the photoproduction regime to

$$W_{\gamma p}^2 \approx ys \tag{1.9}$$

$$y \approx \frac{W_{\gamma p}^2}{4E_e E_p} \tag{1.10}$$

Masses were neglected in these equations.

1.3 The Charmonium System

The Charmonium system is formed by charm-anticharm bound states (figure 1.4). The existence of these bound states can be explained at small distance by a potential like for atoms, but at large distance quarks are confined. As for atoms many radiative transitions are observed between the state of the Charmonium system.

The first member of this family to be discovered was the J/ψ meson. It was discovered simultaneously by two groups in 1974, the so called November revolution. Aubert et al. [1] reported an enhancement in the e^+e^- invariant mass spectrum of the reaction $pBe \longrightarrow e^+e^-X$ at the Brookhaven Laboratory. They called this new particle "J". While Augustin et al. [2] observed a sudden rise in the e^+e^- annihilation cross section at the SPEAR machine in Stanford. The Spark-chamber picture of the figure 1.5 suggested to call this new particle Ψ. In fact this event is a $\psi(2S)$. It was established afterwards that they discovered the same particle, and it was called J/ψ. The discovery was awarded with the 1976 Nobel Price in physics for Samuel C.C. Ting from BNL and Burton Richter from SLAC.

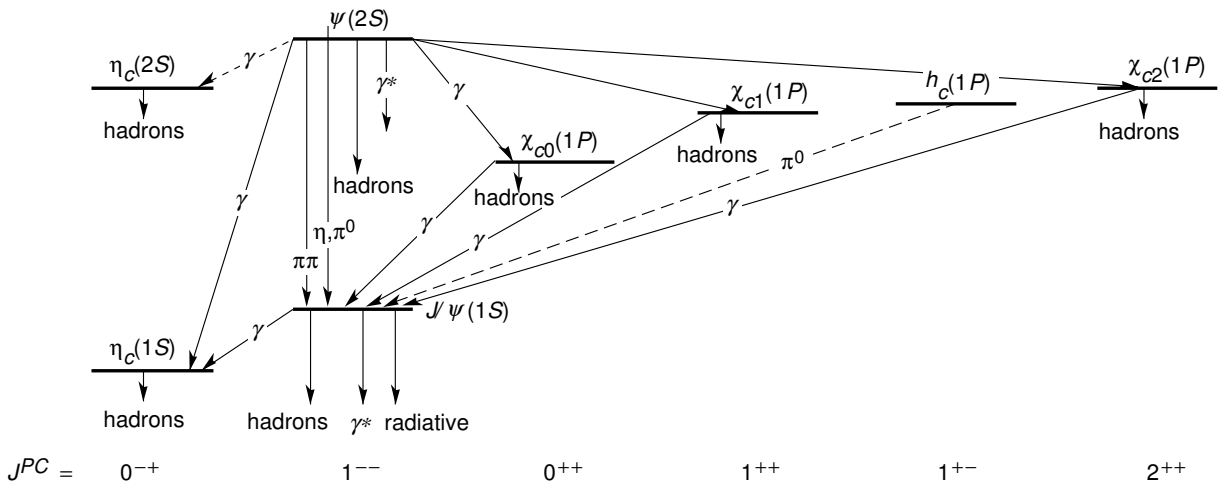

Figure 1.4: The Charmonium spectrum. States and transitions actually known. Picture is extracted from Particle Data Group [3].

The J/ψ meson is the lightest vector meson of this family. It has a mass of $3\,096.916 \pm 0.011$ MeV [3], and the same quantum numbers as the photon $J^{PC} = 1^{--}$. The first radial excitation of the J/ψ meson, the ψ(2S) meson, has a mass of $3\,686 \pm 0.034$ MeV. The most peculiar property of the J/ψ and ψ(2S) meson is probably their extremely small decay width:

$$\begin{aligned} \Gamma_{\mathrm{J}/\psi} &= 91.0 \pm 3.2\,\mathrm{keV}, \\ \Gamma_{\psi(2\mathrm{S})} &= 281 \pm 17\,\mathrm{keV}. \end{aligned}$$

This is about three orders of magnitude below that of typical hadronic decays, e.g. of the ρ meson. The most obvious decay mode would be the decay into two charmed mesons [2] (D mesons), but both the J/ψ and the ψ(2S) meson have masses below the threshold of $\mathrm{D\overline{D}}$ production, since the mass of the lightest D meson, the D^0, is approximately 1 860 MeV. Other hadronic decays can only proceed via diagrams which are forbidden by the Zweig rule, and are thus suppressed. The decays via a single gluon and via two gluons are not possible due to colour and charge-parity conservation, such that at least three gluons are needed for the hadronic decay of the J/ψ meson. The J/ψ meson can also decay via a virtual photon in two leptons.

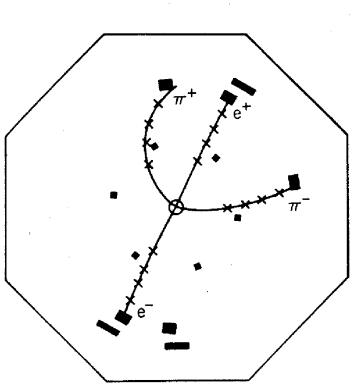

Figure 1.5: Event showing the decay of a ψ(2S) meson in the Spark-chamber

[2] A bound state composed of an up or down quark with a charmed quark

The following table gives the branching ratios of the J/ψ meson:

e^-e^+	5.93 ± 0.10 %
$\mu^-\mu^+$	5.88 ± 0.10 %
total hadrons	87.7 ± 0.5 %

This analysis is focused on the decay J/$\psi \longrightarrow \mu^-\mu^+$. The muonic decay mode is interesting since muons can be tagged by the instrumented iron detector. In particular it was possible to design an efficient trigger for this channel.

The following table gives the branching ratios of the ψ(2S) meson:

$\mu^-\mu^+$	0.73 ± 0.08 %
J/ψ π^+ π^-	31.7 ± 1.1 %
J/ψ anything	57.6 ± 2.0 %
J/ψ neutrals	24.6 ± 1.2 %
J/ψ π^0 π^0	18.8 ± 1.2 %
J/ψ η	3.16 ± 0.22 %

More than 50 % of its decays include a J/ψ meson which leads to significant background contributions for direct J/ψ meson production. The decay ψ(2S) $\longrightarrow$ J/$\psi\pi^+\pi^-$ can be suppressed by requiring more than four tracks, or a cut on the invariant mass for events with exactly four tracks. However the decay with additional neutral particles cannot be suppressed easily, since they do not have tracks but only clusters. The muonic decay is less than 1 %.

The three P wave states χ_{c0}(1P), χ_{c1}(1P), and χ_{c2}(1P) have a mass between the J/ψ and ψ(2S) meson. All χ_c meson can decay into a J/ψ meson via emission of a photon. The following table gives the branching ratios:

χ_{c0}(1P) $\longrightarrow$ J/$\psi\gamma$	1.18 ± 0.14 %
χ_{c1}(1P) $\longrightarrow$ J/$\psi\gamma$	31.6 ± 3.3 %
χ_{c2}(1P) $\longrightarrow$ J/$\psi\gamma$	20.2 ± 1.7 %

1.4 J/ψ Meson Kinematics

Before discussing the theoretical models of J/ψ meson production, an estimator z to measure the elasticity of the collision will be defined and then the polarisation of the J/ψ meson will be described.

1.4.1 The Elasticity

At HERA different production mechanisms are possible for the photoproduction of J/ψ mesons. For all these production mechanisms, the electron acts as a source of quasi-real photons which interact with a gluon from the proton via a specific mechanism that produce the J/ψ meson.

We define the elasticity z by:

$$z \widehat{=} \frac{P_\psi . P}{q . P} \tag{1.11}$$

$$= \frac{(E - Pz)_\psi}{2E_e y} \tag{1.12}$$

where $P_{J/\psi}$ is the four momentum of the J/ψ meson. In the proton rest system the elasticity measures the fraction of the photon energy transferred to the J/ψ meson. This variable is a powerful estimator

to distinguish different production mechanisms. A relativistic collision is defined as elastic, when the kinetic energy, the rest energy, and the mass are conserved. In the case of elastic J/ψ mesons production, the virtual photon fluctuates to a J/ψ meson and all its energy is transferred to the J/ψ meson. On the other hand for inelastic collisions, some energy from the virtual photon is transferred to the proton, provoking its destruction due to the perturbations. Then kinetic energy of the remnant proton particles is transformed in mass during the hadronisation processes. In this way z has a value close to one for elastic production, while z is below one for inelastic processes.

1.4.2 J/ψ Meson Polarisation

The polarisation of the J/ψ meson is an interesting observable because it is expected to differ in the various theoretical approaches discussed later, and could in principle be used to distinguish between them, independently of normalisation uncertainties.

The polarisation can be measured via the decay angular distribution in the muonic decay mode J/$\psi \longrightarrow \mu^-\mu^+$, which can be parametrised in the J/ψ meson rest frame as

$$\frac{d\sigma}{d\Omega dx} \propto 1 + \lambda(x)\cos^2\theta^\star + \mu(x)\sin 2\theta^\star \cos\phi^\star + \frac{\nu(x)}{2}\sin^2\theta^\star \cos 2\phi^\star \tag{1.13}$$

where x stands for a set of variables and the angles $\theta^\star$ and $\phi^\star$ denote the polar and the azimuthal angle of the positive decay muon with respect to a coordinate system defined in the J/ψ meson rest frame. In the following the recoil or s-channel helicity frame will be used, where the z-axis is defined to lie along the direction of the J/ψ three-momentum in the photon-proton centre-of-mass frame. Figure 1.6 illustrates the definition of $\theta^\star$ and $\phi^\star$ in the helicity frame. The parameters λ and ν can be related to the polarisation of the J/ψ meson. The cases $\lambda = 1$ and -1 correspond to complete transverse and longitudinal polarisation of the J/ψ mesons respectively.

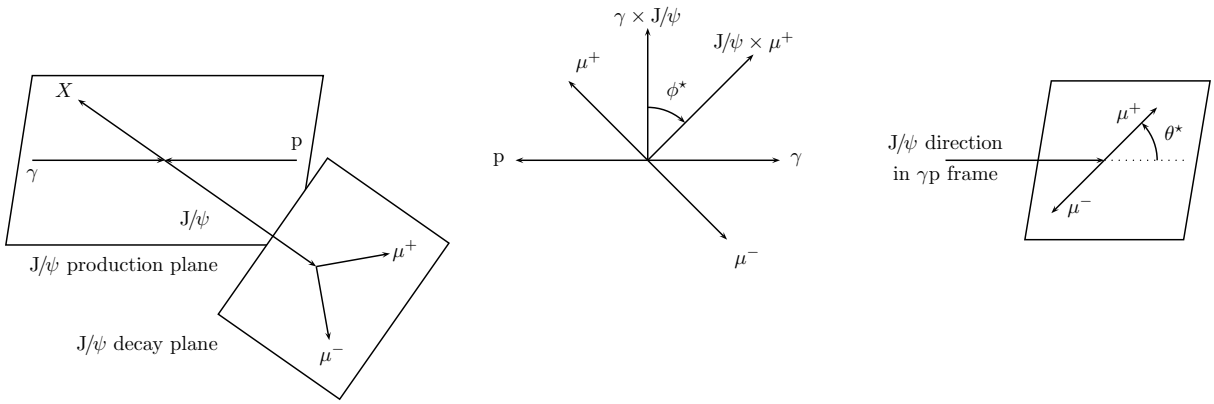

Figure 1.6: Illustration of the decay angles $\theta^\star$ and $\phi^\star$ in the helicity frame for the muonic decay J/$\psi \longrightarrow \mu^-\mu^+$, $\phi^\star$ is the azimuthal angle of the positive decay muon and corresponds to the angle between the J/ψ production and decay planes, $\theta^\star$ is the polar angle of the positive decay muon with respect to the J/ψ meson direction in the J/ψ decay plane.

In the case of limited statistics it is reasonable to study each decay angle separately. The integration of the formula (1.13) leads to

$$\frac{d\sigma}{d\cos\theta^\star dx} \propto 1 + \lambda(x)\cos^2\theta^\star,$$
$$\frac{d\sigma}{d\phi^\star dx} \propto 1 + \frac{\lambda(x)}{3} + \frac{\nu(x)}{3}\cos 2\phi^\star$$

These angles can be expressed in terms of the momentum vectors of the particles [4, 5]:

$$\cos\theta^\star = \frac{\overrightarrow{P_\psi}\cdot\overrightarrow{P_{\mu^\star}}}{\left|\overrightarrow{P_\psi}\right|\left|\overrightarrow{P_{\mu^\star}}\right|}$$

$$\cos\phi^\star = \frac{\left(\overrightarrow{v}\times\overrightarrow{P_\psi}\right)\cdot\left(\overrightarrow{P_\psi}\times\overrightarrow{P_{\mu^\star}}\right)}{\left|\overrightarrow{v}\times\overrightarrow{P_\psi}\right|\left|\overrightarrow{P_\psi}\times\overrightarrow{P_{\mu^\star}}\right|}$$

$$\sin\phi^\star = \frac{-\left[\left(\overrightarrow{v}\times\overrightarrow{P_\psi}\right)\times\overrightarrow{P_\psi}\right]\cdot\left(\overrightarrow{P_\psi}\times\overrightarrow{P_{\mu^\star}}\right)}{\left|\left(\overrightarrow{v}\times\overrightarrow{P_\psi}\right)\times\overrightarrow{P_\psi}\right|\left|\overrightarrow{P_\psi}\times\overrightarrow{P_{\mu^\star}}\right|}$$

where $\overrightarrow{v}$ is equal to $-\overrightarrow{P_{\rm p}}$, and $\overrightarrow{P_{\mu^\star}}$ denotes the momentum vector of the positive muon in the J/ψ meson rest frame.

1.5 Models for Inelastic Production of J/ψ Mesons

In the present section, the three main models for inelastic Charmonium production will be presented in their historical order. Many models have been suggested to describe inelastic J/ψ mesons production in the framework of perturbative Quantum Chromodynamics (pQCD) such as the soft colour interactions, the colour evaporation model, the Colour Singlet Model (CSM), and finally a non-relativistic QCD approach (NRQCD) to accommodate results in $\mathrm{p\overline{p}}$ collisions at the Tevatron.

The following will state an introduction for experimental physicists on the subject. Readers interested to go thoroughly into this subject can find a recent review in the preprint of Jean-Philippe Lansberg [6], as well as in the references given in the followings lines.

For all presented models the production of the $\mathrm{c\overline{c}}$ pair is treated separately from its evolution into a bound state [3]. This method is called factorisation [4], and is considered to be legitimate because the production of the $\mathrm{c\overline{c}}$ pair proceeds on a short time scale of order $1/m_{\rm c}$, while the formation of the bound state is a non-perturbative long distance process on a time scale longer than $1/\Lambda_{\rm QCD}$. The theoretical descriptions of J/ψ meson production differ in many details. One important difference concerns the states they allow for the intermediate $\mathrm{c\overline{c}}$ pair produced in the hard photon gluon interaction in terms of angular momentum and colour. Furthermore they differ in the non perturbative description of the transition from the intermediate $\mathrm{c\overline{c}}$ pair to the J/ψ meson.

Before to provide the relevant theoretical models, the inelastic production of heavy quark pairs at HERA will be now described.

[3] The evolution of the $\mathrm{c\overline{c}}$ pair into a bound state is called *hadronisation*.

[4] One can imagine this factorisation as ($\mathrm{c\overline{c}}$ pair production) $\times$ (evolution into a bound state).

1.5.1 Inelastic Production of Heavy Quark Pairs

Two classes of inelastic production mechanisms of heavy quark pairs are important at HERA, the resolved photon process, which is important at low z, and the direct photon-gluon fusion, important at medium z, which is the dominant process on the overall cross section.

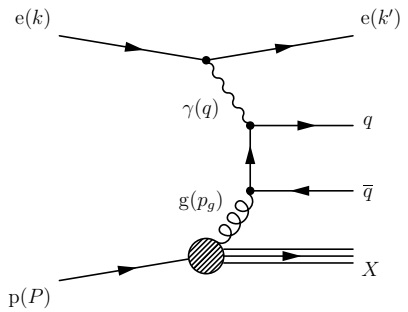

Figure 1.7: Feynman diagram for direct photon-gluon fusion of a $q\overline{q}$ pair in leading order, $\mathcal{O}(\alpha_s)$.

The generic Feynman diagram for direct photon-gluon fusion in leading order, $\mathcal{O}(\alpha_s)$, is shown in figure 1.7. The virtual photon and a gluon from the proton fuse via a virtual c quark. The fractional momentum of the gluon inside the proton is denoted x_g:

$$p_g = x_g P.$$

The gluon content of the proton is described by a parton density function (PDF). Since the full momentum of the photon enters in the production of the c$\overline{\text{c}}$ pair, this reaction is kinematically possible at comparatively small centre of mass energies of the photon-proton system. The elasticity z, which is a measure for the energy transferred from the virtual photon to the J/ψ meson, has typically medium to large values.

The second class of production mechanisms consists of resolved photon processes, where a photon with very small virtuality Q^2 [5] behaves like a hadron, and interacts via its partonic content. The fractional parton momentum inside the photon is denoted x_γ:

$$P_{parton} = x_\gamma P_\gamma.$$

The partonic content of the photon is described by a photon parton density function. For higher order calculations the separation into direct and resolved processes must be handled with care because some of the direct terms may be included in the photon PDF.

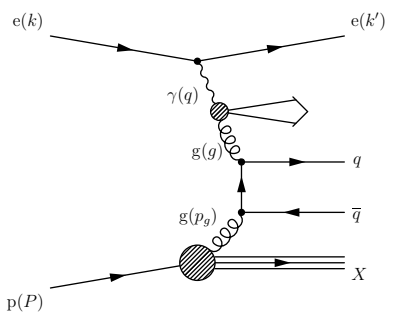

Figure 1.8: Feynman diagram for gluon-gluon fusion in leading order, $\mathcal{O}\left(\alpha_s^2\right)$, as an example for a process with a resolved photon

[5] $Q^2 \to 0$

The dominating process for heavy quark production at HERA with a resolved photon is thought to be gluon-gluon fusion, for which a generic Feynman diagram in leading order, $\mathcal{O}\left(\alpha_s^2\right)$, is shown in figure 1.8. A photon remnant is produced in addition to the proton remnant X in this process. Due to the small photon virtuality, Q^2, the photon remnant is in the direction of the beam of electrons, and therefore not detected. Since only a fraction of the momentum of the photon takes part in the J/ψ mesons production , the elasticity z is typically small, and high photon-proton centre of mass energies are required to produce J/ψ mesons.

1.5.2 The Colour Evaporation Model

The Colour Evaporation Model, also referred to as the "local duality approach", has been developed in the late seventies by Fritzsch et al. [7, 8, 9], and was revived in 1996 by Halzen et al. [10, 11]. Although qualitative agreement with the data is observed, the Colour Evaporation Model receives rather little interest in the literature due to its weak predictive power. Readers can find more details about it in the cited literature.

1.5.3 The Colour Singlet Model

The Colour Singlet Model (CSM) [12, 13, 14, 15], developed since 1980, was the first model to provide quantitative predictions for Charmonium production in a wide variety of environments: hadron collisions, photoproduction and e^-e^+ collisions.

This model is the most natural application of QCD to heavy quarkonium production in the high energy regime. It takes its inspiration in the factorisation theorem of QCD [16] where the hard part is calculated by the strict application of pQCD at leading order and the soft part is factorised in a universal wave function.

It is meant to describe not only the production of the ${}^3S_1$ states, J/ψ, ψ(2S),Υ(1S), Υ(2S) and Υ(3S) meson, but also the singlet S states η_c, and η_b as well as the $P(\chi)$ and D states. The concept of the CSM is based on several approximations or postulates [6]:

- Quarkonium production is decomposed into two steps, first the creation of two on-shell heavy quarks $q\overline{q}$ and second their binding to make the meson (in that case one postulates the factorisation of these two processes) [6].
- As the scale of the first process is approximately $M^2+P_t^2$, one can consider it is a perturbative process. One supposes its cross section is computable with Feynman-diagram methods.
- As we consider only bound states of heavy quarks (charm and bottom quarks), their velocity in the meson must be small. One therefore supposes the meson is created with its two constituent quarks at rest in the meson frame, the static approximation.
- One finally assumes the colour and the spin of the $q\overline{q}$ pair do not change during the binding into a meson. Since the physical states are colourless, one requires the original quark pair to be produced in a colour singlet state. This explains the name Colour Singlet Model. In other words, the model assumes that only $q\overline{q}$ pairs with the same quantum numbers (spin, angular momentum, charge, and parity) as the final meson contribute significantly to the Quarkonium production.

The generic Feynman diagrams for photoproduction of J/ψ mesons in the CSM in leading order are shown in figure 1.9. In direct photon-gluon fusion, an additional gluon is needed to produce a colour singlet state [6], while in gluon-gluon fusion, a gluon or a photon is needed to conserve the angular momentum and parity of the J/ψ meson.

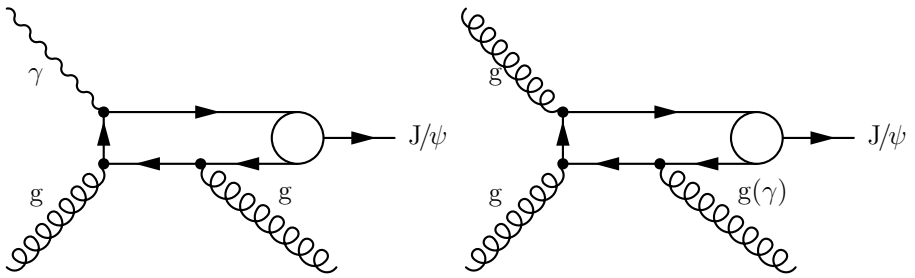

Figure 1.9: Feynman diagrams for J/ψ meson photoproduction in the Colour Singlet Model in (left) direct photon-gluon fusion and (right) gluon-gluon fusion. The c$\overline{\text{c}}$ pair after emission of a hard gluon is produced in the colour and angular momentum state of the J/ψ mesons.

The cross section is factorised into a short distance matrix element describing the c$\overline{\text{c}}$ production in a region of size $1/m_{\text{c}}$, and a long distance factor that describes the non-perturbative dynamics of the bound state formation. The differential cross section for J/ψ meson production can thus be written as:

$$d\sigma\left(\text{J}/\psi + X\right) = d\hat{\sigma}\left(\text{c}\overline{\text{c}}\left(\underline{1},^3 S_1\right) + X\right) \times \left|R_\psi(0)\right|^2, \tag{1.14}$$

where $R_\psi(0)$ is the J/ψ meson radial wave function at the origin, the notation $\left(\underline{1},^3 S_1\right)$ is used to denote that the c$\overline{\text{c}}$ pair is in a colour singlet state, and has the spectroscopic state of the J/ψ meson.

The short distance part $d\hat{\sigma}$ can be calculated using a perturbative expansion in $\alpha_s\left(m_{\text{c}}\right)$, while the long distance part at leading order is related to the measured muonic width $\Gamma_{\mu^-\mu^+}$ of the J/ψ meson:

$$\Gamma_{\mu^-\mu^+} \simeq \frac{4\alpha^2}{9m_{\text{c}}^2}\left|R_\psi(0)\right|^2. \tag{1.15}$$

If the CSM is applied to the production of J/ψ mesons at HERA, the leading contribution in the photon gluon fusion process is of order $\mathcal{O}\left(\alpha, \alpha_s^2\right)$, since at least one additional gluon is needed to produce a c$\overline{\text{c}}$ pair with the quantum numbers of the J/ψ mesons (cf. figure 1.9). In order to ensure the applicability of the perturbative expansion, the additional gluon has to be hard; therefore the Colour Singlet Model prediction is only reliable in the region $z \lesssim 0.9$.

The next-to-leading order (NLO) diagrams $\mathcal{O}\left(\alpha, \alpha_s^3\right)$ have been calculated by Krämer [17] for direct photon-gluon fusion and were found to give large corrections to the leading order prediction for $z \gtrsim 0.8$ and $P_{t,\psi}^2 \lesssim 1\,\text{GeV}^2$, thus further restricting the regime of applicability of the LO calculation. Only LO calculation are available for the resolved process up to now.

The greatest quality of the CSM resides in its predictive power. The only non perturbative parameter required by the model for Quarkonium production, excepted the parton density function, is the wave function $R_\psi(0)$, which is independent of the production process and can be determined from data on decay processes or by application of potential models. Nothing more is required.

On the other hand, severe experimental and theoretical problems persist. Theoretically, the most serious limitation of the Colour Singlet Model is the absence of a general theorem ensuring the validity of the above factorisation. It is not clear whether higher order radiative corrections would respect this factorisation [18]. It can also be considered incomplete, since it does not cover

[6] The colour flow enters by the fused gluon and comes out by the radiated gluon.

the production of $c\overline{c}$ pairs in colour octet states which evolve into colour singlet Charmonium states through the emission of soft gluons. Relativistic effects which may be of importance in the $c\overline{c}$ system are also neglected in the CSM [19]. Moreover predictions in the CSM have a large normalisation uncertainty due to the choice of the proton parton density function, the mass of the charm quark and the value of α_s.

Experimentally, the Colour Singlet Model in leading order is more or less ruled out by several observations. The most prominent failure of the model are the cross sections for prompt [7] J/ψ and ψ(2S) meson production measured by the CDF and D0 collaborations at the Tevatron $p\overline{p}$ collider. For large transverse momenta P_t of the J/ψ meson, the Colour Singlet Model predictions are more than one order of magnitude below the data, cf. figure 1.10. Prior to these measurements, the dominant contribution to Charmonium production at the Tevatron was expected to proceed via gluon gluon fusion in the Colour Singlet Model, with the leading order being approximately α_s^3. In addition cross sections for P wave states like the χ_c, show infrared divergences in the CSM.

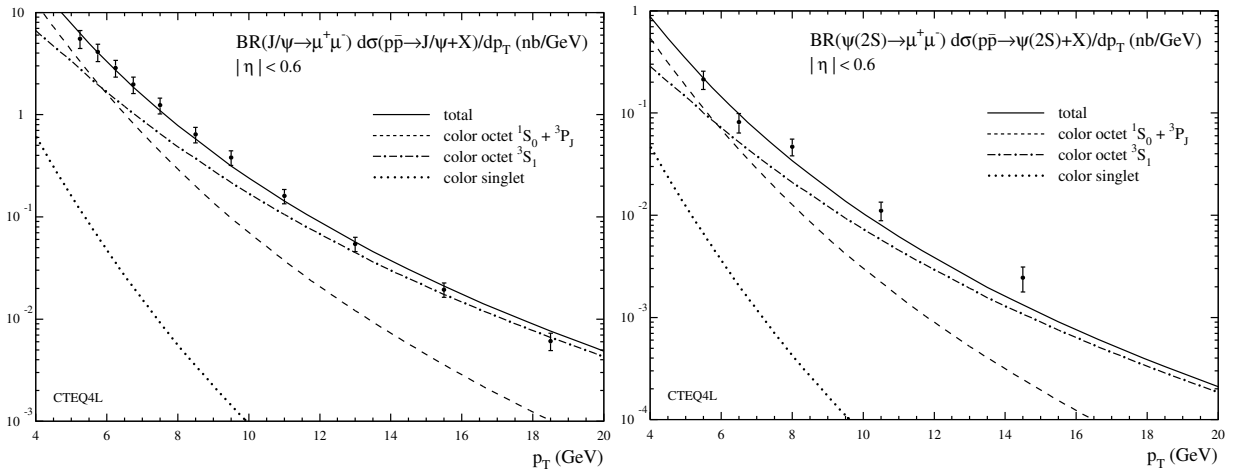

Figure 1.10: Differential cross section $d\sigma/dP_t$ times the branching ratio $\mathcal{B}(\mathrm{J}/\psi \longrightarrow \mu^-\mu^+)$ for (left) direct J/ψ and (right) prompt ψ(2S) mesons production in $p\overline{p}$ collisions measured by CDF at $\sqrt{s} = 1.8\,\mathrm{TeV}$. Contributions from B hadron decays and χ decays have been removed. The lines are the theoretical expectations based on the Colour Singlet Model, and the result of fits of colour octet contributions to J/ψ and, in the case of ψ(2S), of a simultaneous fit to J/ψ and ψ(2S). For the J/ψ meson, the data include feed-down from ψ(2S) decays which is accounted for in the theoretical curves. For the theoretical predictions, CTEQ4L parton distribution functions have been used. Figures are from the publication [20]. For "colour octet" and "feed-down", see note [9].

A mismatch between theoretical expectation and measured cross sections was also found by the UA1 collaboration [21] at CERN in $p\overline{p}$ collisions at $\sqrt{s} = 630\,\mathrm{GeV}$. In fixed target experiments the Colour Singlet Model predictions were found to be up to two orders of magnitude too small [22].

Nevertheless, the Colour Singlet Model has been quite successful in describing inelastic ($z < 0.9$) photoproduction of J/ψ mesons at HERA and at fixed target muoproduction experiments (EMC, NMC). With a specific choice of parameters ($m_c = 1.4\,\mathrm{GeV}$ and $\Lambda = 300\,\mathrm{MeV}$), the differential cross section $d\sigma/dz$ is well described both in shape and normalisation by the aforementioned next-to-leading order calculation.

[7] *Prompt* indicates Charmonium states which are produced directly at the primary vertex, not by decays of B hadrons.

[9] For "colour octet", cf. section 1.5.4. The word "feed-down" refers to the upper state in the Charmonium system decaying in J/ψ meson, and thus constituting a source of pollution of the sample.

1.5.4 The Factorisation Approach within Non-Relativistic QCD

The approach discussed here was first applied for the prediction of decay rates of P wave Charmonium states ($\chi_{c0}(1P)$, $\chi_{c1}(1P)$, $\chi_{c2}(1P)$ and h_c by Bodwin, Braaten and Lepage (BBL) [23]. It was later developed into a complete theory [24, 25], and received much attention due to the ability to describe the large production rates for high P_t hadroproduction of J/ψ and $\psi(2S)$ meson at the Tevatron, first reported by the CDF experiment (cf. figure 1.10).

This model is called Colour Octet Model (COM) as opposed to the Colour Singlet Model, since colour octet states of the $c\overline{c}$ pair can also contribute to Charmonium production via the emission of soft gluons. The $c\overline{c}$ pairs can be produced in colour singlet as well as colour octet states. According to QCD only the final state of the J/ψ meson must be in a colour singlet state.

In the BBL formalism, the production cross section for a Charmonium state can be expressed as

$$d\sigma\left(\mathrm{J}/\psi + X\right) = \sum_n c_n \left(c\overline{c}[n] + X\right) \times \left\langle \mathcal{O}_n^{\mathrm{J}/\psi} \right\rangle, \tag{1.16}$$

where n denotes an on-shell $c\overline{c}$ pair in a definite colour, spin and angular momentum state. The cross section is the sum over all possible states n of the $c\overline{c}$ pair. For each n, the cross section factorises into a short distance part c_n, and a long distance part $\langle \mathcal{O}_n^{\mathrm{J}/\psi} \rangle$. The c_n are short distance parton cross sections for producing a $c\overline{c}$ pair with vanishing relative momentum. They correspond to parts of Feynman diagrams where all internal lines are off-shell by amounts of order m_c, or larger. Therefore they are calculable in a perturbative QCD expansion in $\alpha_s(2m_c)$. The long distance non-perturbative factors $\langle \mathcal{O}_n^{\mathrm{J}/\psi} \rangle$ are called Colour Octet Matrix Elements (COMEs) and describe the evolution of the $c\overline{c}$ pair into a J/ψ meson plus additional soft gluons. They correspond to those parts of the Feynman diagrams where the internal lines are off-shell by amounts much less than m_c. While in the Colour Singlet Model all c_n not corresponding to a colour singlet $c\overline{c}$ are set to zero, the BBL formalism includes states where the $c\overline{c}$ system is in a colour octet state.

The major second ingredient in the theory besides factorisation is the introduction of non relativistic QCD [26] (NRQCD) velocity scaling rules that make the application of equation (1.16) possible. NRQCD is an effective field theory in which the heavy quark and anti-quark are treated non-relativistically. It organises calculations of heavy quarkonium observables into an expansion in powers of v, where v is the relative velocity of the quarks in the heavy quarkonium.

At first sight, equation (1.16) is not particularly useful since it involves an infinite number of non-perturbative factors $\langle \mathcal{O}_n^{\mathrm{J}/\psi} \rangle$. However, it can be deduced from NRQCD that each matrix elements $\langle \mathcal{O}_n^{\mathrm{J}/\psi} \rangle$ scales with a defined power of v. Since v is a small quantity, $v^2 \simeq 0.3$ for the J/ψ meson, the expansion can be truncated to a low order in v. For J/ψ mesons production the leading order term is the colour singlet one $\left(\mathcal{O}^{\mathrm{J}/\psi}\left[\underline{1}, {}^3S_1\right]\right)$ scaling with v^3. The following order scales with v^7 and consists of $\left(\mathcal{O}^{\mathrm{J}/\psi}\left[\underline{8}, {}^1S_0\right]\right)$, $\left(\mathcal{O}^{\mathrm{J}/\psi}\left[\underline{8}, {}^3S_1\right]\right)$ and $\left(\mathcal{O}^{\mathrm{J}/\psi}\left[\underline{8}, {}^3P_{J=0,1,2}\right]\right)$ [10].

In the non relativistic limit $v \to 0$ the Colour Singlet Model is restored. Colour octet contributions are suppressed by powers of v^4, and can only become important when the corresponding short distance coefficients c_n for colour octet states are large.

The Colour Octet Matrix Elements cannot be calculated perturbatively, but they are assumed to be universal if the factorisation holds. Therefore it should be possible to determine their values from one experiment and make predictions for other production processes. The measurement of the colour octet matrix elements provides thus a crucial test of the theory. Moreover they can be computed numerically by lattice QCD.

[10] The notations $\underline{1}$, and $\underline{8}$ refer to the colour configuration of the $c\overline{c}$ pair, $\underline{1}$ for a colour singlet and $\underline{8}$ for a colour octet.

Calculations for photoproduction based on the NRQCD approach, and parametrised by measured COMEs, are available in LO taking into account the contributions $(\mathcal{O}^{J/\psi}\left[\underline{1},^3 S_1\right])$, $(\mathcal{O}^{J/\psi}\left[\underline{8},^1 S_0\right])$, $(\mathcal{O}^{J/\psi}\left[\underline{8},^3 S_1\right])$ and $(\mathcal{O}^{J/\psi}\left[\underline{8},^3 P_{J=0,1,2}\right])$. The relative strength of the colour octet contributions depends crucially on the size of the corresponding COMEs. Unfortunately the values for the COMEs important at HERA still show large uncertainties, a summary can be found in [27]. Early extractions of the COMEs from $p\overline{p}$ data were performed in LO. Subsequent estimates of higher order effects led to considerably smaller values [28, 29, 30, 31].

At HERA the colour octet term which is of leading order in α_s, is the fusion of a photon and a gluon without emission of additional hard gluons (figure 1.11 left). In photoproduction the photon is nearly collinear with the beam electron. In the collinear approach the gluon inside the proton is assumed to follow the proton direction. Thus the J/ψ meson cannot have large transverse momentum if it is the only particle produced. A cut $P_t > 1\,\mathrm{GeV}$ is believed to remove the leading order contribution completely. One of the next-to-leading order $\mathcal{O}\left(\alpha_s^2\right)$, diagrams (right) is similar to the CSM diagram with the difference, that other colour and angular momentum states are allowed for the $c\overline{c}$ pair. The $\left[\underline{8},^3 S_1\right]$ state has the same kinematics as the colour singlet term, but the COME is suppressed by a factor v^4. Therefore it can be neglected in view of the normalisation uncertainty of the CSM. For the $\left[\underline{8},^1 S_0\right]$ and the $\left[\underline{8},^3 P_{J=0,1,2}\right]$ state additional diagrams with t-channel exchange of a gluon contribute. Therefore their perturbative cross sections c_n depend differently on P_t and z. They are expected to dominate at high values of z at HERA, where the distinction from diffraction is not clear.

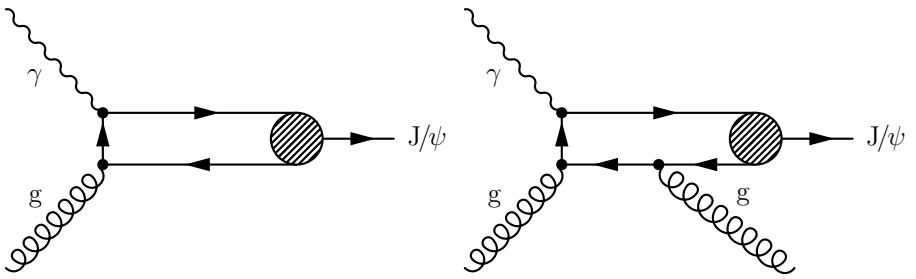

Figure 1.11: Feynman diagrams for J/ψ mesons photoproduction in direct photon-gluon fusion in the Colour Octet Model in (left) leading order $\mathcal{O}\left(\alpha_s\right)$ and (right) next-to-leading order $\mathcal{O}\left(\alpha_s^2\right)$, The $c\overline{c}$ pair can be in a colour singlet or colour octet state. It evolves into the J/ψ meson via emission of soft gluons.

One prediction of NRQCD which can be used to check the consistency of the approach is the polarisation of prompt J/ψ and ψ(2S) at the Tevatron. The colour octet gluon fragmentation, with which the Charmonium state tends to inherit the transverse polarisation of the gluon, should dominate the cross section at large P_t. Therefore the deviations from a full transverse polarisation of the Charmonium state should become smaller with rising P_t. Unfortunately the CDF measurements do not show this behaviour, cf. figure 1.12, neither for the prompt J/ψ nor for the ψ(2S). Moreover the CDF collaboration at present gives no explanation why the data of the run II disagree the run I. But anyway, both disagree the NRQCD model. We can conclude that no satisfactory model is available to describe the Charmonium production at Tevatron, and for the incoming LHC collider.

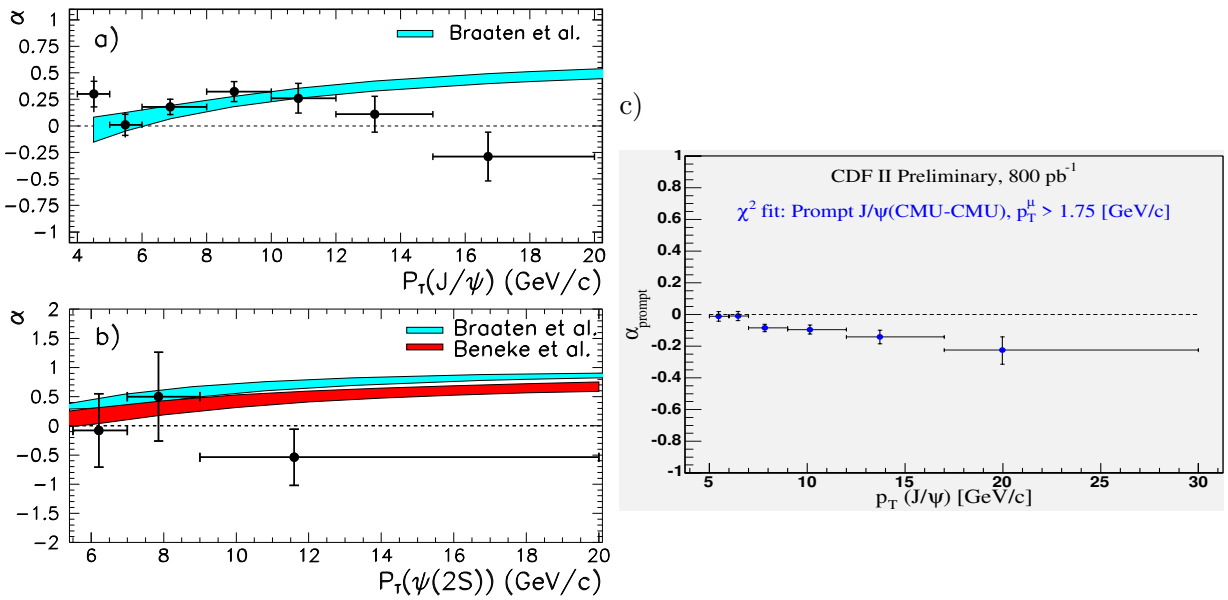

Figure 1.12: Polarisation parameter α (which is noted λ in this thesis for prompt J/ψ and prompt ψ(2S) production in $p\overline{p}$ collisions measured by CDF [32, 33]. a) and b) are for run I and c) for run II. Unpolarised mesons have $\alpha = 0$, whereas $\alpha = +1$ or -1 correspond to fully transverse or fully longitudinal polarisations respectively. The shaded bands show NRQCD predictions.

1.5.5 The Status at HERA

A complete review of the inelastic photoproduction of J/ψ mesons at HERA is given in the publication of the H1 collaboration [34], and for leptoproduction [35]. The published analysis covers the data of the HERA I data taking periods, and thus profits from the statistics of the last two good years, 1999 and 2000. The following will described the main points of this publication. The data selection and the parameters of the models are detailed in the publication and the doctoral theses [36, 37].

1.5.5.1 Comparison of Cross Sections with the Colour Singlet Model

The photon proton cross sections $\sigma_{\gamma p}$, $d\sigma/dz$ and $d\sigma/dP^2_{t,\psi}$, for the medium z range are shown in figures 1.13 and 1.14. The kinematic range is given in figure 1.13. The data are compared with the NLO CSM calculations. The band on the theoretical calculations represents the uncertainties caused by the choice of the mass of the charm quark, $m_c = 1.4 \pm 0.1\,\text{GeV}$, and of $\alpha_s(m_Z) = 0.120\,0 \pm 0.002\,5$. These uncertainties, for the $W_{\gamma p}$ and z distributions, affect mainly their normalisations. The shapes and the normalisations of the calculated cross sections as functions of $W_{\gamma p}$ and z are approximately in agreement with the data for the two parameter sets, $(m_c, \alpha_s(m_Z)) = (1.3\,\text{GeV}, 0.117\,5)$, and $(1.4\,\text{GeV}, 0.122\,5)$. The NLO CSM calculation describes the $P^2_{t,\psi}$ distribution rather well (cf. figure 1.14). This is not the case for the LO CSM calculation, which lies above the data at low $P^2_{t,\psi}$, and falls too steeply towards higher values of $P^2_{t,\psi}$. The dependence in $P^2_{t,\psi}$ is sensitive to the choice of m_c and α_s. The calculations with the two parameter sets, with which the $W_{\gamma p}$ and z distributions are well described, also give a reasonable description of the dependence in $P^2_{t,\psi}$, apart from a tendency to undershoot the data at high $P^2_{t,\psi}$. The $P^2_{t,\psi}$ distribution in bins of z (cf. figure 1.14) is also described well by the NLO CSM calculation. This is interesting because the size of the colour octet contributions in the NRQCD approach is predicted to depend on z.

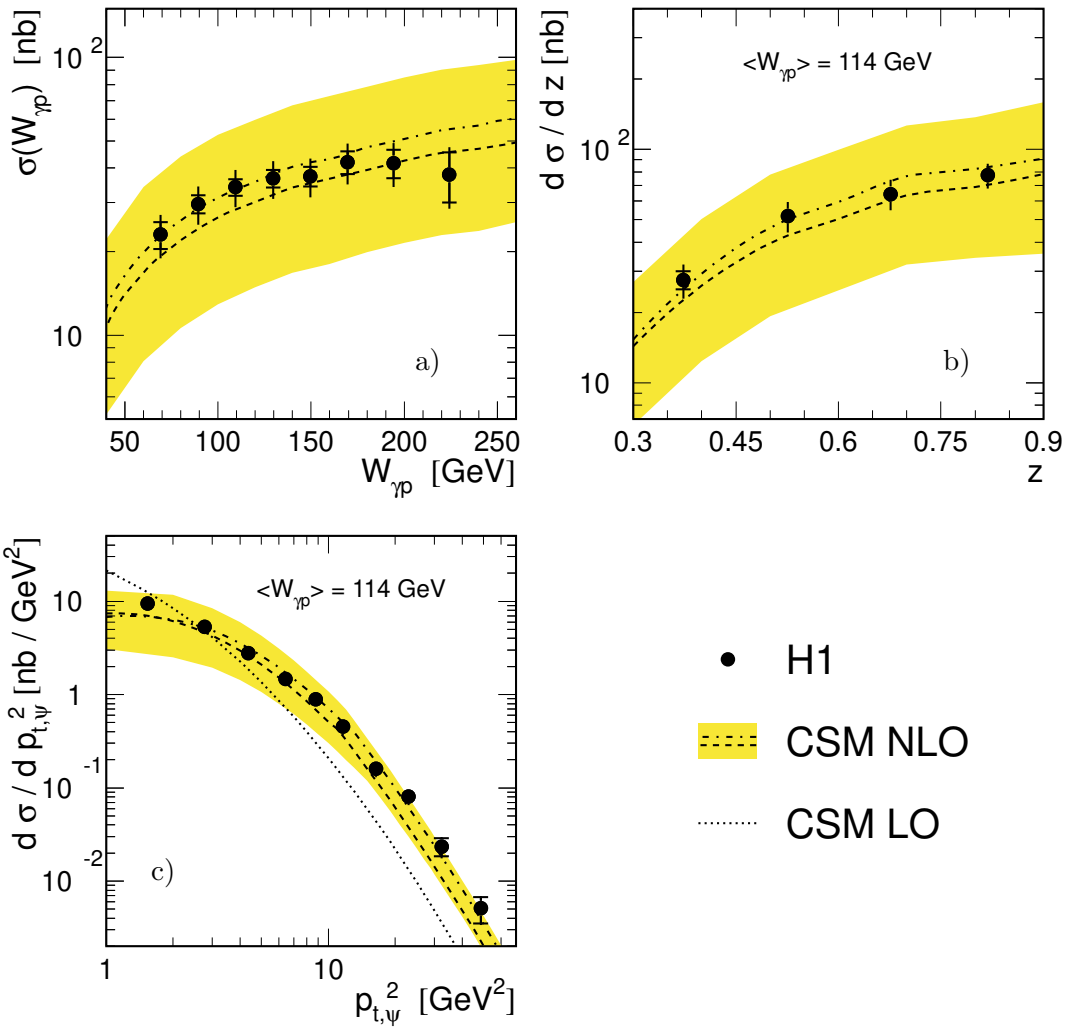

Figure 1.13: Inelastic J/ψ mesons production in the region $60 < W_{\gamma p} < 240\,\mathrm{GeV}$, $0.3 < z < 0.9$ and $P^2_{t,\psi} > 1\,\mathrm{GeV}^2$. a) Total cross section as a function of $W_{\gamma p}$, b) differential cross sections $d\sigma/dz$ and c) $d\sigma/dP^2_{t,\psi}$. The H1 data are shown together with NLO calculations in the Colour Singlet Model with MRST parton density functions ($W_{\gamma p} = 114\,\mathrm{GeV}$ for b) and c)). The shaded band reflects the uncertainties in m_c, and α_s; the dashed (dash-dotted) curve is calculated with $m_c = 1.3(1.4)$ GeV, $\alpha_s(m_Z) = 0.117\,5(0.122\,5)$. In c) a CSM LO calculation with MRST parton distributions, $m_c = 1.3\,\mathrm{GeV}$, $\alpha_s(m_Z) = 0.122\,5$ is also shown (dotted).

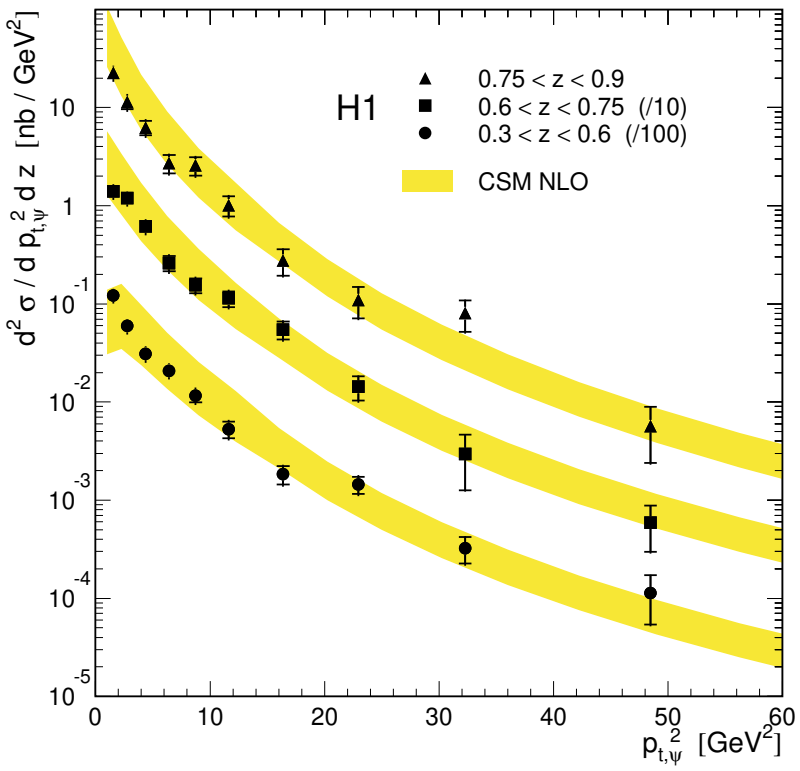

Figure 1.14: Double differential cross section $d^2\sigma/dP^2_{t,\psi}dz$ in the same kinematic region and compared with the same CSM NLO calculations as in figure 1.13.

1.5.5.2 Comparison of Cross Sections with NRQCD Calculations

The comparison of the measured cross sections $d\sigma/dP^2_{t,\psi}$, and $d\sigma/dz$ with the calculations within the NRQCD approach are shown in figures 1.15 and 1.16. For this comparison data in the low z region are included.

The LO NRQCD calculations are spoiled by considerable uncertainties. The band gives an estimate of the main uncertainty, which arises from the COMEs obtained from J/ψ mesons production in $p\overline{p}$ interactions. COMEs extracted in LO are used for the upper limit of the band, while values including estimates of higher orders in the extraction are used for the lower limit [29].

The distributions of $P^2_{t,\psi}$ are shown in figure 1.15 b) for the low and medium z ranges. In both z regions the NRQCD calculation [27] and the data are compatible within experimental and theoretical uncertainties. However the shapes seem to be different, since the data have a slightly harder spectrum than predicted. For the low z range one should keep in mind that the calculation is only for charm, while the data contain feed-down from b quarks, which is expected to contribute a harder transverse momentum distribution. In both z regions the colour singlet contribution alone falls significantly faster than the data.

The differential cross section $d\sigma/dz$ extending over the full z range, $0.05 < z < 0.9$, is compared with the same LO NRQCD calculation [27] in figure 1.16 for a cut $P^2_{t,\psi} > 1\,\mathrm{GeV}^2$. Resolved contributions are found to dominate in the calculation below $z \lesssim 0.15(0.3)$ depending on the choice of the COMEs. In the comparison of data and theory one should note that the contribution from b decays in the data is sizable at low z, of the order of 25 %. Nevertheless one may infer from figure 1.16 that the LO NRQCD calculation, including CS and CO contributions, is able to give a fair description of the data both in shape and in normalisation, if the COMEs are chosen to be close to the lowest available estimates (lower edge of the shaded band).

Using larger COME values in this calculation leads to a strong increase of the theoretical cross sections at high and low z values which is inconsistent with the measurements. The colour singlet contribution alone, which is also shown separately in figure 1.16, is approximately 30 % below the data for $z \gtrsim 0.5$, although the shape is adequately described in this region. At lower z values the colour singlet contribution falls below the data by up to a factor 3.

A different calculation in the NRQCD framework has been carried out by Kniehl et al. [28] and is shown in figure 1.16 labelled by "High Order improved". In this calculation higher order effects were taken into account, approximately using NLO parton density distributions for the photon and proton, and using the COMEs corrected for estimated higher orders effects. This calculation gives a good description of the shape of the data but a normalisation factor of 3, as suggested by the authors [28], is necessary to reconcile the predicted cross section with the data.

Using the higher order improved COMEs the Colour Octet contributions are expected to dominate only above $z > 0.9$, which means that previous analyses and the medium z analysis presented here are not sensitive to them due to the restriction in z.

The colour octet contributions to resolved photon processes are expected to increase the cross section at low z significantly, an order of magnitude based on the first COMEs or about a factor of 3 based on the higher-order improved COMEs.

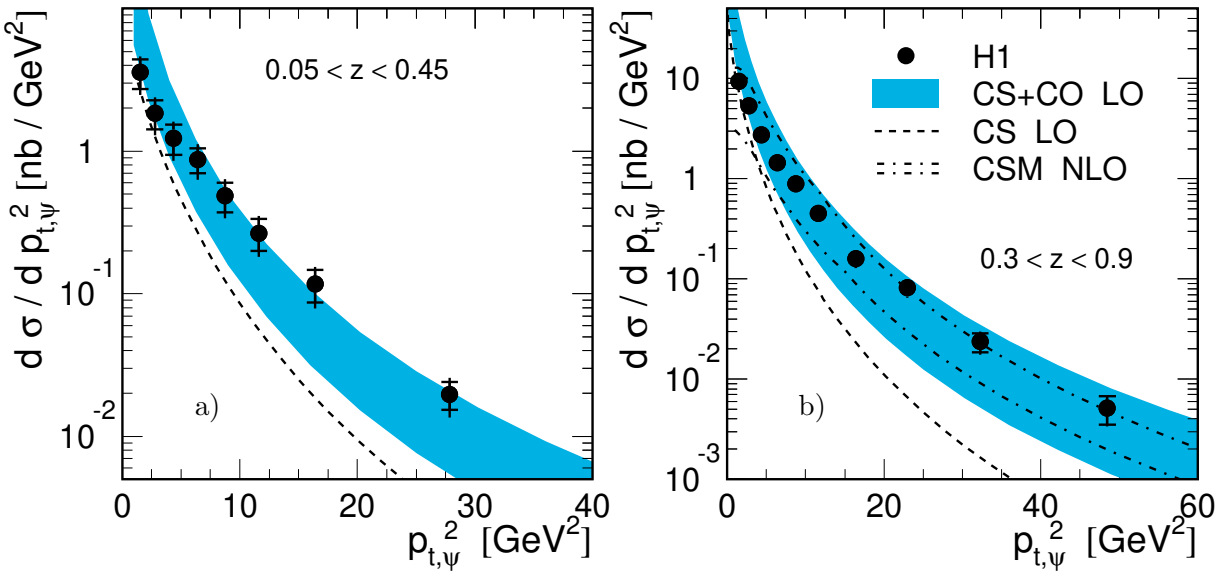

Figure 1.15: Differential cross section $d\sigma/dP^2_{t,\psi}$ for inelastic J/ψ mesons production in two kinematic regions. a) $0.05 < z < 0.45$, $120 < P^2_{t,\psi} < 260\,\text{GeV}$; b) $0.3 < z < 0.9$, $60 < P^2_{t,\psi} < 240\,\text{GeV}$ (same data as in figure 1.13). The data are compared with LO theoretical calculations in the NRQCD framework, including colour octet and colour singlet contributions from direct and resolved photons shown as the shaded band, which reflects the uncertainties due to the COMEs. The dashed line shows the colour singlet contribution separately. In b) the band of the same CSM NLO calculation [17] as in figure 1.13 c) is also shown as dash-dotted lines.

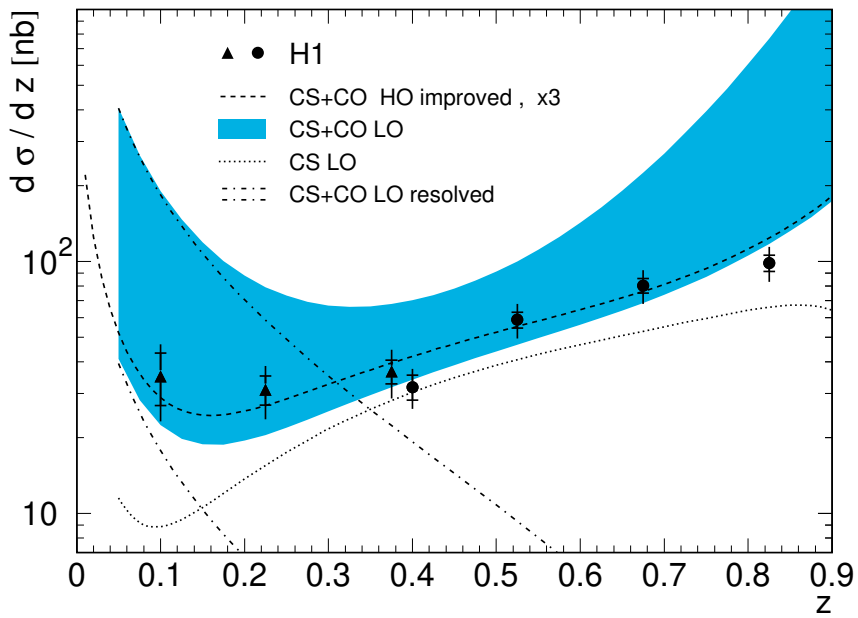

Figure 1.16: Differential cross section $d\sigma/dz$ for $120 < W_{\gamma p} < 260\,\text{GeV}$ and $P^2_{t,\psi} > 1\,\text{GeV}^2$. The data are shown as triangles and points, respectively low and medium z analysis. The two data points from different analyses at $z \approx 0.4$ are statistically correlated and offset for visibility. Theoretical calculations within the NRQCD framework including colour octet and colour singlet contributions from direct and resolved photons are shown for comparison. The shaded band is a calculation by Krämer [27] reflecting the uncertainties due to the COMEs. The two dash-dotted lines mark off the region of the resolved contributions separately. And the dotted line shows the colour singlet contribution. The dashed line is the result of a NRQCD calculation by Kniehl et al. [28], where higher order effects have been estimated and which has been normalised to the data. Note that the theoretical calculations are for charm only, while the data contain a residual background from b quarks at low z.

1.5.5.3 Conclusion of this Overview

The same analysis was performed by the ZEUS collaboration and gave compatible results with the H1 collaboration.

To conclude this overview, the Colour Singlet Model in NLO is sufficient to describe the data at HERA in photoproduction, despite the postulates and approximations made, in particular the restriction to the colour singlet state. The NRQCD approach, which takes into account the colour octet states, only seems necessary to describe the cross section for $p\overline{p}$ data. Moreover this approach fails to describe the polarisation up to now.

An overview of the calculations available in the low and medium z regions is given in table 1.1.

z region	contributing process	available theoretical calculations
medium z $0.3 < z < 0.9$	direct photon-gluon fusion	CSM NLO and LO, NRQCD LO
low z $0.05 < z < 0.45$	direct and resolved photon processes	CSM LO, NRQCD LO

Table 1.1: Overview of the calculations available in the low and medium z regions.

1.5.5.4 Preliminary Results of the ZEUS Collaboration

During this thesis, the ZEUS collaboration published a preliminary [38] covering HERA I and the first half of HERA II. The following will give the conclusion of these preliminary results.

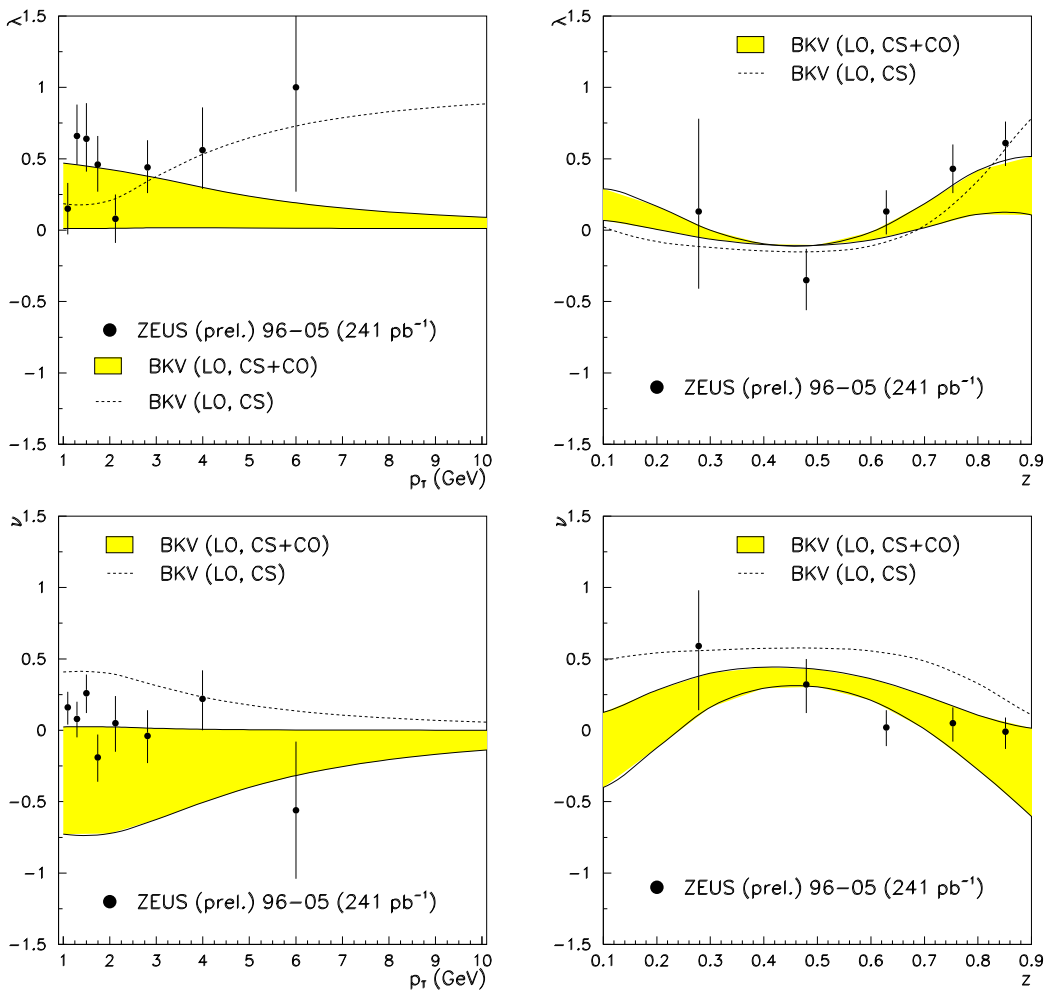

Figure 1.17: Distribution of the helicity parameter λ and ν as a function of $P^2_{t,\psi}$, and z. The error bars correspond to the total experimental uncertainties. The theoretical curves are described in the reference.

The J/ψ helicity distributions in inelastic photoproduction have been measured and compared to leading order QCD predictions in both CSM and COM frameworks. The helicity parameters λ and ν have been extracted (figure 1.17), in the target frame, as a function of the $P^2_{t,\psi}$ and the elasticity z. Within the experimental and theoretical errors, both the CSM and COM predictions have been found to fit the data reasonably well, but from the analysis of the azimuthal distributions the ZEUS data seem to disfavour the colour singlet only picture. This conclusion comes from the analysis of the parameter ν as a function of z and $P^2_{t,\psi}$ in this case ZEUS data are better described by a LO theoretical calculation taking care of CSM and COM contributions. This trend has been confirmed and made stronger by the increased statistics available with respect to the previous ZEUS preliminary result. An explicit NLO calculation is however required to quantify the theoretical uncertainty even if the helicity measurements, being mainly shape measurements, are not expected to be very sensitive to higher order corrections.

1.6 The Diffractive Processes

The cross section of J/ψ mesons is dominated by diffractive processes at high values of the elasticity z, $z \gtrsim 0.95$.

The diffractive processes will be described briefly here because it is only a source of background in this analysis, furthermore a sample of elastic J/ψ events is used to check the simulation of the muon identification in the LAr calorimeter and the instrumented iron detector. An introduction to soft physics can be found in [39].

Two processes are distinguished (cf. figure 1.18), the elastic scattering $\gamma p \longrightarrow J/\psi p$ where the proton stays intact, and proton dissociation $\gamma p \longrightarrow J/\psi X$, where the proton breaks up in a low mass baryonic state.

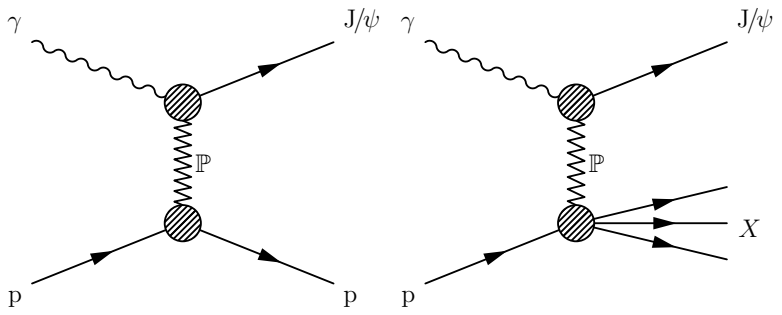

Figure 1.18: Feynman diagrams for diffractive J/ψ photoproduction: (left) elastic and (right) proton dissociative diffraction. The pomeron is denoted by $\mathbb{P}$.

Diffraction can be described within different frameworks. In the Vector Meson Dominance Model (VDM) the photon fluctuates into a vector meson before the interaction with the proton occurs. The scattering of the vector meson and the proton is described within Regge theory via the exchange of a pomeron $\mathbb{P}$, a colourless object with the quantum numbers of the vacuum. The Regge theory was developed to describe diffractive processes on a phenomenological basis and takes its inspiration from the physics of optical diffraction.

While Regge theory can reproduce the cross sections for light meson photoproduction such as ρ [40, 41] and ϕ [42], the $W_{\gamma p}$ dependence of the J/ψ photoproduction cross section shows a much steeper behaviour than expected with a single universal pomeron [43, 44].

Models based on perturbative QCD which predict a steeper rise should be applicable in the presence of a hard scale, like high values of Q^2 or a heavy mass of the vector meson. In pQCD based models the interaction between the photon and the proton factorises into three parts: the fluctuation of the photon into a $q\overline{q}$ pair, the interaction by exchange of a "regge-ised" gluon ladder, with the quantum numbers of the vacuum, and finally the formation of the vector meson.

In diffractive processes $\psi(2S)$ mesons are also produced, which is a significant background for inelastic J/ψ production. For the decay mode $\psi(2S) \longrightarrow J/\psi\pi^-\pi^+$, the pions can lead to a lower reconstructed value of z and therefore to the wrong assumption of an inelastic event.

In addition to the elasticity z, the transverse momentum squared of the J/ψ meson $P^2_{t,\psi}$ can be used to distinguish diffractive processes from inelastic processes, since the cross section for elastic diffraction falls much more steeply with $P^2_{t,\psi}$ than the inelastic cross section. A cut $P_{t,\psi} > 1\,\mathrm{GeV}$ was proposed by theorists to remove diffractive contributions.

Chapter 2

The H1 Detector at HERA

In this chapter first the HERA collider is presented. Then the H1 detector is described with emphasis on the relevant components for this analysis. Finally the trigger system is described.

2.1 The HERA Collider

The HERA collider stands for "Hadron Elektron Ring Anlage" in German, or "Hadron Elektron storage ring facility" in English. It is in service at DESY (Deutsches Electronen SYnchroton) in Germany at Hamburg since 1992. This collider has the particularity to be composed of two distinct storage rings. The first accelerates beam protons, the probed objects. But with some modification, it could also accelerate deuterons, a proton with a neutron in addition. The second accelerates a polarised electron or positron beams, the probe. The four possibilities ${e^-}_R$, ${e^-}_L$, ${e^+}_R$, and ${e^+}_L$ are mandatory for exhaustive NC and CC measurements. HERA is the first and the unique machine in the world to operate like this. The previous experiments used fix targets probed by electron beam. Figure 2.1 shows the HERA coverage of the kinematic plane in comparison to previous fixed target experiments. The acceleration of the proton permits to have higher centre of mass energy $s = 4E_{\mathrm{p}}E_{\mathrm{e}}$ instead of $s = 2M_{\mathrm{p}}E_{\mathrm{e}}$ for fixed target. And thus gives access to higher Q^2 and lower x according to the relation $Q^2 = sxy$. HERA extends the accessible kinematic range by about two orders of magnitude.

The HERA III project proposed a third phase with deuterons in order to measure the structure function of the neutron. However this project will not be realised, since the current injector PETRA II will be replaced by PETRA III, thus ending HERA II in 2007. PETRA III is designed for synchrotron radiation physics, and has a domain of applications close to the ESRF.

HERA has four interaction regions for experiments. The beams are collided in the north hall and south hall where two multi-purpose detectors H1 and ZEUS are installed. In the east hall HERMES is installed. This experiment uses the polarised beam electrons colliding with a polarised atomic beam in order to study the spin structure of the proton. The HERA-B experiment installed in the west hall is a spectrometer using the collisions between the halo of the proton beam and a wire. The aim of this experiment was to cover the physics of CP violation in the B sector. Some data was taken from 2000 to 2003, but it did not achieve the goals and did not restart in October 2003 for HERA II.

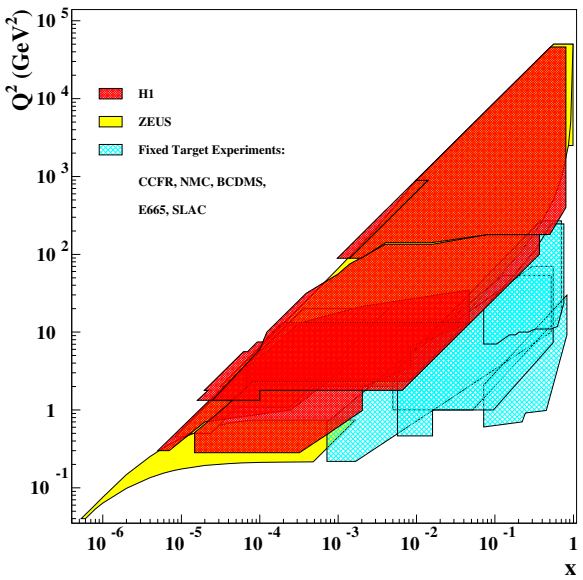

Figure 2.1: The HERA coverage of the kinematic plane in comparison to previous fixed target experiments. Fixed target regions are only located at large x and small Q^2 with just a tiny overlap with H1 and ZEUS.

2.1.1 HERA Operation

Figure 2.2 shows the scheme of HERA and its pre-injectors. Electrons and protons are packed in bunches since their formation in the accelerator chain. Proton and electron bunches consist typically of $2.1 \cdot 10^{13}$ protons and $0.8 \cdot 10^{13}$ electrons, respectively.

Electrons are produced at 500 MeV by a linear accelerator (LINAC), then accelerated by the machine DESY-II up to 7.5 GeV. Up to 60 bunches can be formed and filled in the machine PETRA-II where they are accelerated up to 12 GeV. This process is repeated several times to fill the Hera electron ring. When the filling is complete, the HERA electron ring brings them to 27.6 GeV.

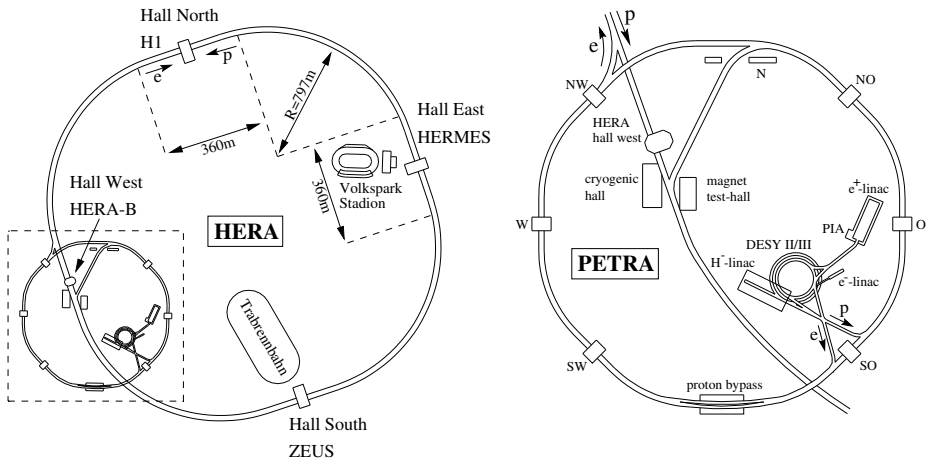

Figure 2.2: The electron proton storage ring facility HERA is shown on the left hand side. An enlarged view of the pre-accelerators is presented on the right hand side. The length of the straight section is 360 m, and the radius of the circular section is 797 m. The circumference is 6 336 m.

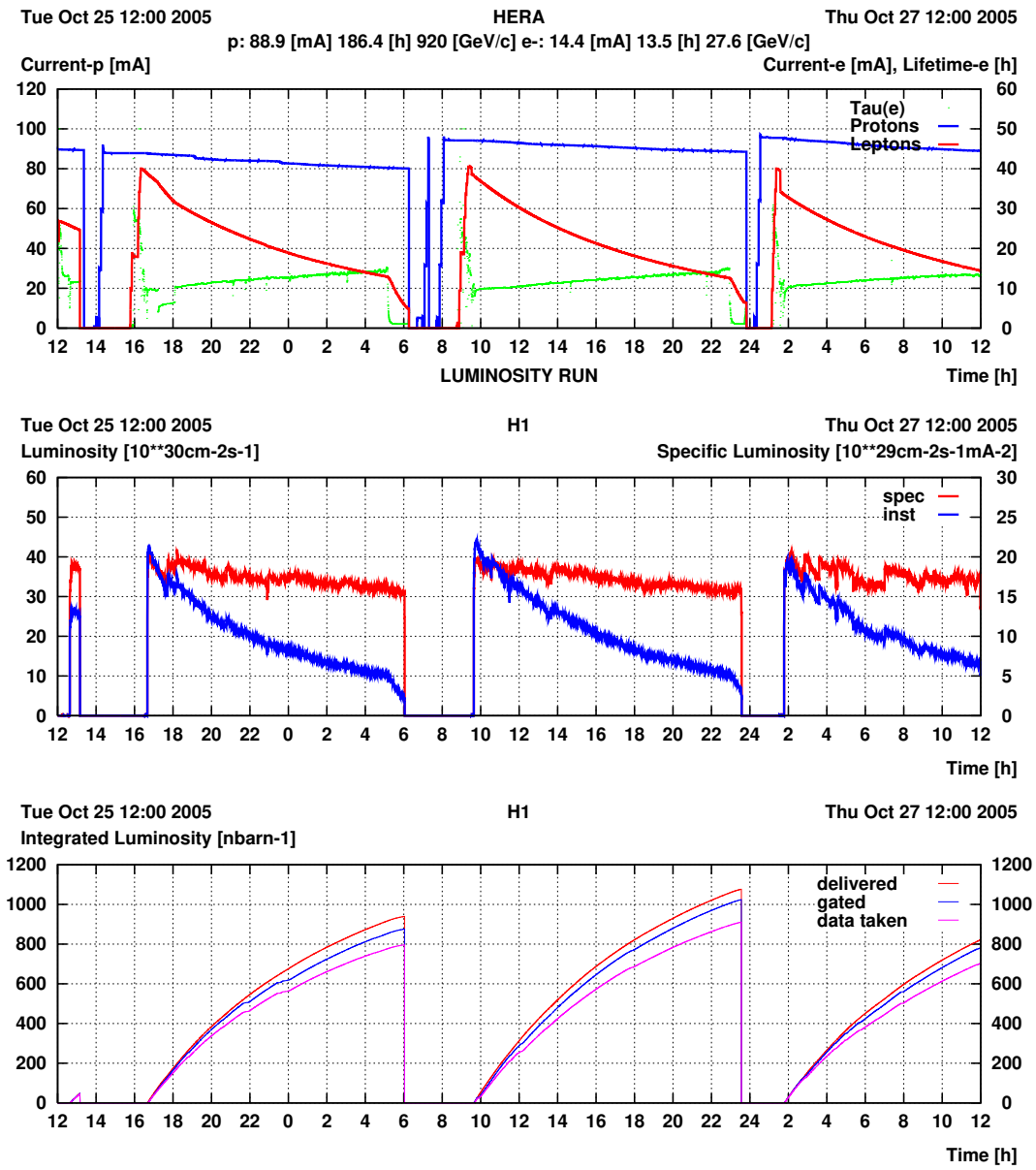

Figure 2.3: Example of luminosity fills during HERA operation in October 2005. The plot at the top shows the currents of the beams and the lifetime of the electron beam (denoted by *tau*). The plot in the middle shows the specific luminosity and the instantaneous luminosity. The plot at the bottom shows the integrated luminosity delivered by HERA, gated by H1 and when data was taken.

Protons are produces with H^- ions accelerated up to 50 MeV by the H^--LINAC, then accelerated by the machine DESY-III at 7.5 GeV. Up to 70 bunches can be formed and filled in the machine PETRA-II where they are accelerated up to 40 GeV. The HERA protons ring brings them to 920 GeV.

While the beam electron energy is limited by the energy lost due to synchrotron radiation, the strength of the magnetic field of approximately 5 T of the superconducting dipole magnets of the proton ring sets the limit for the proton beam energy.

HERA has in total 220 bunch places in parallel on both storage rings. Taking the 220 bunch places and the circumference of 6 336 m into account, the resulting frequency of proton-electron bunch collisions is 10.4 MHz, which corresponds to a bunch distance of 96 ns. In order to study the proton background and especially the synchrotron radiation for the luminosity measurement, some bunch crossing positions, called *pilot bunch* crossings, are filled with only electrons or protons. Moreover in practise it is impossible to fill these 220 bunch places due to the extreme complexity of the HERA machine.

The electron bunches have a longitudinal size of 2 cm, and a transverse size of $\sigma_x \times \sigma_y = 250 \times 20\,\mu m^2$ at the interaction point, whereas the proton bunches have a longitudinal size of 11 cm, and a transverse size of $\sigma_x \times \sigma_y = 300 \times 60\,\mu m^2$. The longitudinal structure is more complex, due to the presence of *satellite* bunches made during the acceleration phase. These satellite bunches are earlier and later compared with the HERA clock.

Figure 2.3 shows an efficient HERA operation period. A period of data taking with the same fill of electrons and protons is called a *luminosity fill*. The lifetime of the beam protons is approximately 100 hours, but the duration of a luminosity fill is limited by the lifetime of approximately 12 hours of the beam electrons. When the electron current has dropped to 13 mA, the instantaneous luminosity is no longer interesting for H1 and ZEUS. Then HERMES increases considerably the pressure of the target in order to increase their event rate, which reduces quickly the lifetime of the beam electrons. This period is called *high density run*. After two hours both beams are dumped, and a new filling procedure starts. Often the filling requires several attempts to achieve stable beams, due to the complexity of the HERA machine. In particular it is challenging to realise simultaneously high polarisation, high specific luminosity, and beam stability. The refilling time has a non negligible impact on the accumulated luminosity, at least a dead time of two hours. The drop at the electron current peak visible in figure 2.3, is due to the optics and luminosity tuning. While the drop at the end corresponds to the high density run.

Tables 2.1 show the HERA II parameters for the 2003-2004 e^+ and 2004-2005 e^- data taking periods compared to the best HERA I period, achieved in 2000 with positrons. It will be discussed in more details in the next section.

parameter	2000 e^+	2003-2004 e^+	2004-2005 e^-	unit
$\langle L \rangle$	6.47	12.47	17.20	$[10^{30}\,cm^{-2}s^{-1}]$
Peak luminosity	17.90	38.00	48.01	$[10^{30}\,cm^{-2}s^{-1}]$
$\langle \mathcal{L}_{sp} \rangle$	0.62	1.14	1.56	$[10^{30}\,cm^{-2}s^{-1}mA^{-2}]$
$\langle \mathcal{L}_{sp} \rangle$ max	0.99	1.95	4.00	$[10^{30}\,cm^{-2}s^{-1}mA^{-2}]$
$\langle I_p \rangle$	86.77	79.96	77.57	[mA]
$\langle I_p \rangle$ max	109.22	122.07	102.03	[mA]
$\langle I_e \rangle$	25.12	24.99	22.06	[mA]
$\langle I_e \rangle$ max	51.81	52.52	42.00	[mA]

typical bunch configurations	
2000	175 × 175 + 14 e + 6p
2003-2004 e^+	174 × 174 + 10 e + 10p
2004-2005 e^-	134 × 134 + 8 e + 6p

Table 2.1: HERA parameters for 2000, the **2003-2004** e^+ and **2004-2005** e^- data taking periods [45].

2.1.2 The Second Phase of HERA

This analysis uses data of the second phase of HERA. The first phase was operating from 1992 to 2000, and delivered to H1 and ZEUS a total luminosity of 190 pb^{-1} each. Before the end of HERA I, a proposal for a second phase was initiated [46]. The motivation was to increase the instantaneous luminosity by a factor four and to polarise longitudinally the electron beam in H1 and ZEUS. Higher luminosity will yield enhanced statistics, thus increased the precision and reduced statistic fluctuations on hypothetical signals. For HERA I only HERMES was equipped with spin rotators. The installation of spin rotators around H1 and ZEUS will permit to study neutral and charged current processes

HERA was already improved during the first phase. In 1998 the proton beam energy was increased from the original value of 820 GeV to 920 GeV. From 1992 to 2000, the instantaneous luminosity was continuously increased and finally exceeded its design luminosity of $17 \cdot 10^{30}\,cm^{-2}s^{-1}$ at the end [1].

From September 2000 to April 2002, a shutdown took place in order to upgrade the storage ring and the experiments for the second phase. Spin rotators were installed around the H1 and ZEUS experiments in order to have electrons with longitudinal polarisation at the interaction point.

The instantaneous luminosity depends on the bunch crossing frequency f, the numbers of particles N_e and N_p in the electron and proton bunches and the collimation of the beams in the transverse direction σ^e_{xy} and σ^p_{xy},

$$\mathcal{L} = \frac{f N_e N_p}{2\pi \sigma^e_{xy} \sigma^p_{xy}}$$

The number of expected ep interactions N is proportional to the integrated luminosity,

$$L = \int \mathcal{L} dt$$

and the total ep cross section σ,

$$N = L\sigma.$$

For HERA II, the instantaneous luminosity was increased to $74 \cdot 10^{30}\,cm^{-2}s^{-1}$ (design value), by increasing the number of particles N_p in the proton bunches and attaining a stronger focus of the electron and proton beams that reduces the transverse beam spreads σ^e_{xy} and σ^p_{xy}. An overview of the HERA beam parameters before and after the upgrade is given in table 2.2.

parameter	HERA I		HERA II	
	e beam	p beam	e beam	p beam
N_{ppb} $[1 \cdot 10^{10}]$	3.5	7.3	4.0	10.3
σ_x [µm]	192	189	112	112
σ_y [µm]	50	50	30	30
σ_z [mm]	11.3	191	10.3	191

Table 2.2: Luminosity design parameters before (HERA I) and after upgrade (HERA II); N_{ppb} means number of particle per bunch [46].

[1] The design luminosity was $15 \cdot 10^{30}\,cm^{-2}s^{-1}$

In order to achieve the stronger focusing of the proton beam and the electron beam, two new magnets "GO" and "GG" were installed inside the H1 detector around the interaction point.

At the restart, the upgraded luminosity was accompanied by an unforeseen increase of synchrotron radiation emitted close to the H1 and ZEUS experiments [47] [48]. This flux of synchrotron radiation heated and degassed the wall of the beam pipe, increasing drastically the rate of beam gas interaction, and provoking dangerous currents in the drift chambers. During the summer shutdown in 2003, additional shielding was added. That permits to reduce the background by a factor five, and thus permitted to operate securely the detector up to now.

The shutdown was an opportunity for the H1 detector to update obsolete detectors or unadapted detectors for the high luminosity.

2.2 The H1 Detector

The H1 detector [49] is designed as a general purpose design detector to study high energy interactions between electrons and protons at HERA. The aim is to identify particles resulting from the interaction, to measure their four-vectors and charges over the maximum solid angle in order to minimise the energy flow loss. The detector as usual in high energy physics is made of several sub-detectors arranged in concentric layers around the beam pipe. Since the energy of the proton beam is two orders of magnitude greater than the electron beam, particles are boosted in the direction of the proton beam. This property of HERA implies an asymmetric design of the detector, disposition and granularity of the sub-detectors depends of the θ polar angle. Instrumentation is predominantly concentrated in the forward and central region, while the backward region is less densely instrumented and dedicated mainly to the detection of the scattered electron.

The detector can only "see" particles resulting from the interaction that are sufficiently stable, interacting with the materials and energetic to reach the "active" materials. These particles are for example e, μ, γ, and hadrons like n, p, and π^+. The neutrinos are never detected in this type of detector. A vertex detector permits to tag via a secondary vertex unstable long-lived particles like beauty mesons. The sub-detectors exploit the properties of the particle like the charge and their interaction mode with the materials, electromagnetic or hadronic interaction, and the amounts of interaction, shower or minimum ionising.

Before going to details of the detector, a simple review of it will be given. The H1 central detector is composed of the following sub-detectors, listed in the outwards order from the beam axis:

Tracking system to identify charged particles and reconstruct their momentum, and localise the primary and secondary vertices. The tracking system is located in the centre in order to measure the momentum before particles lose energy by interaction with the detector.

Calorimeters with an electromagnetic and hadronic layer, to identify from the shower the interaction mode of the particle and estimate its energy.

A superconducting coil produces a magnetic field of 1.16 T parallel to the beam axis for the tracking system. It is located behind the calorimeter in order to minimise the dead material.

Iron return yoke closing the magnetic field. The huge amount of iron material in association with instrumentation is also used to tag muons.

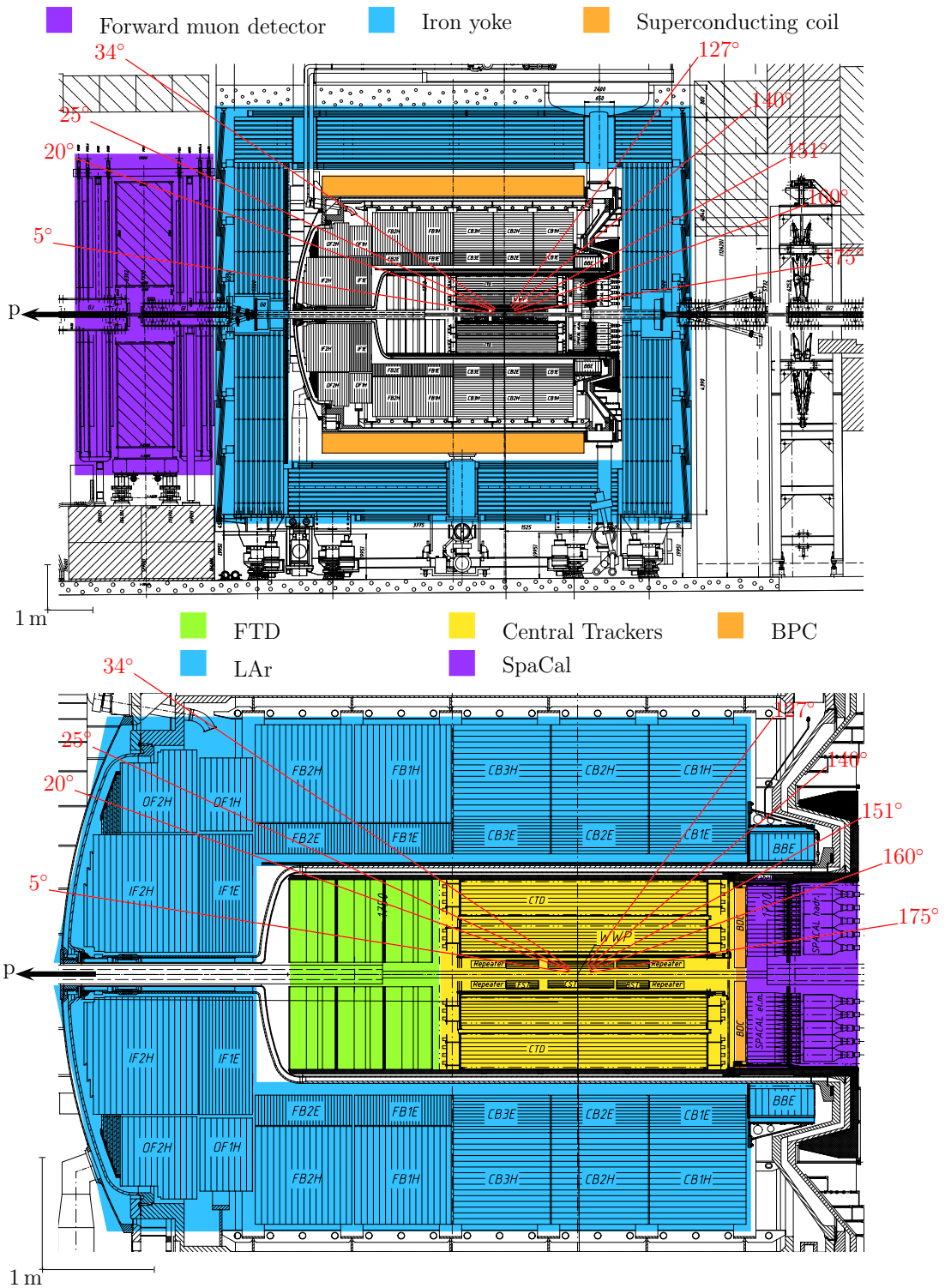

Figure 2.4: Side view of the H1 detector during the phase of HERA II. The main detector has a size of $12 \times 10 \times 15\,\mathrm{m}^3$ (length $\times$ width $\times$ height) and a weight of 2 800 Tons. On this picture is indicated: the proton direction, the scale, and some typical polar angles.

The picture 2.5 illustrates the principle of particle identification in the H1 detector for some representative particles:

- e is a charged electromagnetic particle. It ionises the chambers and produce a track, then interacts in the electromagnetic part of the calorimeter, producing an electromagnetic shower. In general electromagnetic particles do not reach the hadronic layer.
- μ^- is a charged electromagnetic particle like the electron but interacts little with the material since the typical energy corresponds to a low ionisation. The signature of the muon is a track extended with some energy deposits in the calorimeter and for more energetic muon some energy deposit in the instrumented iron detector. Only muons or neutrinos can go through such amount of material. Since only muons interact, a signal in the instrumented iron detector is an unambiguous tag for them.
- γ is a neutral electromagnetic particle. So contrary to electrons there is only an electromagnetic shower and no track.
- π^+ is a charged hadronic particle. Hadronic particles start to interact in the electromagnetic part of the calorimeter and continue in the hadronic part producing a hadronic shower and sometimes for very energetic hadron even outside, in the iron yoke.
- n is a neutral hadronic particle. So it produces only a hadronic shower without a track, and a small energy deposit in the electromagnetic part of the calorimeter.

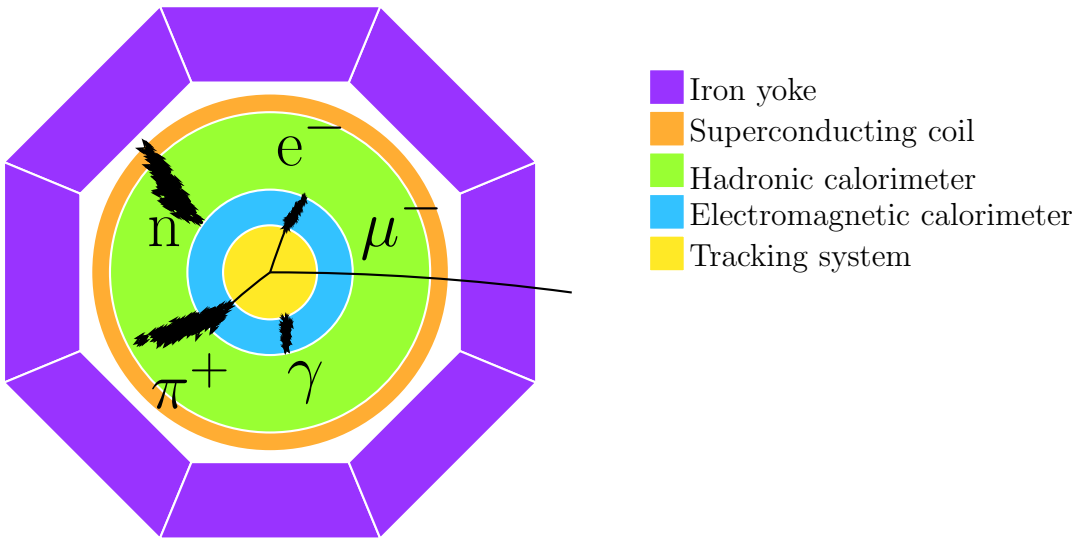

Figure 2.5: Principle of particle identification (H1 radial view)

The following table gives a summary:

particle	tracking system	calorimeter		instrumented iron yoke
		electromagnetic	hadronic	
e	track	shower		
μ^-	track	energy deposit		signal if enough energy
γ		shower		
π^+	track	shower		
n			shower	

This table shows the minimal signal, if particles are more energetic a signal is always possible in the following detector.

2.2.1 The Tracking Systems

The tracking system is subdivided in three z regions: forward, central, and backward region. As it was said in introduction, particles are predominantly produced in the forward region due to the boost. This requires to use a specific tracking system to handle forward tracks in addition of the central tracking system. Each system is optimised for its polar angular region acceptance. Moreover a small sub-detector helps to measure very backward tracks in order to reconstruct the scattered electron. Nearest of the beam pipe, three vertex detectors cover the three z regions, and provide a precise measurement of the primary vertex and the second vertexes for beauty physics. The measurement of the momentum is done by drift chambers.

2.2.1.1 The Central Tracking System

The central tracking system cover the polar angular region $20° < \theta < 160°$ and is composed of several concentric sub-detector as shown on figure 2.6:

Central Silicon tracker (CST) is one of the three vertex detectors. It covers the angular range $30° < \theta < 150°$. The CST improves the impact parameter resolution of CJC tracks from 200 µm to 20 µm at high transverse momentum. It consists of two layers of double sided silicon strip sensors.

Central Inner Proportional chamber (CIP 2000) is used for trigger purposes, in order to reject background. This detector has a fast response and can achieve

- An estimation of the z position of the vertex within 2 µs, which provides a significance of the vertex. The resolution in z is 1.5 cm.
- The computation of the number of tracks yields the so called *track multiplicity*.
- And the time of the event with a resolution of 25 ns.

This detector is composed of 5 layers composed of gaseous cells inside a capacity and working in the proportional regime. It means a charged particle crossing a cell will ionise the gas, then electrons coming from the primary ionisation will also provoke a ionisation and so on, which will be collected by the capacity.

Central Jet Chamber 1 (CJC1) is the first of the two cylindrical drift chambers. In fact the CJC is split in two in order to have the Central Outer Z (COZ) chamber located at a medium radius (see next item).

Their drift volume is segmented in the azimuthal direction into independent trapezoidal drift cells. In the centre of each drift cell, a plane of anode wires is located, bounded by two planes of cathode wires on either side, creating an electric field in both sides. The anode wires are stretched parallel to the beam axis, and have a length of 2.2 m. Figure 2.6 shows the topology of the wires in the $r\phi$ plane. The Orientation of the planes was chosen so as to have the best precision on the reconstruction. The cells are installed inside a cylindrical tank filled with a gas mixture.

These drift chambers measure the projection of the tracks in the $r\phi$ plane with a spatial hit resolution of 170 µm. The momentum resolution is $\frac{\sigma_{P_t}}{P_t} \approx 0.01\ P_t$ GeV^{-1}, and the estimation of the $\mathrm{d}E/\mathrm{d}x$ has an accuracy of 8 %.

In the z direction along the anode wire a resolution of 2 cm is attained by charge division.

The CJC provides also a mean time of the event with a temporal resolution of 1 ns.

Central Outer Z chamber (COZ) is a drift chamber inserted between the two CJC. This chamber has an improved resolution in z of approximately 220 µm that permits to measure accurately the z position of the track at a medium radius. This precise measure is used to reconstruct the polar angle of the tracks.

Central Outer Proportional chamber (COP) has a rapidity of 60 ns and was used for trigger purposes. This detector is a relic of HERA I. It is not used any longer.

Central Jet Chamber 2 (CJC2) is the second part of the CJC, and has a similar design as the CJC1.

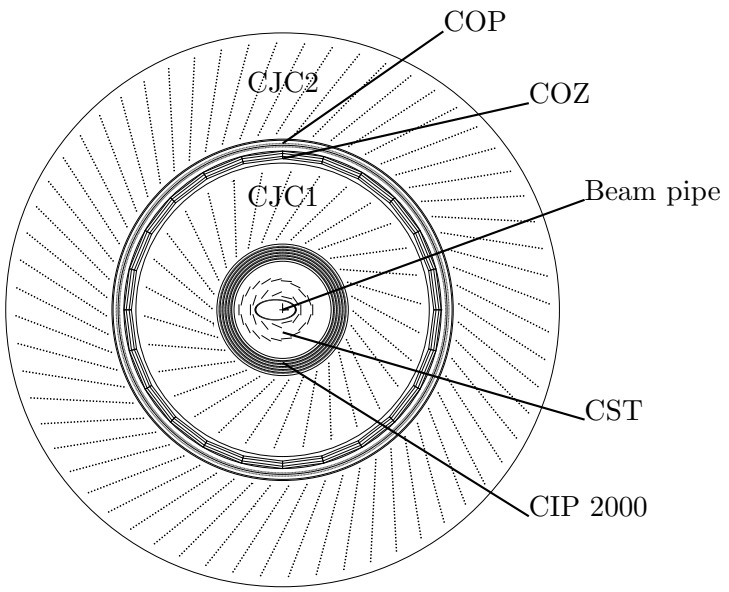

Figure 2.6: Radial view of the central tracking system after the upgrade for HERA II

2.2.1.2 The Forward Tracking System

- The Forward Silicon tracker (FST) covers the angular range $8° < \theta < 16°$. The FST was fatally damaged in 2004, and was removed in 2005 for repair and put back in 2006.
- The Forward Tracking Detector (FTD) is a drift chamber that covers the polar angular region $5° < \theta < 25°$. This detector replaces by a new design the old forward tracking system used during HERA I. The previous one had an efficiency of reconstruction less than 50 % for events with high multiplicity of tracks. The FTD is made of several layers of planar drift chambers with different orientation of wires.

2.2.1.3 The Backward Tracking System

- The Backward Silicon tracker (BST) covers the angular range $162° < \theta < 176°$.
- The Backward Proportional Chamber (BPC) in conjunction with the BST and the SpaCal calorimeter permit to achieved an angular resolution on the scattered electron of approximately 0.5 mrad.

2.2.2 The Calorimeters

The H1 detector has two main calorimeters: the liquid argon calorimeter (LAr) covering the forward and central region, and the SpaCal calorimeter covering the backward region.

2.2.2.1 The Liquid Argon Calorimeter

The liquid argon calorimeter (LAr) surrounds the central tracking system and covers the angular range $4° < \theta < 153°$. The transverse and the cross section of the LAr calorimeter is shown in figure 2.7. The LAr has two layers, an inner electromagnetic layer, followed by an outer hadronic layer. It is placed inside the superconducting coil, in order to minimise both the amount of dead material in front of the electromagnetic calorimeter and the overall size and weight of the calorimeter.

This calorimeter uses liquid argon as active medium, and as absorbing material, lead plates for the electromagnetic part and steel plates for the hadronic part. The showers develop in the metallic plates, while the liquid Argon converts the deposited energy in electronic charges, which are collected by a capacity. The electromagnetic part has a depth between 20 to 30 radiation lengths and the hadronic part between 5 to 8 interaction lengths.

Moreover the LAr is segmented along the beam axis in eight wheels, and each of them segmented in ϕ into eight identical octants. The two forward wheels are assembled as two half rings. The most backward wheel called *BBE* does not have a hadronic layer. It is why the backward corner of the calorimeter constitutes a lack of material. Since particles are boosted in the forward region, it is better to have a hermetic forward region than the backward region. The backward side of the detector is used as access point to insert the tracking system.

The LAr calorimeter is not compensating, i.e. the response of the detector for a pion and an electron of the same energy is different. The ratio of the energies $\frac{e}{\pi}$ is approximately 1.35 for particles of 10 GeV and decreases logarithmically. However the difference of the shapes of an electromagnetic and a hadronic shower permits to distinguish them and apply a correction on the energy response.

The calorimeter has an important noise due to the readout electronics, the length of the wires, and the pileup of the energy deposit of the particles coming from the ep interaction and cosmic rays. The level of noise is of the order of 15 to 30 MeV per cell. The noise is more important in the central region where the capacities are larger.

The energy resolution in the electromagnetic section as measured in a test beam is

$$\frac{\sigma_E}{E} = \frac{12\,\%}{\sqrt{E\mathrm{GeV}}} \oplus 1\,\%$$

and for hadrons in the hadronic section

$$\frac{\sigma_E}{E} = \frac{50\,\%}{\sqrt{E\mathrm{GeV}}} \oplus 2\,\%.$$

The less accurate resolution of the hadronic part is due to the hadronic shower process, which is subject to large statistical fluctuation.

As the majority of the other detectors, the LAr provides a time measurement of the event with a resolution of 10 ns. This time corresponds to a mean of the signals from the cells.

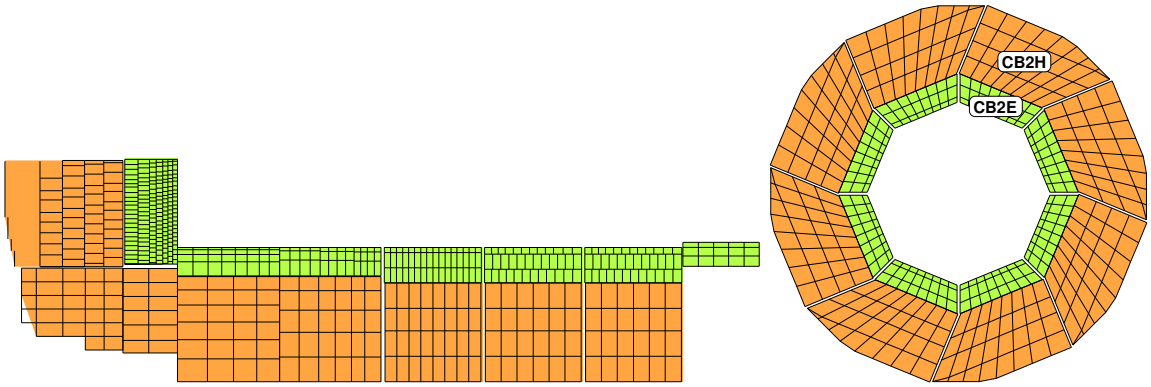

Figure 2.7: Transverse and cross section of the LAr.

2.2.2.2 The Spaghetti Calorimeter (SpaCal)

The Spaghetti Calorimeter (Spacal) realises the calorimetric measurement in the backward region covering the polar angular region of $153° < \theta < 174°$. The acceptance was a little bit reduced around the beam pipe due to the introduction of the GG magnet for HERA II. The previous acceptance was 177.5°. The SpaCal is designed for a precise measurement of the energy of the scattered electron at low Q^2 between 1 and 150 GeV^2. As its name suggests, the SpaCal is a sandwich of lead fibres as absorbing material and scintillating fibres as active material. The incident particles develop a shower in the lead. Then particles from this shower will lead to emission of scintillating light in the fibres which is collected by photomultipliers. The SpaCal has an electromagnetic section depth 28 radiation lengths and a hadronic section of depth 2 interaction lengths only. The very fine granularity (1 192 cells) permits a spatial resolution of a few millimetres for the scattered electron. This measurement is helped by the proportional chamber (BPC) located in front of the SpaCal. The energy resolution for electromagnetic showers is

$$\frac{\sigma_E}{E} = \frac{7\,\%}{\sqrt{E[\mathrm{GeV}]}} \oplus 1\,\%$$

and for hadronic showers

$$\frac{\sigma_E}{E} = \frac{13\,\%}{\sqrt{E[\mathrm{GeV}]}} \oplus 4\,\%.$$

2.2.2.3 The Plug2k

The plug sub-detector is surrounding the beam pipe in the forward iron end-cap in order to close the detector. It covers the region $1.9° < \theta < 3.2°$. The Plug2k replaces the old *plug* calorimeter used for HERA I due to the insertion of the *GO* coil. This detector is used by the time of flight system (PToF) and as tagger for diffractive events.

2.2.2.4 The Tail Catcher

The Tail catcher calorimeter corresponds to the pad electrodes of the limited streamer tubes in the instrumented iron detector. Look in section 2.2.3.1 for more details. This instrumentation permits an approximate energy measure of the part of the hadronic shower going outside the hadronic layer of the LAr. The depth corresponds to 4 interaction lengths. The energy resolution is

$$\frac{\sigma_E}{E} = \frac{100\,\%}{\sqrt{E[\mathrm{GeV}]}}.$$

2.2.3 The Muon Detectors

The H1 detectors has two sub-detectors for the identification of muons: the central muon detector (CMD) in the central region, and the forward muon detector (FMD) covering the forward region. In this analysis only the central muon detector is used.

2.2.3.1 The Central Muon Detector

The central muon detector surrounds all the sub-detectors of the main detector. It is made of the association of an iron yoke closing the magnetic field of the superconducting coil, and instruments sandwiched between the iron plates composing the yoke. The iron shields the instrumentation against the hadrons leaking out of the calorimeters. It is divided into 64 modules arranged in four parts, the forward end-cap $5° \lesssim \theta \lesssim 35°$, the forward and backward barrel $35° \lesssim \theta \lesssim 130°$, and the backward end-cap $130° \lesssim \theta \lesssim 175°$. The barrel has the shape of an octagon.

Limited streamer tubes are used for the instrumentation. The tubes consist of a sense wire inside an extruded square profile of $1\,\mathrm{cm}^2$ filled with a gas mixture. A high tension is applied between the inner wall of the tube and the wire. When a charged particle crosses a tube, a current is created by the ionisation of the gas providing a digital signal. The tubes are aligned side by side in order to form a layer, and oriented parallel to the beam axis for the barrel and to the x axis for the end-caps. Figure 2.8 shows the cross section of a module of the CMD. There are eight single layers and a double layer installed between ten iron plates. On the inside and the outside of the iron yoke are placed three additional layers, so called *muon boxes*, in order to improve the track measurement. In order to identify the position of the tracks along the beam axis, two layers of each muon boxes and one layer at an intermediate position inside the iron yoke (the double layer) are equipped with *strip electrodes*. The strips are regularly spaced along the tube in order to locate the position of the ionisation. The resolution in the longitudinal direction is comprised from 10 to 15 mm, and in the perpendicular direction from 3 to 4 mm.

The other eleven layers are equipped with *pad electrodes*, which can be used to resolve track ambiguities and to detect hadronic energy leaking from the LAr and the SpaCal calorimeters (Look in section 2.2.2.4 for this usage). Pad electrodes are similar to the strips but with a larger area and with an analog readout instead of a digital one.

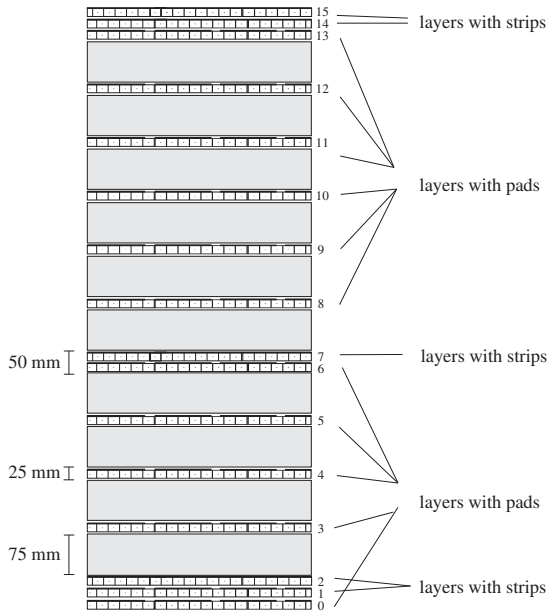

Figure 2.8: Cross section of a module of the Central Muon Detector.

2.2.3.2 The Forward Muon Detector

The Forward muon detector (FMD) is a spectrometer consisting of three double layers of drift chambers in front of and behind a toroidal magnet. It covers the polar angular region $3° < \theta < 17°$, and provides identification and momentum measurements for muons with $P \gtrsim 5\,\text{GeV}$. Since the momentum threshold is high compared to the typical momenta of the decay muons of inelastic J/ψ mesons, the yield of event with decay muons in the FMD is too low for this analysis. Thus the FMD is not used in this analysis.

2.2.4 The Time of Flight System

An important part of the background comes from events produced by the interaction of beam particles with residual gas or the collimators of the accelerators. When the event is located at the nominal interaction position, particles are produced approximately in all the direction from the centre of the detector. But if the event is located outside of the detector, in the background side especially, particles will reach first the backward side of the detector and then the forward side. In this case particles go in the wrong direction. In order to veto such events, several fast plastic scintillators detectors with a time resolution of 1 ns are placed at different z position, inside and outside the H1 detector. If we assume particles travel at the light speed, it corresponds to a time of flight of 1 ns for 30 cm. The locations of the detectors of the *time of flight system* is shown in figure 2.9.

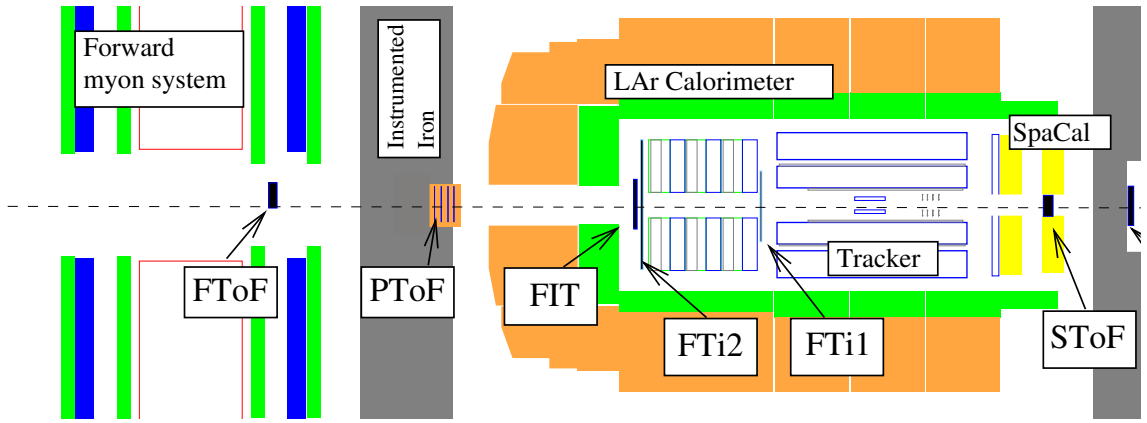

Figure 2.9: Time of Flight System

2.2.5 The Measurement of the Luminosity

The purpose of this analysis and many others is to compute the "probability of interaction" of a process, the *cross section*. When the signal has been extracted and corrected, we obtain a number of events for our data taking period. In order to have an independent quantity of the beam condition, we have to "scale" our number of events with a reference process. At HERA, the Bethe-Heitler process $e^- p \longrightarrow e^- p \gamma$ is used as reference process. The cross section of the Bethe-Heitler process is precisely calculable within quantum-electro-dynamics (QED) with an theoretical uncertainty of 0.5 %. This process is studied in the configuration where the incident electron, the photon, and the scattered electron are almost collinear. The cross section is very large, of the order of 170 mb, which permits to have large statistics. The luminosity L is defined as

$$L = \frac{N_{\mathrm{BH}}}{\sigma_{\mathrm{BH}}}$$

where N_{BH} is the number of Bethe-Heitler processes and σ_{BH} its cross section.

The Bethe-Heitler process occurs also with the proton of the residual gas in the beam according to the reaction $e^- A \longrightarrow e^- A \gamma$. It is the main source of background for the luminosity measurement. This contribution is of the order of 10 %, and is determined with the electron pilot bunch.

The luminosity system, shown in figure 2.10, consists of two detectors the *Photon Detector* (PD) at −100 m of the main detector, and the *Electron Tagger* (ET) at −6 m. It was upgraded for the enhanced luminosity. The Photon Detector is an electromagnetic calorimeter using Čherenkov light, which gives a fast response at the rate of the HERA clock. It is made of a layer of tungsten to initiate a shower and then of lead as absorber. The active material is composed of planes of quartz connected to photomultipliers.

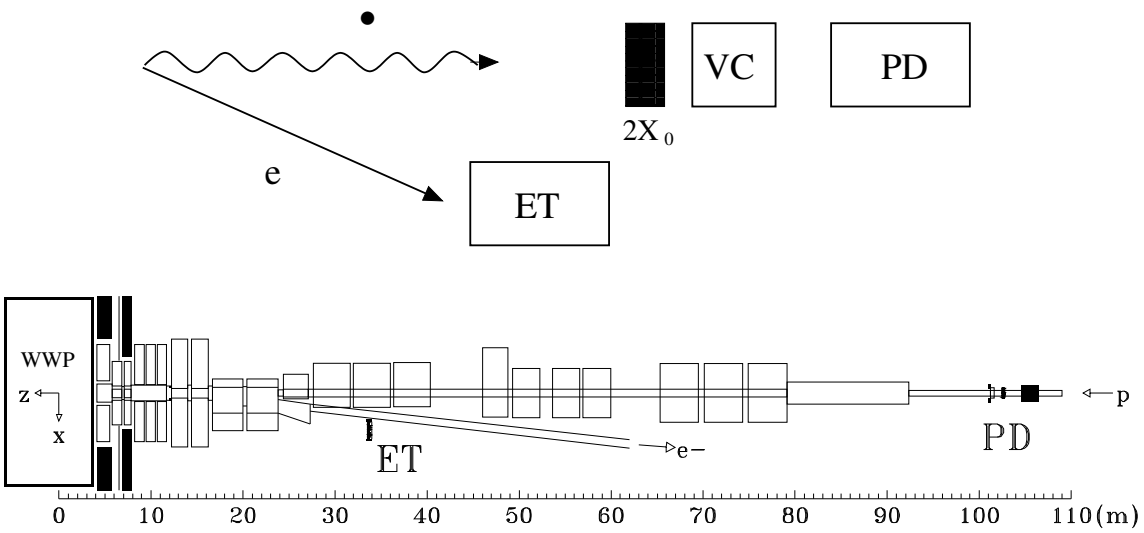

Figure 2.10: The luminosity system. Here the Electron Tagger is located at −33 m, the HERA I configuration, instead of −6 m for HERA II.

2.2.6 Detectors Installed in the Ring

In addition to the luminosity system, an electron detector is installed at −40 m. But for reasons of a too large rate of radiation this detector stays in the rest position outside the beam. In the positive z side roman pots are installed at several positions close to the beam in order to detect the scattered proton.

2.3 The Trigger System

The interactions at HERA are dominated by background instead of ep interactions. Indeed the cross section of ep interactions corresponds to weak and electromagnetic interaction processes while the background comes from strong interaction processes. Table 2.3 shows some typical values. Notice that the maximum event rate of 50 kHz is inferior to the HERA collision frequency. Since matter is mainly constituted of vacuum, a bunch crossing can be "transparent" and thus produce no event.

proton-gas interaction	50	kHz	depends on the proton beam
photoproduction	1 000	Hz	
cosmic muons	700	Hz	independent of HERA
$c\overline{c}$ total	15	Hz	
DIS NC low Q^2	2.2	Hz	
DIS NC high Q^2 (electron in LAr)	1.4	min^{-1}	
DIS CC $P_t > 25$ GeV	3	h^{-1}	
W production	0.5	d^{-1}	

Table 2.3: Event rates for a luminosity of $1.5 \cdot 10^{31}\,cm^{-2}s^{-1}$. Non ep interaction are emphasised in bold face.

The main sources of background at HERA are: beam-gas interactions, beam-wall interactions, synchrotron radiation, and cosmic radiation, which are described in the following.

Beam-gas interactions are the dominant source of background. These events comes from collisions between the proton and the residual gas inside the beam pipe, thus by strong interaction.

Beam-wall interactions Protons from the halo of the beam protons interact with the beam pipe or parts of the detectors. They are topologically very similar to beam-gas interactions.

Synchrotron radiation The beam electrons are bent by magnets in order to collide with the beam protons with null angle. It causes synchrotron radiation emitted by the electron beam. A large fraction of this background can be rejected by collimators.

Cosmic radiation Muons from cosmic radiation hit the detector. Sometime it is even possible to see cosmic showers in the detector.

Halo muons are produced far away before the interaction point by beam-gas or beam-wall interaction. When the momentum of these muons are "compatible" with the protons from the proton ring, they can travel in the beam pipe until the H1 detector. As they are always at small angle, at some point they go out of the beam pipe and cross the detector in parallel to the beam axis. These muons can sometimes be detected.

Sources of background originating from the beams are necessarily correlated with the HERA clock. Only cosmic radiation is completely independent of HERA. However beam-gas interactions and beam-wall interactions involved only the proton beam, therefore the correlation is not absolute. For ep interaction, both beams are involved, this constrains the z vertex distribution to be a Gaussian of width of 35 cm at the nominal beam crossing position. This property can be used to reject part of these sources of background. Another possibility is to require a temporal coincidence with the HERA clock.

The H1 detector is made of several independent detectors using different technology. Table 2.4 shows the time scale involved in HERA and H1. As you can see the drift time in the CJC or the integration time of the LAr preamplifier's are not equal and much longer than the delay between two bunch crossing.

width of a proton bunch	1.4	ns
distance to the next satellite bunch	5	ns
flight time from the backward ToF to nominal interaction region	6	ns
flight time from the Central Muon Detector to nominal interaction region	20	ns
delay between two bunch crossing	96	ns
longest drift time in the CJC	1	µs
integration time of the LAr preamplifier's	1.5	µs
response time for the L1 trigger	2.3	µs

Table 2.4: Time scales involved in HERA and H1

In order to cope with these delays, each detector digitalises its channels with ADCs in synchronisation with the HERA clock and fill a pipeline, which can hold up to 30 bunch crossings.

Because the H1 experiment was designed in the eighties, it is not possible to take data at a rate of 50 kHz. The detector has to readout something like 270 000 channels over a cube of a side of approximately 50 m. The full synchronisation of the element on the buses, the bandwidth of the buses, and the delay in the long cables imply a complete readout time of approximately 1 ms for an event size of approximately 110 kB. At 50 kHz, the data flow is 5.5 GB/s, this is unrealistic with technologies of the eighties. The readout time of the detector corresponds to a rate of 1 kHz. The data flow at this rate is still to much for the H1 data logging, since the maximal data logging rate

is 50 Hz. In order to reduce the rate, and take only the most interesting events for physics H1 used a four level trigger system. The principle of this multi-level trigger is: each trigger level uses more time to refine the decision of the previous level, and therefore reduces more and more the event rate. Figure 2.11 shows the principle of the H1 trigger system.

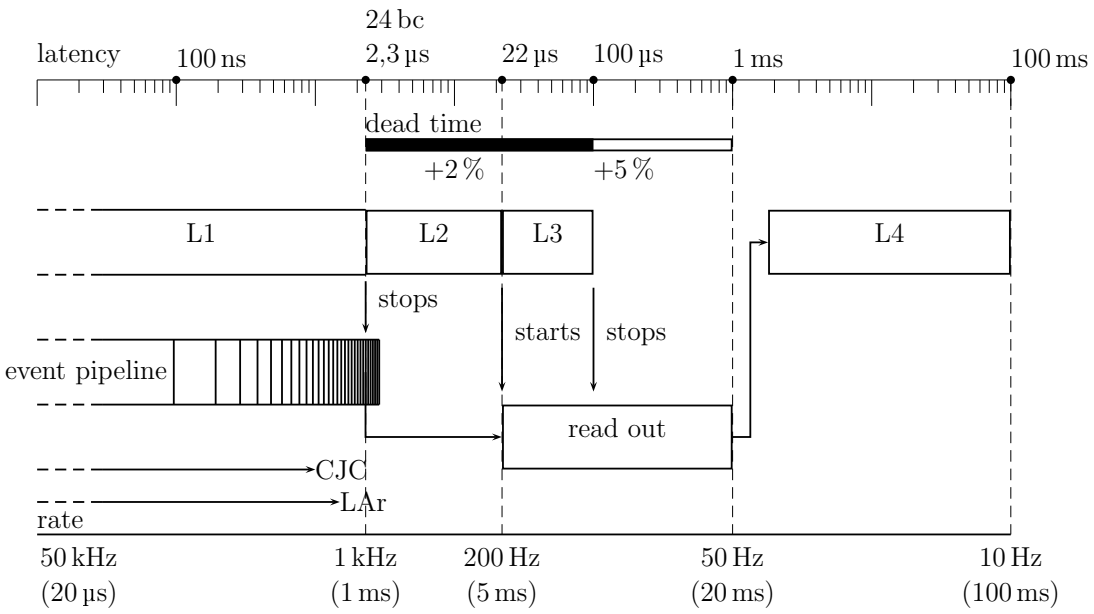

Figure 2.11: H1 trigger system

2.3.1 Level 1

Most detectors compute for each bunch crossing some useful characteristic quantities to trigger the event. These fast data are called *level 1 trigger elements*. The H1 detector provides in total 196 triggers elements (up to 256) to the central trigger.

Up to 128 *subtriggers* can be defined by logical combinations of the trigger elements. The central trigger computes the logical value of these subtriggers after synchronisation of the trigger elements in pipelines. Since the information is stored in pipelines, the level 1 trigger introduces only a latency of 2.3 µs (24 HERA bunch crossing).

As table 2.3 shows, physics channel rates differ by several orders. In order to balance the physics channels, some subtriggers are *prescaled*. For a prescale of n, a fired subtrigger will be validated only one event in n. The logical value of the subtriggers are stored in the *raw level 1 subtriggers* and their prescaled status in the *actual level 1 subtriggers*. Prescaled subtriggers are those concerning soft physics of high cross section and for monitoring, the high Q^2 event are never prescaled. Prescales are set according to a strategy taking into account the budget rate for the channels, the background conditions and their actual rates. The settings are computed every 2 h during a luminosity fill to take into account the reduction of the instantaneous luminosity, see section 4.1.1 for more details.

The L1 decision corresponds to the logical *or* over all the actual subtrigger bits. If one of the subtriggers fired, the pipeline is frozen and data are transmited to the second level. The dead time starts at this point. If no subtriggers fired, pipeline filling continues, and the event is lost at the end of the pipeline.

2.3.2 Level 2

The length of the pipeline of the H1 detector was limited for cost reason at the design time. Without intermediate trigger level, the level 1 would have to restrict its output to 50 Hz for the level 4 with harder cuts and prescales. When level 1 triggers an event, the pipeline is halted for 1 ms, where potentially more interesting events can be lost during this time. The idea of the level 2 trigger is to take 20 µs to verify the decision of level 1 before starting the readout, and thus reduce the dead time. If the trigger decision is verified, then the readout is started, else the pipeline is resumed. The level 2 trigger has a decision time of 20 µs, corresponding to a contribution of 2 % to the dead time.

To achieve this, the second level has in parallel three systems: the topological trigger, the neural network trigger, and for HERA II a Fast Track Trigger (FTT) was added and a jet trigger level 2 trigger in 2006. The neural network trigger (L2NN) was used during HERA I to reject background for subtriggers like subtrigger s15. The topological trigger (L2TT) searches for spatial correlations in the level 1 trigger signals, using a 16×16 binned representation of the detector in the θ-ϕ polar-azimuthal angle space.

2.3.3 Level 3

This level was never used before 2006. Its purpose is to contradict quickly the decision of the previous level within 100 µs, and thus to stop the readout. This new trigger level uses the level 2 FTT information to compute invariant masses.

2.3.4 Level 4

When the readout is finished the pipelines are restarted and the event data is transmitted to a computer farm. This constitutes the last trigger level of H1 at which events are still rejected irrecoverably. This farm performs several actions. Events are treated asynchronously and in parallel. It reconstructs the event to make the decision on the basis of best available quantities. Then it does an event classification based on a first level analysis in order to keep only the most interesting events. This trigger level is a legacy in order to reduce the detector output rate from 50 Hz to 10 Hz for the tape storage system and the computer farm. It is also a danger since wrongly classified events are irrecoverably lost.

The sequence of actions is performed in this order:

- Trigger verification of the level 1 and level 2 subtriggers following a steering. If the verification fails, some subtriggers are eventually reset. The event is marked *L4REJECT* if all level 1 subtriggers are false after the verification. Typically this action rejects non-ep background with a z vertex cut. For monitoring 10% of these events are kept and classified in the junk class. In "100% keep mode" all *L4REJECT* events are kept in this class.
- Reconstruct the event.
- Classify hard scale physics like high Q^2, high P_t, Et miss, etc. Events classified as hard scale physics are always kept.
- Finders for exclusive final states are run: multi-jets, diffraction, heavy flavour, etc. Events matching at least one finder are always kept.

- Downscale soft physics. When the event is not a hard scale physics or satisfies no finder, it is considered as soft physics and downscaled according to these weights:

channels	weight
for inclusive eTAG	20
untagged γp $y_{jb} > 0.9$	40
untagged γp $y_{jb} < 0.9$	60

- Set some event signature, like muons, electron in SpaCal, etc.
- Write the event in various output records: physics, random events, monitor, etc.

2.3.5 Level 1 Triggers Elements

In this section are described the level 1 trigger elements relevant for this analysis.

2.3.5.1 CIP Trigger Elements

The CIP trigger capacity is shortly described in section 2.2.1.1.

2.3.5.2 DC$r\phi$ Trigger Elements

The central drift chambers CJC1 and CJC2 provide trigger information, which consists of fast information about track candidates in the $r\phi$ plane. The system is called Drift Chamber $r\phi$-trigger (DC$r\phi$-trigger). The DC$r\phi$-trigger uses 10 out of the 56 wire layers of the CJC1 and CJC2 drift chambers. The signals are digitised and compared to 10^4 masks in order to identify track candidates. There are masks for tracks of positively and negatively charged particles with high ($P_t > 800\,\text{MeV}$) and low ($400 < P_t < 800\,\text{MeV}$) transverse momentum. The masks are only activated, if the distance of closest approach (DCA) of the track to the z-axis is less than 2 cm. By this the background from beam-wall-events and synchrotron radiation is massively reduced. The number of matching masks for each combination high/pos, high/neg, low/pos and low/neg is counted in 45 sectors in ϕ. With this information the DC$r\phi$-trigger builds several level 1 trigger elements.

2.3.5.3 FTT Trigger Elements

For DIS events the detection of the electron in the LAr or SpaCal calorimeter provides a clear trigger signal. Unfortunately for photoproduction it is not possible to use this strategy since the scattered electron escapes in the beam pipe. At the end of HERA I, it was clearly established, for example for J/ψ mesons, that the efficiency of the trigger is limited by the iron trigger. This motivated the design of a replacement of the DC$r\phi$ trigger for HERA II, the Fast Track Trigger (FTT), with a better P_t granularity and able to reconstruct the invariant masses of decay particles at the level 3.

The FTT level 1 trigger provides information like track multiplicities for different P_t thresholds and track topologies based on the ϕ distribution of the tracks. The lowest P_t threshold is 100 MeV compared to 400 MeV for the DC$r\phi$ trigger. Then during the latency of the second trigger level, a three dimensional track reconstruction of up to 48 tracks is performed. The information provided by this level is similar to the first level, comprising P_t ranges, P_t sums, charge sums and topologies in the $r\phi$ plane, but has higher precision. Finally on the third level it is possible to calculate and cut on the invariant mass of two prong vector meson decays and D* mesons.

2.3.5.4 Muon Trigger Elements

The Muon trigger uses five layers of the central muon detector (layer 3, 4, 5, 8, and 12). The coincidence conditions differ between the detector regions. In the barrel (Mu_Bar) two of the innermost four trigger layers are required. In the backward end-cap (inner Mu_BIEC and outer Mu_BOEC) and the forward outer end-cap (Mu_FOEC) three out of five layers are required and in the forward inner end-cap (Mu_FIEC) four out of five layers. In addition trigger elements demanding two coincidences in the backward (Mu_2_BIoOEC) or forward (Mu_2_FIoOEC) end-cap exist. The trigger elements are combined into a coincidence in the outer end-caps (Mu_ECQ = Mu_BOEC $\vee$ Mu_2_BIoOEC $\vee$ Mu_FOEC) and into a signal covering the complete CMD (Mu_any = Mu_BIEC $\vee$ Mu_BOEC $\vee$ Mu_Bar $\vee$ Mu_FOEC $\vee$ Mu_FIEC).

Two main sources contribute to the efficiency of the iron trigger. The single layer efficiency of the streamer tubes of approximately 80 % is stable and rather well known and contributes also to the reconstruction efficiency of tracks in the CMD. Because of drift times of the order of 100 ns and cable delays the track reconstruction uses the hits of four successive bunch crossings. This is however not possible for the trigger since it would increase the rate drastically. Only hits in two time windows of 96 ns are considered, and a sophisticated system of signal stretching and delays is used to set the trigger bit only in the first bunch crossing of the coincidence. The "timing inefficiency" introduced varies between modules and data taking periods.

2.3.5.5 SpaCal Trigger Elements

The SpaCal trigger produces energy sums in two separate branches according to whether the arrival time of particles corresponds to nominal ep interactions (ToF) or to upstream background (AToF). The *inclusive electron trigger* (IET) uses the highly segmented ToF branch to compare the energy in a trigger tower of 16 electromagnetic SpaCal cells to three adjustable thresholds. The trigger elements are formed in an inner (IET_Cen, $r < 16\,\mathrm{cm}$) and an outer ($r > 16\,\mathrm{cm}$) region of the SpaCal. In the AToF branch coarse energy sums are formed that are used to veto non ep background.

The good time resolution of approximately 0.4 ns is used to reject upstream beam-related background. These background events have a difference in their time-of-flight of approximately 10 ns with respect to events originating from the nominal interaction point. With this method a part of the high rate beam-gas and beam-wall background caused by the proton beam can be rejected on trigger level 1.

2.3.5.6 Time of Flight Trigger Elements

The trigger elements are built from information of the time of flight system and tag events where the detector response corresponds to the time window of an electron-bunch crossing with a proton-bunch or not.

2.3.6 The Level 4 "Heavy Flavour Closed" Finder

The trigger level 4 has several finders for the different physics analyses. These finders overlap to some extent. But only the "Heavy Flavour Closed" finder No. 16 is specifically designed to save the data used in this analysis. This finder is fully described in the note [50]. The following will give a summary of it. This description is valid until April 2006.

The aim of the finder No. 16 is to save events covering elastic and inclusive J/ψ and Υ decays both in the muon and electron decay channels as well as inclusive muons for beauty measurements.

Apart from these events, which fulfil already relatively hard cuts compared to the final selection criteria, a few minimum bias events for efficiency and systematic studies are needed.

The finder No. 16 is running on all events independently of the fired subtriggers, but a few cuts are applied in addition, if certain subtriggers have fired. For SpaCal subtriggers (s0 to s11 and s61) a minimal SpaCal cluster energy of $E > 10\,\text{GeV}$ and a $E - Pz > 35.75\,\text{GeV}$ are required.

The finder No. 16 has six classes and can be divided into four different steps: first of all those events are taken into account, where at least two leptons are identified (AJPSI and 2ELEC), then those events with only one identified lepton but at most five KTKX tracks (ATWOMU and ATWOEL), those with exactly two CJKT tracks but without lepton identification required (2PRONG), and finally the inclusive muons (AOPEN). A cosmic filter is used in addition for the classes AJPSI, ATWOMU and 2PRONG for events with exactly two tracks (all tracks are counted without any track quality criteria). If an event fulfils all the cuts associated with at least one of the subclasses it is accepted by the finder No. 16, and by this it is classified as class 16 and passes the trigger level 4. The definition of these classes is given in table 2.5.

AJPSI (bit 3)

- $\geqslant 2$ iron, FMD or calorimeter ($\text{Quality}_\mu \geqslant 2$, $\theta_\mu > 18°$) muons with good associated tracks
- $\sum_{i=1}^{2} \text{Quality}_\mu^i \geqslant 5$ for events without iron or FMD muons
- cosmic filter
- $M_{12} > 2\,\text{GeV}$

ATWOMU (bit 1)

- $\text{N}_{\text{KTKX}} \leqslant 5$
- 1 iron, FMD or calorimeter ($\text{Quality}_\mu = 3$) muon with good associated track ($\theta_\mu > 18°$ or $P_\mu > 4\,\text{GeV}$ or FMD + iron)
- 1 KTKX track ($P > 0.7\,\text{GeV}$, $\theta_\mu > 18°$ or $P > 4\,\text{GeV}$) (no quality criteria for KTKT and CJKT tracks, good track cuts for FTKT tracks
- cosmic filter
- $M_{12} > 2\,\text{GeV}$

2PRONG (bit 5)

- $\text{N}_{\text{CJKT}} = 2$
- no identified leptons required
- both tracks with $P > 0.7\,\text{GeV}$ and $\theta > 18°$ (no track quality criteria)
- cosmic filter
- $M_{12} > 2\,\text{GeV}$

AOPEN (bit 0)

- 1 iron ($\text{N}_{\text{layer}} \geqslant 6$ for endcaps) or FMD muon
- central muon ($\theta > 18°$): $P_t > 1.5\,\text{GeV}$
- forward muon ($\theta < 18°$): $P > 5\,\text{GeV}$ and ($\theta > 15°$ for FMD validation)
- $\text{N}_{\text{KTKX}} \geqslant 4$

Table 2.5: Definition of the "Heavy Flavour Closed" Finder classes. The two classes concerning the electron decay mode, ATWOEL and 2ELEC, are not given.

Chapter 3

Monte Carlo Simulation and Reconstruction of the Kinematic Variables

This chapter will describe the Monte Carlo program used for this analysis, and presents a study of the quality of the reconstruction of the kinematic variables used to measure the cross section.

The Monte Carlo [1] simulation of physics processes is used to correct measured data for detector effects like acceptance, to estimate contributions from background processes and to compare cross sections with different models.

3.1 Simulation Process

The simulation process is done in three steps, cf. figure 3.1. On generator level the Monte Carlo program generates four-vectors of particles according to a physics model. The generated events constitute a random sampling in the kinematic phase space. Then decays of unstable particles and interactions with the detector are simulated with the program H1SIM [51] based on GEANT [52], where the detector response and the trigger decision is also derived. The last step is the same for Monte Carlo as for measured data. The raw Monte Carlo data are reconstructed by the reconstruction software H1REC and logged with additional information from the generator containing the generated kinematics and the particle listings.

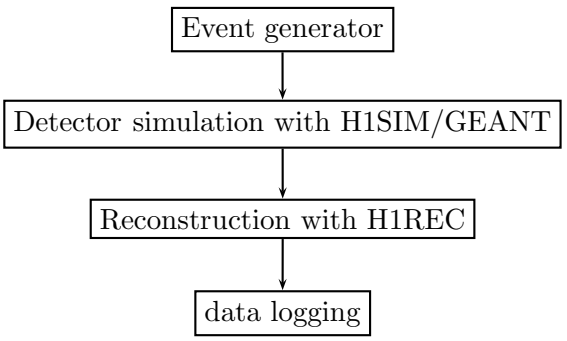

Figure 3.1: Simulation process

[1] The method is called after Monte Carlo, a quarter of the Monaco principality on the French riviera. It alludes to the "roulette" hazard game in the casino of Monaco. The first random generator, appeared in France in 17th century.

3.2 Monte Carlo Programs

For the present analysis three Monte Carlo programs are used: EPJPSI for the simulation of J/ψ meson production via direct photon-gluon fusion and resolved photon processes and DIFFVM to check the simulation of the muon identification in the LAr calorimeter and the instrumented iron detector.

3.2.1 EPJPSI

EPJPSI [53] is a Monte Carlo program which simulates the production of J/ψ mesons in high energy γp, ep, μ^-p, p$\overline{\text{p}}$ and pp collisions using the CSM model as described in section 1.5.3.

The relevant production mechanisms for the present analysis are direct photon-gluon fusion and gluon-gluon fusion as the dominant process for resolved photons. The simulation of direct photon-gluon fusion (EPJPSI-direct) and gluon-gluon fusion in processes with resolved photons (EPJPSI-resolved) is used to correct the data for detector effects and to calculate cross sections.

The interaction between an electron and a proton is described via exchange of photons in the equivalent photon approximation. The parton density functions for the proton and the photon are chosen from the PDFLIB [54, 55]. In this analysis the standard parton density function CTEQ 5L (1004046) [56] is used for the proton and GRV92 LO (3005003) [57, 58] for the photon respectively.

The scale for the evaluation of the parton density functions can be chosen as M_ψ^2, $M_\psi^2 + P_{t,\psi}^2$ and the centre of mass energy squared s of the particles taking part in the hard interaction. The mass of the J/ψ meson is used for this analysis. The matrix elements of the production processes are calculated in leading order in α_s. The value of the strong coupling constant is fixed at $\alpha_s = 0.3$ for this analysis. Alternatively it can be calculated according to the one-loop formula

$$\alpha_s(\mu) = \frac{6\pi}{(33 - 2n_f)\ln(\mu/\Lambda)}$$

For example with MRS(A'), $n_f = 4$ free flavours and $\Lambda = 231\,\text{MeV}$ this would result in $\alpha_s = 0.29$ at a scale of $\mu = M_\psi$.

Higher order QCD effects are taken into account using a parton shower approach with a backward evolution from the hard scattering process to the initiating partons according to the Altarelli-Parisi equations. The hadronisation is performed with the Lund string fragmentation by the JETSET package [59].

An overview over the predicted elasticity dependence of the differential electron-proton cross section for the direct and resolved J/ψ meson production mechanisms is shown in figure 3.2.

Direct photon-gluon fusion dominates the J/ψ meson production in the region of medium to high elasticities, direct and resolved cross sections differs of one order of magnitude at $z \approx 0.4$. While gluon-gluon fusion in resolved photon events is the most important process at low elasticities $z \lesssim 0.2$, they differ of one order of magnitude at $z \approx 0.8$. However a significant contribution from the direct process remains down to $z \approx 0.1$.

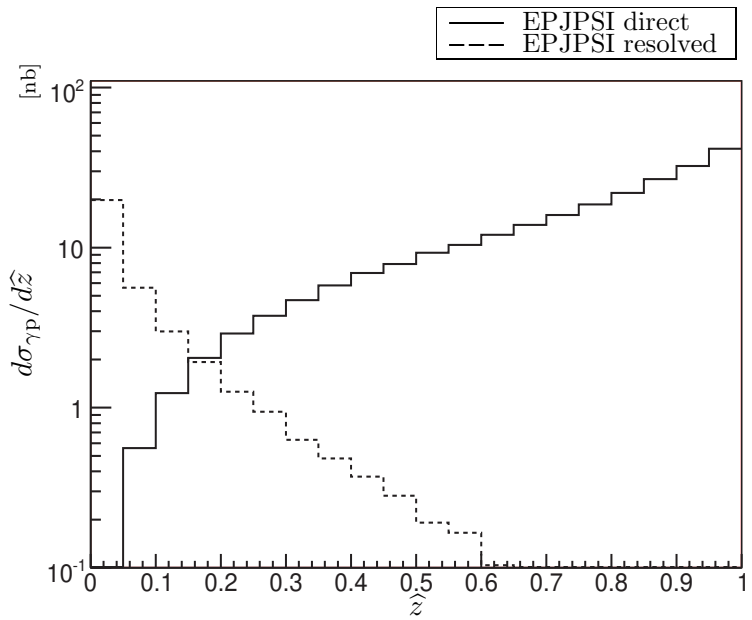

Figure 3.2: Differential electron-proton cross section for resolved and direct J/ψ meson production mechanisms as a function of the elasticity z in the photoproduction domain as predicted by the EPJPSI Monte Carlo program. Only the shape is expected to be correct.

The calculation of J/ψ production in direct photon-gluon fusion is performed according to [15] in the Colour Singlet Model. Relativistic corrections due to a relative motion of the quarks inside the J/ψ meson can be taken into account [60]. These corrections lead to a rise at high z (cf. figure 3.2) in contrast to the decrease predicted at $z \approx 1$ due to vanishing phase space.

The coupling of the J/ψ meson to the $c\overline{c}$ pair is determined from a leptonic decay width of $\Gamma_{\ell\overline{\ell}} = 5.4\,\mathrm{keV}$ including QCD corrections. The value of the charm mass, which has a strong influence on the normalisation of the cross section, is set to half of the J/ψ meson mass.

The resolved photoproduction of J/ψ mesons is dominated by gluon-gluon fusion via the subprocesses $gg \longrightarrow J/\psi g$ and $gg \longrightarrow J/\psi\gamma$. The cross section of the second subprocess is about a factor 5 lower than the cross section of $gg \longrightarrow J/\psi g$. Both cross sections are calculated in the Colour Singlet Model. Since the gluon has the same quantum numbers as the photon except for the colour, the matrix elements differ from direct photon-gluon fusion only by colour factors and coupling constants. In addition the parton density of the photon is taken into account.

3.2.2 DIFFVM

The DIFFVM Monte Carlo Program is used to check the simulation of the muon identification in the LAr calorimeter and the instrumented iron detector.

DIFFVM [61] is a Monte Carlo program which simulates diffractive processes in ep scattering within the framework of Regge phenomenology and the Vector Dominance Model (VDM) as described in section 1.6. In this approach the electron emits a photon which fluctuates into a virtual vector meson. This vector meson then interacts diffractively, i.e. by pomeron exchange, with the proton. The vector meson as well as the proton may emerge intact from the interaction, or dissociate diffractively. Diffractive processes are describe in more detail in section 1.6.

The slope parameter b, which describes the exponential decrease of the cross section with the four-momentum transfer at the proton vertex, is set to 4.80 GeV for the elastic process and 1.60 GeV for the proton dissociative process.

3.3 Reconstruction of the Kinematic Variables

This section will discuss the reconstruction of the kinematic variables used in this analysis to measure the cross section: the transverse momentum squared of the J/ψ meson $P^2_{t,\psi}$, the photon-proton centre-of-mass energy $W_{\gamma \mathrm{p}}$ and the elasticity z. These kinematic variables depend on the reconstruction of the decay muons of the J/ψ mesons, as well as on the Hadronic Final State (HFS) reconstruction. The resolution achieved is an essential element to choose the size of the bins for the cross section measurements. The same binning will be used for this analysis as those of the previous measurements [34], excepted for some bins where the statistics is lower for this analysis. In this case adjacent bins are merged in order to increase the statistics. The reconstruction of the hadronic final state is performed in this analysis by the new algorithm HADROO 2 of the H1OO framework [62], preceding analyses used the FORTRAN framework. In order to validate the binning for this analysis, the purity and the stability will be studied. The same two component simulation of direct and resolved processes with the EPJPSI Monte Carlo program is used for this study as for the analysis. The relative normalisation of these two components is given in section 7.3.2. Events are selected with the selection given in table 4.6 for the medium z selection and in table 4.8 for the low z selection. The trigger selection is not applied.

The notation $\widehat{x}$ denotes a generated observable

3.3.1 Reconstruction of the Decay Muons

Muons are reconstructed within the H1OO framework by the so called muon finder. It will be presented and then the resolutions of the muon reconstruction will be shown.

The muon finder is implemented with algorithms described in [63, 64]. It links tracks and clusters from several sub-detectors, tracking systems, calorimeters and the instrumented iron detector.

Muons with low momentum are usually stopped before they reach the instrumented iron detector. For this reason there are two classes of muons: calorimeter muons and iron muons. As the typical energy deposit of these muons corresponds to the minimum of ionisation, they produce only few cells with energy in both calorimeters, electromagnetic and hadronic. This property is used to distinguish them from the other particles, electron and photon, producing electromagnetic showers in the electromagnetic calorimeter. When a muon has enough energy to survive until it reaches the instrumented return yoke of the H1 magnet, signals from the instrumented iron detector permit to tag it unambiguously as a muon. Therefore the calorimeters and the instrumented iron detector are used as muon tagger, and the tracking systems to reconstruct the four-vector from the track information.

In order to avoid double counting of energy, it is necessary *to lock* the muon cells, i.e. attribute and remove the cells from the list of hadronic final states. This is necessary to reconstruct kinematic variables like the elasticity z correctly. In practise cells contained in a volume corresponding to the extrusion of a circle perpendicular and along the helix of the tracks and its extrapolation, are assumed to be muon radiation. The radius of the circle is determined according to the resolution of the detectors. It is a compromise, a too large radius will lock cells from other particles, while a too small radius will omit cells from muons. At the start of this thesis, the H1oo framework was still at an early stage, and thus affected by several malfunctions. The locking mechanism was fixed and verified during this thesis. Figure 3.3 shows the number of hadronic final state objects versus the polar angle of the muon θ_μ for events generated by a single muon Monte Carlo simulation. A sample of muons and anti-muons was generated with a uniform phase space covering the full range of the polar and azimuthal angles and a momentum up to 5 GeV. Since the decay muons of the J/ψ mesons have typically a momentum lower than 5 GeV, muons with higher momentum are negligible.

The simulation of the noise in the LAr calorimeter was disabled for the simulation process in order to have any noise cells, which could perturb the interpretation. Despite an improvement of the locking, the locking is still not perfect in the SpaCal.

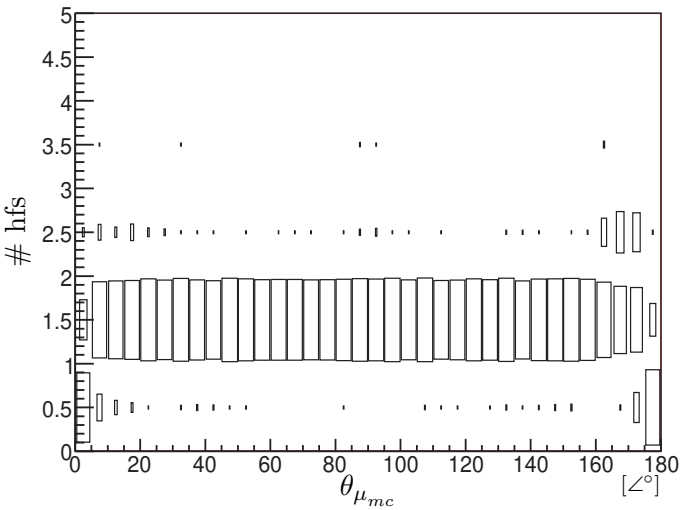

Figure 3.3: Number of hadronic final state objects as a function of the polar angle of the muon θ_μ for events generated by a single muon Monte Carlo simulation. The number zero means the muon is not reconstructed, one means the muon is reconstructed, and more than one means there is additional hadronic final states and thus the locking was faulty.

The muon finder tags muon with a so called "Lee West quality". This quality is defined as:

$$Q_{\mathrm{LW}} = Q_{\mathrm{Calorimeter}} + 10 \times Q_{\mathrm{Iron}} + 100 \times Q_{\mathrm{FMD}}$$

where the qualities $Q_{\mathrm{Calorimeter}}$, Q_{Iron}, and Q_{FMD} lie in the range $[0,3]$, $[0,1]$ and $[0,1]$ respectively. For the calorimeter quality, the numbers mean respectively "bad", "low", "medium" and "high" quality, see the note of Lee West [65] for their definitions.

Figure 3.4 shows the resolutions of the momentum P_μ, the transverse momentum $P_{t,\mu}$, the azimuthal angle ϕ_μ, the polar angle θ_μ, and $(E - Pz)_\mu$. Events were generated by the previously mentioned single muon Monte Carlo simulation. These distributions are fitted with a double Gaussian. But the real shape is still more complex due to the momentum dependence of the trackers resolutions. For this domain of momentum the trajectory is a helix, and the kinematics is obtained from a fit on the hits of the trajectory, which gives a relatively good and accurate reconstruction. The resolution of $(E - Pz)_\mu$, equal to $\sqrt{P_\mu^2 + M_\mu^2} - P_\mu.\overrightarrow{z}$, benefits naturally of the good precision on the momentum.

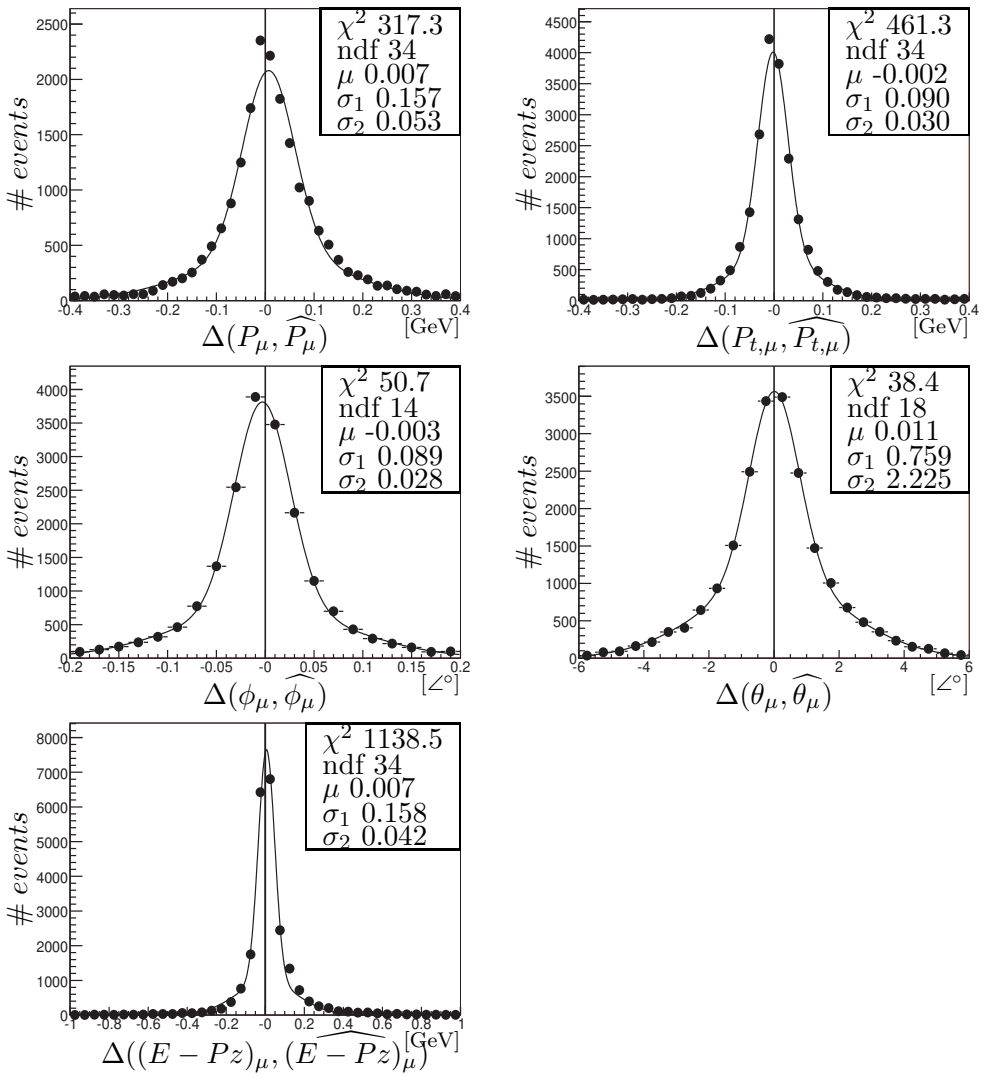

Figure 3.4: Resolutions of P_μ, $P_{t,\mu}$, ϕ_μ, θ_μ and $(E - Pz)_\mu$. The **box in the top right corner** gives the χ^2 and the number of degrees of freedom of the fit with two Gaussians, μ denotes the mean and $\sigma_{1,2}$ the widths of the Gaussians.

3.3.2 Reconstruction of the J/ψ Mesons and the Transverse Momentum Squared of the J/ψ Meson $P^2_{t,\psi}$

The J/ψ meson is reconstructed from two decay muon candidates selected by the selection described in section 4.1.3. Thus the standard deviation of $E - Pz$ is that of figure 3.4 multiplied by a factor $\sqrt{2}$.

Figure 3.7 shows the resolution of $P^2_{t,\psi}$ for the medium z selection, as well as the means and the standard deviation in bins of $P^2_{t,\psi}$. The resolution for the low z selection is shown in figure 3.5. The relative resolution is shown in figure 3.8 for the medium z selection, and in figure 3.6 for the low z selection, respectively. The good precision of the muon reconstruction gives a good accuracy, the relative resolution is close to zero. The standard deviation shows a linear dependence (at the first order) as a function of $P^2_{t,\psi}$, which comes from the momentum resolution of the central tracking chambers (cf. section 2.2.1.1). All the bins are much larger than the standard deviation.

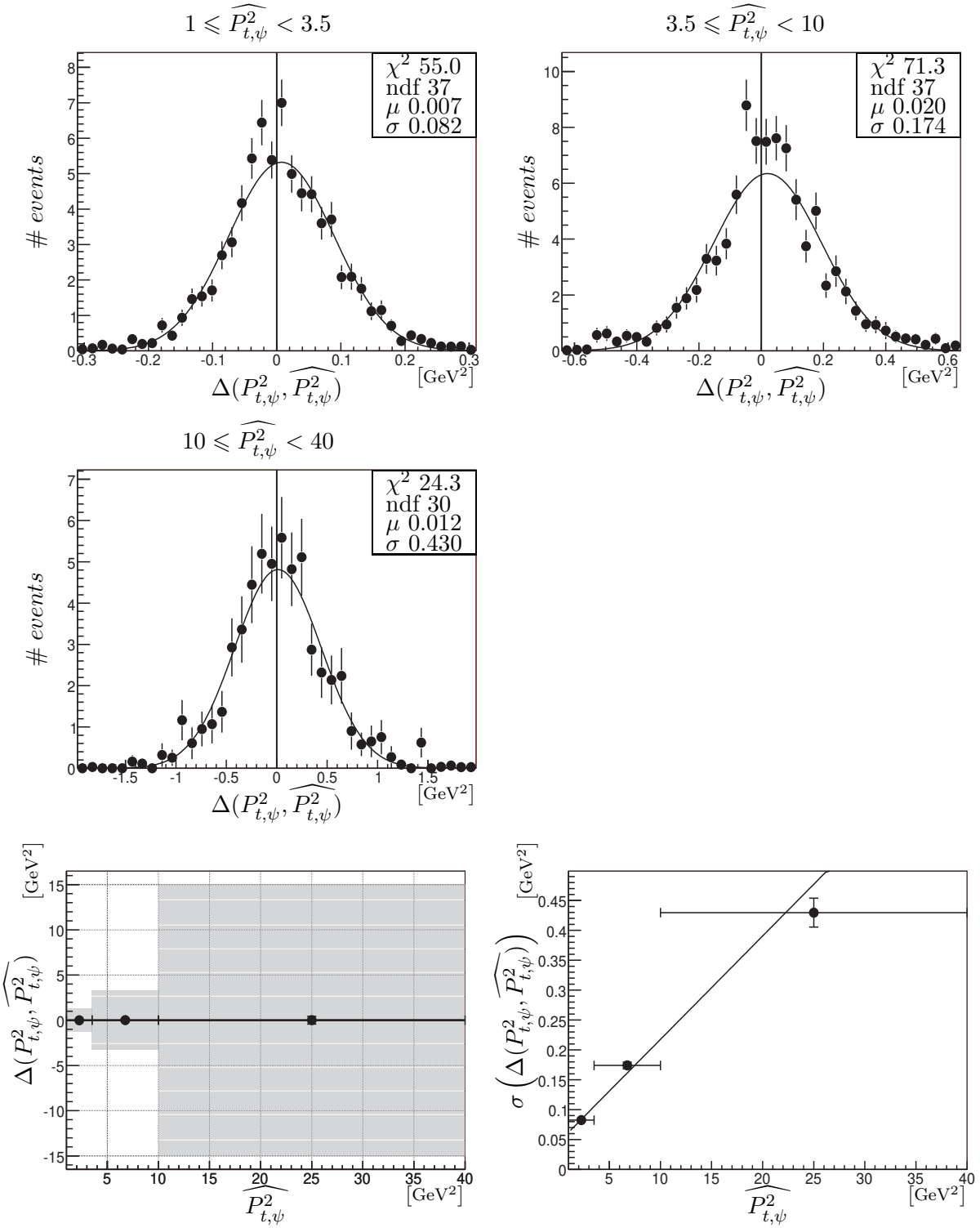

Figure 3.5: Resolution of $P^2_{t,\psi}$, $\Delta(P^2_{t,\psi}, \widehat{P^2_{t,\psi}})$, in the analysis bins for the **low** z selection. Means and standard deviations of the distributions on top are shown as a function of $\widehat{P^2_{t,\psi}}$ at the bottom. The shaded region shows the bin width.

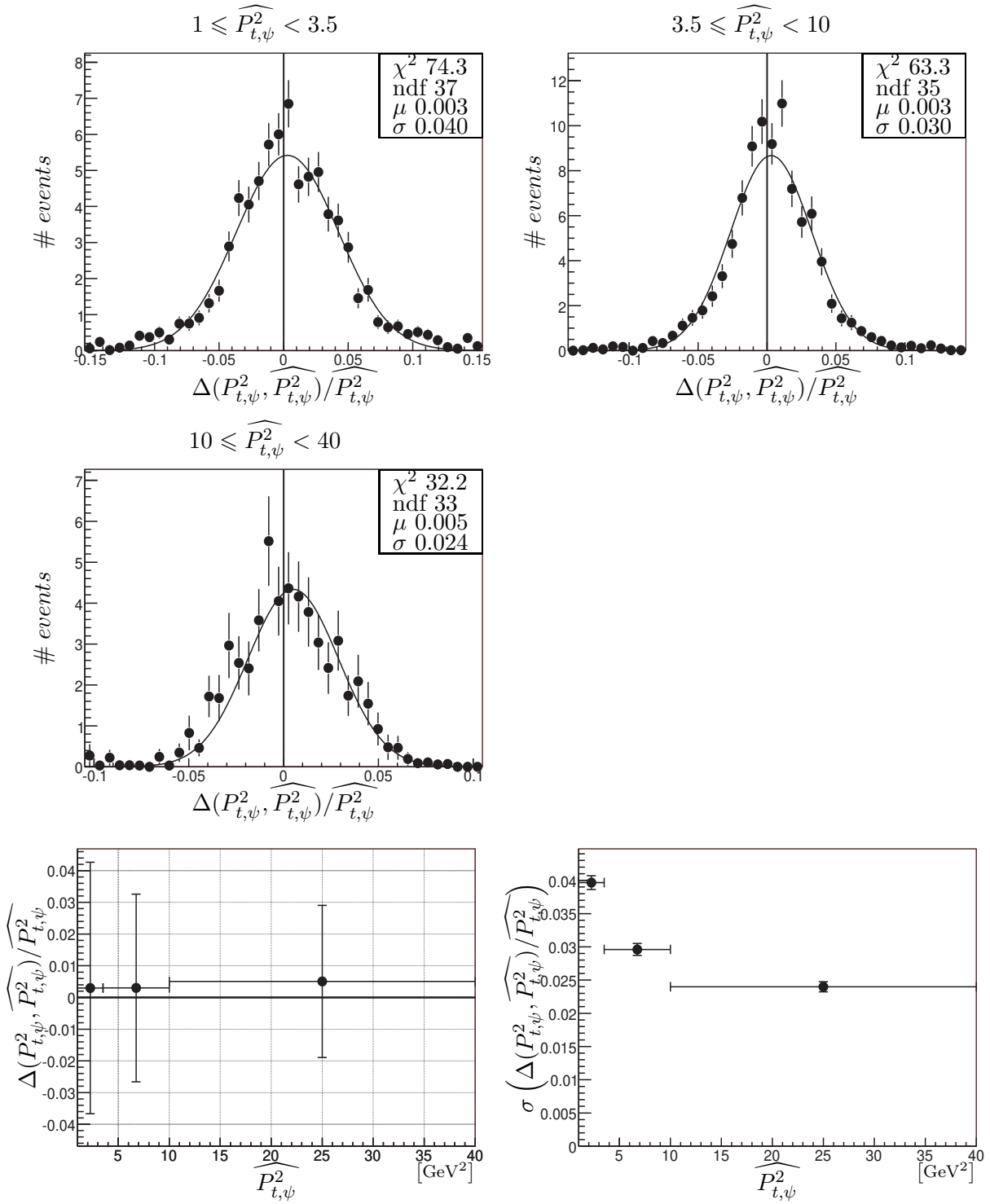

Figure 3.6: Relative resolution of $P^2_{t,\psi}$, $\Delta(P^2_{t,\psi}, \widehat{P^2_{t,\psi}})/\widehat{P^2_{t,\psi}}$, in the analysis bins for the **low** z selection. Means and standard deviations of the distributions on top are shown as a function of $\widehat{P^2_{t,\psi}}$ at the bottom. The shaded region shows the bin width.

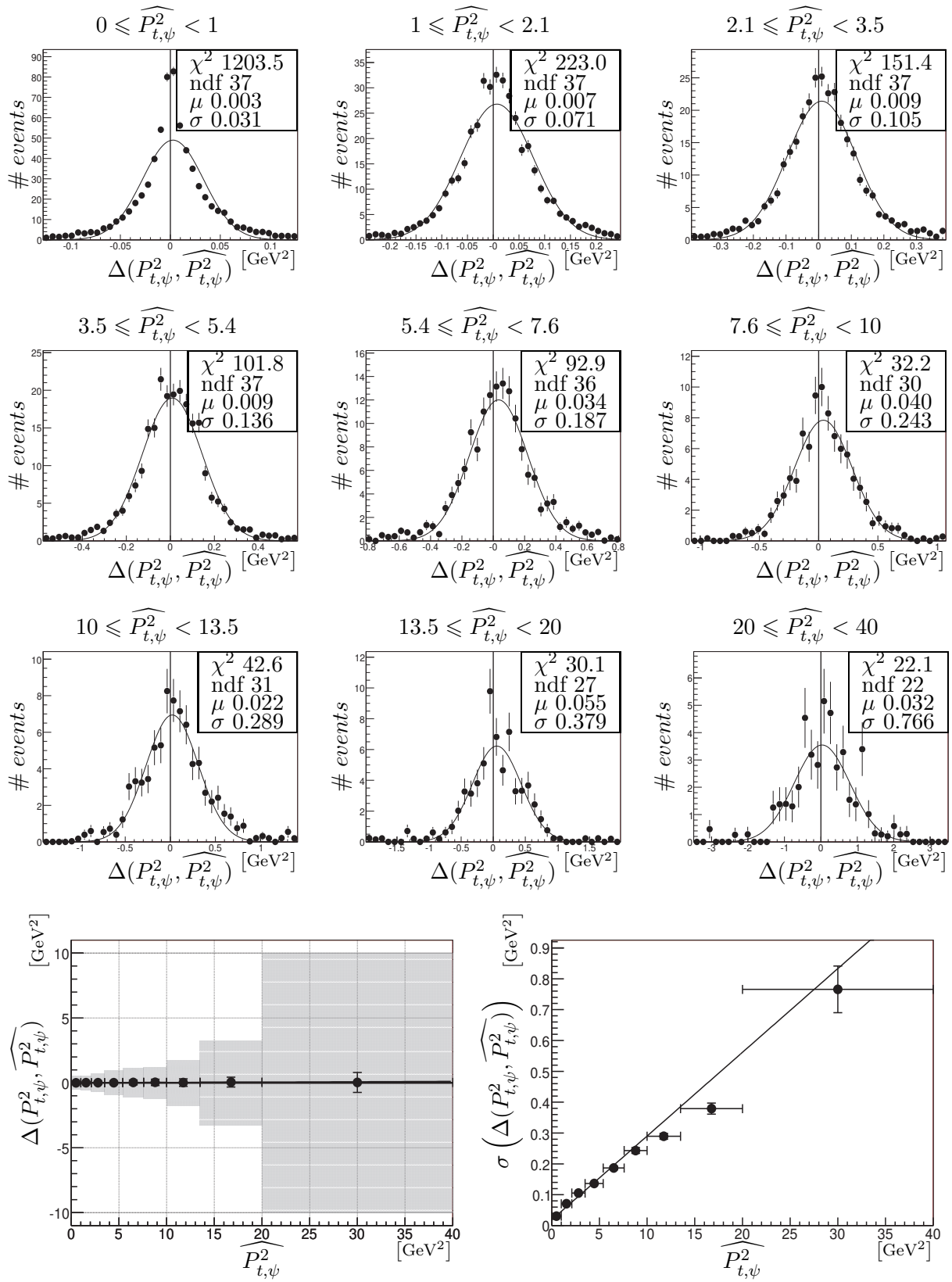

Figure 3.7: Resolution of $P^2_{t,\psi}$, $\Delta(P^2_{t,\psi}, \widehat{P^2_{t,\psi}})$, in the analysis bins for the **medium** z selection. Means and standard deviations of the distributions on top are shown as a function of $\widehat{P^2_{t,\psi}}$ at the bottom. The shaded region shows the bin width.

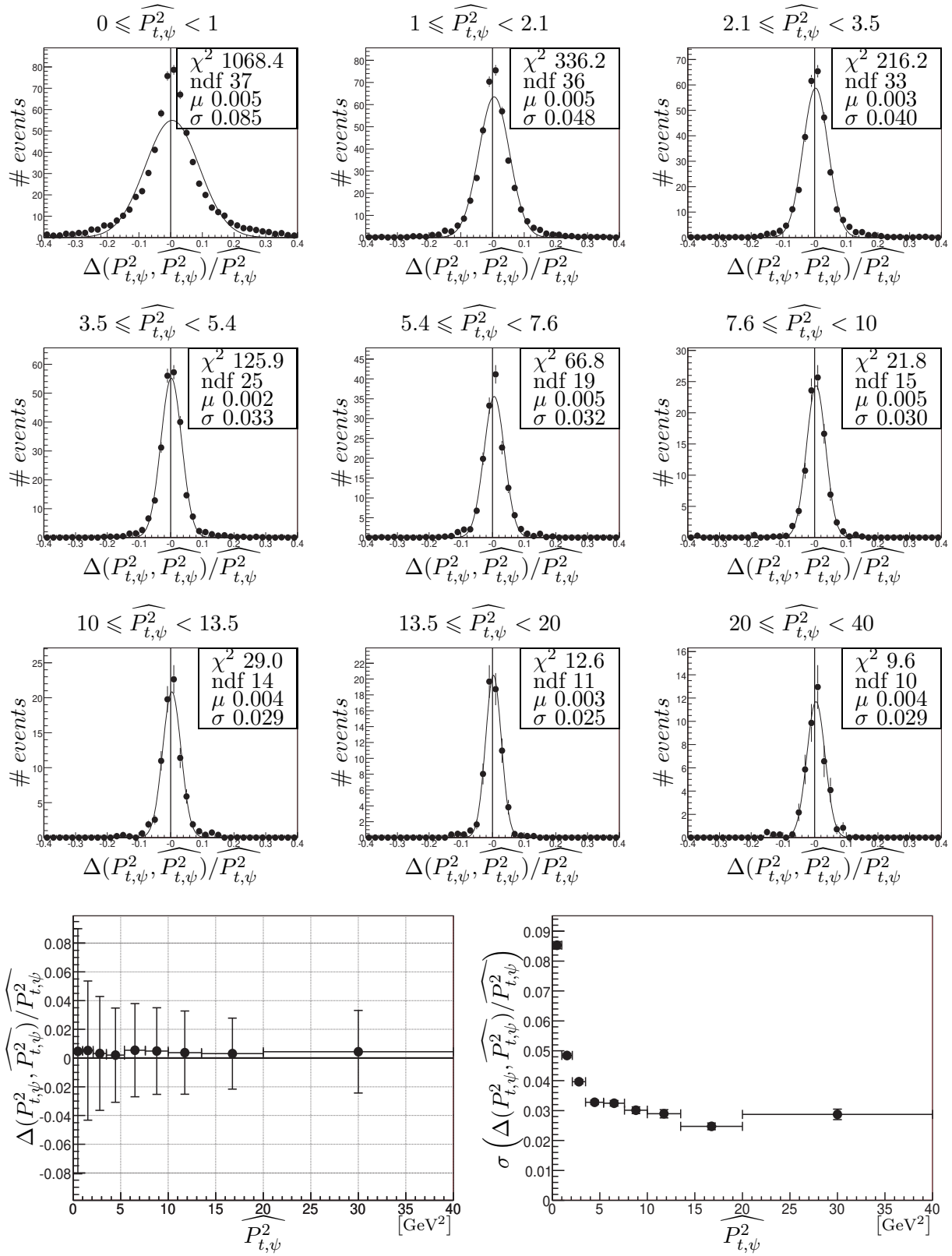

Figure 3.8: Relative resolution of $P^2_{t,\psi}$, $\Delta(P^2_{t,\psi}, \widehat{P^2_{t,\psi}})/\widehat{P^2_{t,\psi}}$, in the analysis bins for the **medium** z selection. Means and standard deviations of the distributions on top are shown as a function of $\widehat{P^2_{t,\psi}}$ at the bottom. The shaded region shows the bin width.

3.3.3 Reconstruction of the Kinematic Variables $W_{\gamma p}$ and z

In the preceding sections 1.2 and 1.4, it was shown that $W_{\gamma p}$ can be expressed only by y and the energies of the beams, see the equations (1.9) and (1.12), respectively. From the definition of y, equation (1.5), and the equation (1.1) we obtain the following relation

$$y \approx \frac{q.P}{2E_e E_p}.$$

This relation shows that y depends only on the energies of the beams, the momentum of the incoming particles, and on the momentum of the scattered electron via the momentum of the virtual photon.

In photoproduction the scattered electron is not detected in the main detector but scattered at low angle in the beam pipe. Therefore its momentum cannot be measured directly. The only way to measure indirectly the momentum of the virtual photon is to use the hadronic final state. Since particles are lost through the beampipe in the forward and backward direction of the detector, a method which minimises the error on the reconstructed variables is needed.

Let H be the four momentum of the hadronic final state. We have the following relation

$$H \cdot P = (q + P) \cdot P = q \cdot P + m_p^2 \tag{3.1}$$

$$= \sum H_i \cdot P = E_p \sum (E - Pz)_i, \tag{3.2}$$

where H_i denotes the four-vector of an hadronic final state object. The summation is performed on the overall of the hadronic final state objects. If we neglect the proton mass, we obtain finally

$$y_{jb} = \frac{1}{2E_e} \sum (E - Pz)_i \tag{3.3}$$

The quantity $(E - Pz)_i$ is equivalent to $P_i(1 - \cos\theta_i)$, if we neglect the mass of the particle. Let's look at the error of the reconstruction in the forward and backward directions.

- At $\theta_i \to 0$, $E_i - Pz_i = P_{t,i}\frac{\theta_i}{2}$. The transverse momentum is badly measured, but this contribution is suppressed by $\theta_i \sim 0$.
- At $\theta_i = \pi$, $E_i - Pz_i = 2P_i$ which is not necessarily a negligible quantity. But it can be considered negligible, since due to the boost only a small portion of the particles go in the backward direction, as can be verified in figure 3.9.

This method was proposed by Jacquet and Blondel in the report [66], and has the required property to minimise the errors on the reconstruction.

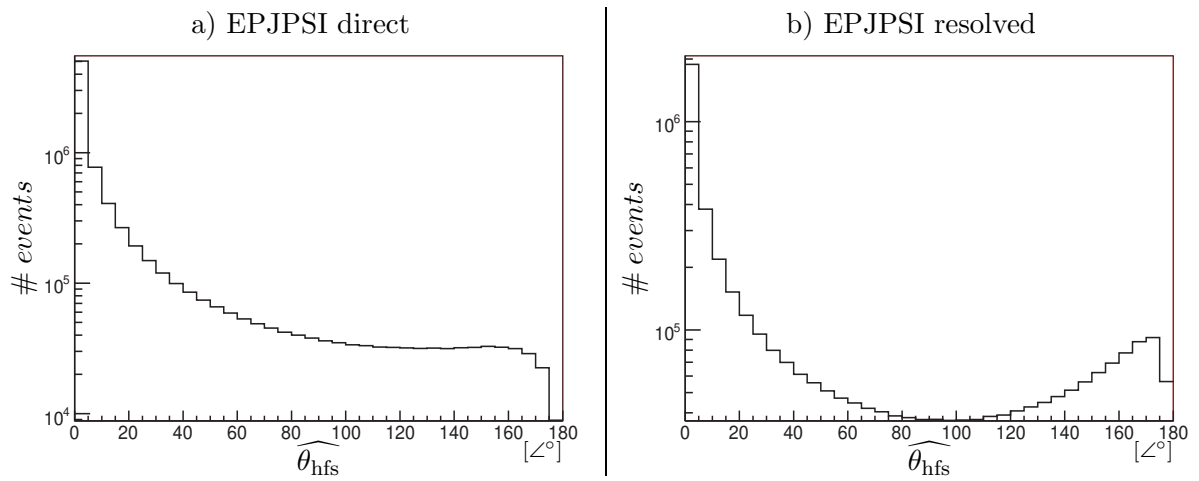

Figure 3.9: Angular distribution of the Hadronic Final State. a) Events are generated with the Monte Carlo program EPJPSI direct with the medium z selection. b) Events are generated with the Monte Carlo program EPJPSI resolved with the low z selection.

We can now express $W_{\gamma\mathrm{p}}$ and z as follows:

$$W^2_{\gamma\mathrm{p}} = 2E_{\mathrm{p}} \sum (E - Pz)_i \tag{3.4}$$

$$z = \frac{(E - Pz)_\psi}{\sum (E - Pz)_i} \tag{3.5}$$

These two formulae will be used to reconstructed $W_{\gamma\mathrm{p}}$ and z. The summation is performed over the HFS particle list within the H1oo framework. The hadronic final state is reconstructed by the Hadroo2 algorithm, which is described in detail in the note [62]. The pion mass is used in the computation for all HFS particles, except for the two decay muons.

Figure 3.10 shows the resolution of $W_{\gamma\mathrm{p}}$ for the medium z selection, as well as the means and the standard deviation in bins of $W_{\gamma\mathrm{p}}$. The relative resolution is shown in figure 3.12. The distribution is not always well described by a Gaussian, but it is not crucial. A systematic loss from 2 % to 3 % per GeV in the energy flow is observed. The standard deviation shows a rising linear dependence as a function of $W_{\gamma\mathrm{p}}$. Some events are reconstructed in the preceding bin for $W_{\gamma\mathrm{p}}$ above 140 GeV.

The resolution and the relative resolution for the low z selection are shown in figure 3.13 and in figure 3.14, respectively. A systematic loss from 5 % to 10 % per GeV in the energy flow is observed, and thus more important than for the medium z selection. Indeed the loss in the energy flow is proportional to the number of particles of the event, and thus inversely proportional to the elasticity. As for the medium z selection, some events are reconstructed in the preceding bin for $W_{\gamma\mathrm{p}}$ above 150 GeV. Half of the events of the last bin are reconstructed in the preceding bin.

Figure 3.15 shows the resolution of the elasticity z for the medium z selection. The relative resolution is shown in figure 3.16. The relative resolution and its standard deviation decrease linearly as a function of z to zero for $z \approx 1$, which is coherent with the value of z for elastic J/ψ mesons. Since z is computed with the inverse of $W_{\gamma\mathrm{p}}$, the reconstructed value of z is systematically overestimated. Some events are reconstructed in the following bin for $.3 < z < .75$.

The resolution and the relative resolution for the low z selection are shown in figure 3.17 and in figure 3.18, respectively. The same behaviour is observed as for the medium z selection. Some events are reconstructed outside the analysis range for z above 0.3.

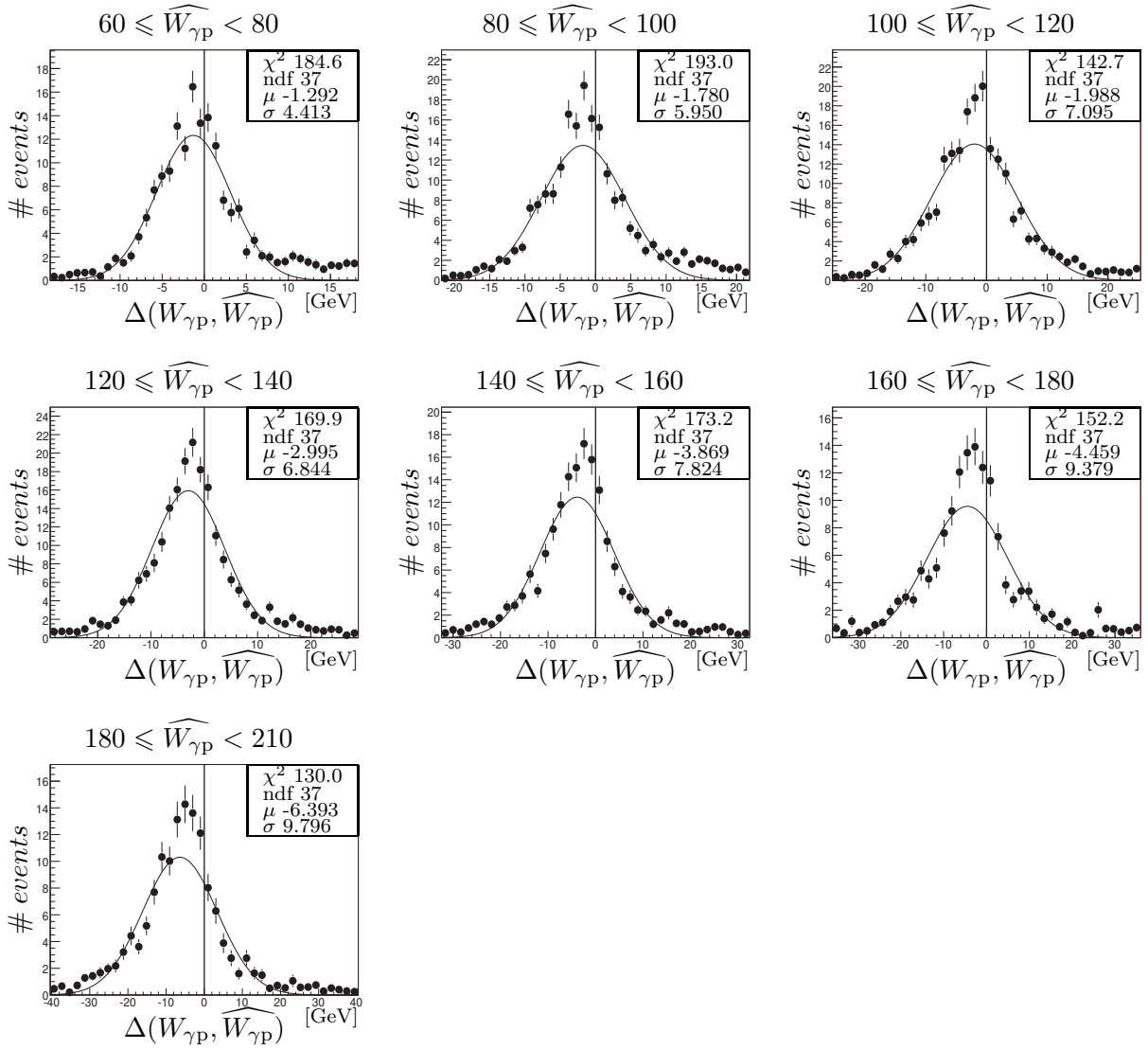

Figure 3.10: Resolution of $W_{\gamma p}$, $\Delta(W_{\gamma p}, \widehat{W_{\gamma p}})$, in the analysis bins for the **medium** z selection. See figure 3.11 for the rest.

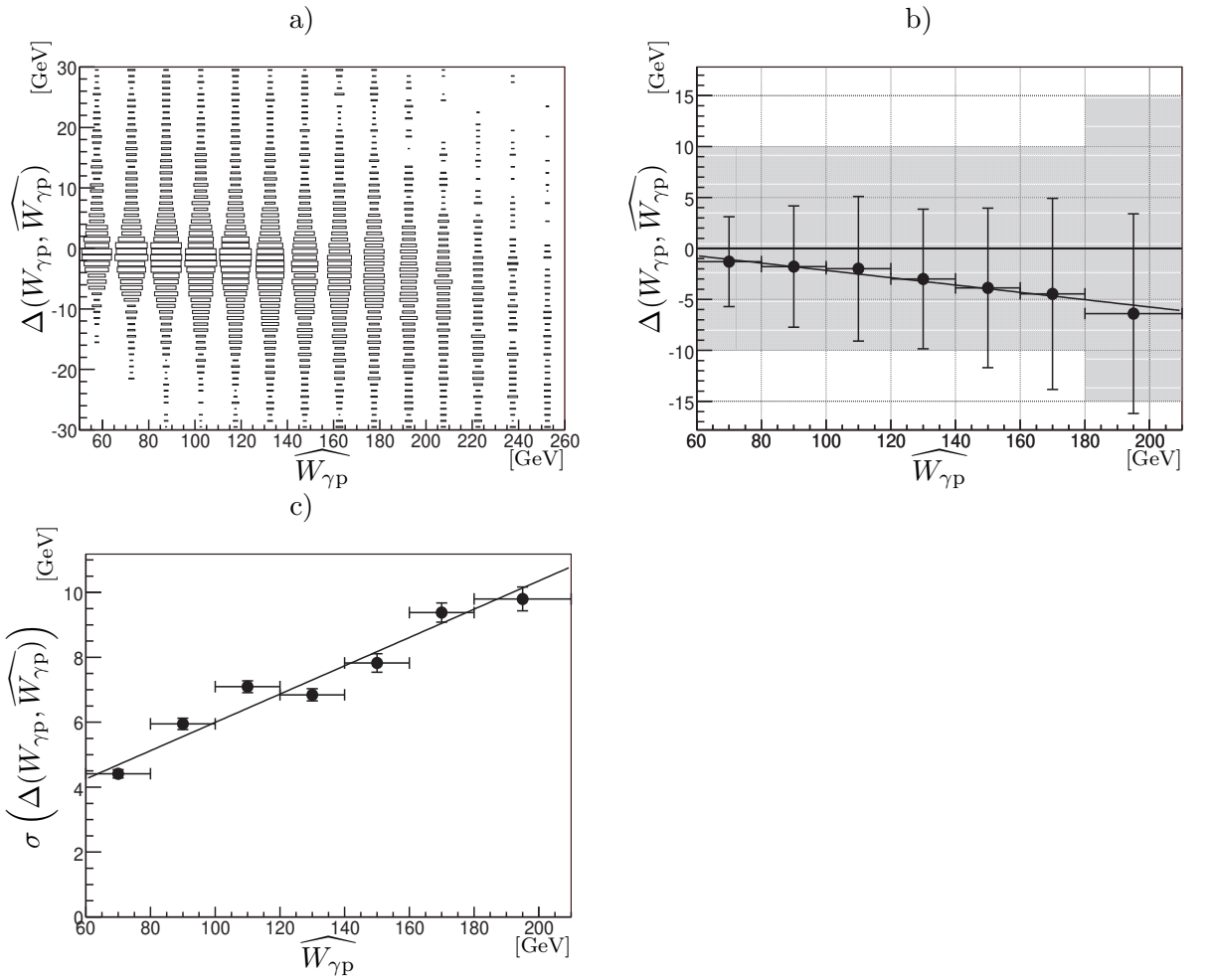

Figure 3.11: Continuation of figure 3.10. a) b) Means and c) standard deviations of the distributions on top are shown as a function of $\widehat{W_{\gamma p}}$. The shaded region shows the bin width.

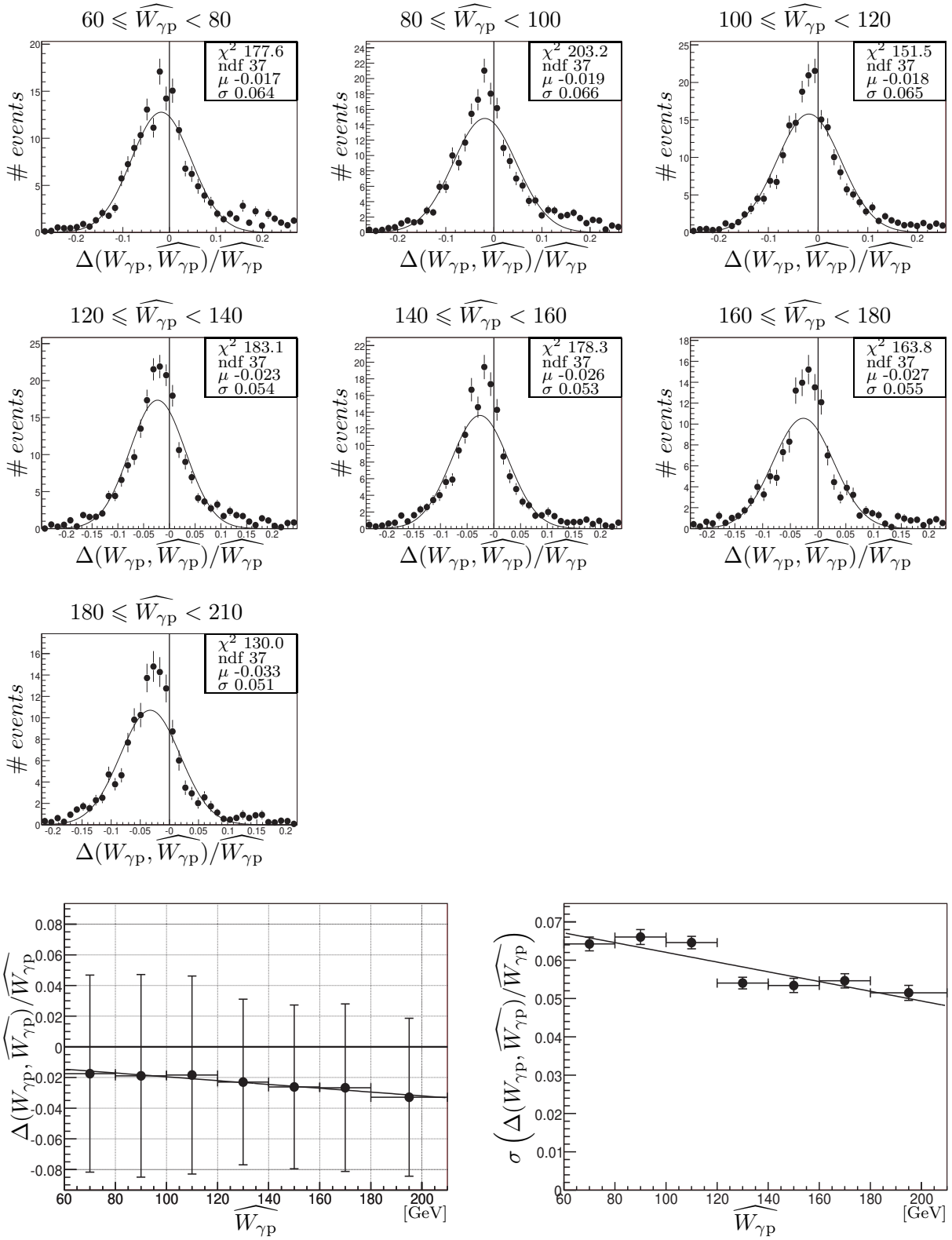

Figure 3.12: Relative resolution of $W_{\gamma p}$, $\Delta(W_{\gamma p}, \widehat{W_{\gamma p}})/\widehat{W_{\gamma p}}$, in the analysis bins for the **medium** z selection. Means and standard deviations of the distributions on top are shown as a function of $\widehat{W_{\gamma p}}$ at the bottom. The shaded region shows the bin width.

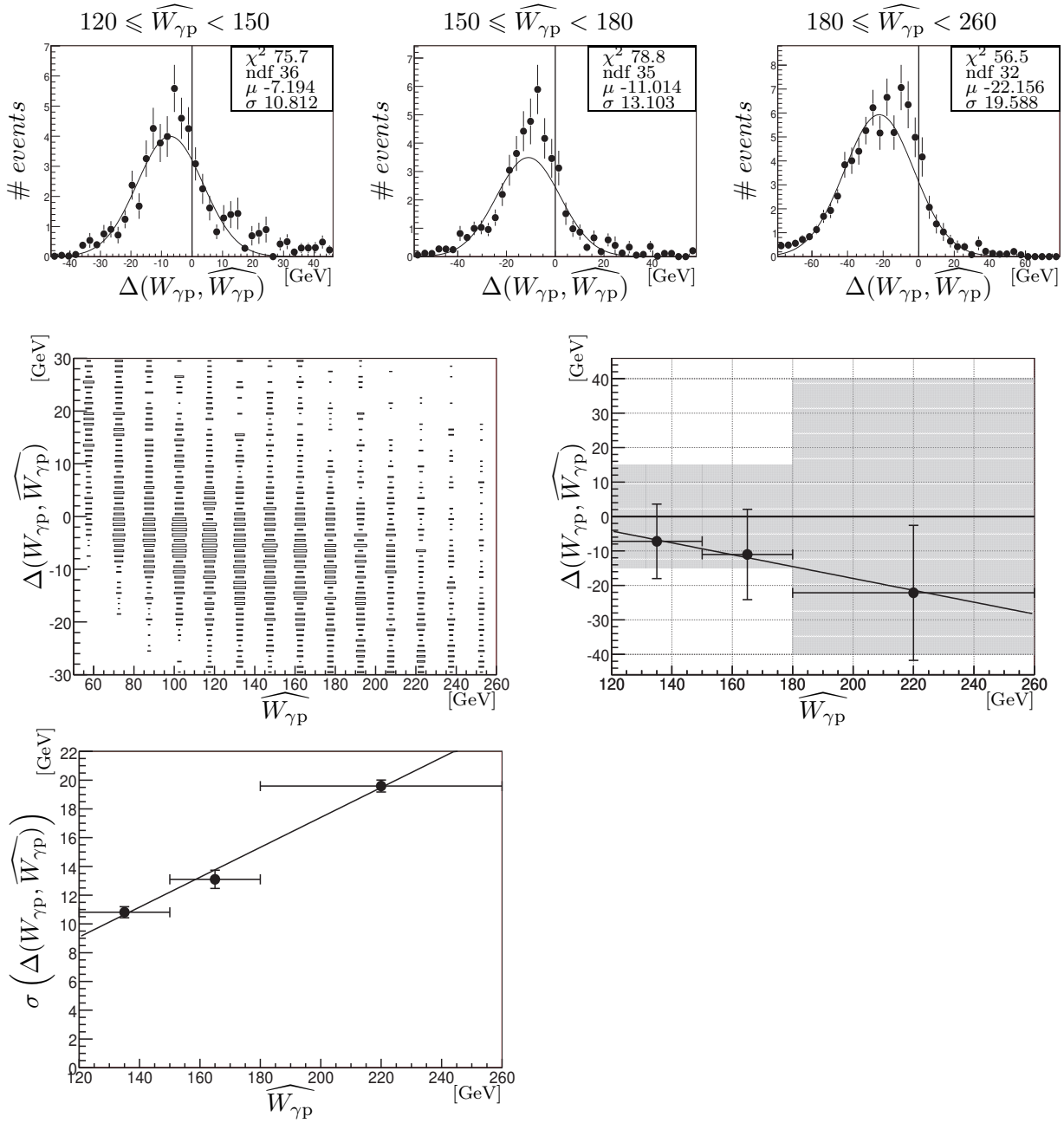

Figure 3.13: Resolution of $W_{\gamma p}$, $\Delta(W_{\gamma p}, \widehat{W_{\gamma p}})$, in the analysis bins for the **low** z selection. Means and standard deviations of the distributions on top are shown as a function of $\widehat{W_{\gamma p}}$ at the bottom. The shaded region shows the bin width.

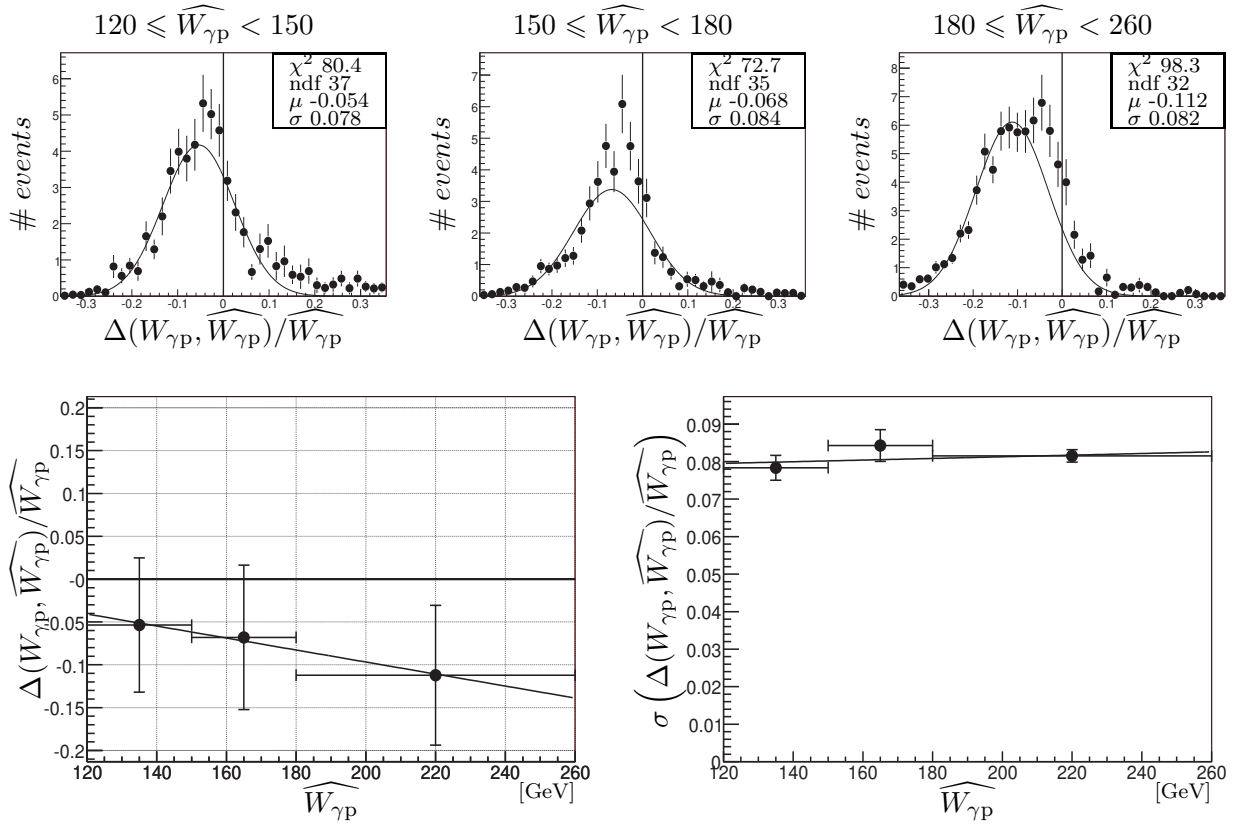

Figure 3.14: Relative resolution of $W_{\gamma p}$, $\Delta(W_{\gamma p}, \widehat{W_{\gamma p}})/\widehat{W_{\gamma p}}$, in the analysis bins for the **low** z selection. Means and standard deviations of the distributions on top are shown as a function of $\widehat{W_{\gamma p}}$ at the bottom. The shaded region shows the bin width.

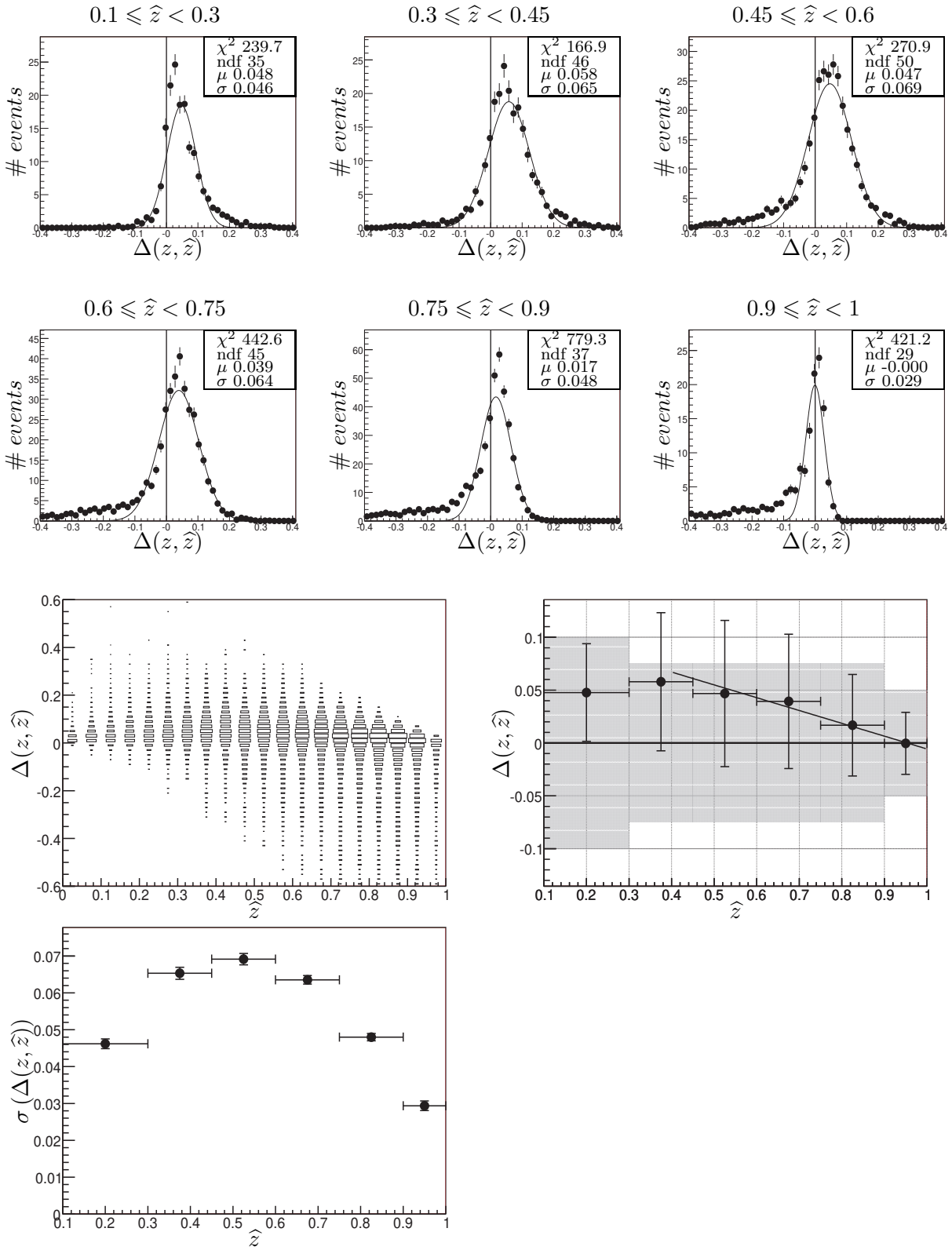

Figure 3.15: Resolution of z, $\Delta(z, \widehat{z})$, in the analysis bins for the **medium** z selection. Means and standard deviations of the distributions on top are shown as a function of $\widehat{z}$ at the bottom. The shaded region shows the bin width.

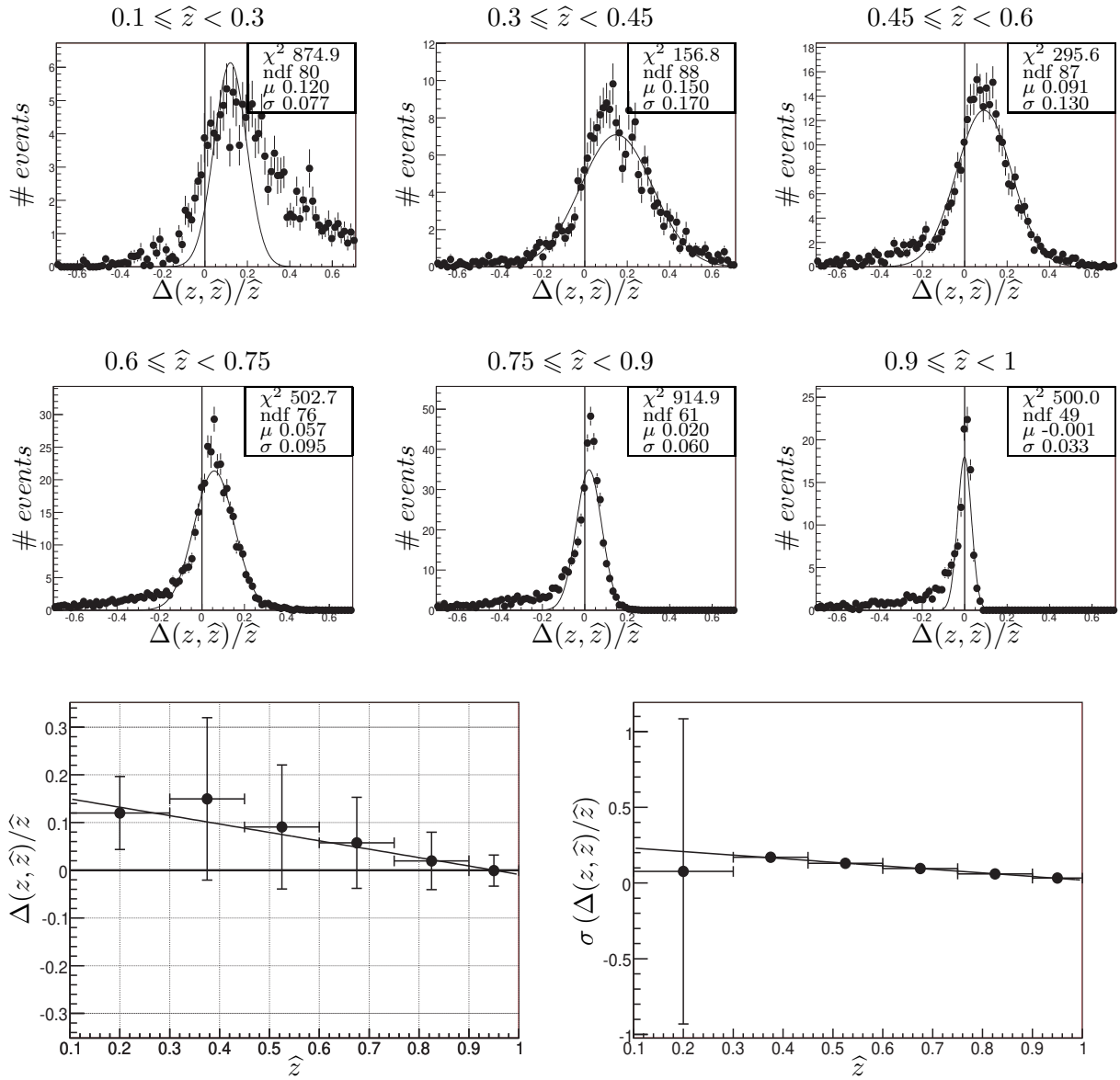

Figure 3.16: Relative resolution of z, $\Delta(z,\widehat{z})/\widehat{z}$, in the analysis bins for the **medium** z selection. Means and standard deviations of the distributions on top are shown as a function of $\widehat{z}$ at the bottom. The shaded region shows the bin width.

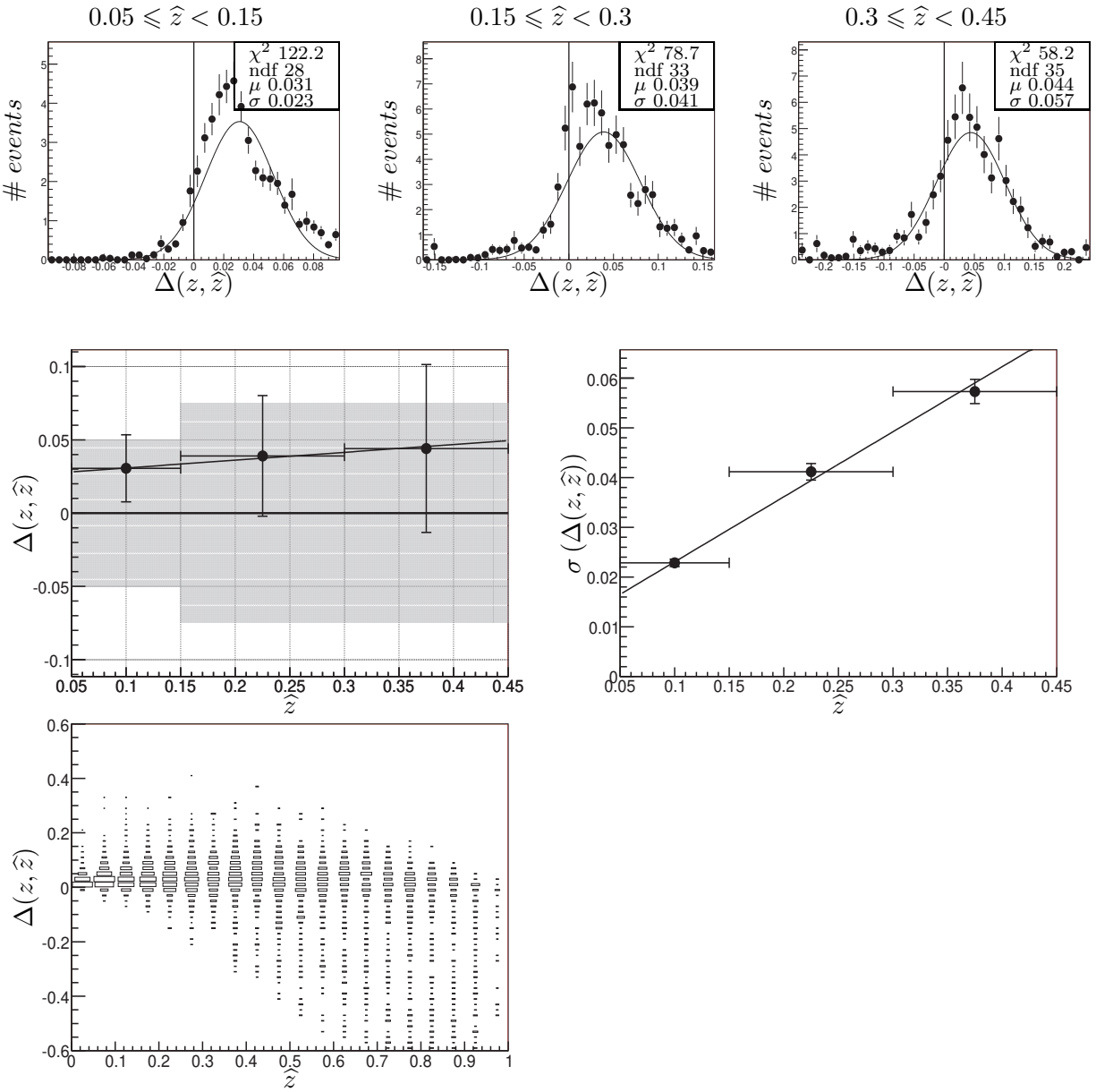

Figure 3.17: Resolution of z, $\Delta(z, \widehat{z})$, in the analysis bins for the **low** z selection. Means and standard deviations of the distributions on top are shown as a function of $\widehat{z}$ at the bottom. The shaded region shows the bin width.

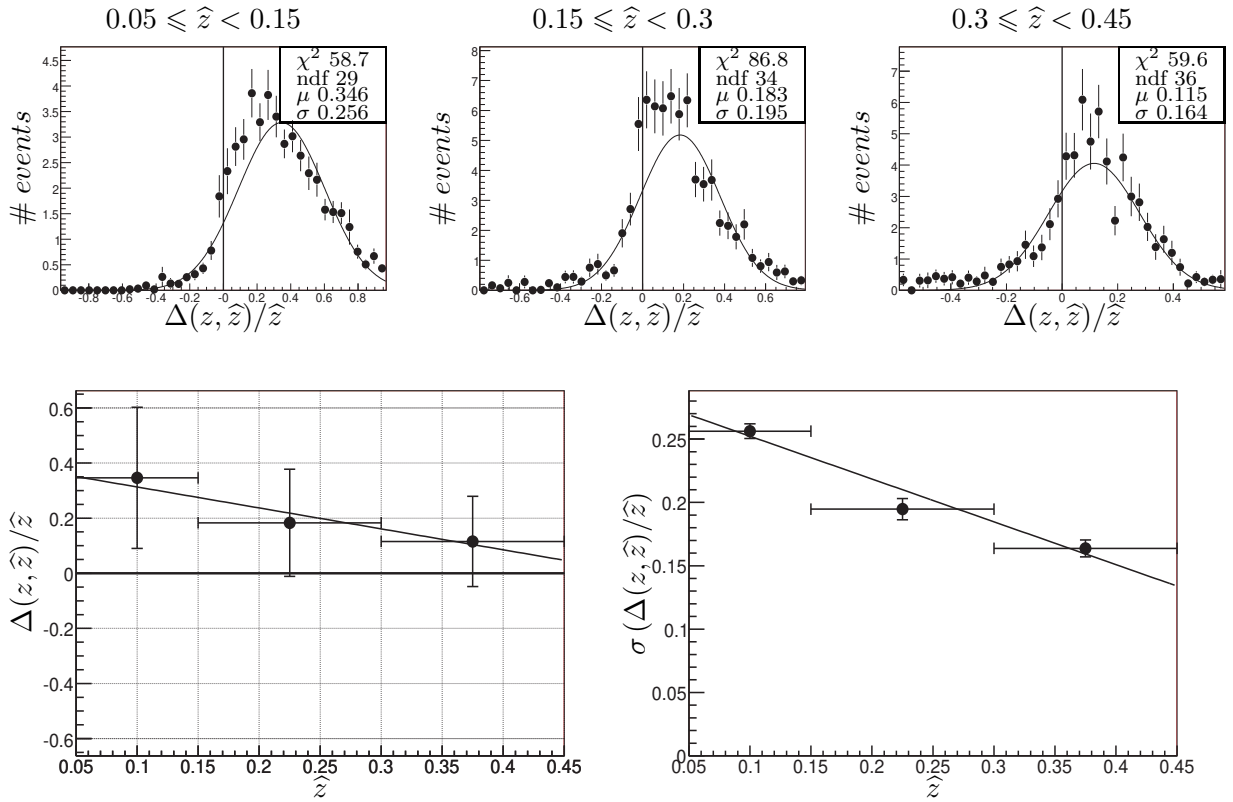

Figure 3.18: Relative resolution of z, $\Delta(z,\widehat{z})/\widehat{z}$, in the analysis bins for the **low** z selection. Means and standard deviations of the distributions on top are shown as a function of $\widehat{z}$ at the bottom. The shaded region shows the bin width.

3.3.4 Reconstruction of the Polarisation Variables $\cos\theta^\star$ and $\phi^\star$

The reconstruction of the polarisation variables $\cos\theta^\star$ and $\phi^\star$ is given for information in the following.

The polarisation variables $\cos\theta^\star$ and $\phi^\star$ are reconstructed using the equations given in the section 1.4.2. In order to compute the boost into the photon-proton centre-of-mass frame, the virtual photon four-vector has to be reconstructed, in photoproduction we have $q = \left(E_\gamma, -E_\gamma \overrightarrow{z}\right)$. The energy of the virtual photon can be derived from the equations (3.1):

$$2E_\gamma = \sum (E - Pz)_i \tag{3.6}$$

Figure 3.19 (3.23) shows the resolution of $\cos\theta^\star$ for the elasticity range $0.3 \leqslant z < 0.6$ ($0.6 \leqslant z < 0.9$), as well as the means and the standard deviation in bins of $\cos\theta^\star$. The relative resolution is shown in figure 3.20 (3.24). Figure 3.21 (3.25) shows the resolution of $\phi^\star$ for the elasticity range $0.3 \leqslant z < 0.6$ ($0.6 \leqslant z < 0.9$). The relative resolution is shown in figure 3.22 (3.26). All the events are reconstructed in the same bins, since the Gaussians are well centred around zero, and the width of the binning is much larger than the standard deviation.

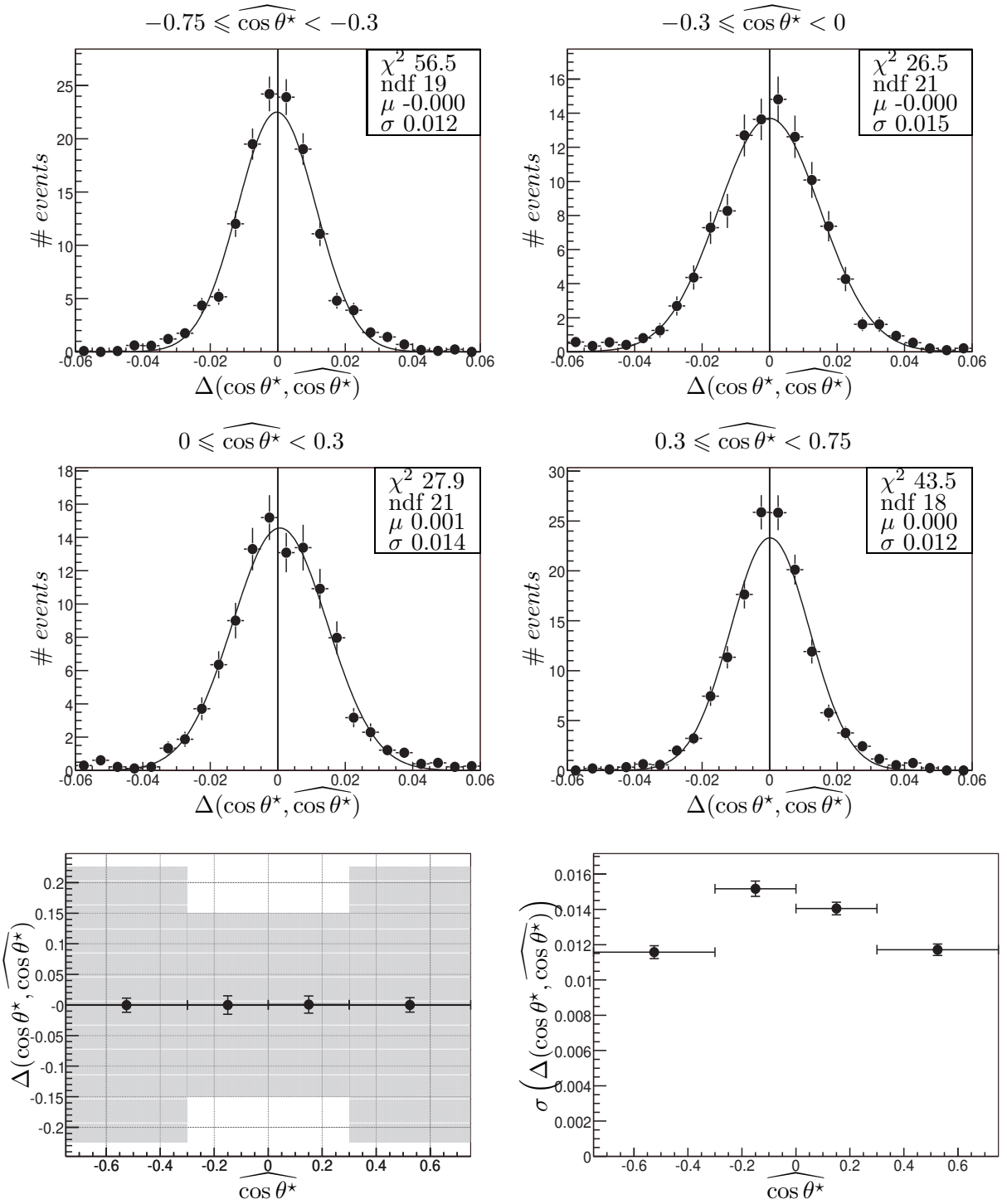

Figure 3.19: Resolution of $\cos\theta^\star$, $\Delta(\cos\theta^\star, \widehat{\cos\theta^\star})$, in the four analysis bins for the elasticity range $0.3 \leqslant z < 0.6$. Means and standard deviations of the distributions on top are shown as a function of $\widehat{\cos\theta^\star}$ at the bottom. The shaded region shows the bin width.

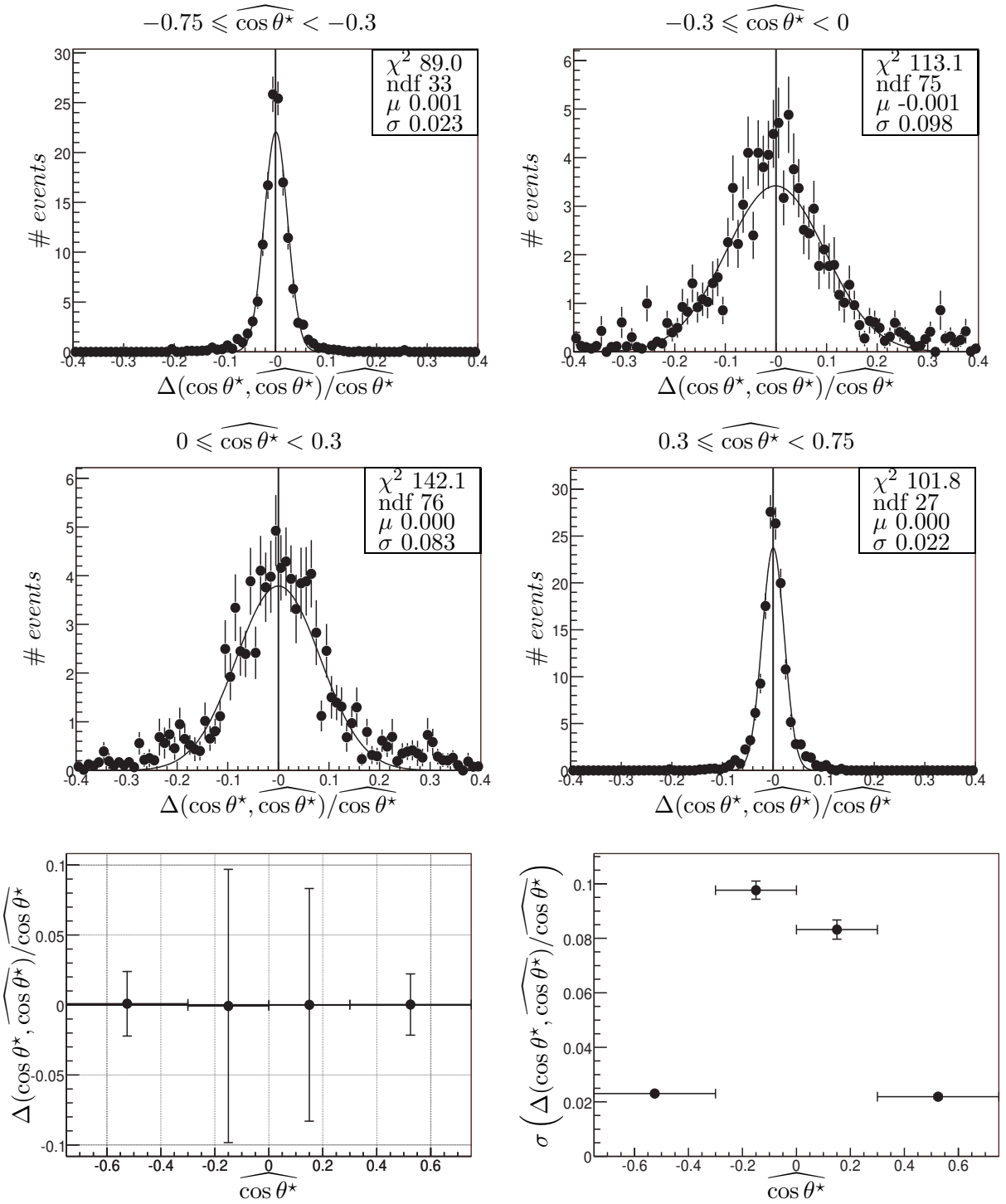

Figure 3.20: Relative resolution of $\cos\theta^\star$, $\Delta(\cos\theta^\star, \widehat{\cos\theta^\star})/\widehat{\cos\theta^\star}$, in the four analysis bins for the elasticity range $0.3 \leqslant z < 0.6$. Means and standard deviations of the distributions on top are shown as a function of $\widehat{\cos\theta^\star}$ at the bottom. The shaded region shows the bin width.

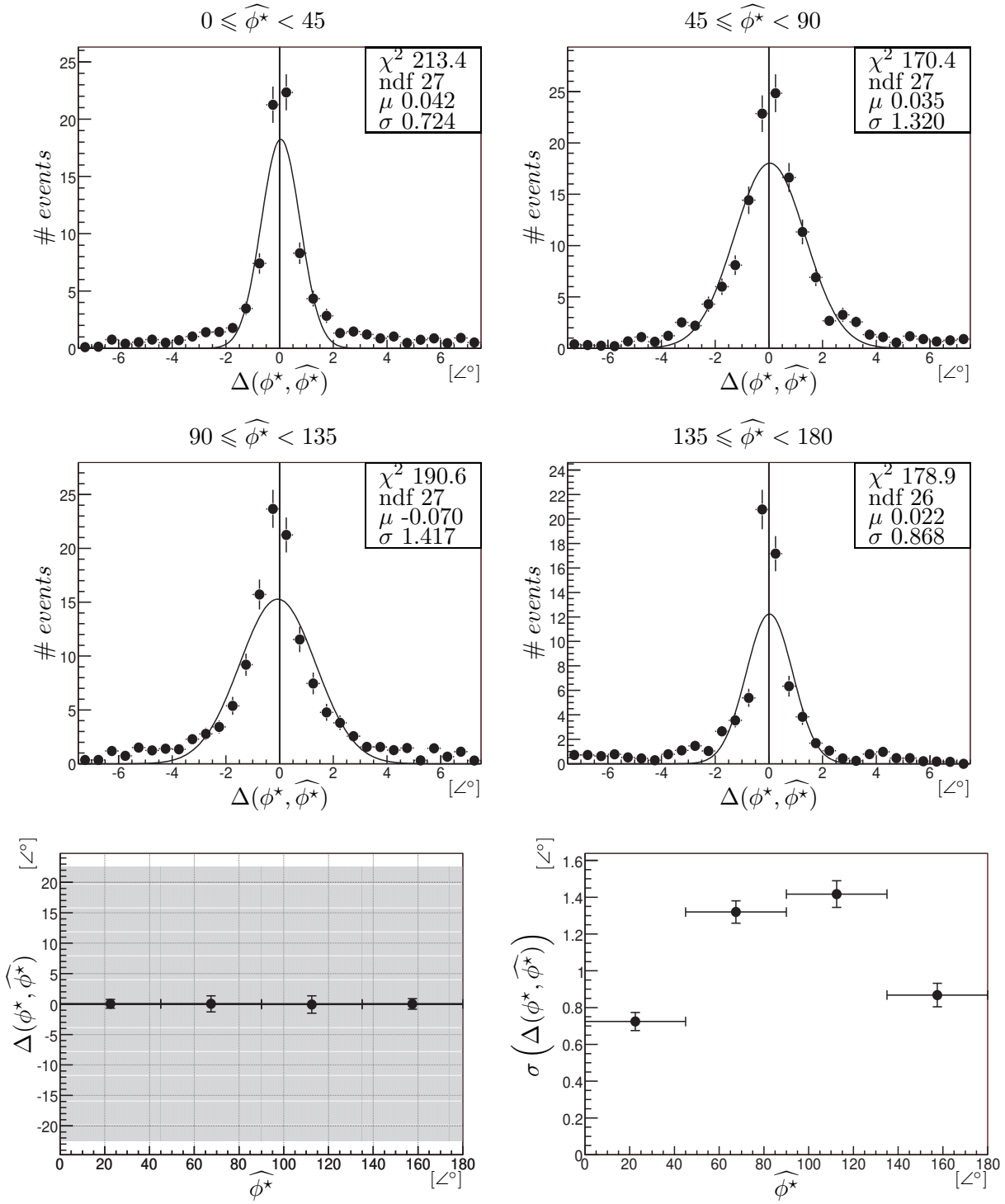

Figure 3.21: Resolution of $\phi^\star$, $\Delta(\phi^\star, \widehat{\phi^\star})$, in the analysis bins for the elasticity range $0.3 \leqslant z < 0.6$. Means and standard deviations of the distributions on top are shown as a function of $\widehat{\phi^\star}$ at the bottom. The shaded region shows the bin width.

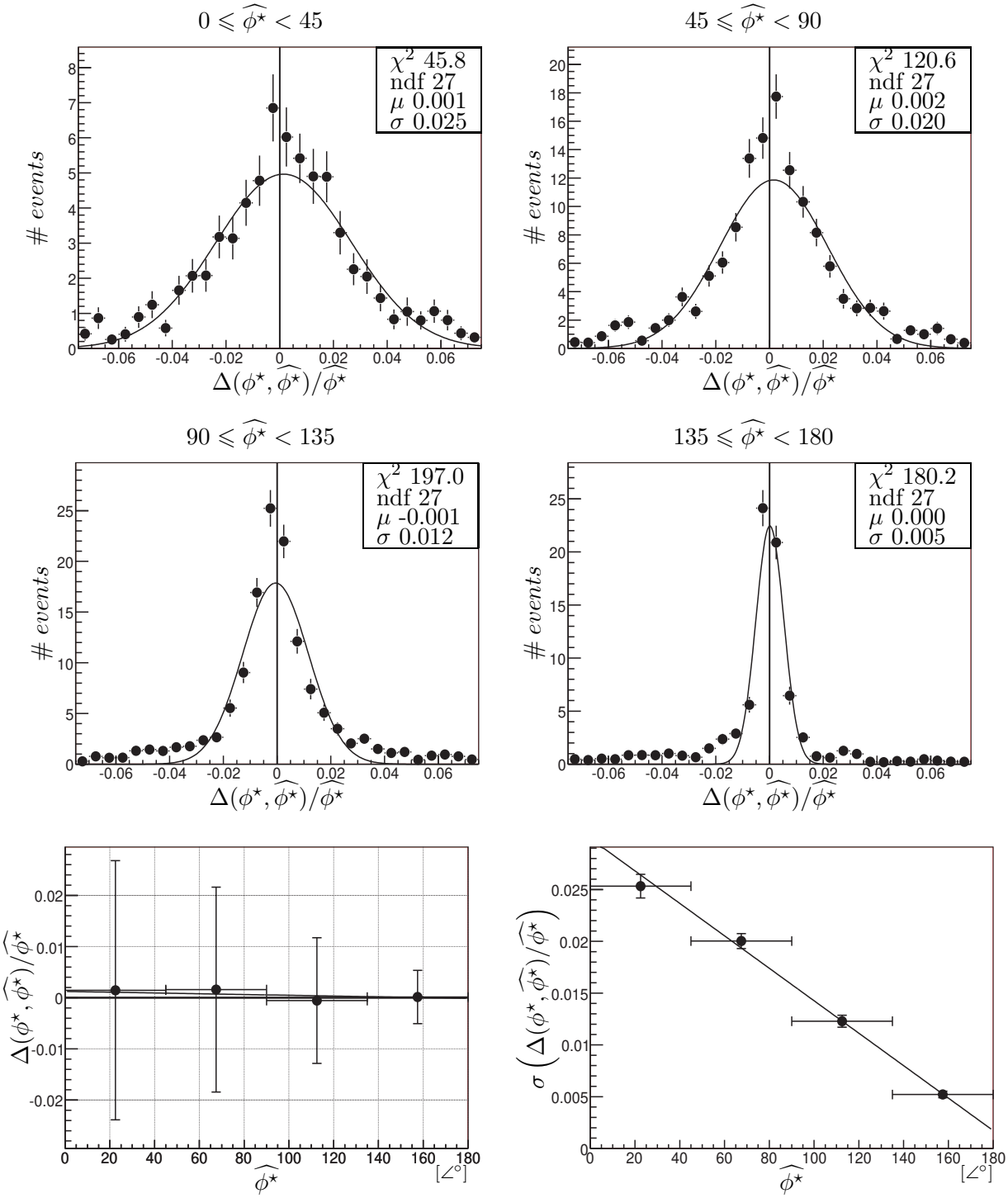

Figure 3.22: Relative resolution of $\phi^\star$, $\Delta(\phi^\star, \widehat{\phi^\star})/\widehat{\phi^\star}$, in the analysis bins for the elasticity range $0.3 \leqslant z < 0.6$. Means and standard deviations of the distributions on top are shown as a function of $\widehat{\phi^\star}$ at the bottom. The shaded region shows the bin width.

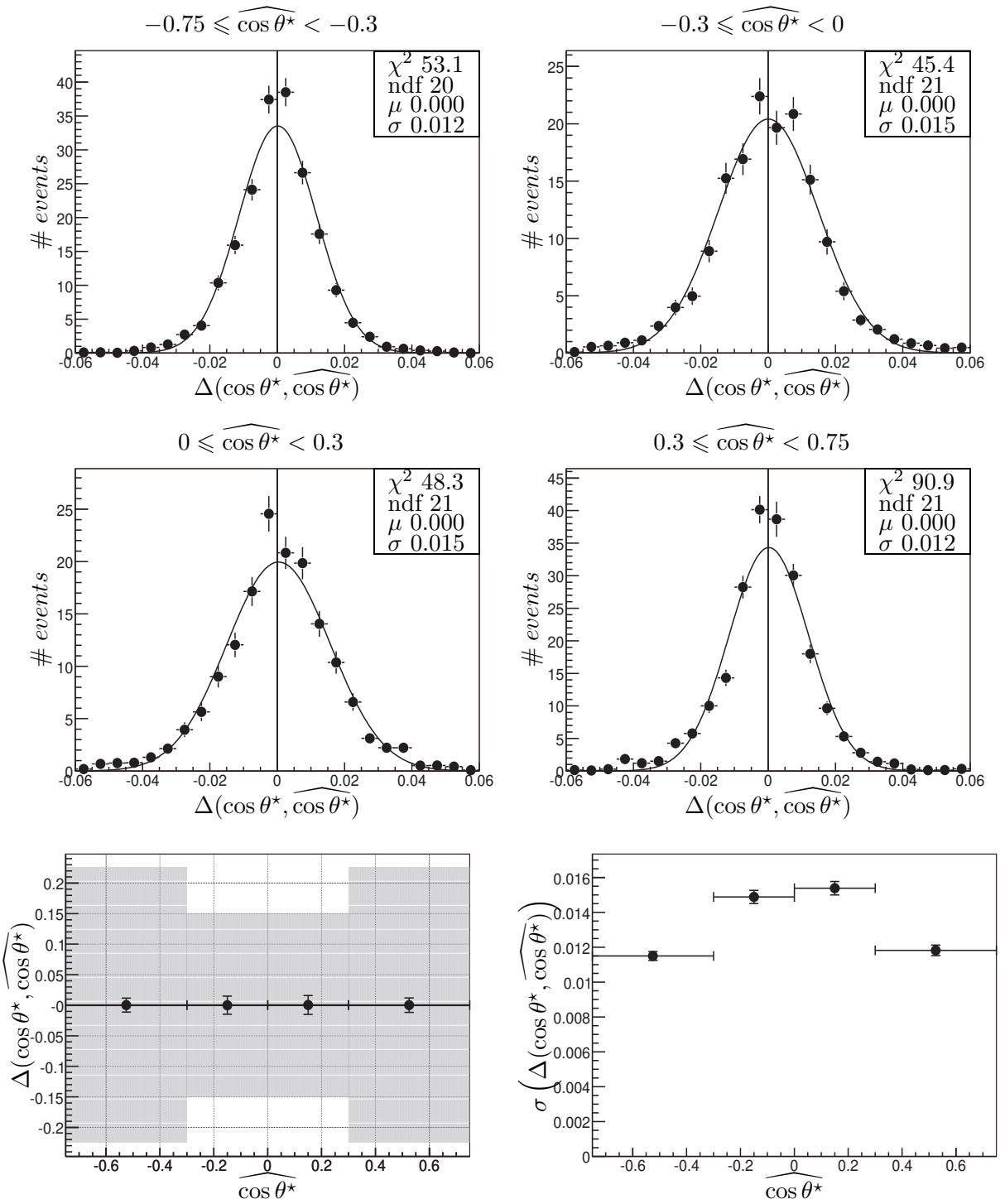

Figure 3.23: Resolution of $\cos\theta^\star$, $\Delta(\cos\theta^\star, \widehat{\cos\theta^\star})$, in the four analysis bins for the elasticity range $0.6 \leqslant z < 0.9$. Means and standard deviations of the distributions on top are shown as a function of $\widehat{\cos\theta^\star}$ at the bottom. The shaded region shows the bin width.

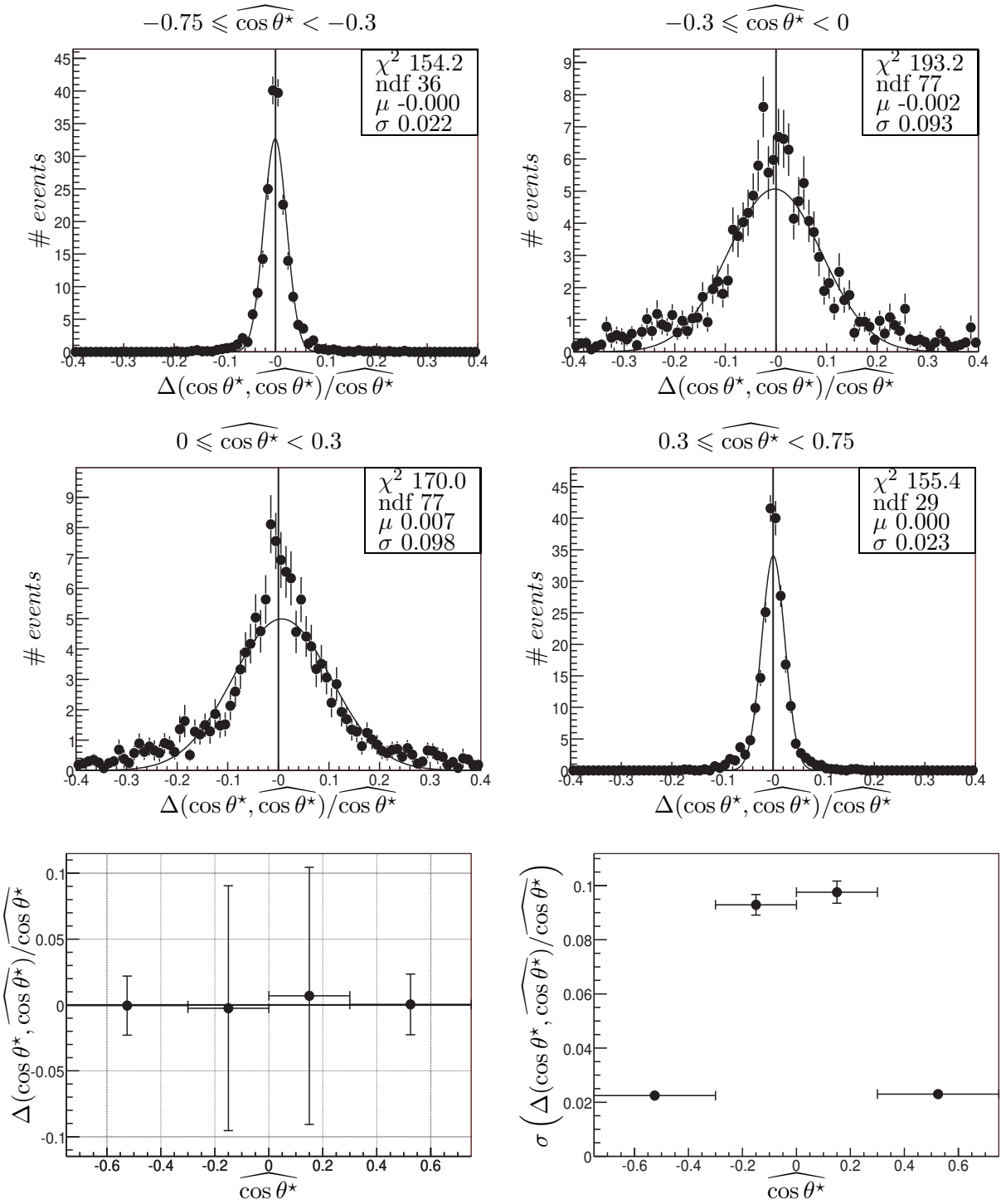

Figure 3.24: Relative resolution of $\cos\theta^\star$, $\Delta(\cos\theta^\star, \widehat{\cos\theta^\star})/\widehat{\cos\theta^\star}$, in the four analysis bins for the elasticity range $0.6 \leqslant z < 0.9$. Means and standard deviations of the distributions on top are shown as a function of $\widehat{\cos\theta^\star}$ at the bottom. The shaded region shows the bin width.

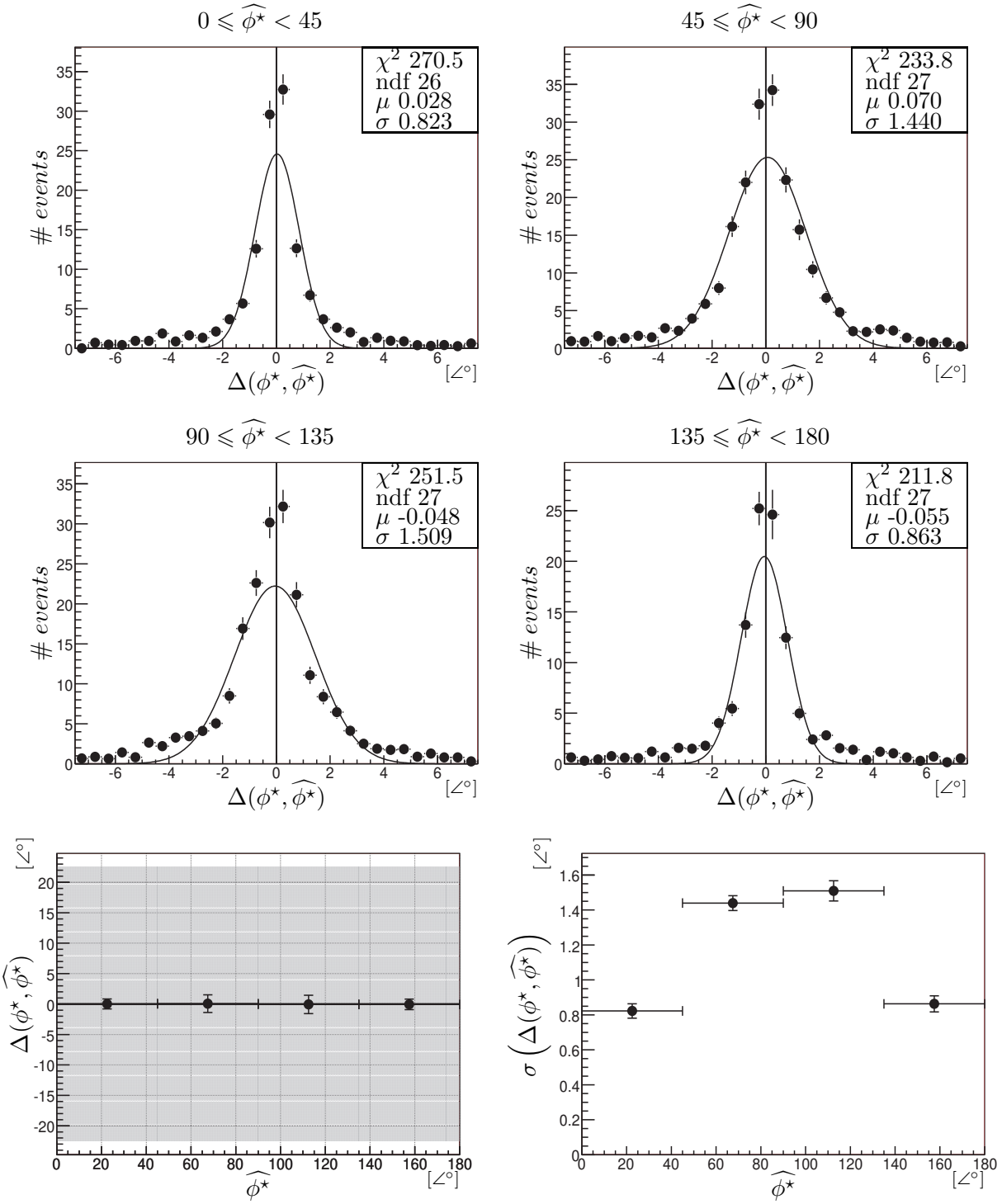

Figure 3.25: Resolution of $\phi^\star$, $\Delta(\phi^\star, \widehat{\phi^\star})$, in the analysis bins for the elasticity range $0.6 \leqslant z < 0.9$. Means and standard deviations of the distributions on top are shown as a function of $\widehat{\phi^\star}$ at the bottom. The shaded region shows the bin width.

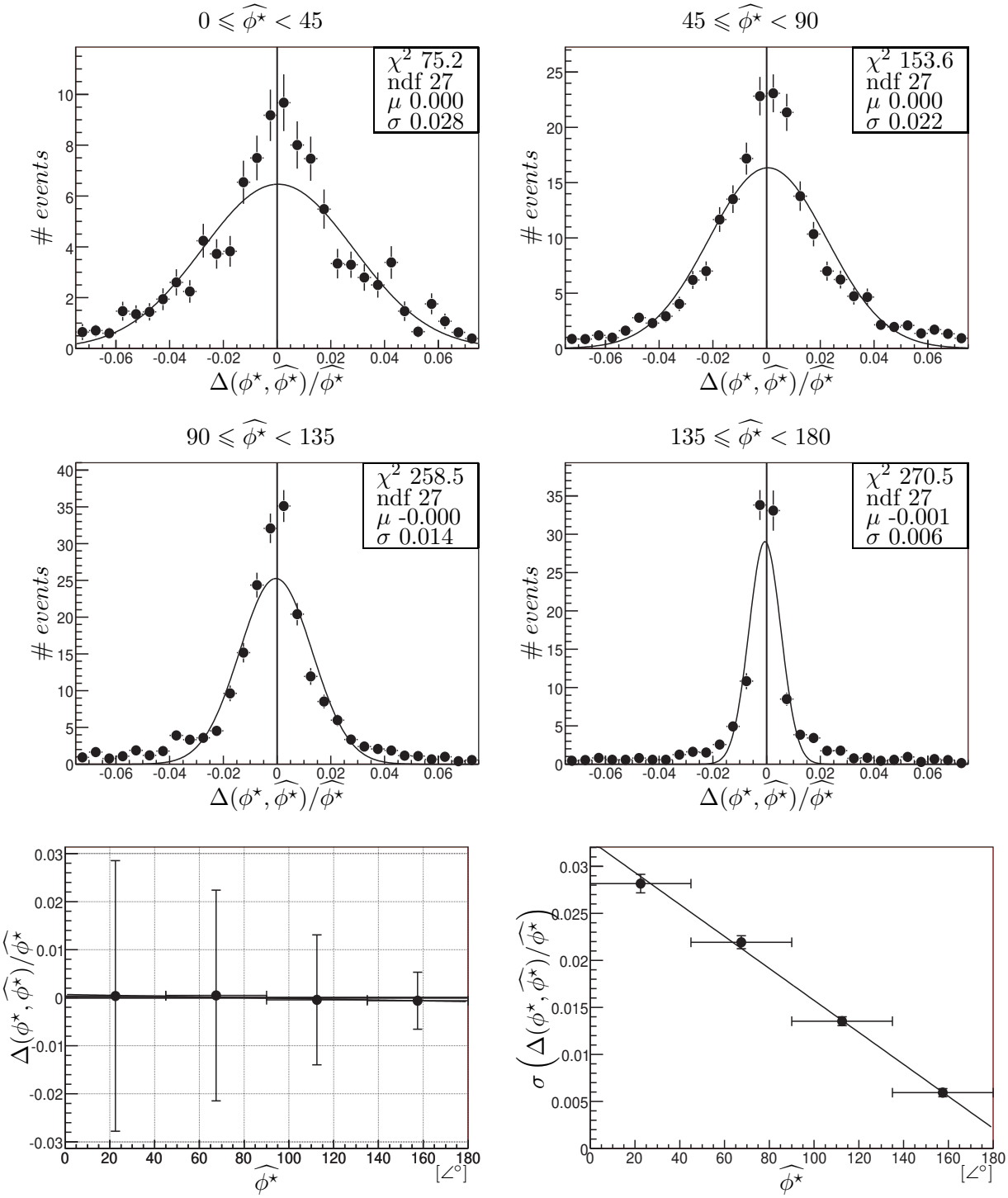

Figure 3.26: Relative resolution of $\phi^\star$, $\Delta(\phi^\star, \widehat{\phi^\star})/\widehat{\phi^\star}$, in the analysis bins for the elasticity range $0.6 \leqslant z < 0.9$. Means and standard deviations of the distributions on top are shown as a function of $\widehat{\phi^\star}$ at the bottom. The shaded region shows the bin width.

3.3.5 Purity and Stability

The error on the kinematic variables wrongly reconstructs events in a generated bin in the adjacent bins. This migration effect, with the statistic, limits the number of points of measure on the cross section. A too large number of bins will result in large bin-to-bin correlation.

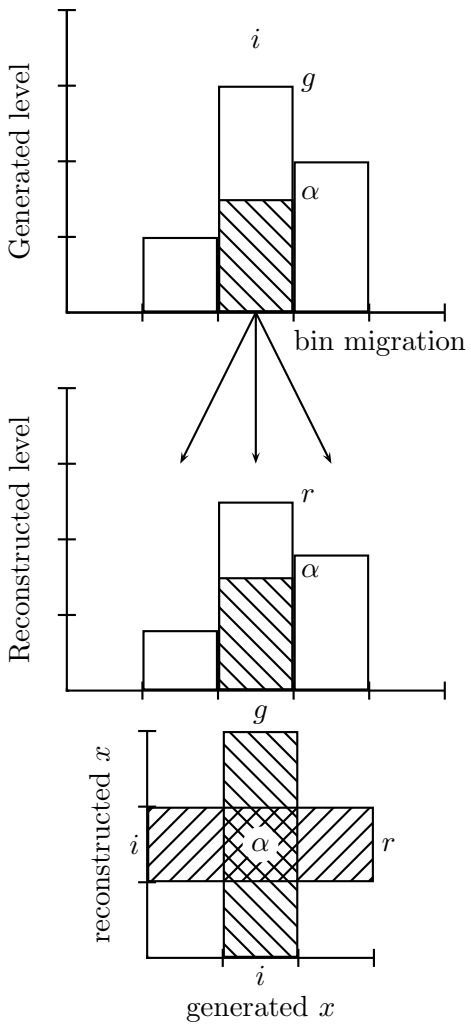

Figure 3.27: Bin migration

In order to quantify the effect of the migrations of bins, two indicators will be defined: the stability and the purity. For a bin, let g be the number of events generated, r the number of events reconstructed, and α the number of events generated and reconstructed in this bin (cf. figure 3.27). The stability and the purity are defined as follow:

$$\text{Purity} \mathrel{\widehat{=}} \frac{\alpha}{r} \tag{3.7}$$

$$\text{Stability} \mathrel{\widehat{=}} \frac{\alpha}{g} \tag{3.8}$$

The stability represents the proportion of the events that stay inside the generated bin, while the purity represents the proportion of the events in the reconstructed bin that were also generated in this bin.
The bins will are chosen in order to optimise the purity and the number of measured points. Larger bins will improve automatically the purity.

Figure 3.28 shows the purity and the stability for $P^2_{t,\psi}$, $W_{\gamma\mathrm{p}}$ and z for the medium z selection. These estimators depend on the resolution of the reconstruction and especially of the bias on the reconstructed value. It is quite good for $P^2_{t,\psi}$ but worse for $W_{\gamma\mathrm{p}}$ and z. All the bins have a purity and a stability higher than 50 %, which means than at least half of the events are correctly reconstructed in the bins, and thus validate the binning for this analysis.

The purity and the stability for the low z selection is shown in figure 3.29. Only the two first bins of $W_{\gamma\mathrm{p}}$ have a purity of 40 %, else the purity and the stability is higher than 50 % as for the medium z selection.

Figure 3.30 (3.31) shows the purity and the stability for $\cos\theta^\star$ and $\phi^\star$ for the elasticity range $0.3 \leqslant z < 0.6$ ($0.6 \leqslant z < 0.9$). Since the binning for the polarisation observables is much larger than the reconstruction accuracy, the purity and the stability reach at least 90 %.

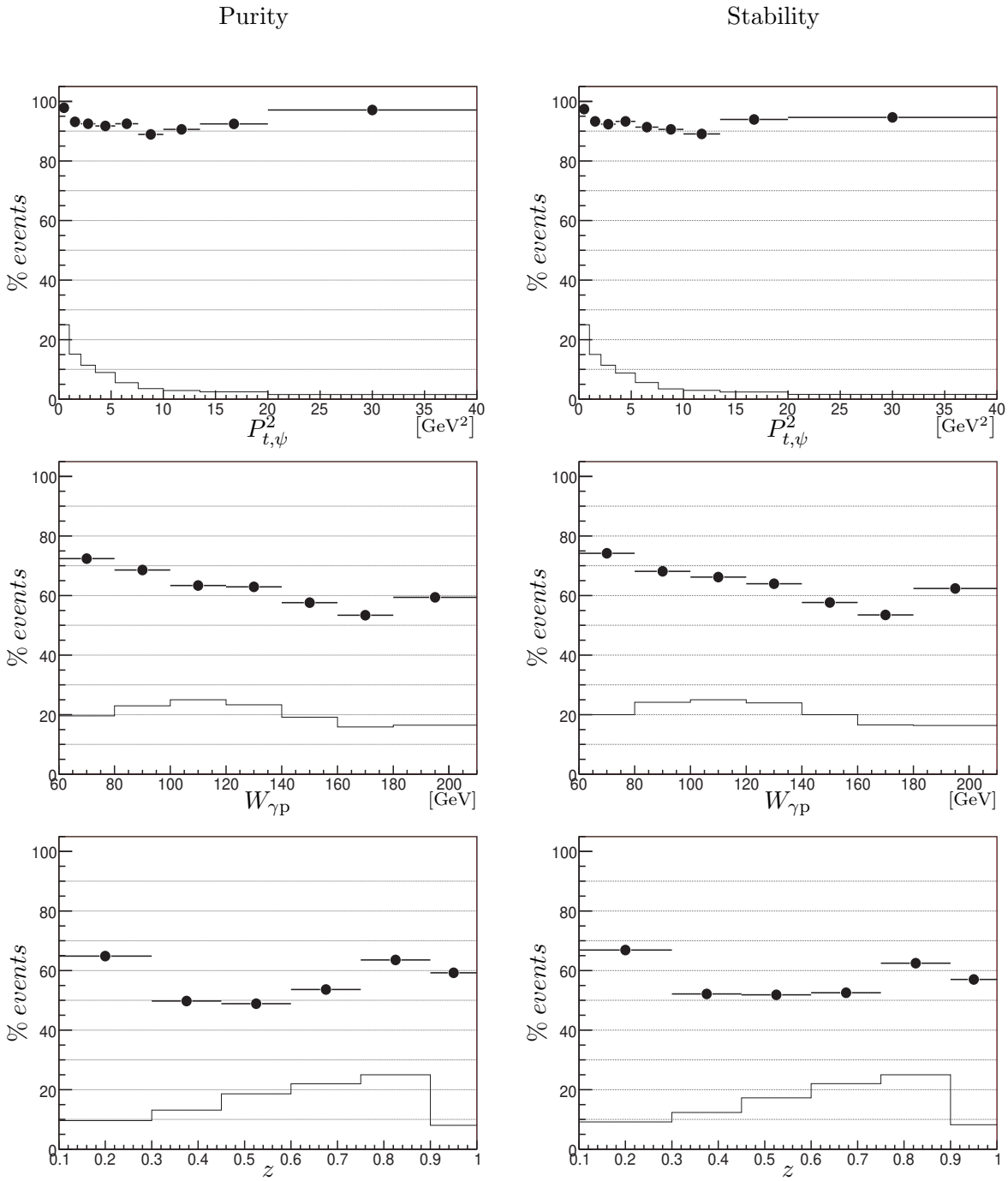

Figure 3.28: Purity and stability for $P^2_{t,\psi}$, $W_{\gamma p}$ and z for the **medium** z selection. The lower histograms shows the statistics.

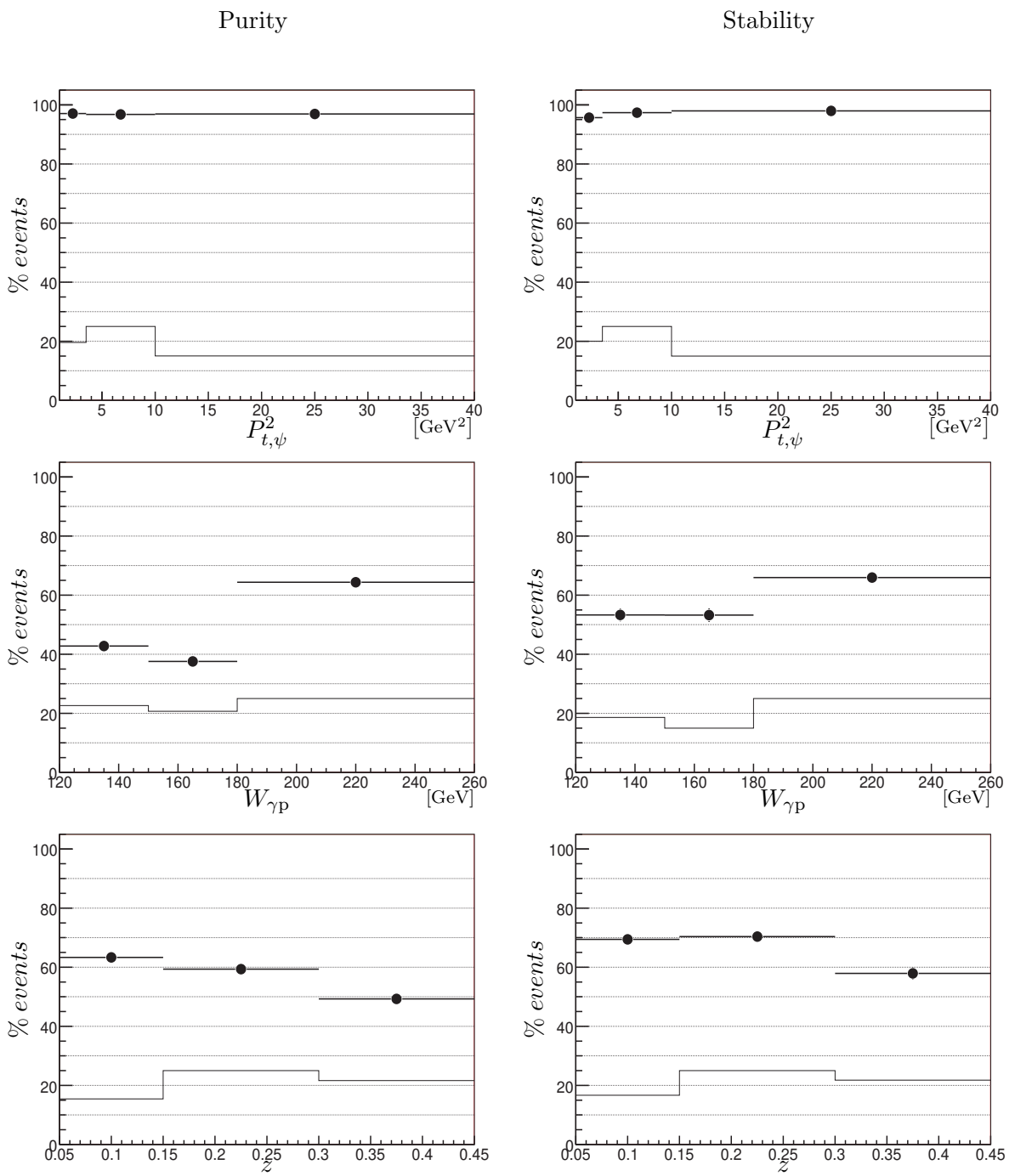

Figure 3.29: Purity and stability for $P^2_{t,\psi}$, $W_{\gamma p}$ and z for the **low** z selection. The lower histograms shows the statistics.

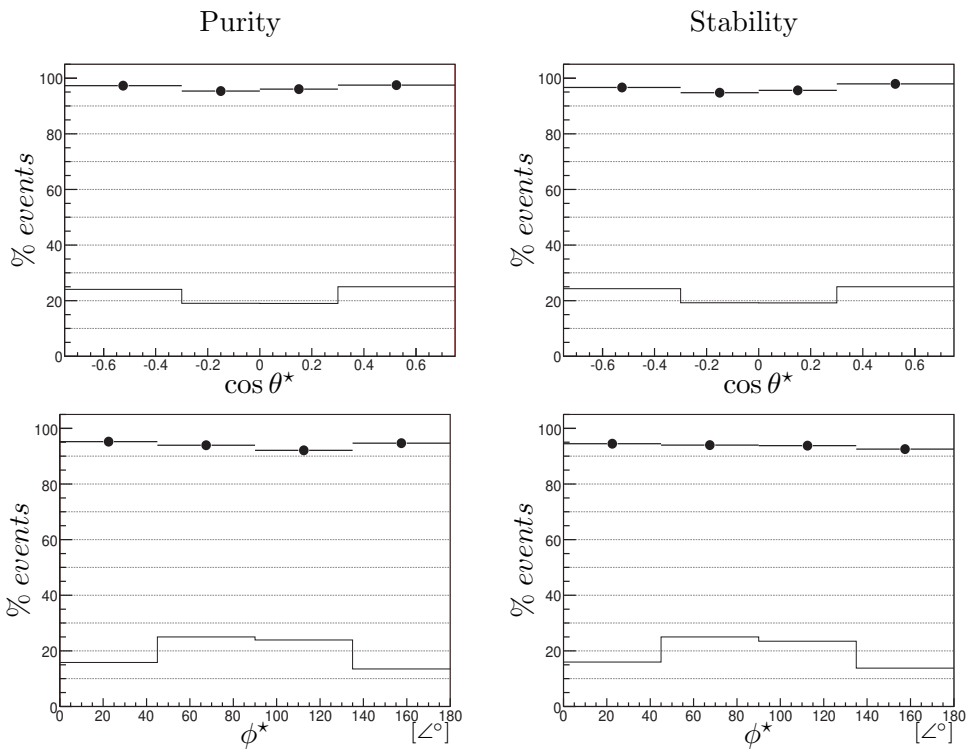

Figure 3.30: Purity and stability for $\cos\theta^\star$ and $\phi^\star$ for the elasticity range $0.3 \leqslant z < 0.6$. The lower histograms shows the statistics.

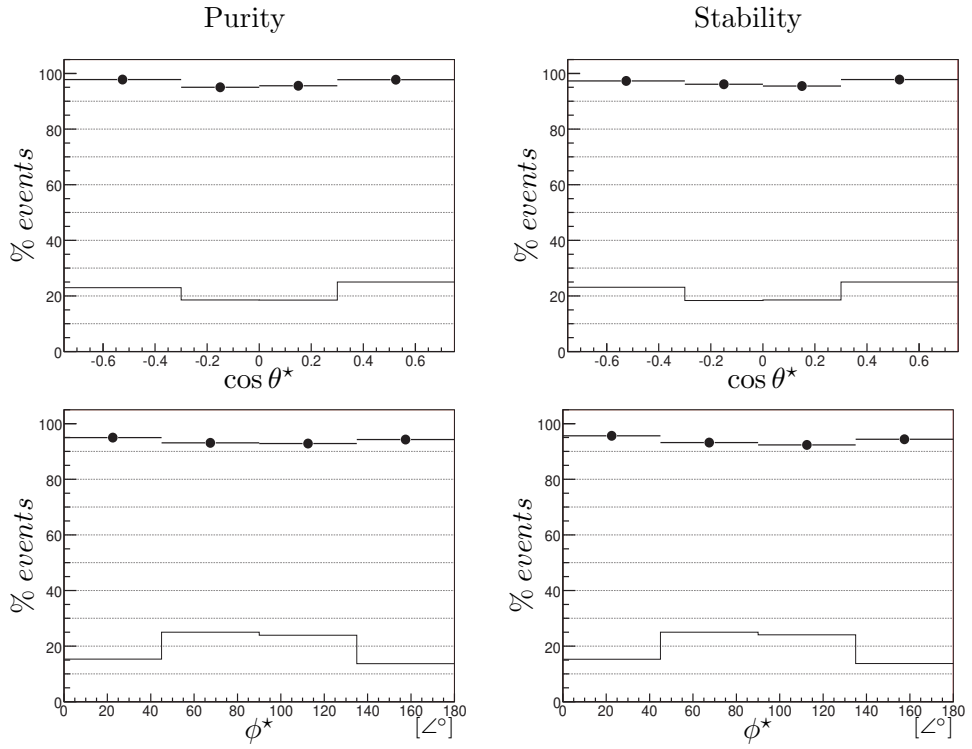

Figure 3.31: Purity and stability for $\cos\theta^\star$ and $\phi^\star$ for the elasticity range $0.6 \leqslant z < 0.9$. The lower histograms shows the statistics.

Chapter 4

Selection of J/ψ Mesons in Photoproduction

This chapter will describe the selection of J/ψ mesons in photoproduction for the two analysis regions, medium and low z. The first section will introduce how the J/ψ mesons are selected and presents the preselection which is common to both analyses. The second will give the selections and their efficiencies for each analysis region.

4.1 Preselection

Figure 4.1 shows the data flow in the H1 experiment. Data are selected at two levels, online and then offline. An online selection is done by the trigger in order to log only the most interesting data for analysis. The purpose of the trigger was explained in chapter 2, while subtrigger combinations used for this analysis will be explained in chapter 5.

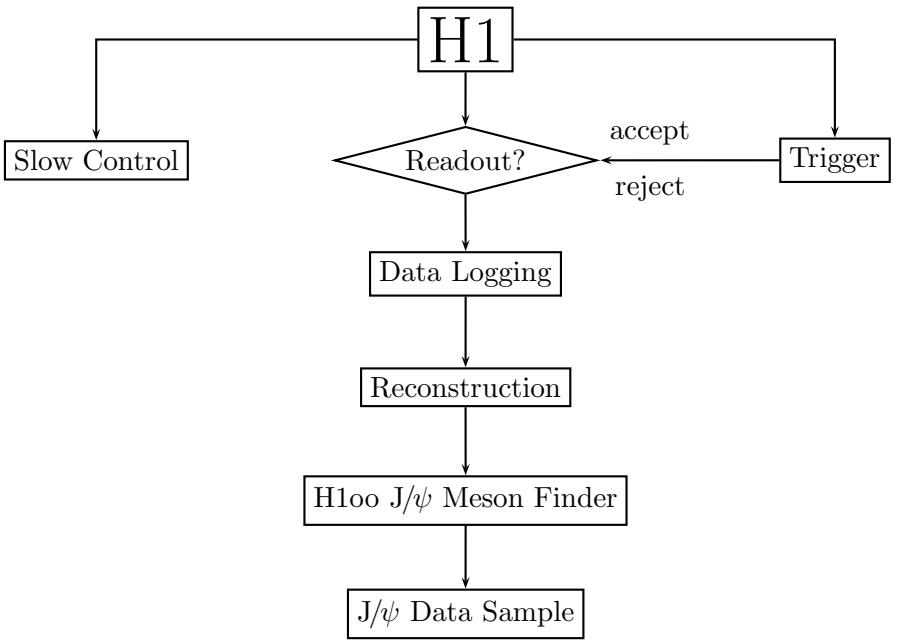

Figure 4.1: Data flow in the H1 experience

Next an offline selection is done by software in several steps. Firstly a subset of the data is made with the help of the particle finder classification. Only events containing particles involved in the analysis are kept, i.e. containing J/ψ mesons for this analysis. Then bad data taking periods are excluded of the data subset. Finally the analysis selection is applied to this subset. To be safe the online selection should be the least restrictive possible, since rejected events are lost. For this reason it is best to try to log the maximum of data and then select them offline.

4.1.1 Run Selection

In order to know the status of the detector for a particular event, its status is continuously logged in a data base by the "slow control" system [1]. All the detectors have in addition to readout electronics a slow control detector to check the temperature, voltage, or other sensors indicating a failure. Also computers are equipped with watch dogs in order to prove they are still running. The slow control is indispensable to know the validity of an event. For example, events when the tracking chambers are not completely on are not usable in most cases.

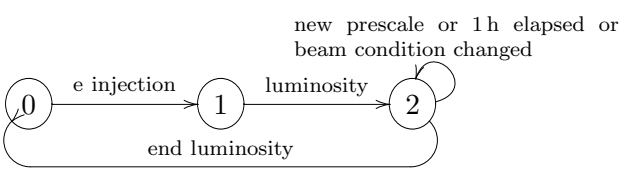

Figure 4.2: Trigger phases

In addition to the online control a higher level of slow control is needed, the run quality. Figure 4.2 shows the "trigger phase graph". The nodes represent the three trigger phases numbered from 0 to 2. The edges represent the transition to a new run and eventually a trigger phase transition. The condition of these transitions are labelled on the edges. Trigger phase 2 corresponds to the interesting period for physics. During this phase, a new run is started every hour to take into account new trigger prescales. This time corresponds to a significant rate reduction due to the reduction of the currents of the beams, which implies to recompute the prescales. However if the beam conditions become really bad, e.g. chambers trip continuously and must be switched off, the shift crews have to start a new run so as to isolate this bad period. Then if some machine tuning was successful and the condition becomes again quiet, a new run is started. Later and offline, a quality (poor, medium, and good) is attributed to each run by data quality experts. The beam condition is not the only reason to exclude runs, technical problems in the detector can also lead to bad runs. This analysis requires medium or good runs.

Since the H1 detector is a multi-purpose detector, each analysis requires only a subset of the detector. It is also a good reason to select data offline instead of freezing the data logging when the slow control reports faulty elements in the detectors. This analysis requires the sub-detectors listed below to be on for each event:

- Central Jet Chambers 1 and 2
- Central Outer Z chambers
- Central Inner Proportional chambers
- Central Outer Proportional chambers

[1] Slow control means the control is not done at the rate of the HERA clock, but approximately every 10 s

- Liquid Argon calorimeter
- SpaCal
- Central Muon Detector
- Time Of Flight
- Veto wall
- Luminosity system

All these sub-detectors are relevant for this analysis in order to measure and to trigger the events. Also the subtriggers used are required to be enabled. The run ranges and subtrigger combinations used for this analysis will be discussed later in chapter 5.

4.1.2 Integrated Luminosity

The previous requirements permit to compute the integrated luminosity corresponding to the data set. The run selection and the luminosity calculation is shortly described in the note [67].

Table 4.1 shows the HERA II operation periods from 2003 until 2005. The storage ring started with positrons at the end of 2003 then switched to electrons at the end of 2004 and finally came back to positrons until the scheduled end of HERA II in July 2007. Table 4.2 shows the corresponding integrated luminosities for theses periods. The luminosity is given at different levels. The last lines of this table gives the corresponding integrated luminosity for the run selection and the slow control requirements given in the precedent section. The large difference between the integrated luminosity delivered to H1 and the integrated luminosity resulting from the slow control requirements is due to bad background conditions, which caused frequent trips in the chambers.

date		run number		beams
12/10/2003	02/01/2004	356 093	367 231	e^+ p
02/01/2004	12/08/2004	367 253	392 213	e^+ p
05/12/2004	22/12/2004	396 667	398 818	e^- p
03/01/2005	11/11/2005	399 098	436 893	e^- p

Table 4.1: Running periods of HERA II

		2003-2004 e^+	2004-2005 e^-	sum
produced by HERA		101 383.96	220 019.65	321 403.61
delivered to H1	"luminosity declared"	95 745.72	209 196.41	304 942.13
H1 runs	DAQ efficiency	91 829.83	201 341.55	293 171.38
H1 on tape	deadtime	84 591.47	183 322.76	267 914.23
H1 physics	"typical" HV	64 479.97	168 197.98	232 677.95
this analysis		43 017.71	93 753.73	133 075.17

Table 4.2: Integrated luminosities [nb^{-1}] for the running periods given in table 4.1.

4.1.3 J/ψ Meson Finder

When the H1oo framework builds the μ-ODS and the HAT data analysis levels, it runs physics algorithms, so-called "particle finders", in order to find particles involved in the events. Particle finders are available for several particles like electrons, muons etc. The J/ψ meson finder is the one responsible to reconstruct J/ψ mesons.

Firstly the topology of the J/ψ mesons at H1 will be described, and then the selection by the J/ψ meson finder will be provided.

4.1.3.1 J/ψ Meson Topology

The J/ψ meson has two leptonic decay modes, to electrons and to muons (cf. section 1.3). As electrons produce tracks in the chambers and clusters in the SpaCal and LAr calorimeters, the kinematics can be reconstruct with the momentum measurement of the chambers and the energy measurement from the calorimeters. The acceptance of the central chambers is approximately $20^\circ \leqslant \theta \leqslant 160^\circ$. For backward particles the tracks in the chambers are too short to measure properly the momentum. In this case for electrons, the kinematics is extracted from the SpaCal calorimeter, and hits in the BST and BDC can help to determine the direction of the electron. However muons are at the minimum of ionisation. So they produce only few cells in the SpaCal and LAr calorimeters, and the energy deposit is independent of energy. For central muons, the momentum is obtained from the central chambers. But for backward muons it is not possible, since backward muons are out of the acceptance of the tracking system. Consequently there are three possibilities for the topology of J/ψ mesons decayed to electron: track-track, track-cluster and cluster-cluster. But for the muonic decay mode, only track-track is possible.

4.1.3.2 J/ψ Meson Selection

In order to find J/ψ meson candidates the J/ψ meson finder algorithm performs a combinatorial analysis with the calorimeter clusters and the track candidates. Since this analysis concerns only the muonic decay and the track-track topology, only this case will be described.

The J/ψ meson finder requires two tracks of opposite charge and an invariant mass that covers the mass range from J/ψ up to Υ mesons:

$$2 < M_{\mu\mu} < 15\,\mathrm{GeV} \ \wedge \ \widehat{\mathbf{C}}\mu_1 = -\widehat{\mathbf{C}}\mu_2.$$

The tracks are preselected with the so-called Lee West selection described in the note [65]. The selection criterion for tracks are:

kinematic range	acceptance cuts
elastic	$20^\circ \leqslant \theta \leqslant 160^\circ \quad P_t > 0.8\,\mathrm{GeV}$
inelastic	$4^\circ \leqslant \theta \leqslant 165^\circ \quad P > 0.8\,\mathrm{GeV}$

For both tracks a clear separation from the scattered electron is required with the cuts

$$\left|\theta - \theta_\mathrm{e}\right| \geqslant 5^\circ \ \wedge \ \left|\phi - \phi_\mathrm{e}\right| \geqslant 10^\circ,$$

where θ_e and ϕ_e are the polar and azimuthal angle of the scattered electron.

In addition to the *topology* tag, the J/ψ meson finder classifies the events as *elastic*, *cosmic*, and *inelastic*. If a candidate matches the *elastic* selection criteria then it is tagged as *elastic*. These classes are defined as follows:

class	possible cosmic tag value	# tracks required
elastic	true/false	exactly two tracks [2]
inelastic	false	at least two identified muons

The inelastic selection of the J/ψ meson finder is based on events with two identified muons. Since low elasticities are correlated with a high number of tracks, the combinatorial background for only one identified muon would be too high. The number of tracks required for inelastic J/ψ mesons by the J/ψ meson finder is less than the minimum of three tracks required later. This analysis does not use explicitly the inelastic tag, but requires events with at least one J/ψ meson found by the finder.

The elastic J/ψ meson topology is very similar to cosmic muons when the transverse momentum is low, two back-to-back iron muons in azimuthal angle ϕ. But there is a low probability that cosmic tracks fit the primary vertex and the beam-beam time window. Consequently a Cosmic tag is defined like this:

$$\begin{aligned} \text{Cosmic} \;=\; & \quad \chi^2 < 10 \\ & \vee \quad (|dca_1| > 0.1\,\text{cm} \;\wedge\; |dca_2| > 0.1\,\text{cm}) \\ & \vee \quad |t_{0_1} - t_{0_2}| > 12\,\text{T}_{\text{HERA}} \end{aligned} \tag{4.1}$$

where *dca* means distance of closest approach to the primary vertex, t_0 means the time reference of the track, and the χ^2 corresponds to the fit of the two tracks to one single track. There is no cosmic classification for inelastic J/ψ mesons, the cosmic tag is always set to false.

4.1.4 Common Selection of the Inelastic J/ψ Mesons

Figure 4.4 shows the selection procedure applied to the data. The elastic branch will be explained later, here the emphasis is on the inelastic J/ψ meson selection. A subset of the data is made of the events containing at least one J/ψ meson found by the J/ψ meson finder. Thus the selection described in section 4.1.3.2, which includes already acceptance cuts, is applied to the data. For this subset events outside the interaction window are rejected by a z vertex cut. Then events that do not fulfil the run selection and the high voltage requirements are rejected. A track-track topology with at least one identified muon is required in order to select the J/$\psi \longrightarrow \mu^-\mu^+$ process. A second identified muon is required later by the muon quality selection. For the inelastic branch at least three Lee West tracks are required to select only inelastic J/ψ mesons and to reject elastic events. Events passing this preselection are selected for the analysis. Table 4.3 gives the number of events for each step and the percentage of remaining events. Sometimes events contain more than one J/ψ meson candidate. These additional J/ψ meson candidates will be suppressed later at the end of the full selection. The production of two J/ψ mesons is theoretically possible, but the cross section is expected to be much more lower, and thus probably not accessible at HERA. Pions misidentified as muons can explain these events.

Figure 4.3 shows the invariant mass distribution for this preselection. Since the selection of the J/ψ meson finder is relatively open, subtriggers are required in order to suppress background. For the 2003-2004 e^+ data taking period subtrigger s15 or s18 are required and for the 2004-2005 e^- data taking period s19, s23 or s18. This choice will be motivated in chapter 5. The J/ψ meson peak is clearly visible in 2003-2004 e^+, but the signal over background ratio is worse in 2004-2005 e^-. The reason will be explained in section 5.4.2.

[2] For the elastic tag the scattered electron is not counted.

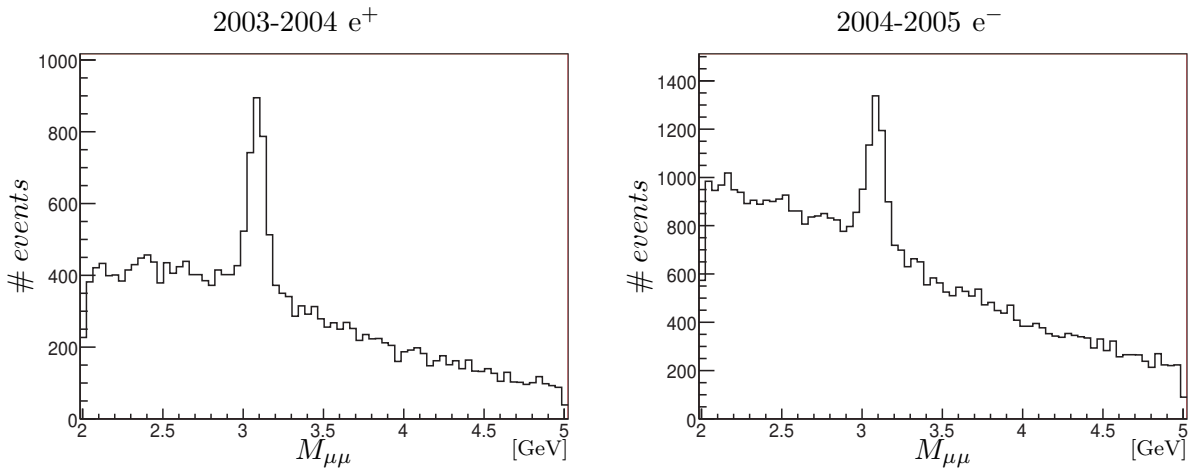

Figure 4.3: Invariant mass distribution for the inelastic J/ψ mesons for the 2003-2004 e^+ and 2004-2005 e^- data taking periods after the preselection. For the 2003-2004 e^+ data taking period subtrigger s15 or s18 are required and for the 2004-2005 e^- data taking period s19, s23 or s18.

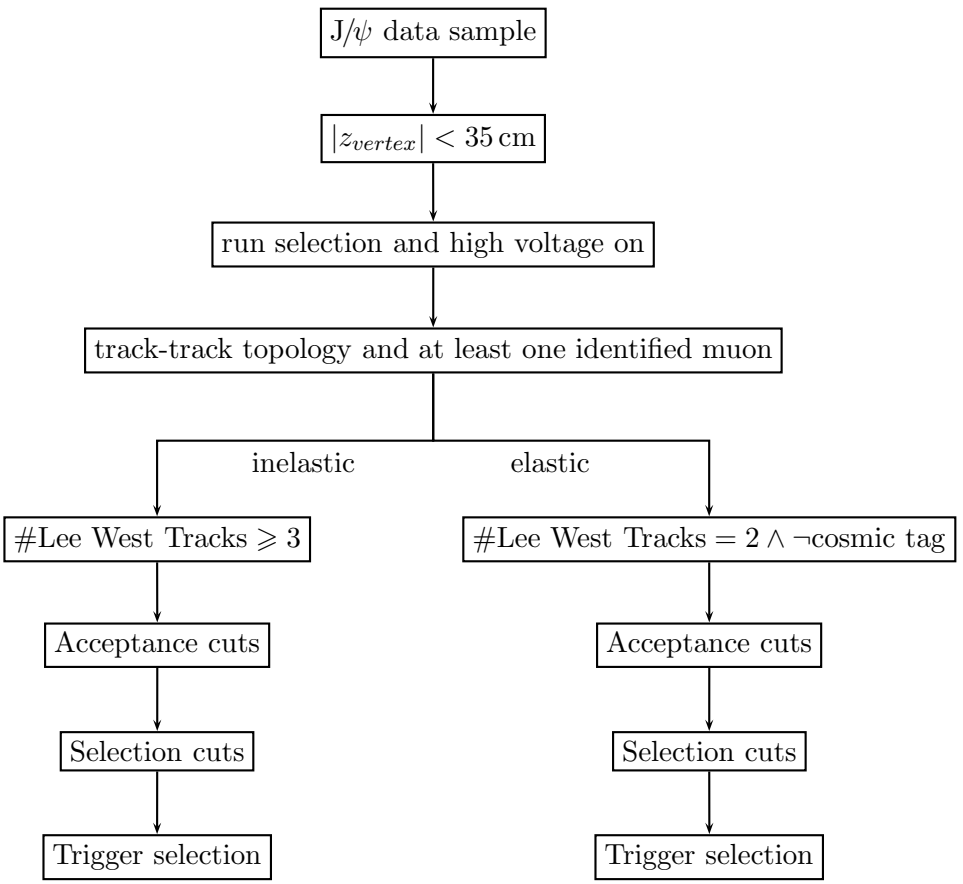

Figure 4.4: Common selection of the J/ψ mesons. The J/ψ meson data sample corresponds to a subset of the data, where at least one J/ψ meson was found by the J/ψ meson finder. Inelastic and elastic branches are shown. The elastic branch is used in this thesis for the muon identification efficiency determination.

selection	2003-2004 e^+		2004-2005 e^-	
# events containing at least one J/ψ meson	1 910 092		3 774 276	
# events after the z_{vertex} cut	1 758 824	92.1 %	3 550 966	94.1 %
# events inside the run range	835 857	47.5 %	2 383 825	67.1 %
# events with run selected and high voltage on	672 086	80.4 %	1 789 285	75.1 %
# selected events for the analysis	110 508	16.4 %	286 097	16.0 %
# J/ψ candidates	114 913	104.0 %	298 224	104.2 %

Table 4.3: Number of events for each step of the preselection for the analysed runs of the **2003-2004** e^+ and **2004-2005** e^- data taking periods.

The next section will discuss for the low and medium z selections the acceptances of the H1 detector and the selections used to extract the J/ψ meson signal. The separation of the elasticity in a low and medium z selection permits to study separately the photon-gluon and gluon-gluon processes. The EPJPSI Monte Carlo program will be used for the simulation in order to compute the efficiencies of the acceptance and the selection cuts.

The cross section is only measured for a particular phase space, the kinematic region for the medium and low z selection is defined in table 4.4.

low z	medium z
generator level: $Q^2 < 2.5\,\mathrm{GeV}^2$ reconstructed level: no scattered electron in the main detector	
$0.05 \leqslant z \leqslant 0.45$	$0.3 \leqslant z \leqslant 0.9$
$P^2_{t,\psi} > 1\,\mathrm{GeV}^2$	
$120 \leqslant W_{\gamma\mathrm{p}} \leqslant 260\,\mathrm{GeV}$	$60 \leqslant W_{\gamma\mathrm{p}} \leqslant 240\,\mathrm{GeV}$

Table 4.4: Kinematic region for the **medium** and **low** z selection

The cut on the four-momentum squared of the exchanged photon Q^2 restricts the kinematics to the photoproduction domain. In order to make room for the new optics of HERA II, the SpaCal calorimeter acceptance was reduced. In comparison to HERA I, the threshold of detection of the scattered electron as a function of Q^2 is thus higher. Within the H1OO framework the electron reconstructed in the main detector having the highest transverse momentum and an energy above 8 GeV is considered as the scattered electron. Figure 4.5 shows the percentage of events without "detected" scattered electron in the main detector as a function of the generated Q^2. While for HERA I a percentage of 40 % corresponded to a Q^2 of approximately $1\,\mathrm{GeV}^2$ [68], it is shifted to approximately $2.5\,\mathrm{GeV}^2$ for HERA II. Consequently the definition of the photoproduction domain has to be updated for this analysis. On the generator level the photoproduction selection consists to applied the cut $Q^2 < 2.5\,\mathrm{GeV}^2$, and on the reconstructed level only events, where the scattered electron is not detected in the main detector, are accepted. Consequently the selected events for the analysis have a reconstructed Q^2 set to zero.

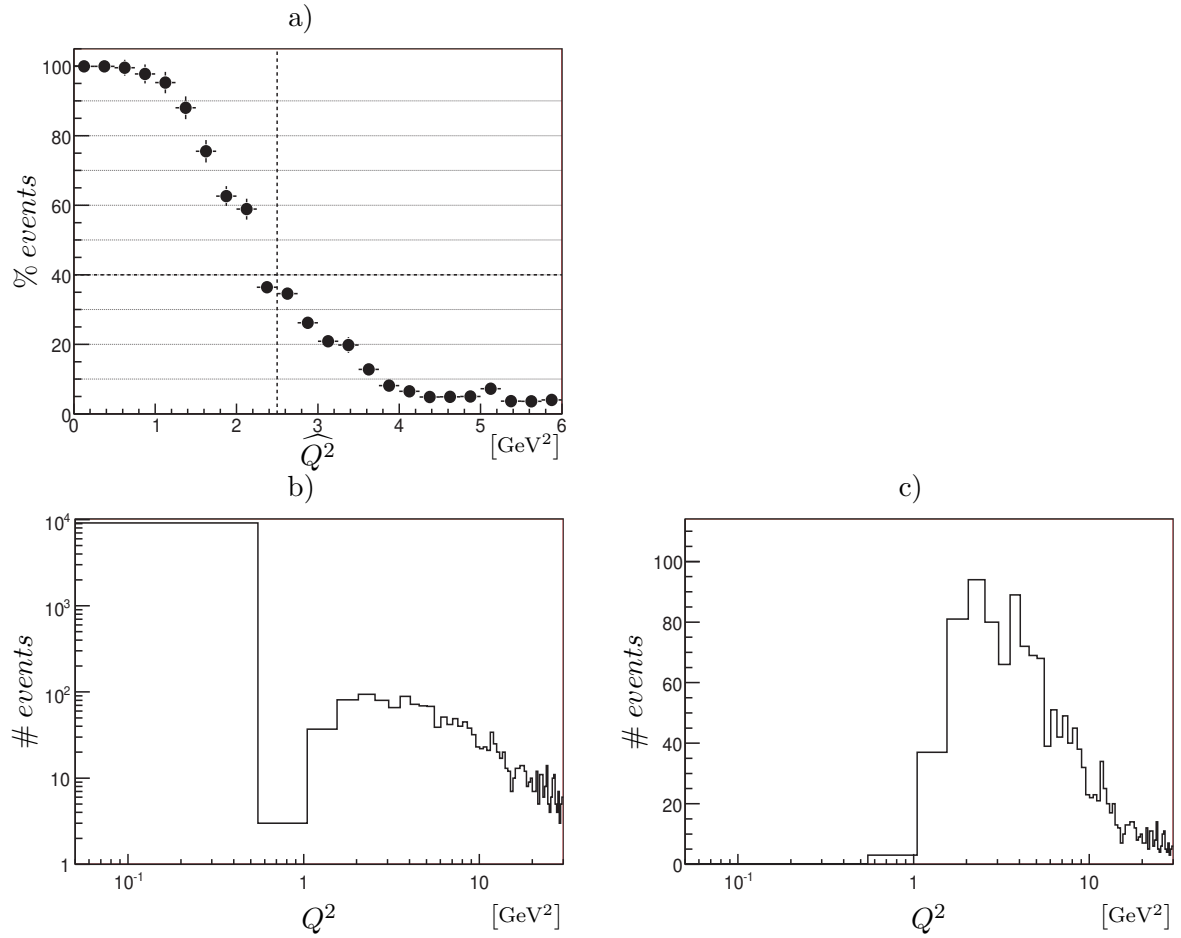

Figure 4.5: a) Percentage of events without "detected" scattered electron in the main detector as a function of the generated Q^2. Events are simulated with the EPJPSI Monte Carlo Program. See text for the definition of "detected scattered electron". b) Distribution of the Q^2 after the preselection, and in c) for only events with the scattered electron inside the main detector.

The cuts on the elasticity z separate the photon-gluon and gluon-gluon processes. The separation of these two processes corresponds to approximately $z \approx 0.45$ (cf. figure 3.2). The upper cut on the elasticity $z \leqslant 0.9$ suppresses the quasi-elastic J/ψ mesons, as well as the ψ(2S) mesons. The lower cut on $z \geqslant 0.05$ and the cut on the photon-proton centre-of-mass energy $W_{\gamma \mathrm{p}}$ is due to the acceptance and will be explained later. The cut on the transverse momentum squared of the J/ψ meson $P^2_{t,\psi}$ has several reasons. This cut is applied by theorists for the cross section computations. Moreover it reduces significantly the pollution from the J/ψ mesons originating from the decay of ψ(2S) mesons which are produced in elastic and proton dissociative processes. It affects the polar angle and momentum distributions of the decay muons and is therefore taken into account for the acceptance and efficiency calculation.

4.2 Acceptance and Selection of J/ψ Mesons at Medium z

4.2.1 Acceptance

Since the instrumentation of the H1 detector has energy thresholds and does not cover the full solid-angle, the acceptance cut will restrict the phase space of the analysis to what can be measured with the H1 detector. In particular the acceptance for the two decay muons from J/ψ mesons has to be defined. The acceptance of the proton remnant particles are taken into account by the reconstruction of the kinematic variables, which minimises the influence of the loss of the energy flow in the beam pipe.

The relevant instrumentation for muons was described in section 2.2. This analysis uses only the Central Muon Detector and not the Forward Muon Detector. For HERA I the forward tracking chambers were not very efficient, and thus the polar angle of the decayed muons was restricted to the acceptance of the central tracking chamber, which is $20° \leqslant \theta_\mu \leqslant 160°$. The same polar angle region is used for this analysis. However it would be interesting to extend for next analyses the Lee West track selection to the new forward tracking system, since it is relatively efficient. Indeed it will be shown in the next paragraphs the lower angular cut restricts the accessible $W_{\gamma \mathrm{p}}$ domain at low values.

The identification of muons in the LAr calorimeter is only possible for a momentum greater than 0.8 GeV. This cut is already applied by the J/ψ meson finder. However in the instrumented iron detector the threshold is higher, since muons have to cross more material before they reach the streamer tubes. Since the events of this analysis are triggered by subtriggers requiring iron trigger elements, the majority of the decay muons will be a pair of a calorimeter muon and an iron muon, and less frequently a pair of two iron muons. A more restrictive cut will improve the muon identification, but will also reduce the statistics. Consequently the cut on the momentum has to be chosen as an optimum. However it can be different for calorimeter and iron muons.

Figure 4.6 shows the polar angle, the momentum, and the transverse momentum of calorimeter and iron muons.

The polar angle distribution of the calorimeter muons drops at approximately 130 °, which corresponds to the acceptance of the CB1 wheel. Muons are not detected in the BBE wheel and in the SpaCal calorimeter, but are instead detected in the instrumented iron detector. The lack of material after the BBE wheel explains the rise in the polar angle distribution of the iron muons.

The distribution of the momentum of the muons peaks at around half the mass of the J/ψ mesons with a long tail towards higher values. In the J/ψ meson rest frame both muons have $P^\star_\mu \approx M_\psi/2$, which is smeared out by the boost to the laboratory frame. The distribution of the momentum of the calorimeter muons has it maximum at approximately 1 GeV, then decreases up to 3 GeV. On the other hand for iron muons the maximum is at approximately 2.5 GeV and then decreases up to 5 GeV. The two types of muons are relatively well separated in momentum. In figure 4.6 the percentage of remaining muons is also shown as function of the momentum cut for both calorimeter and iron muons. For calorimeter muons, the available statistics does not allow to require a higher momentum than the default one. However for the iron muon, it is possible to require a minimal momentum of 2 GeV. If an higher cut is applied for iron muons, the case where both decay muons have an iron quality has to be considered in addition to the case where one of the decay muons is a calorimeter muon. In order to have the largest statistics this analysis does not require an harder cut on the momentum than the J/ψ meson finder applies. It was verified results are closed with an additional cut requiring $P > 2$ GeV for the iron muons.

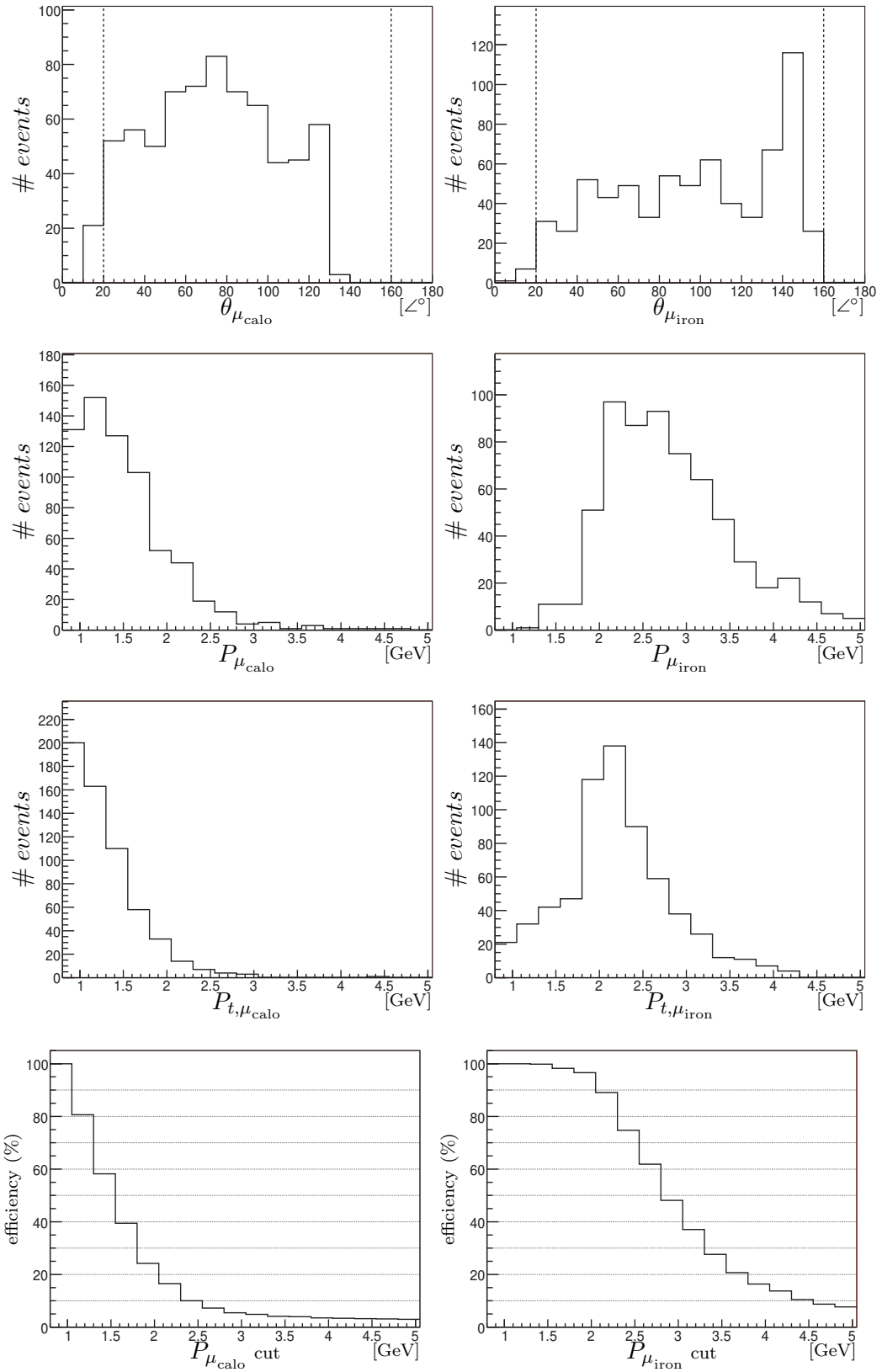

Figure 4.6: Distribution of the polar angle, the momentum, the transverse momentum of the calorimeter and the iron muons. The vertical lines show the angular cut defined in table 4.5. The percentage of remaining muons as function of the momentum cut is shown in the last line. Data are from the **2003-2004** e^+ data taking period and selected with the **medium** z selection given in table 4.6. The non-resonant background is not subtracted.

Consequently the cuts given in table 4.5 are used to define the acceptance for the medium z selection.

angular cut	$20^\circ \leqslant \theta_\mu \leqslant 160^\circ$
momentum cut	$P_\mu > 0.8\,\mathrm{GeV}$

Table 4.5: Acceptance cuts for the **medium** z selection

Figure 4.7 shows the effects of the acceptance on several observables. Since most of the decay muons are produced in the forward or backward directions[3], the restriction to the central region has a large impact on other quantities. In order to clarify the message of the previous figure the corresponding efficiencies of these restrictions are shown in figure 4.8. The angular cut affects the muons with high and low momentum around 1.5 GeV and rejects nearly all events below $W_{\gamma\mathrm{p}} = 40\,\mathrm{GeV}$ and above $W_{\gamma\mathrm{p}} = 200\,\mathrm{GeV}$. The momentum cut rejects up to 10 % of the central muons, and rejects backward muons above 160 °. This behaviour is reflected in $W_{\gamma\mathrm{p}}$, where primarily events at intermediate values are rejected. The acceptance cuts reject events of low elasticity, and hollows the z distribution towards the higher elasticity.

In order to study the correlations, figure 4.9 shows the correlation of the elasticity z and the polar angle θ_μ of the decay muons with the photon-proton centre-of-mass energy $W_{\gamma\mathrm{p}}$. The J/ψ mesons originating from direct photon-gluon fusion are predominantly produced at high z and small $W_{\gamma\mathrm{p}}$. Towards lower z and higher $W_{\gamma\mathrm{p}}$ the number of J/ψ mesons decreases significantly. The profile plot shows a clear correlation between the polar angle θ_μ and $W_{\gamma\mathrm{p}}$. Consequently the acceptance of the central tracking chamber restricts the accessible $W_{\gamma\mathrm{p}}$ region. The angular cut is approximately equivalent to restrict the $W_{\gamma\mathrm{p}}$ range to $20 \leqslant W_{\gamma\mathrm{p}} \leqslant 250\,\mathrm{GeV}$ at one standard deviation. The same $W_{\gamma\mathrm{p}}$ range is used for this analysis as the one of the previous analyses.

[3]Due to the boost, the decay plane has mainly a small angle compared with the horizontal plane.

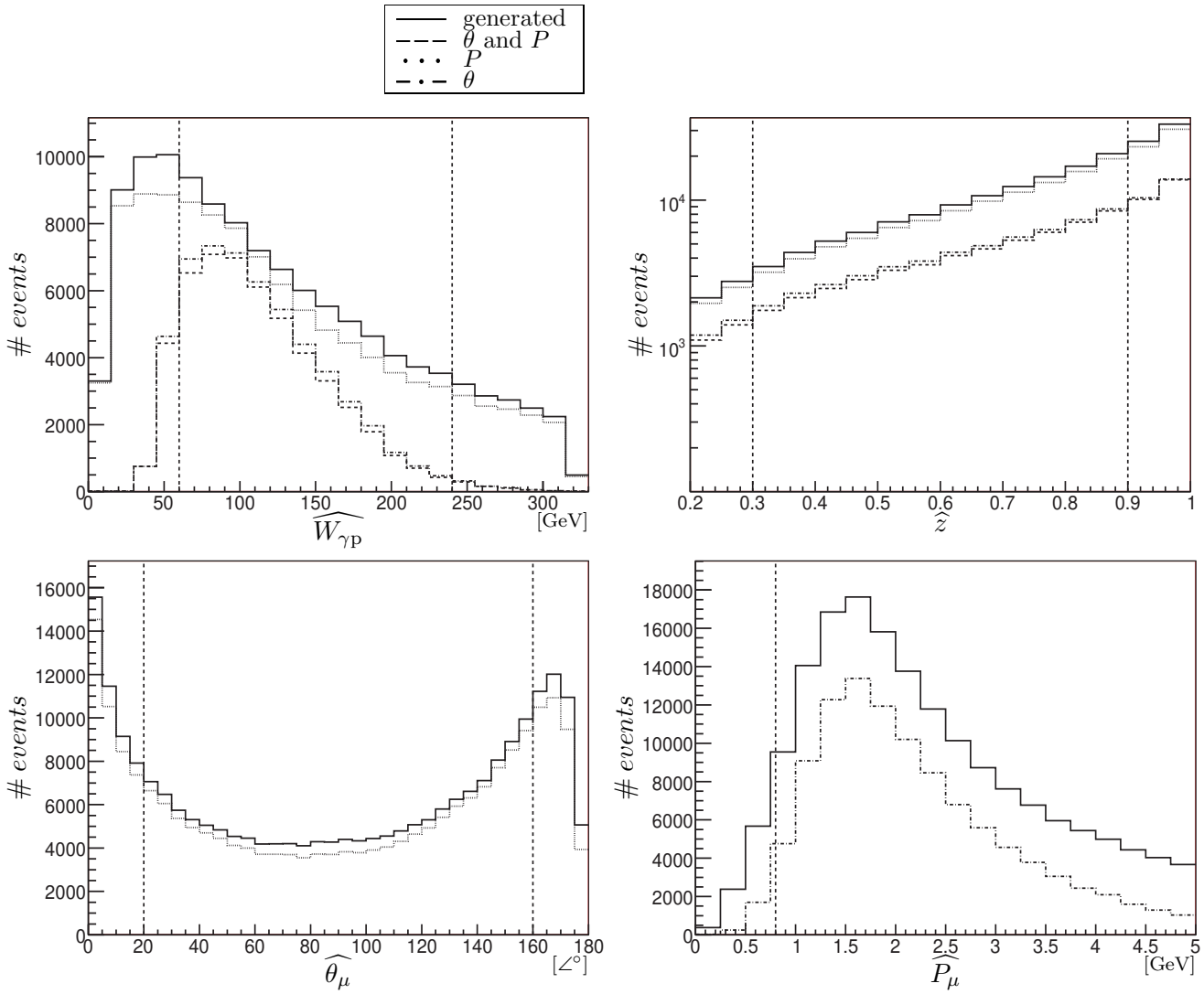

Figure 4.7: Influence of the restrictions $P_\mu > 0.8\,\text{GeV}$, $20° \leqslant \theta_\mu \leqslant 160°$ and of both on the distribution of the photon-proton centre-of-mass energy $W_{\gamma p}$, the elasticity z, the polar angle θ_μ, and the momentum P_μ of the decay muons. The phase space is limited to photoproduction and to the elasticity domain $0.3 \leqslant z \leqslant 0.9$. Events are generated with the Monte Carlo program EPJPSI in direct photon-gluon fusion. The vertical lines show the acceptance cuts defined in table 4.5 and the kinematic cuts defined in table 4.4.

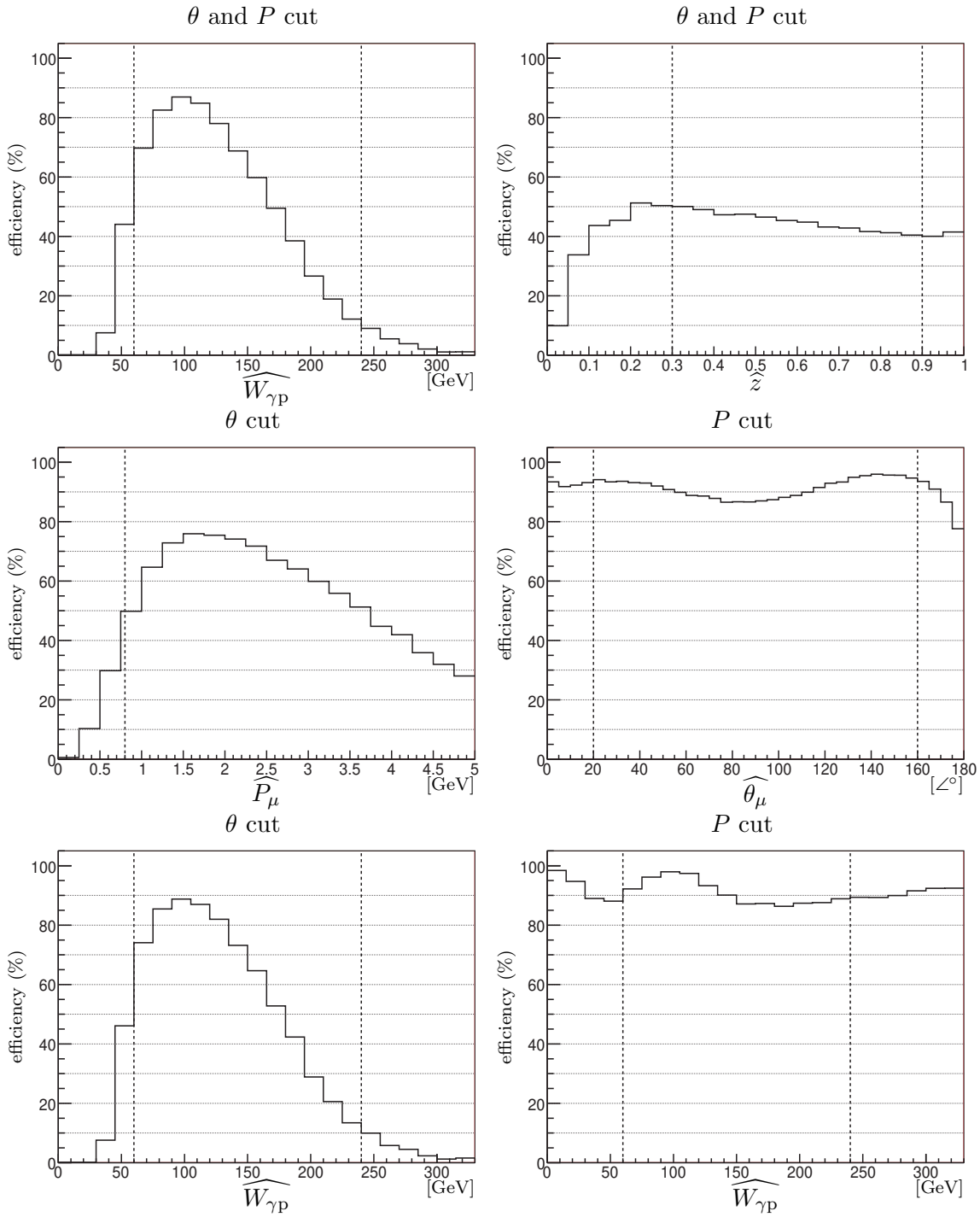

Figure 4.8: Efficiencies corresponding to figure 4.7. The plots have the same disposition. For z and $W_{\gamma p}$ the efficiency corresponds to the cuts on the polar angle θ and the momentum P. The last two plots show the efficiency of the single cuts on the $W_{\gamma p}$ distribution.

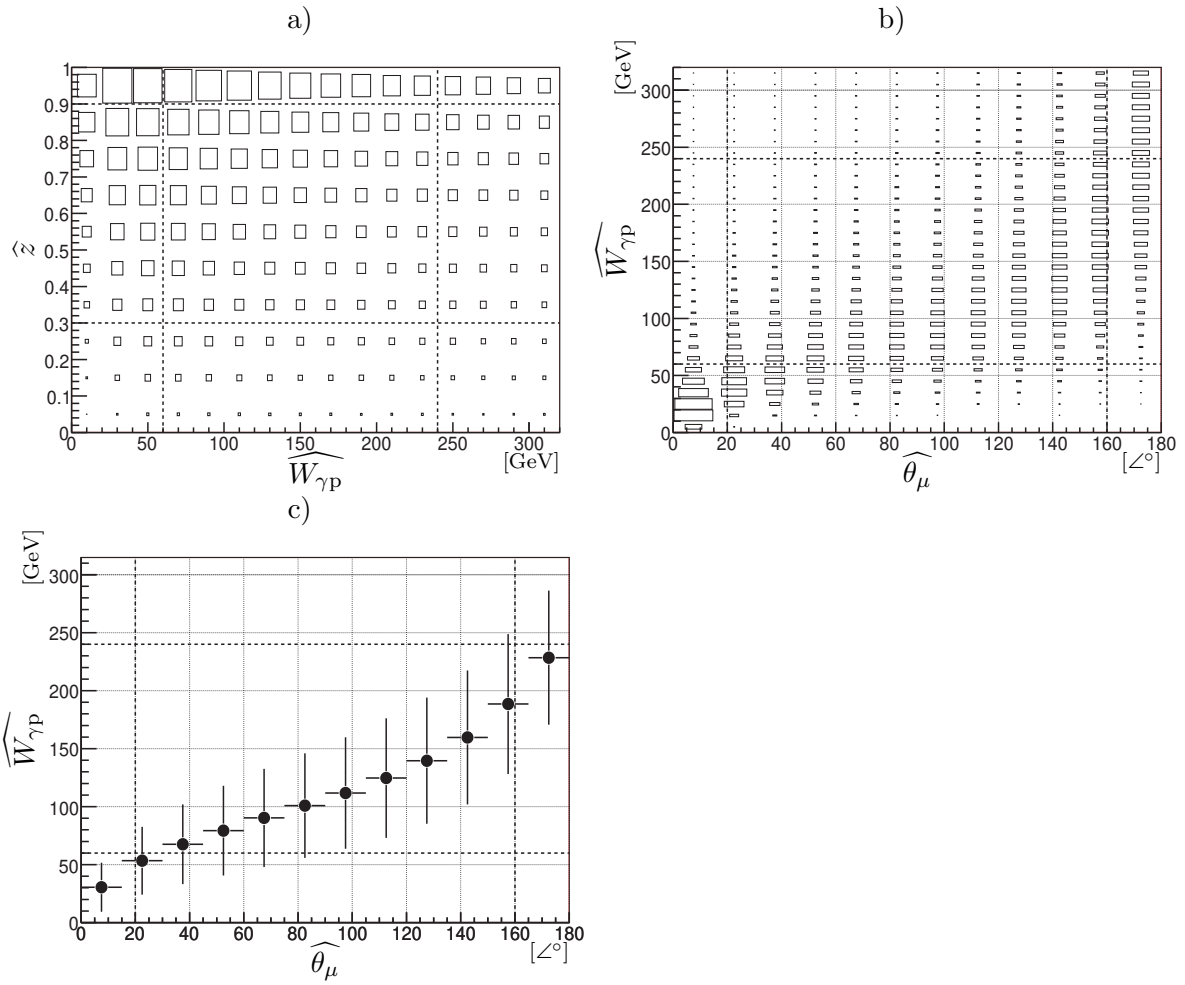

Figure 4.9: a) Correlation between the photon-proton centre-of-mass energy $W_{\gamma p}$ and the elasticity z. b) Correlation between $W_{\gamma p}$ and the polar angle θ_μ of the decay muons. In c) is shown a profile of the two dimensional distribution in b). Events are generated with the Monte Carlo program EPJPSI in direct photon-gluon fusion. The vertical and horizontal lines show the acceptance cuts defined in table 4.5 and the kinematic cuts defined in table 4.4.

The formula to compute the acceptance is:

$$\text{acceptance} \mathrel{\widehat{=}} \frac{\text{kinematic and acceptance cuts on the generator level}}{\text{kinematic cuts on the generator level}}$$

The resulting acceptance is shown in figure 4.10 as a function of the observables used for the measurement of the inelastic J/ψ meson cross section. In comparison to the efficiencies shown in figure 4.8 all the kinematic cuts of the table 4.4 are applied. The acceptance as a function of $W_{\gamma p}$ reflects the previous studies on the correlations, and suggests to cut at 60 GeV in order to suppress the steep rise and to cut at 240 GeV so as to have an acceptance above approximately 10 %. The restriction on the photon-proton centre-of-mass energy $W_{\gamma p}$ suppresses events at high elasticity and increase the drops at low z. The acceptance as a function of $P^2_{t,\psi}$ is nearly constant.

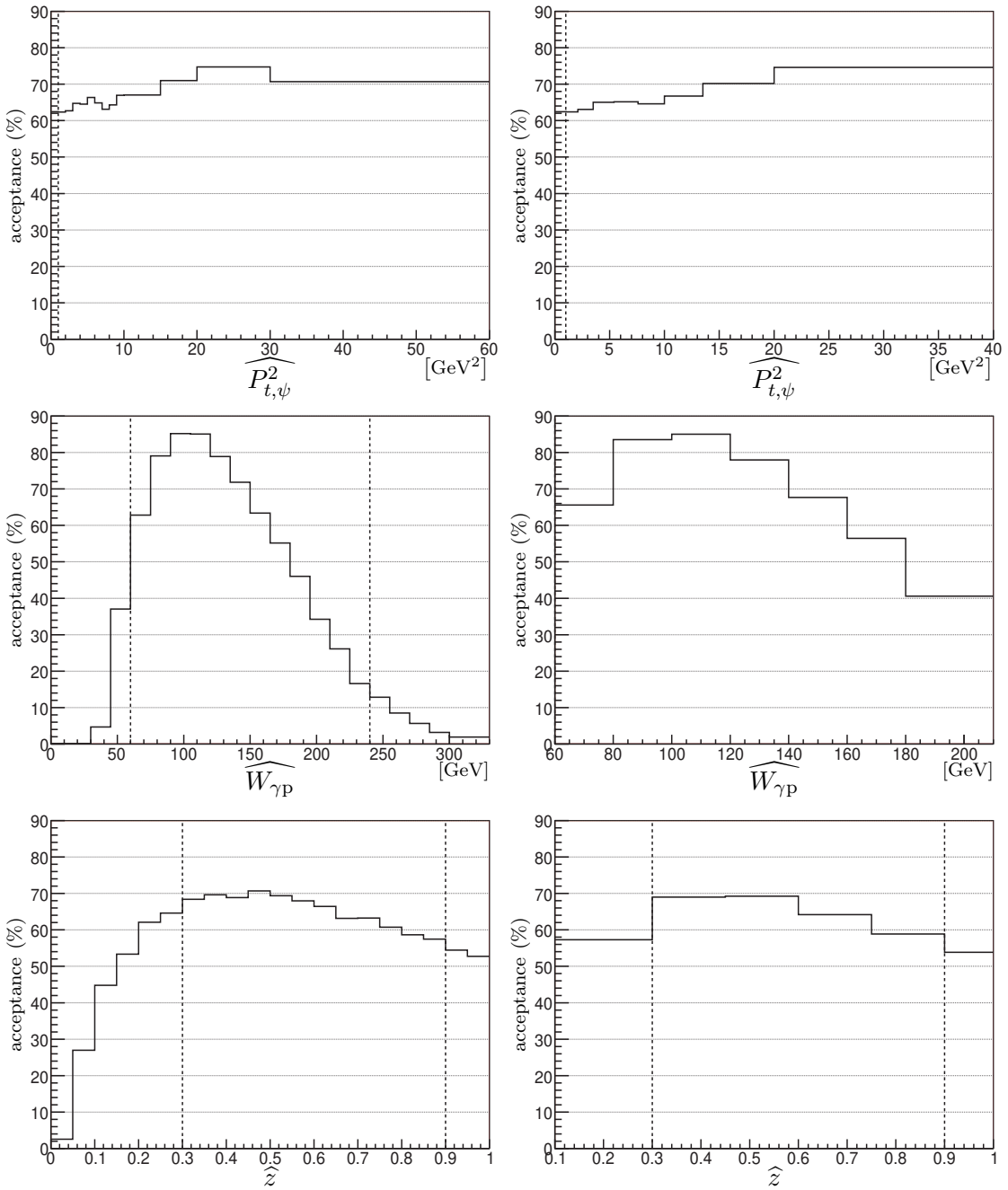

Figure 4.10: Acceptance of the requirement $20^\circ \leqslant \theta_\mu \leqslant 160^\circ$ and $P_\mu > 0.8\,\mathrm{GeV}$ as a function of $P^2_{t,\psi}$, $W_{\gamma p}$, and z. Events are generated with the two component simulation of the Monte Carlo program EPJPSI, using direct photon-gluon fusion and resolved gluon-gluon fusion (cf. section 7.3.2). The distributions on the right hand side are shown in the binning used for the measurement of the cross sections and on the left hand side in a finer binning. The vertical lines show the kinematic cuts defined in table 4.4.

4.2.2 Selection Cuts

Here the selection of the data at medium z will be defined. Figure 4.11 shows the distribution of the muon qualities after the acceptance cut. The second plot shows the lower quality versus the higher quality for the two muons. For many events at least one track is not identified as a muon [4] (see bin corresponding to a quality of -1) [5]. In order to be consistent with the subtrigger selection, at least one muon with an iron quality is required (Quality$_\mu \geqslant 10$). For the second muon, a good calorimeter quality is required (Quality$_\mu \geqslant 2$). Most of the background is suppressed by these requirements.

For muons with a polar angle greater than 140 °, a number of at least six hit layers are required to be identified as a muon. Since the LAr calorimeter does not extend to the backward region, and the SpaCal is not deep enough, hadrons can hit the streamer tube of the backward iron instrumented detector.

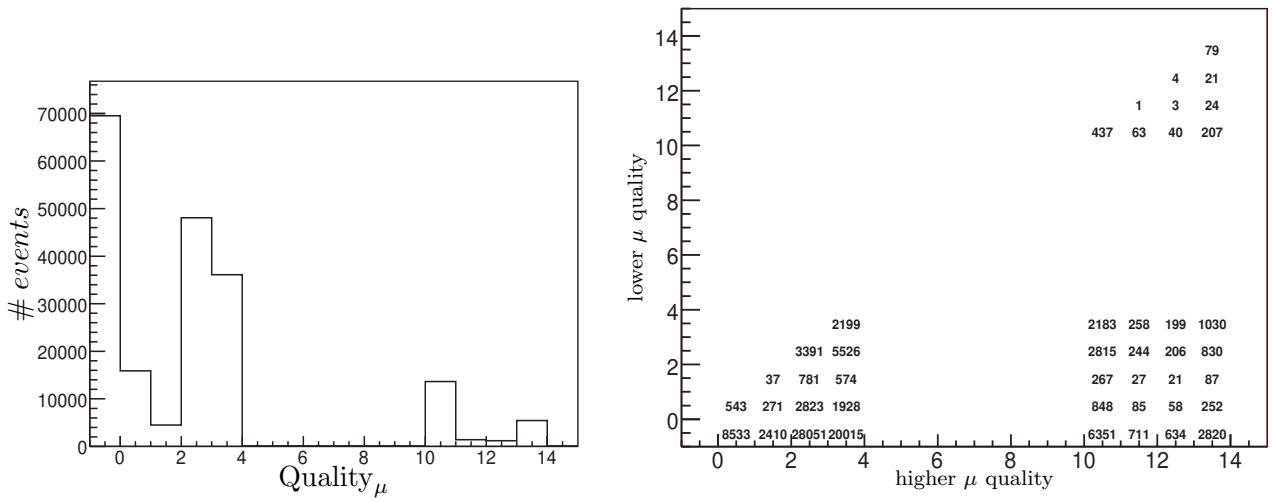

Figure 4.11: Distribution of the muon qualities after the acceptance cuts. Data are from the **2003-2004** e^+ data taking period. The second plot shows the lower quality versus the higher quality.

An invariant mass window of approximately 5σ (cf. table 7.4), is used to reject background around the J/ψ meson signal. Moreover the kinematic cuts of table 4.4 and the acceptance cuts of table 4.5 are included in this selection. Photoproduction events are selected at the reconstruction level by requiring the scattered electron is not detected in the main detector (cf. section 4.1.4). Consequently the cuts in table 4.6 are used for the medium z selection.

[4] The *inelastic* tag of the J/ψ finder is not used.

[5] For a quality of 0 the track is identified has a muon.

Selection cuts	
inelastic	#Lee West Tracks $\geqslant 3$
photoproduction medium elasticity	no scattered electron in the main detector $0.3 \leqslant z \leqslant 0.9$ $P^2_{t,\psi} > 1\,\mathrm{GeV}^2$ $60 \leqslant W_{\gamma\mathrm{p}} \leqslant 240\,\mathrm{GeV}$
angular cut momentum cut	$20^\circ \leqslant \theta_\mu \leqslant 160^\circ$ $P_\mu > 0.8\,\mathrm{GeV}$
Muons qualities	higher μ quality $\geqslant 10$ lower μ quality $\geqslant 2$
Invariant mass window	$2.8 \leqslant M_{\mu\mu} \leqslant 3.4\,\mathrm{GeV}$
Subtrigger combination	
2003-2004 e^+ 2004-2005 e^-	s15 or s18 s19 or s23 or s18

Table 4.6: Selection cuts for the **medium** z selection including the kinematic cuts of table 4.4 and the acceptance cuts of table 4.5. The subtrigger combination used for each data taking period are also given (cf. table 5.1).

4.2.3 Minimum Number of Tracks and Rejection of Background Originating from Diffractive ψ(2S)

The ψ(2S) meson has cascade decays $\psi(2\mathrm{S}) \longrightarrow \mathrm{J}/\psi + X$, which can constitute a source of background for this analysis. The direct decay mode $\psi(2\mathrm{S}) \longrightarrow \mu^-\mu^+$ or modes with additional neutrals are suppressed by the requirement of at least three tracks. But this requirement is not sufficient to suppress the decay mode $\psi(2\mathrm{S}) \longrightarrow \mathrm{J}/\psi(1\mathrm{S})\pi^-\pi^+$, since it has four tracks. This decay mode has a branching ratio of $31.7 \pm 1.1\,\%$. The other decay mode $\psi(2\mathrm{S}) \longrightarrow \mathrm{J}/\psi(1\mathrm{S})\eta$ with a branching ratio of $3\,\%$ is negligible. This source of background would be suppressed with a requirement of at least five tracks.

Figure 4.12 shows for data the distribution of the number Lee West tracks, and figure 4.13 shows this distribution in elasticity bins. Since the number of tracks is strongly correlated with the elasticity of the event, the position of the maximum moves towards lower number of tracks with the elasticity. In order to quantify the effect of a cut on the number of tracks, figure 4.14 shows the cumulative distribution for rejecting an event as a function of the cut on the number of Lee West tracks. A cut at five reduces the statistics at medium elasticity, up to $55\,\%$ in the bin $0.75 \leqslant z < 0.9$. For the amount of statistics available of this analysis, it is not possible to require this number of tracks.

Inelastic ψ(2S) mesons cannot be separated from inelastic J/ψ mesons, since the number of tracks is not constrained as for diffractive ψ(2S), but correlated with the elasticity as for inelastic J/ψ mesons.

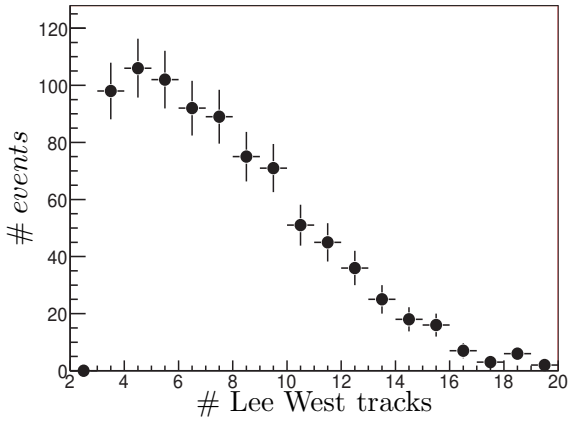

Figure 4.12: Distribution of the number of Lee West tracks. Data are from the **2003-2004** e^+ data taking period and are selected with the **medium** z selection given in table 4.6.

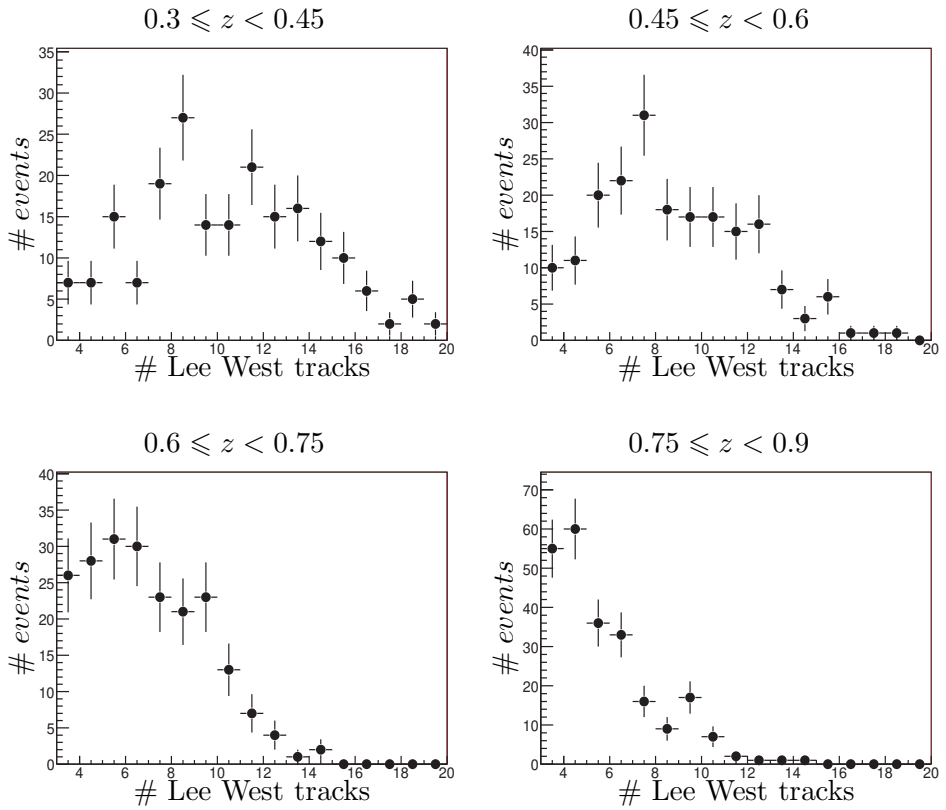

Figure 4.13: Distribution of the number of Lee West tracks in bins of z for the **medium** z selection.

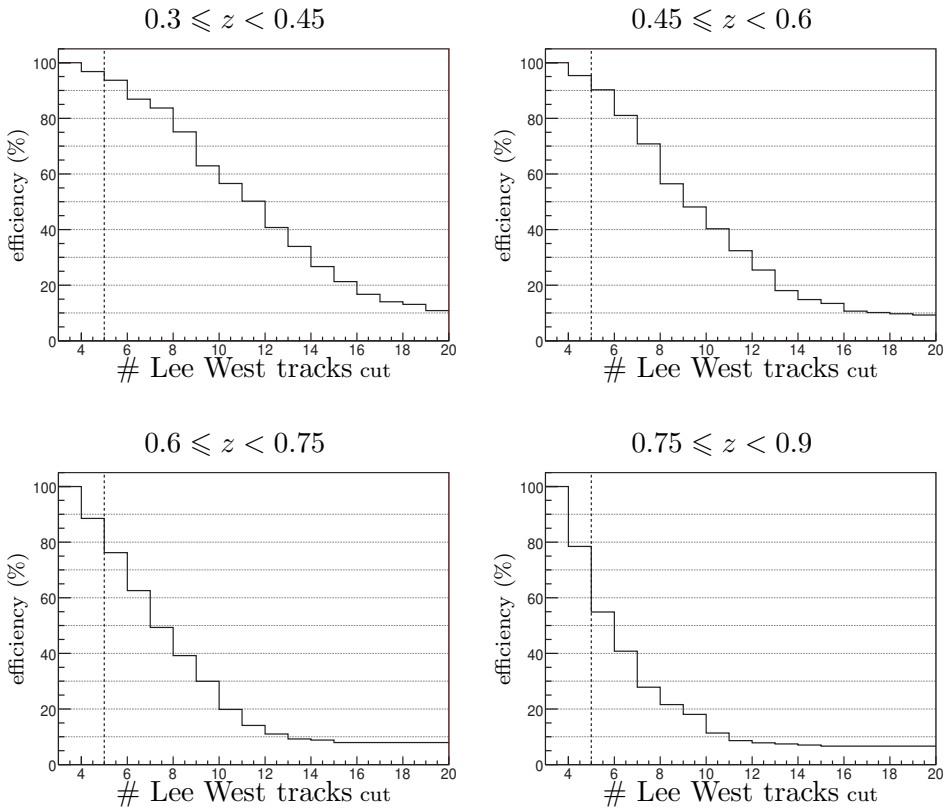

Figure 4.14: Cumulative distribution for rejecting an event as a function of the cut on the number of Lee West tracks in z bins for the **medium** z selection. The vertical dotted lines show the amount of remaining event for a cut at five tracks.

4.2.4 Selection Efficiency

The formula to compute the selection efficiency is:

$$\text{selection efficiency} \mathrel{\widehat{=}} \frac{\text{acceptance and selection cuts on the reconstructed level}}{\text{kinematic and acceptance cuts on the generator level}}$$

The resulting selection efficiency is shown in figure 4.15 as a function of the observables used for the measurement of the inelastic J/ψ meson cross section. The efficiency increases towards higher values of $P^2_{t,\psi}$ and $W_{\gamma\mathrm{p}}$, while the efficiency as a function of the elasticity z is nearly constant in the medium z range, but drops at high elasticity in the last bin. The efficiency as function of $W_{\gamma\mathrm{p}}$ shows at low $W_{\gamma\mathrm{p}}$ a steep rise similar to the acceptance.

The combination of the acceptance and the selection efficiency is shown in figure 4.16. The efficiency as a function of $P^2_{t,\psi}$ is rising as the acceptance and the selection efficiency, from 20 % to 50 %. For $W_{\gamma\mathrm{p}}$ the efficiency takes the shape of the acceptance. And for z the efficiency drops towards higher elasticity as the acceptance. The efficiencies as function of $W_{\gamma\mathrm{p}}$ and z are comprised between 20 % and 30 %.

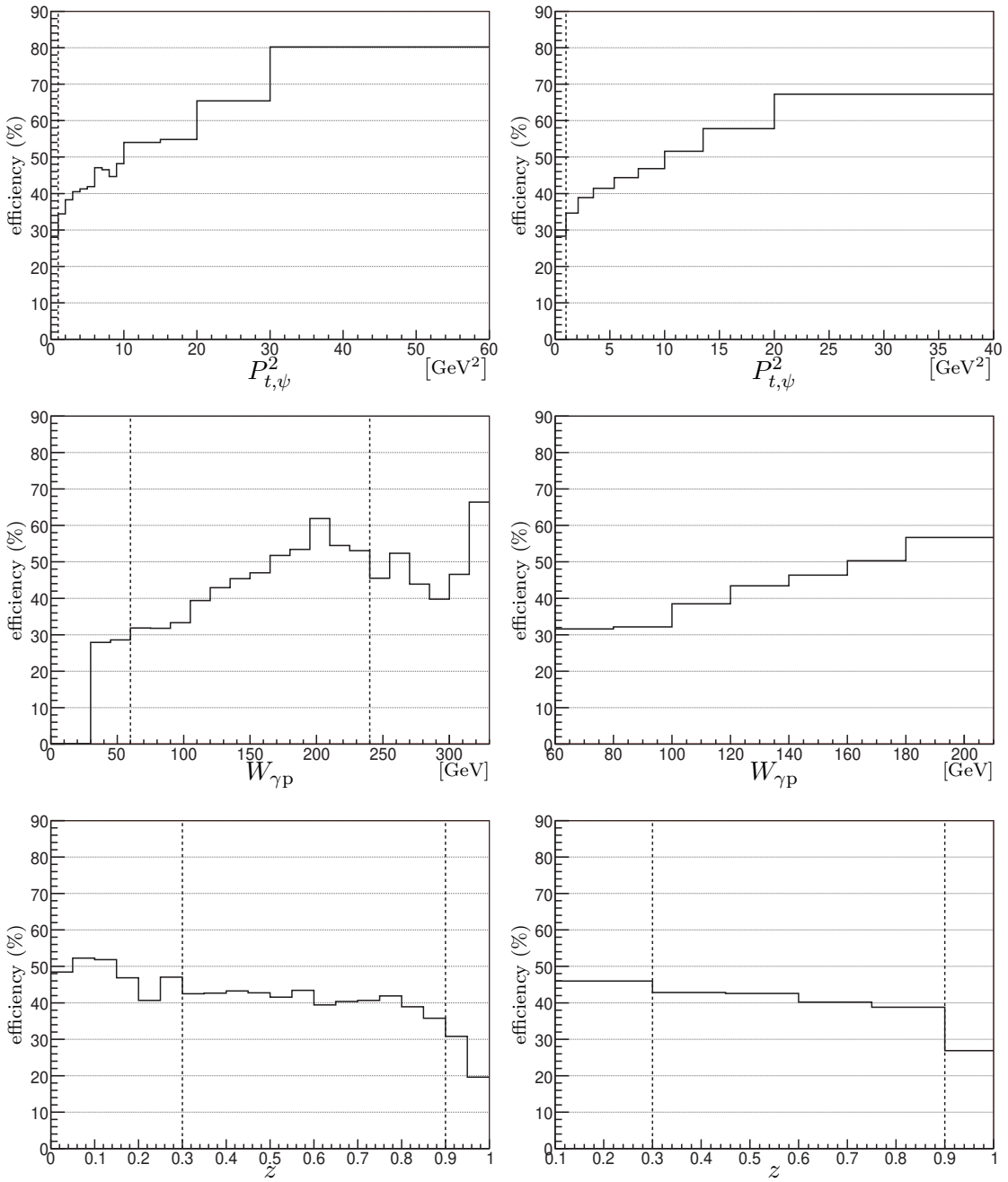

Figure 4.15: Selection efficiency as a function of $P^2_{t,\psi}$, $W_{\gamma p}$, and z. Events are generated with the two component simulation of the Monte Carlo program EPJPSI, using direct photon-gluon fusion and resolved gluon-gluon fusion (cf. section 7.3.2). The distributions on the right hand side are shown in the binning used for the measurement of the cross sections and on the left hand side in a finer binning. The vertical lines show the kinematic cuts defined in table 4.4.

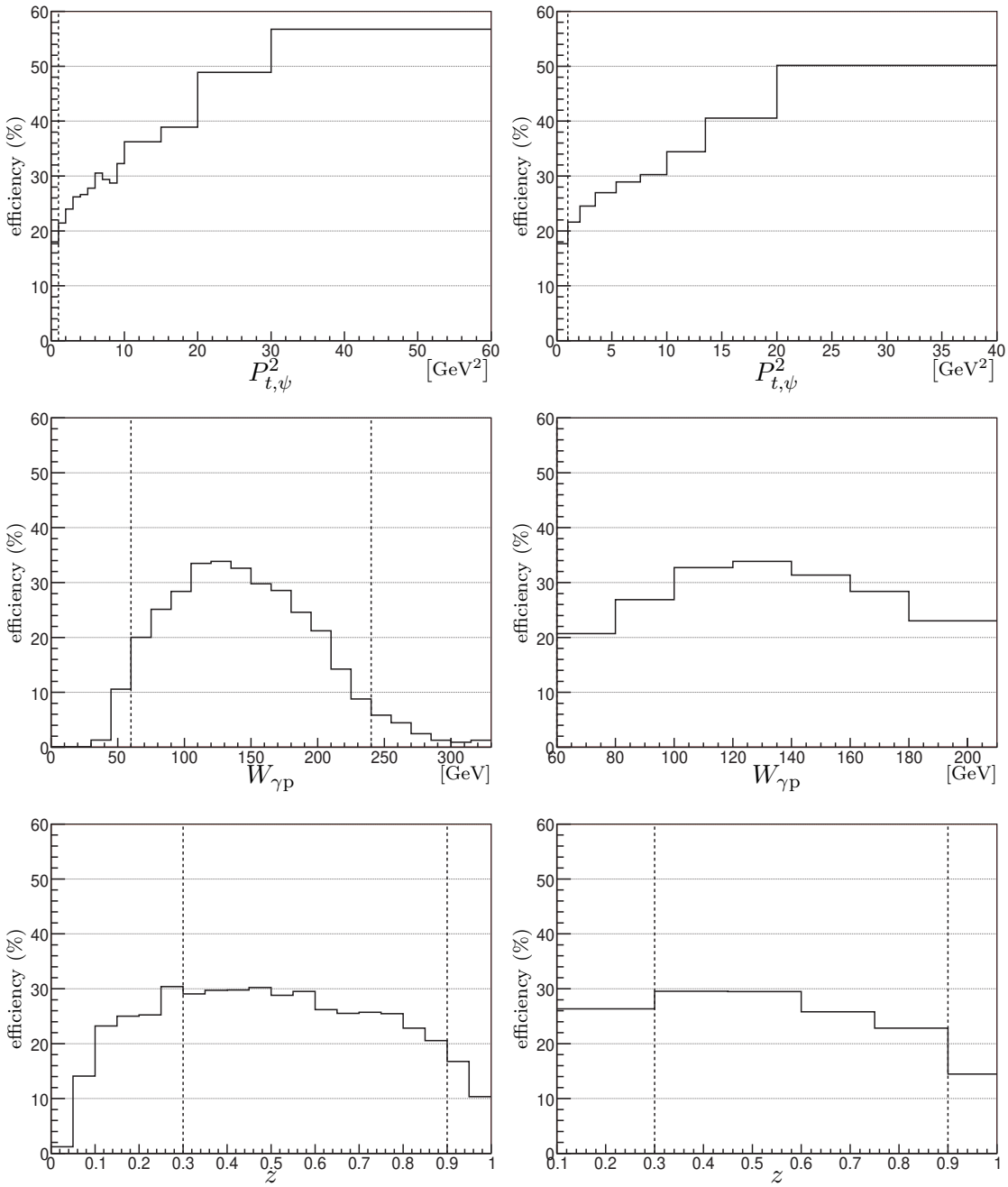

Figure 4.16: Acceptance and selection efficiency combined as a function of $P^2_{t,\psi}$, $W_{\gamma p}$, and z. See figure 4.15 for explanation.

4.3 Acceptance and Selection of J/ψ Mesons at Low z

Production of J/ψ mesons in the region of small elasticities, $z < 0.45$, proceeds dominantly through resolved photon processes which are dominated by gluon-gluon fusion processes and secondarily via direct photon-gluon fusion. Consequently the efficiencies which are used to correct the number of J/ψ mesons are determined with the combination of simulations of gluon-gluon fusion (EPJPSI-resolved Monte Carlo) and direct photon-gluon fusion (EPJPSI-direct Monte Carlo). The relative normalisation of the two contributions will be discussed in section 7.3.2.

4.3.1 Acceptance

As for the analysis at medium z the decay muons of the J/ψ meson have to lie in the acceptance region of the central tracking chambers. However at low elasticities the J/ψ meson only has a small fraction of the photon momentum, which results in small polar angles for the J/ψ and its decay particles (cf. figure 4.19). At large polar angles the non-resonant background originating from hadrons mis-identified as muons exceeds the expected J/ψ signal by orders of magnitude. Therefore the polar angle of the decay muons is restricted to $20^\circ \leqslant \theta_\mu \leqslant 140^\circ$. On the other hand the momentum cut is chosen to be as low as possible for the muon identification, $P_\mu > 0.8\,\mathrm{GeV}$, in order to improve the acceptance. Figure 4.18 shows the polar angle, the momentum, and the transverse momentum of calorimeter and iron muons.

Consequently the cuts given in table 4.7 are used to define the acceptance for the low z selection.

angular cut	$20^\circ \leqslant \theta_\mu \leqslant 140^\circ$
momentum cut	$P_\mu > 0.8\,\mathrm{GeV}$

Table 4.7: Acceptance cuts for the **low** z selection

Here the influence of these requirements will be discussed. Processes with resolved photons differ from direct photon-gluon fusion not only in the elasticity. While direct photon-gluon fusion occurs predominantly at high elasticities and small $W_{\gamma\mathrm{p}}$, gluon-gluon fusion events have very low z at medium to high $W_{\gamma\mathrm{p}}$. The correlation for resolved processes are shown in figure 4.17. The correlation between $W_{\gamma\mathrm{p}}$ and the polar angle of the decay muons is much smaller in resolved processes, nearly all muons lie in the very forward direction.

Figure 4.19 and figure 4.21 show the effects on several observables for a gluon-gluon fusion Monte Carlo and a photon-gluon fusion Monte Carlo respectively. In order to enhance the message of the previous figures, figure 4.20 and figure 4.22 show the corresponding efficiencies of these restrictions.

Compared with the direct photon-gluon fusion simulation in the same elasticity region, the polar angular distribution of the decay muons for resolved processes is peaked much stronger in the forward region outside of the detector acceptance ($\theta \leqslant 20^\circ$). The maximum is at nine times the level of the plateau, against five for the direct processes (cf. figures figure 4.19 and 4.21 for comparison).

The generated $W_{\gamma\mathrm{p}}$ distribution in resolved processes is not peaked at around 40 GeV, as in the direct process, but has a very broad maximum around 60–90 GeV. In resolved processes a higher value of $W_{\gamma\mathrm{p}}$ is needed on average, since only a part of the photon momentum enters in the production of the J/ψ meson. The effect of the cut on the polar angle of the decay muons is rather different from the direct photon-gluon fusion case. While the $W_{\gamma\mathrm{p}}$ region from 60 to 200 GeV shows a significant number of events passing this cut for direct photon-gluon fusion, in resolved processes this region starts at around 100 GeV and goes up to the kinematic limit.

Resolved events at very small elasticities $z < 0.02$, where the cross section is highest, are nearly all rejected by the polar angle cut.

For the direct process, shown in figure 4.21, the low elasticity region contributes only very little to the total cross section. The generated polar angle and momentum distributions of the decay muons and the $W_{\gamma p}$ distribution are similar to the medium z range (cf. figure 4.7). The elasticity shows a steeper rise at very low values, $z < 0.2$. The reduced upper limit on the polar angle θ_μ increases the impact of the polar angle restriction. The $W_{\gamma p}$ distribution after both restrictions is shifted of approximately 20 GeV towards higher values compared to the medium z region.

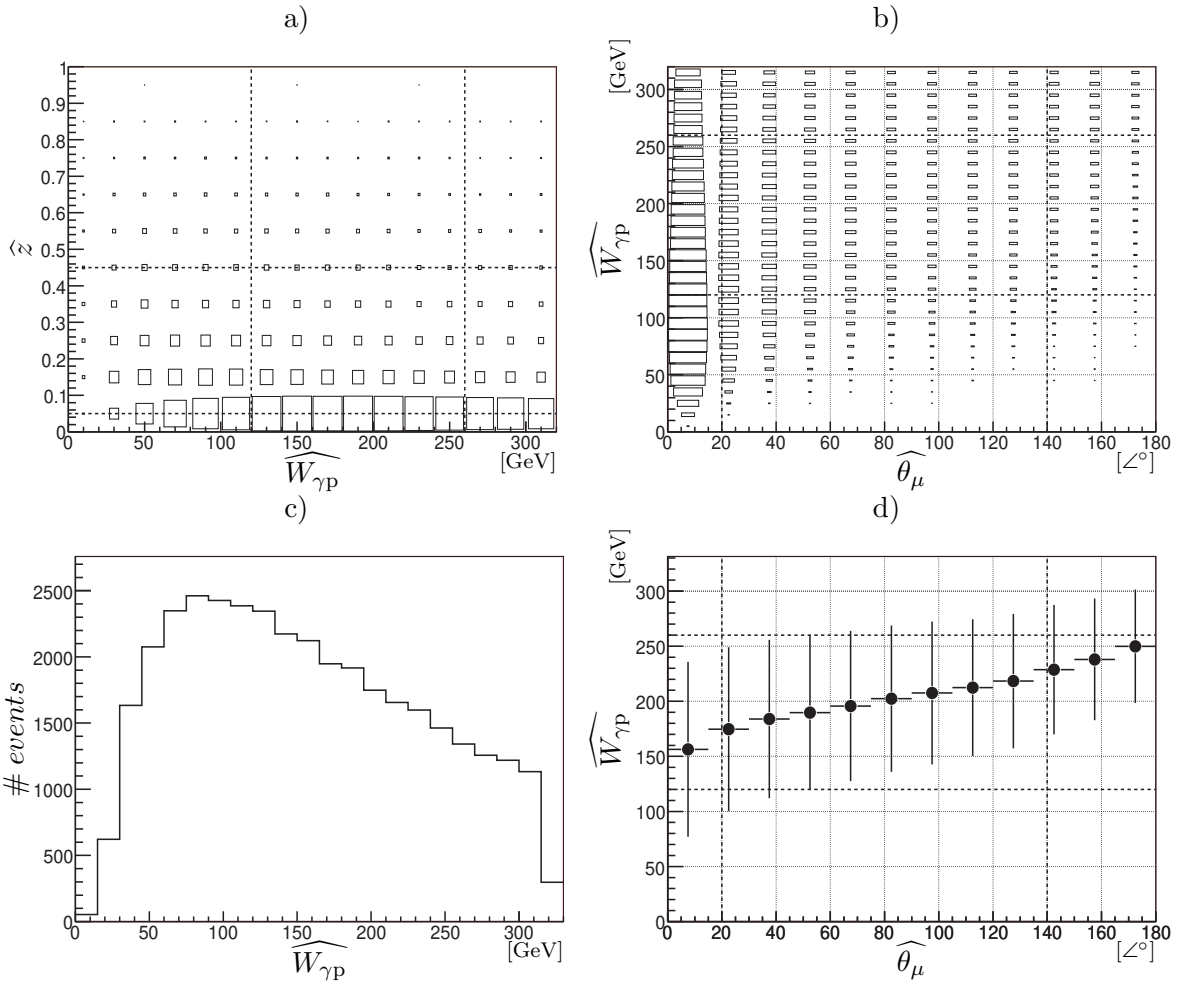

Figure 4.17: a) Correlation between the photon-proton centre-of-mass energy $W_{\gamma p}$ and the elasticity z. b) Correlation between $W_{\gamma p}$ and the polar angle θ_μ of the decay muons. c) Distribution of $W_{\gamma p}$ with θ_μ restricted in the forward region $0° \leqslant \theta_\mu < 20°$. The last plot d) is a profile of the two dimensional distribution in b). Events are generated with the Monte Carlo EPJPSI program in **resolved gluon-gluon fusion**. The vertical and horizontal lines show the acceptance cuts defined in table 4.7 and the kinematic cuts defined in table 4.4.

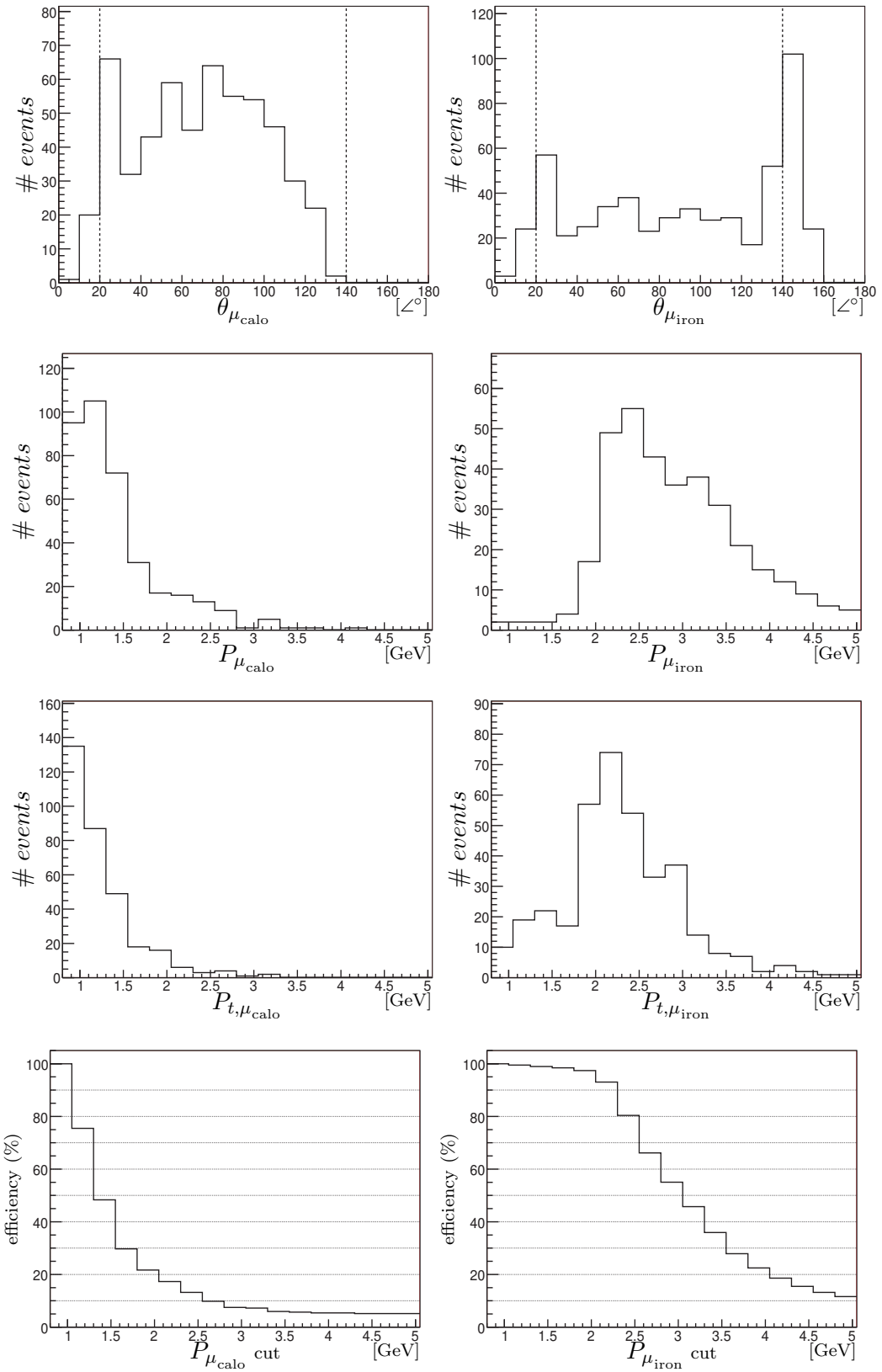

Figure 4.18: Distribution of the polar angle, the momentum, the transverse momentum of the calorimeter and the iron muons. The vertical lines show the angular cut defined in table 4.7. The percentage of remaining muons as function of the momentum cut is shown in the last line. Data are from the **2003-2004** e^+ data taking period and selected with the **low** z selection given in table 4.8. The non-resonant background is not subtracted.

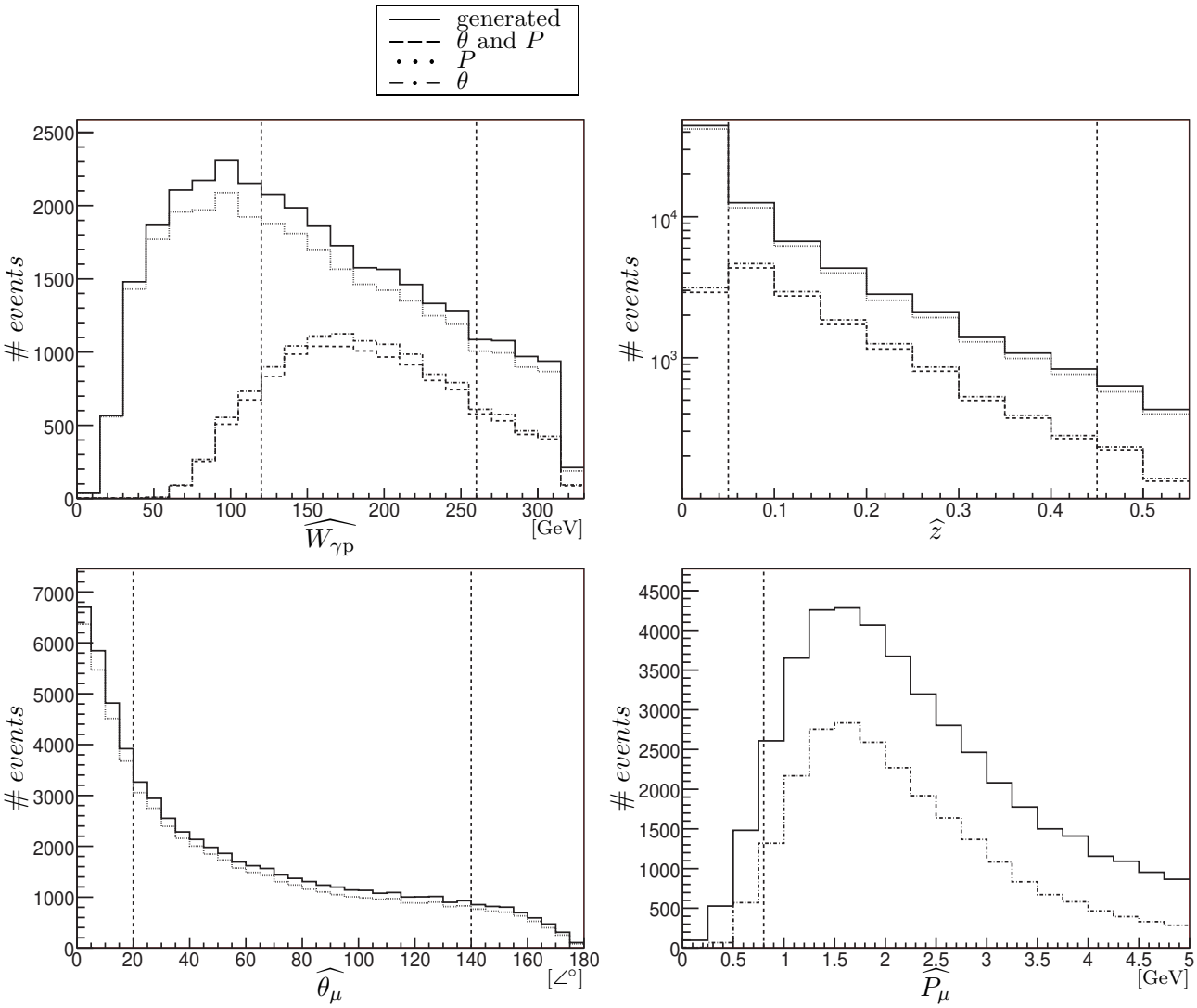

Figure 4.19: Influence of the restrictions $P_\mu > 0.8\,\text{GeV}$, $20° \leqslant \theta_\mu \leqslant 140°$ and of both on the distribution of the photon-proton centre-of-mass energy $W_{\gamma p}$, the elasticity z, the polar angle θ_μ, and the momentum P_μ of the decay muons. The phase space is limited to photoproduction and to the elasticity domain $0.05 \leqslant z \leqslant 0.45$. Events are generated with the Monte Carlo program EPJPSI in **resolved gluon-gluon fusion**. The vertical lines show the acceptance cuts defined in table 4.7 and the kinematic cuts defined in table 4.4.

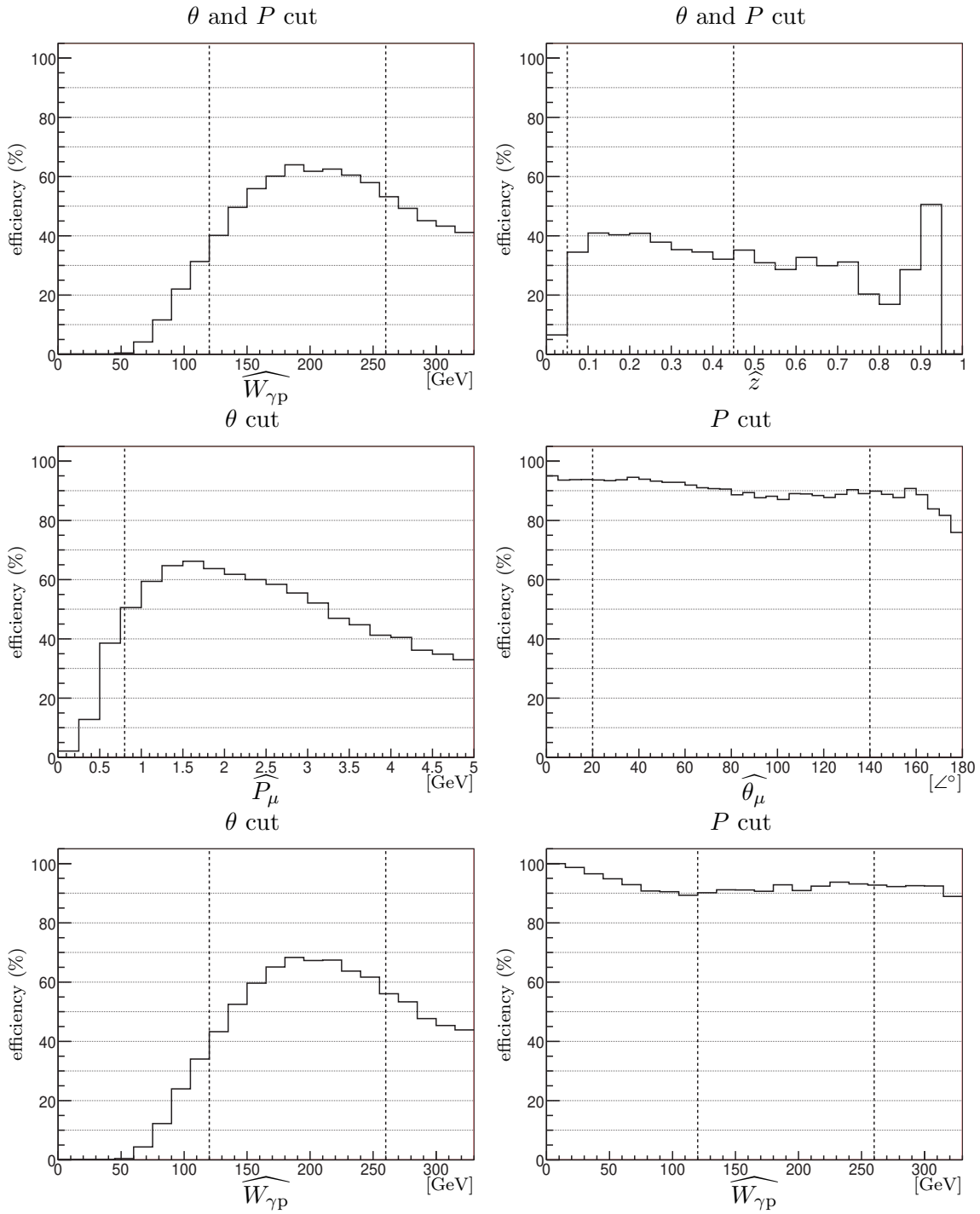

Figure 4.20: Efficiencies corresponding to figure 4.19. The plots have the same disposition. For z and $W_{\gamma p}$ the efficiency corresponds to the cuts on the polar angle θ and the momentum P. The last line shows the efficiency of these cuts on the $W_{\gamma p}$ distribution.

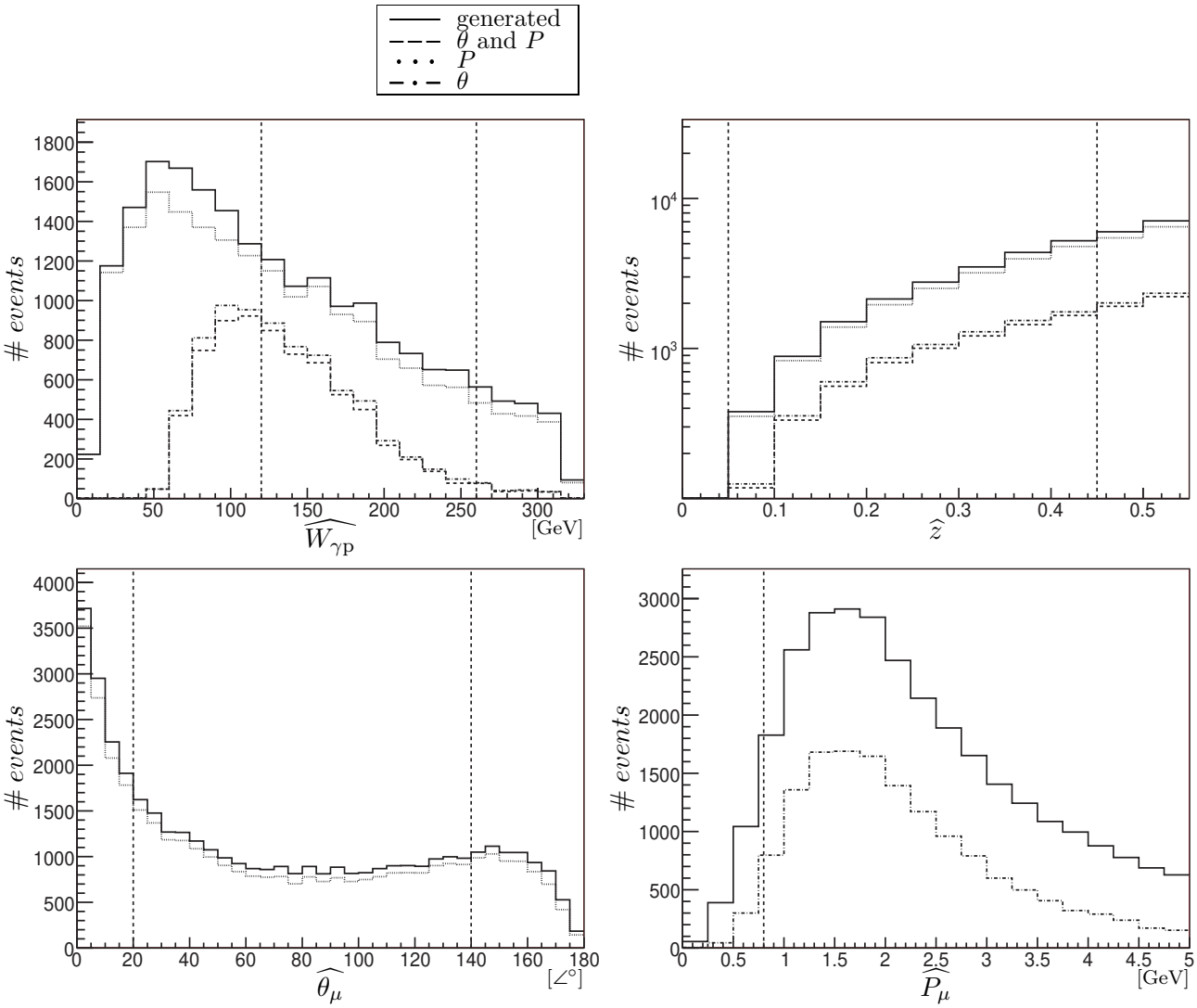

Figure 4.21: Influence of the restrictions $P_\mu > 0.8\,\text{GeV}$, $20° \leqslant \theta_\mu \leqslant 140°$ and of both on the distribution of the photon-proton centre-of-mass energy $W_{\gamma p}$, the elasticity z, the polar angle θ_μ, and the momentum P_μ of the decay muons. The phase space is limited to photoproduction and to the elasticity domain $0.05 \leqslant z \leqslant 0.45$. Events are generated with the Monte Carlo program EPJPSI in **direct photon-gluon fusion**. The vertical lines show the acceptance cuts defined in table 4.7 and the kinematic cuts defined in table 4.4.

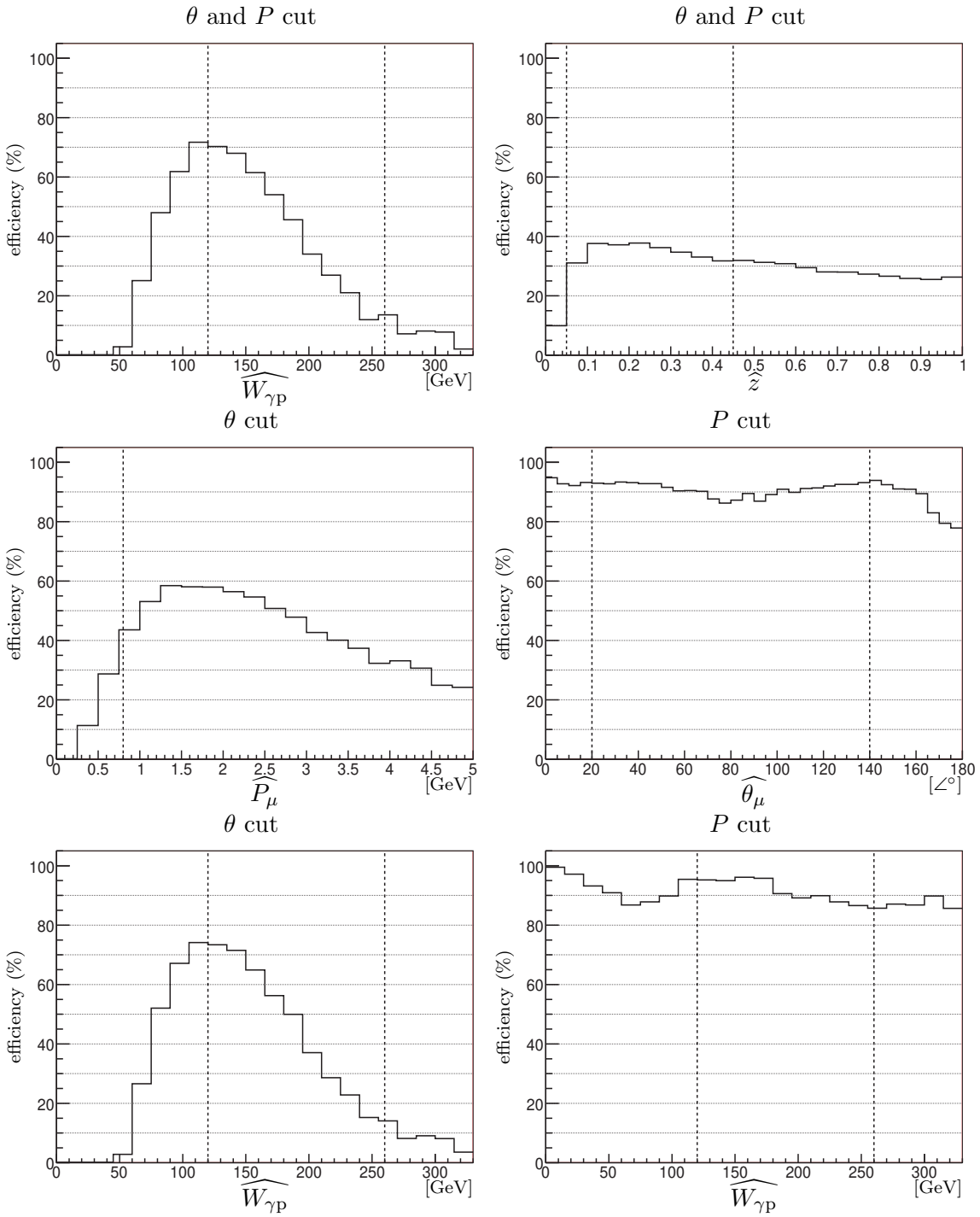

Figure 4.22: Efficiencies corresponding to figure 4.21. The plots have the same disposition. For z and $W_{\gamma p}$ the efficiency corresponds to the cuts on the polar angle θ and the momentum P. The last line shows the efficiency of these cuts on the $W_{\gamma p}$ distribution.

The resulting acceptance is shown in figure 4.24 as a function of the observables used for the measurement of the inelastic J/ψ meson cross section. The efficiency as a function of $W_{\gamma p}$ is shown separately for both direct and resolved processes in figure 4.23. These two distributions have the same behaviour as for the previous plots where the cut on $P^2_{t,\psi}$ was not included. The acceptance for direct photon-gluon fusion has a similar dependence on $W_{\gamma p}$ in comparison to the medium z selection (cf. figure 4.10), but its maximum is at much lower $W_{\gamma p}$ values. The acceptance as a function of the $W_{\gamma p}$ suggests to cut at 120 GeV and 260 GeV so as to have a sufficient acceptance. In the kinematic region of the low z analysis the acceptance does not only depend on $W_{\gamma p}$ but also depends strongly on z. For very low values of z, the acceptance tends towards zero. To avoid large uncertainties, the analysis is restricted to the range $0.05 \leqslant z \leqslant 0.45$.

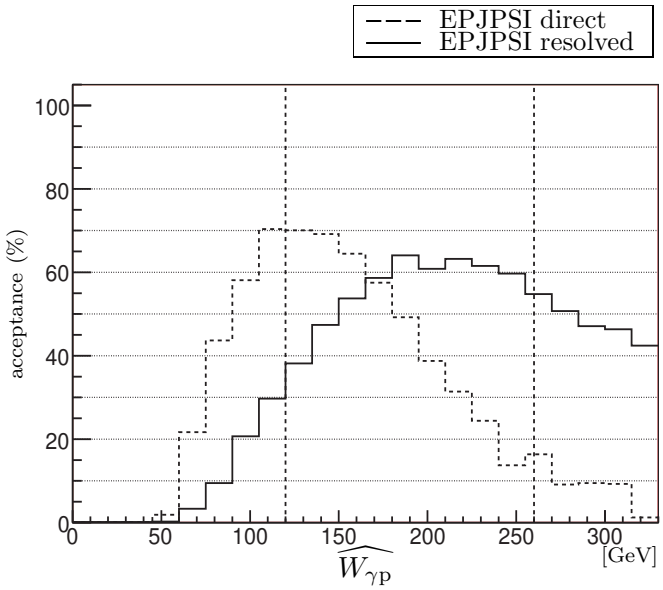

Figure 4.23: Acceptance as a function of $W_{\gamma p}$ shown separately for both direct and resolved processes. Events are generated with the Monte Carlo program EPJPSI in direct photon-gluon fusion and resolved gluon-gluon fusion. The vertical lines show the kinematic cuts defined in table 4.4.

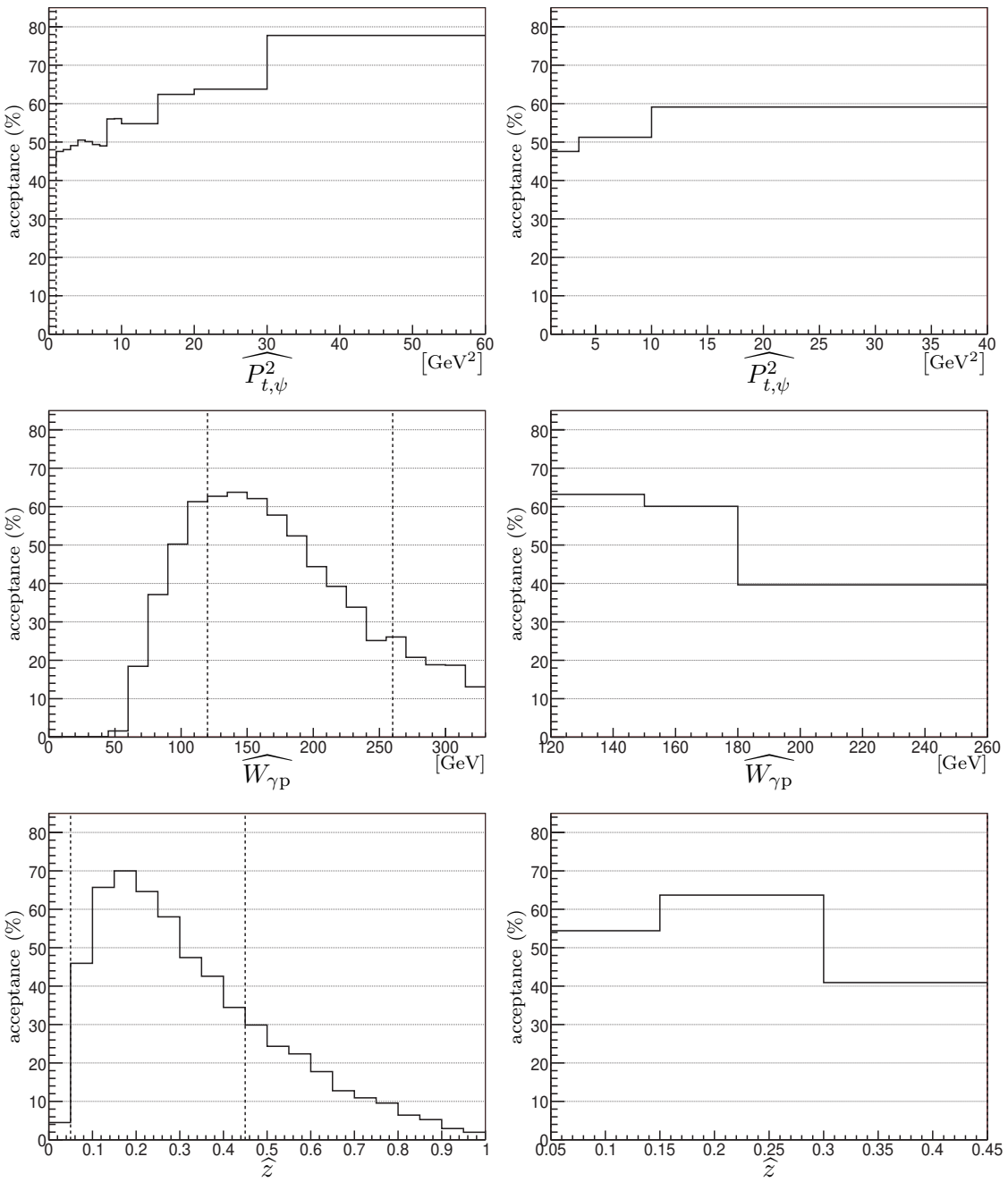

Figure 4.24: Acceptance of $20° \leqslant \theta_\mu \leqslant 140°$ and $P_\mu > 0.8\,\text{GeV}$ as a function of $P^2_{t,\psi}$, $W_{\gamma p}$, and z. The distributions on the right hand side are shown in the binning used for the measurement of the cross sections and on the left hand side in a finer binning. Events are generated with the two component simulation of the Monte Carlo program EPJPSI in direct photon-gluon fusion and resolved gluon-gluon fusion (cf. section 7.3.2). The vertical lines show the kinematic cuts defined in table 4.4.

4.3.2 Selection Cuts

Here the selection of the data at low z will be defined in a similar way as for the medium z selection. Excepted for the z and $W_{\gamma p}$ cuts the same cuts are applied as for the medium z selection. Consequently the cuts in table 4.8 are used for the low z selection.

Selection cuts	
inelastic	#Lee West Tracks $\geqslant 3$
photoproduction low elasticity	no scattered electron in the main detector $0.05 \leqslant z \leqslant 0.45$ $P^2_{t,\psi} > 1\,\mathrm{GeV}^2$ $120 \leqslant W_{\gamma p} \leqslant 260\,\mathrm{GeV}$
angular cut momentum cut	$20^\circ \leqslant \theta_\mu \leqslant 140^\circ$ $P_\mu > 0.8\,\mathrm{GeV}$
Muons qualities	higher μ quality $\geqslant 10$ lower μ quality $\geqslant 2$
Invariant mass window	$2.8 \leqslant M_{\mu\mu} \leqslant 3.4\,\mathrm{GeV}$
Subtrigger combination	
2003-2004 e^+ 2004-2005 e^-	s15 or s18 s19 or s23 or s18

Table 4.8: Selection cuts for the **low** z selection including the kinematic cuts of table 4.4 and the acceptance cuts of table 4.7. The subtrigger combination used for each data taking period are also given (cf. table 5.1).

As for the medium z selection, figure 4.25 shows the distribution of the number of Lee West tracks, and figure 4.26 shows this distribution in elasticity bins. Figure 4.27 shows the cumulative distribution for rejecting an event as a function of the cut on the number of Lee West tracks. The distribution does not depend clearly on the elasticity as opposed to medium values of z. At least 95 % of the events have more than five tracks.

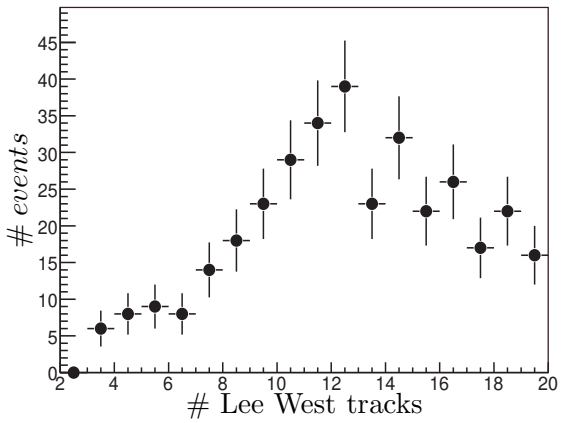

Figure 4.25: Distribution of the number of Lee West tracks. Data are from the **2003-2004** e^+ data taking period and selected with the **low** z selection given in table 4.8.

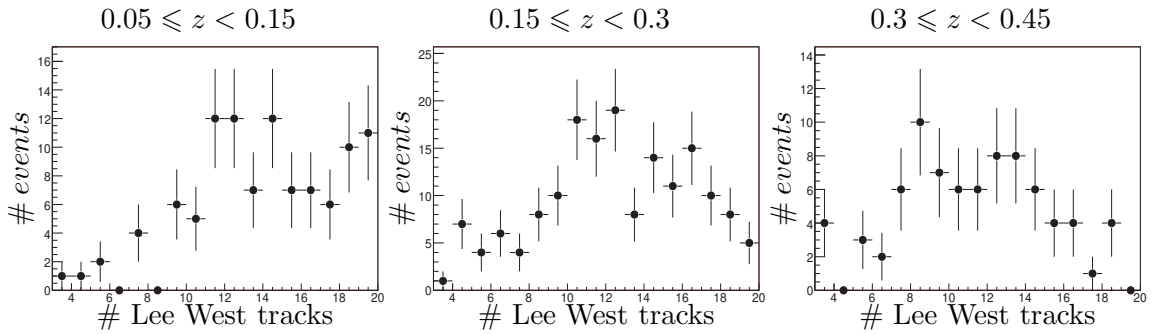

Figure 4.26: Distribution of the number of Lee West tracks in bins of z for the **low** z selection.

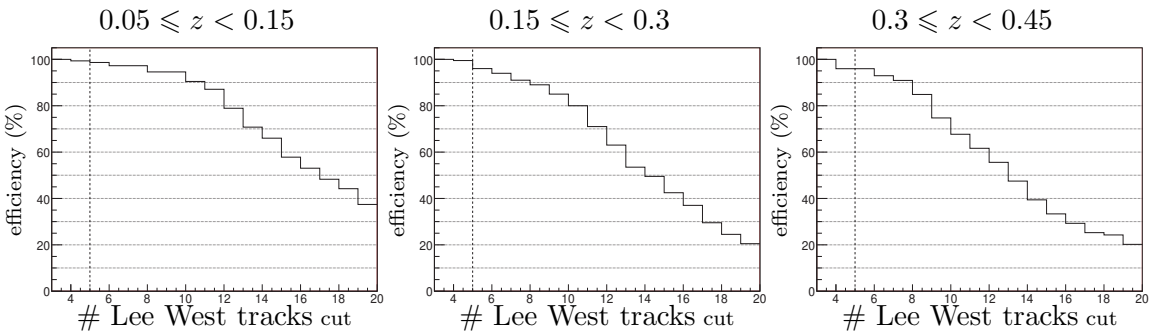

Figure 4.27: Cumulative distribution for rejecting an event as a function of the cut on the number of Lee West tracks in z bins for the **low** z selection. The vertical dotted lines show the amount of remaining event for a cut at five tracks.

4.3.3 Selection Efficiency

The resulting selection efficiency is shown in figure 4.28 as a function of the observables used for the measurement of the inelastic J/ψ meson cross section. The selection efficiency as a function of $P^2_{t,\psi}$ increases towards higher values like for the medium z selection. The selection efficiency as a function of $W_{\gamma\mathrm{p}}$ is nearly constant. And the selection efficiency as a function of z decreases towards higher elasticity.

The combination of the acceptance and the selection efficiency is shown in figure 4.29. The efficiency as a function of $P^2_{t,\psi}$ is rising as the acceptance and the selection efficiency, from 16 % to 37 %. For $W_{\gamma\mathrm{p}}$ the efficiency peaks around 150 GeV, and then drops due to the acceptance. For z the efficiency peaks around 0.2, and then drops towards higher elasticity. The efficiencies as function of $W_{\gamma\mathrm{p}}$ and z are comprised between 16 % and 27 %.

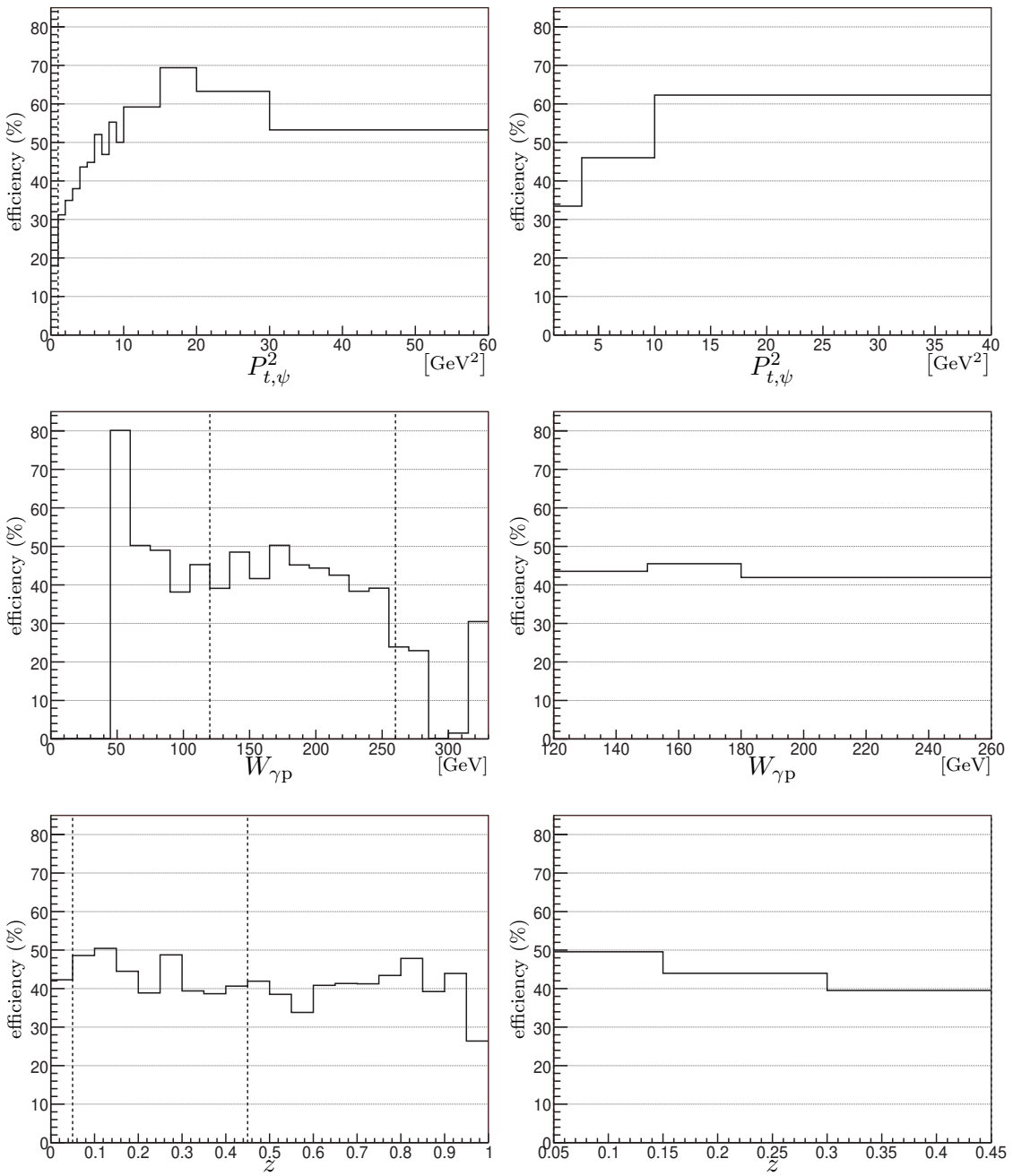

Figure 4.28: Selection efficiency as a function of $P^2_{t,\psi}$, $W_{\gamma p}$, and z. Events are generated with the two components simulation of the Monte Carlo program EPJPSI in direct photon-gluon fusion and resolved gluon-gluon fusion. The distributions on the right hand side are shown in the binning used for the measurement of the cross sections and on the left hand side in a finer binning. The vertical lines show the kinematic cuts defined in table 4.4.

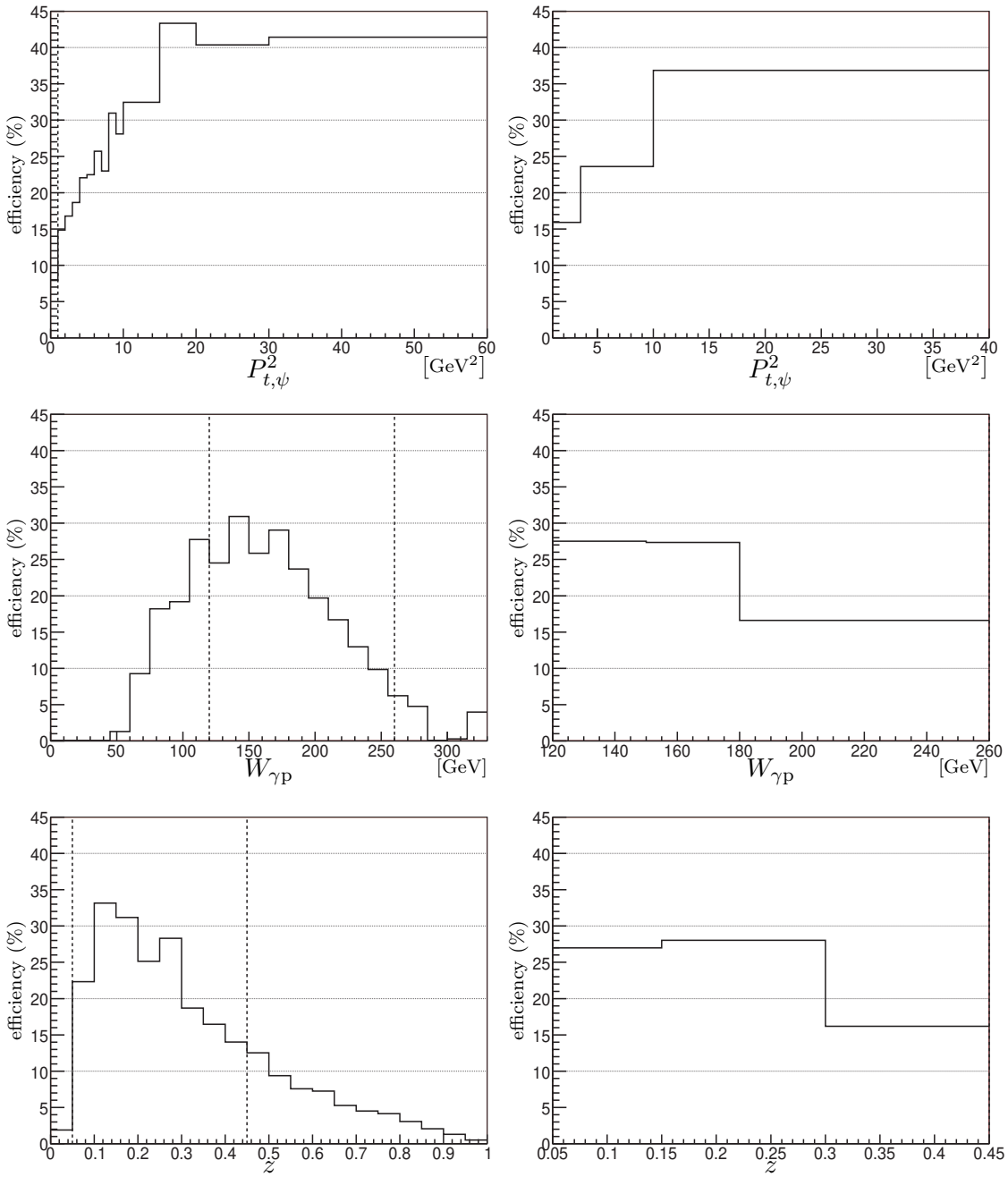

Figure 4.29: Acceptance and selection efficiency combined as a function of $P^2_{t,\psi}$, $W_{\gamma p}$, and z. See figure 4.28 for explanation.

Chapter 5

Data Taking Periods and Trigger Efficiency

In this chapter, the subtrigger yields for the 2003-2004 e^+ and 2004-2005 e^- data taking periods will be discussed. The choice of the subtrigger combination and the data taking periods analysed, which are summarised in table 5.1, will be defined. Then the efficiency of the trigger system will be studied. Finally the prescale correction will be discussed.

data taking periods	subtriggers	run range	integrated luminosity
2003-2004 e^+	s15 or s18	from 374 272 to 386 559	23 522 nb^{-1}
2004-2005 e^-	s19 or s23 or s18	from 415 620 to 437 154	60 132 nb^{-1}

Table 5.1: Subtrigger combination and the run ranges used for each data taking periods

This analysis uses subtriggers s15, s18, s19, and s23. This choice will be motivated in the following sections for each data taking periods. An overview of the number of entries per subtriggers can be found in page 128. The definition of theses subtriggers is described in section 5.4.1. Subtriggers s15, s19, and s23 are designed for an elasticity $z \lesssim 0.9$, while subtrigger s18 is designed for elastic and quasi-elastic J/ψ mesons. Subtriggers s19 and s23 are orthogonal and cover the same elasticity range as subtrigger s15. For HERA I, a neural network (L2NN) was used for subtrigger s15 at the trigger level 2 in order to reduce the rate, and thus control the prescale (cf. section 2.3.1). But for HERA II, the L2NN is no longer operational. Consequently a new approach is used to maintain the prescale close to one. The subtrigger s15 is split in two parts, subtrigger s19 covers the central region, while subtrigger s23 covers the endcap regions. When background conditions are unfavourable only subtrigger s23 is downscaled, since particles are mainly directed to the forward endcap detectors due to the boost. In this way subtrigger s19 is never affected and the overall prescale factor is kept close to one. The correction for the prescale is discussed in section 5.5.

Table 5.2 shows the prescale corrected integrated luminosity and the average prescale factor of these subtriggers for the run selection of this analysis (cf. section 4.1.1). The prescale factors are higher for the period with electrons on account of more background for electron beams. The prescale factor of subtrigger s18 is close to one due to its elastic selection which suppresses the background efficiently. As previously introduced, the prescale for subtrigger s15 is greater than one. On the other hand for subtrigger s19 the prescale is close to one. And of course a little bit higher for subtrigger s23, but lower than the one of subtrigger s15.

subtrigger	2003-2004 e^+		2004-2005 e^-	
	luminosity [nb^{-1}]	average prescale	luminosity [nb^{-1}]	average prescale
15	29 205.75	1.47	62 132.61	1.51
18	42 066.72	1.02	84 846.96	1.10
19	39 579.78	1.01	90 432.40	1.04
23	39 468.17	1.01	80 006.62	1.17

Table 5.2: Prescale corrected integrated luminosity for subtrigger s15, s18, s19 and s23. For subtriggers s19 and s23 during the data taking period 2003-2004 e^+, the run range is from run No. 369 461 to run No. 393 239, which corresponds to an integrated luminosity of 39 933.12 nb^{-1}. Subtrigger s23 was not defined before run No. 369 461.

5.1 The 2003-2004 e^+ Data Taking Period

For the 2003-2004 e^+ data taking period subtrigger s23 (endcap region) was defined since run No. 369 461 in January 2004, but it was falsely classified as monitor until February 2005 and thus rejected by the trigger level 4 [69]. This subtrigger was active at the level 1 trigger, and could take data when subtrigger s15 was strongly prescaled at the beginning of 2004. Since subtrigger s19 (central region) alone has a lower acceptance than subtrigger s15 and thus a lower yield, subtrigger s15 has a better statistics for this period. Therefore subtriggers s15 and s18 are used for this data taking period.

Figure 5.2 and figure 5.4 show for the medium z selection and the low z selection respectively the prescale and the number of J/ψ mesons per pb^{-1} for subtriggers s15, s18, s19 and s61 in luminosity bins for this data taking period. Subtrigger s61 is used as monitor trigger and shown as reference. The number of J/ψ is shown with and without prescale correction.

The data taking period is subdivided in run periods so as to have a luminosity of approximately 5 pb^{-1}. This value is a compromise between the granularity and the statistics. Smaller values are more susceptible to fluctuations. In practise runs are merged until the summed luminosity is equal or exceeds this value. For the last bin, the summed luminosity is free, but if the summed luminosity is too small the bin is merged with the previous bin in order to have enough statistics in the bin.

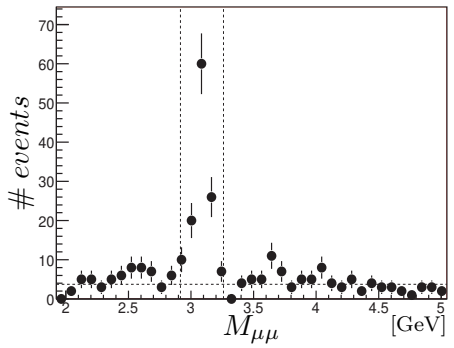

Figure 5.1: Example of invariant mass distribution in a luminosity bin showing the background subtraction.

For many bins, the statistics is very low and does not permit to fit the invariant mass distribution with a Gaussian correctly. Instead the non-resonant background is fitted with a constant, and then subtracted from the number of entries in the mass window $[\mu_{J/\psi} - 3\sigma_{J/\psi}, \mu_{J/\psi} + 3\sigma_{J/\psi}]$, where the position $\mu_{J/\psi}$ and the width $\sigma_{J/\psi}$ of the Gaussian are determined in the full data set and given in table 7.4. Figure 5.1 shows an example. The square root of the number of entries in the mass window is used as an estimator for the error. The determined values are not very accurate and thus have to be considered carefully.

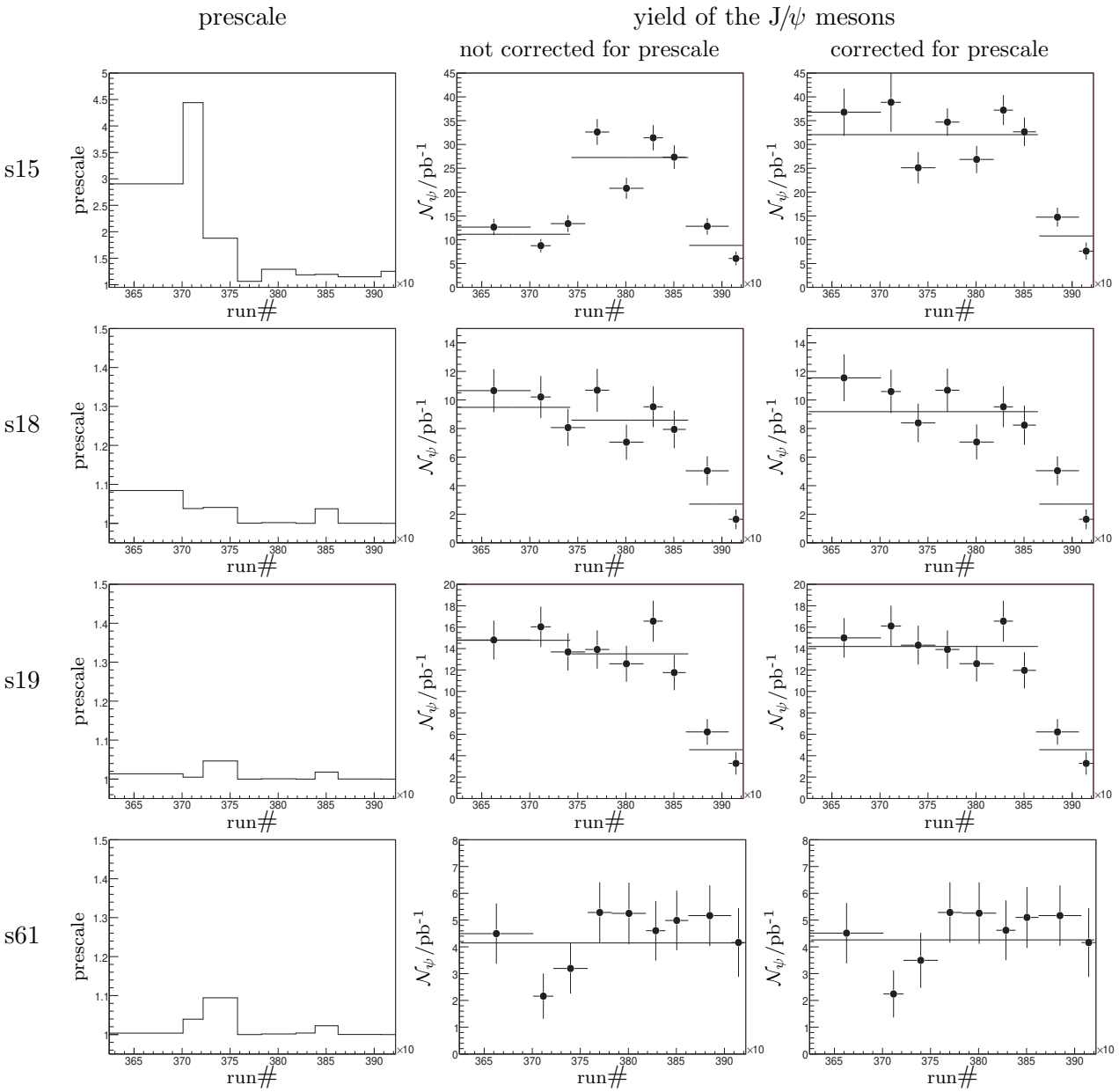

Figure 5.2: Prescale and number of J/ψ mesons per pb^{-1} for subtriggers s15, s18, s19 and s61 for the **2003-2004** e^+ data taking period and the **medium** z selection. Each data point corresponds to a run period with an integrated luminosity of approximately 5 pb^{-1} (see text for details). Subtrigger combinations are shown in figure 5.3.

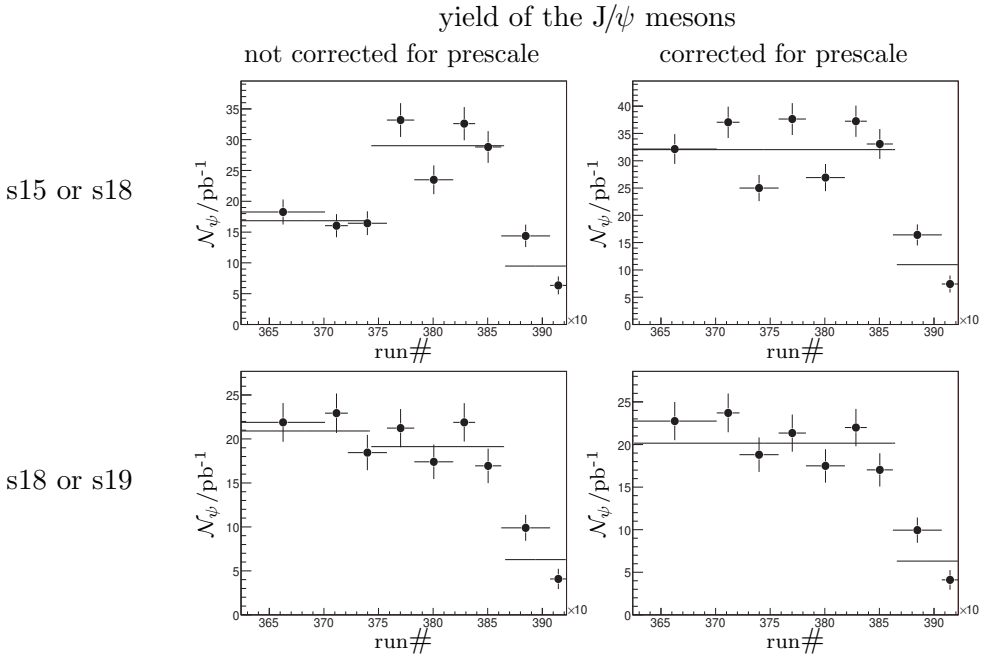

Figure 5.3: Number of J/ψ mesons per pb^{-1} for two subtrigger combinations during the **2003-2004** e$^+$ data taking period and for the **medium** z selection.

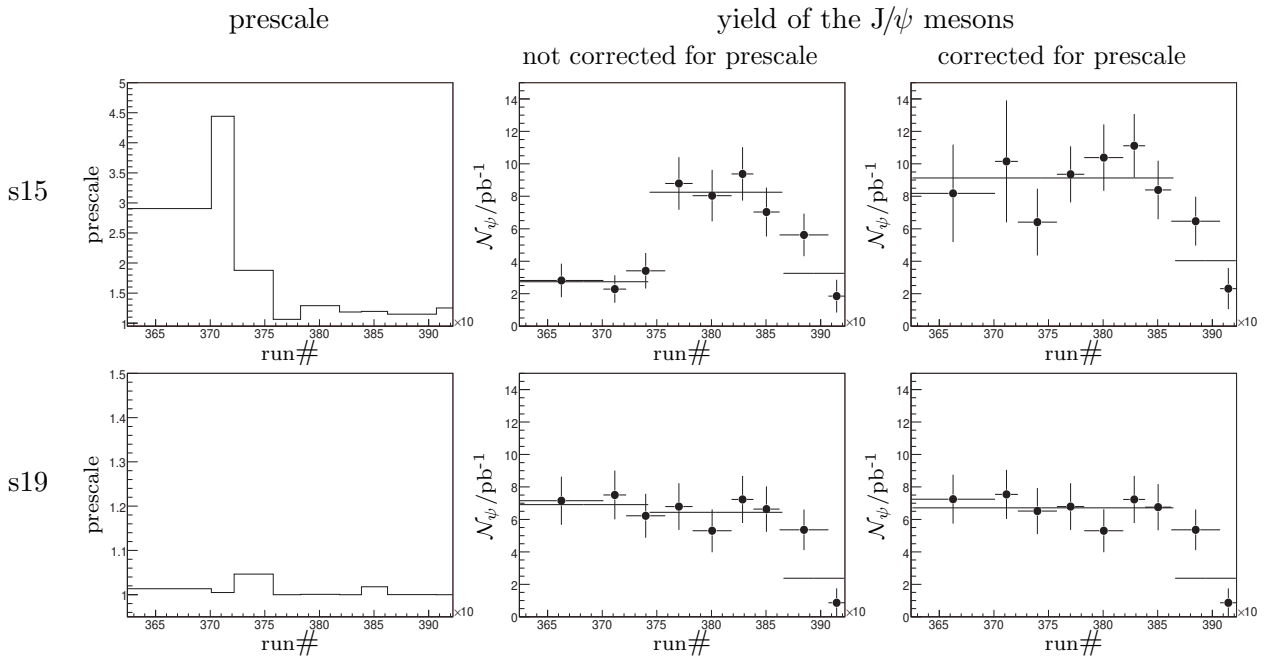

Figure 5.4: Prescale and number of J/ψ mesons per pb^{-1} for subtriggers s15 and s19 for the **2003-2004** e$^+$ data taking period and the **low** z selection. Each data point corresponds to a run period with an integrated luminosity of approximately 5 pb^{-1}. Other subtriggers are not shown since their yields are comparatively low for the low z selection. Subtrigger combinations are shown in figure 5.5.

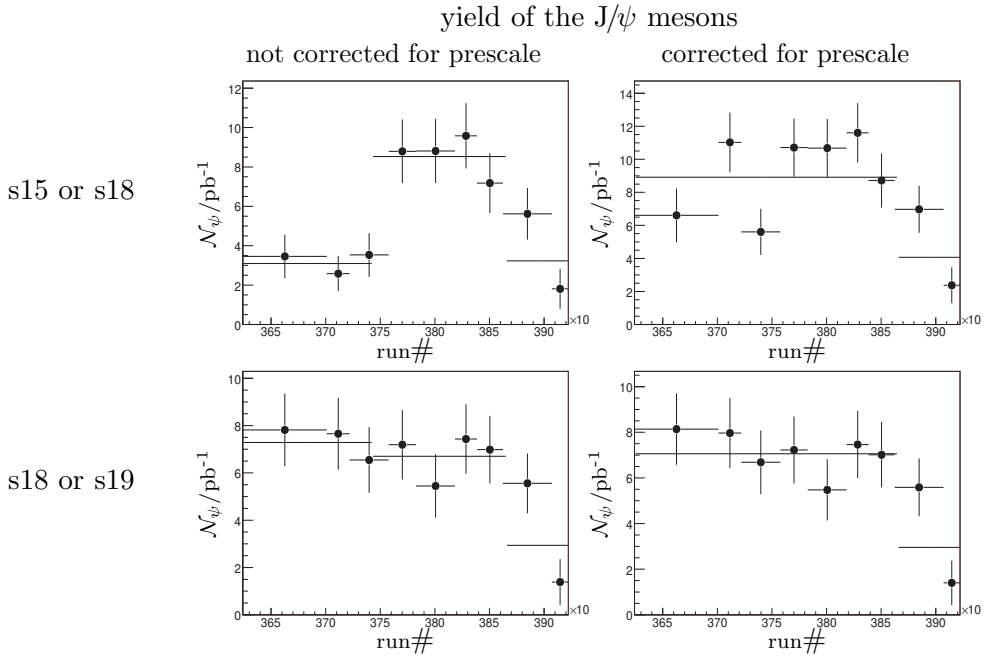

Figure 5.5: Number of J/ψ mesons per pb^{-1} for two subtrigger combinations during the **2003-2004** e^+ data taking period and for the **low** z selection.

Here the main points of the 2003-2004 e^+ data taking period will be outlined. Figure 5.2 shows the prescale and yield evolution in the periods that are discussed here. The definition of subtrigger s15 started without L2NN enabled and using DC$r\phi$ trigger elements. Then these three points have to be considered:

- From the beginning until run No. 374 272 (March 2004) the prescale for subtrigger s15 was quite high. Then the trigger condition CIP_mul < 11 was successfully added in order to suppress background with a track multiplicity greater than 190. The yield of subtrigger s15 is approximately multiplied by a factor two.
- From run No. 386 560 (June 2004) L2NN was enabled and trained for this period.
- From run No. 387 288 (June 2004) to run No. 454 705 (April 2006) only the subclass "2PRONG" of the level 4 "Heavy Flavour Closed" finder was in order (cf. section 2.3.4 and section 5.4.2). It explains the simultaneous drop of the number of J/ψ for subtriggers s15, s19, and s18 in the last bin. For subtrigger s15 the number of J/ψ drops approximately from 30 to 5 J/ψ mesons per pb^{-1}. The consequence and the reason of the malfunction of the level 4 "Heavy Flavour Closed" finder will be discussed in section 5.4.2.

These three points imply to split the data set in three periods:

run range	integrated luminosity		comment
from 356 093 to 374 271	12 624 nb^{-1}	29 %	not analysed due to high prescale
from 374 271 to 386 559	23 275 nb^{-1}	54 %	analysed
from 386 560 to 392 213	7 405 nb^{-1}	17 %	not analysed due to level 4 malfunction
total	43 305 nb^{-1}	↑ percent of the total integrated luminosity	

Due to the huge cross section of photoproduction at HERA in comparison to that of high Q^2, and also to the fact that non-ep events fire low Q^2 subtrigger at a significant rate, subtriggers dedicated to photoproduction channels can be downscaled with a prescale factor greater than two. When the prescale factor is different from one, the number of events has to be corrected as explained in section 5.5. A prescale factor greater than two has to be considered carefully. Firstly, if the events are not well distributed in the phase space, especially when the statistics is limited, fluctuations can bias the results. Secondly, for weighted distributions the variance in a particular bin corresponds to the sum of the weights squared [70]. It means that the larger the weights are the larger is the error. Therefore even if the inclusion of events with large prescales in an analysis will increase the statistics, these events will probably spoil the number of events resulting from the background subtraction.

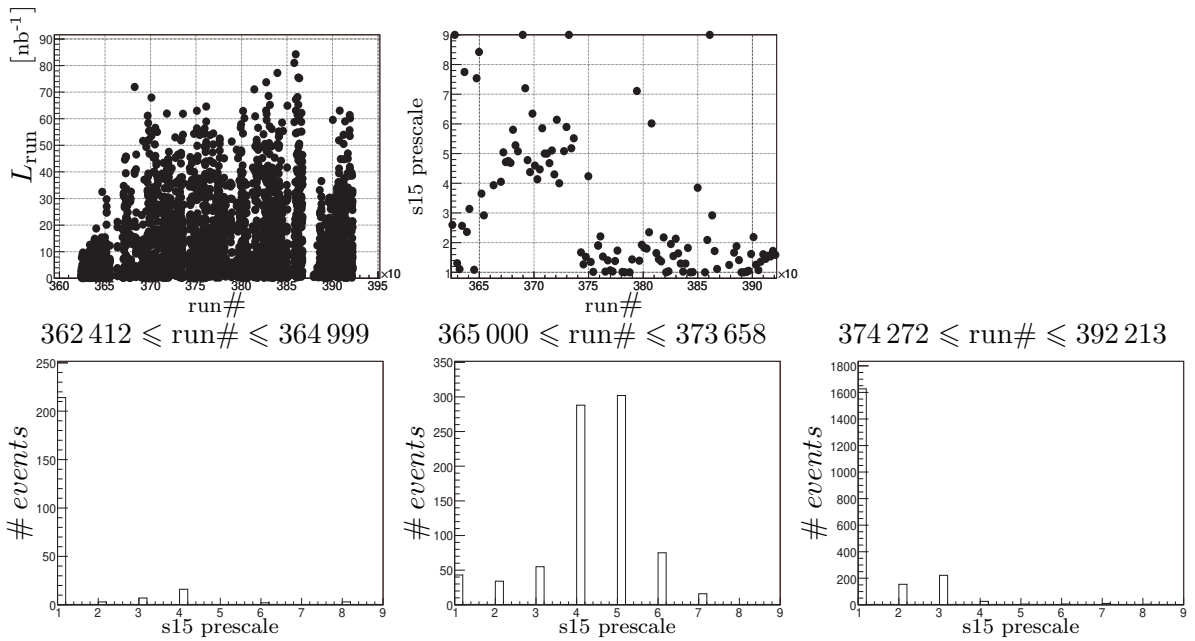

Figure 5.6: Integrated luminosity of the runs, prescale factor of subtrigger s15 as a function of the run period. The distribution of the prescale is shown in three run periods of the **2003-2004** e^+ data taking period, where the prescale has approximately the same distribution. Only the run selection is applied. The integrated luminosities for the three run periods are respectively, 867 nb^{-1}, 11 080 nb^{-1} and 23 048 nb^{-1}.

In particular the prescale of subtrigger s15 was quite high at the beginning of this data taking period. Figure 5.6 shows for subtrigger s15 the integrated luminosity of the runs, the prescale factor as a function of the run period, and the distribution of these prescale factors in three run periods. In order to enhance the message of the plot showing the prescale as a function of the run period, the prescale corresponds to the average of the prescales of the runs in the bin weighted by their integrated luminosities. These plots show at the beginning of this data taking period, a first period with a lower luminosity per run and prescales usually at one [1]; then a second period with mainly a prescale of four or five, and finally a third period with a prescale close to one. These high prescales at the beginning of the 2003-2004 e^+ data taking period motivate the first subdivision at the run No. 374 271.

[1] This point is not so evident here, but the event weights to correct for prescale are a little bit higher than the third period (cf. section 5.5).

The introduction of L2NN requires a separate study of the trigger efficiency. But the malfunction of the trigger level 4 appearing just after the introduction of L2NN and at the end of the 2003-2004 e^+ data taking period suppresses the hope to have sufficient statistics [2] to carry out such a study. Moreover the next luminosity period uses electrons instead of positrons and introduces the FTT trigger. Consequently the extrapolation to this period is impossible. Unfortunately, the data since the L2NN activation seems [3] irreparably lost. In conclusion for the 2003-2004 e^+ data taking period only the second period will be analysed, which corresponds to $23\,pb^{-1}$ of integrated luminosity. An amount of approximately $20\,pb^{-1}$ of integrated luminosity is lost.

5.2 The 2004-2005 e^- Data Taking Period

For the 2004-2005 e^- data taking period subtriggers s15, s19 (barrel) $\oplus$ s23 (end-cap) and s18 were all available.

The DC$r\phi$ trigger elements were replaced by the FTT trigger after 2 weeks (run No. 401 617 in January 2005). But the FTT was not yet available for L2NN, thus subtrigger s15 was not really operational until run No. 431 583 (October 2005).

Figure 5.8 and figure 5.9 show for the low z selection and the medium z selection respectively, the prescale and the number of J/ψ mesons per pb^{-1} for these subtriggers and subtrigger s61 in luminosity bins for this data taking period [4]. The "Heavy Flavour Closed" finder was affected by the malfunction during the whole data taking period. Therefore the yield of J/ψ mesons per luminosity is affected by the same inefficiency as for the end of the 2003-2004 e^+ data taking period.

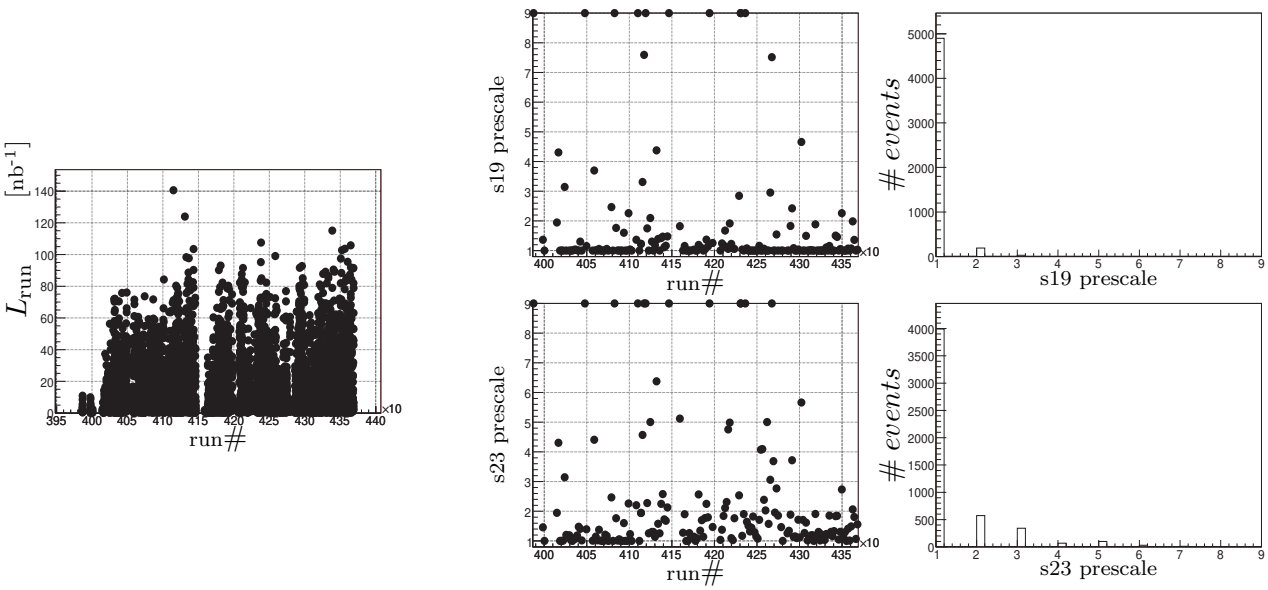

Figure 5.7: Integrated luminosity of the runs, prescale factor of subtriggers s19 and s23 as a function of the run period, and the distributions of these prescales for the **2004-2005** e^- data taking period.

[2] There is of the order of 50 J/ψ mesons saved during this period. This number is very low for the corresponding luminosity and the cross section of this channel. Moreover the number of saved J/ψ is of the same order than the downscaling (60 for the soft physics class).

[3] Of course it is possible to estimate the global inefficiency and thus the cross section. But the very limited statistics will spoil the result with statistics fluctuations and huge errors in comparison with the Hera I result.

[4] Cf. section 5.1 for remarks on these plots.

Since subtrigger s23 was usable for this data taking period [5], the advantage over the prescale to split the subtrigger s15 in two triggers, an endcap and a barrel subtriggers, can be verified. The prescale plots show that subtrigger s15 is clearly more sensitive to background conditions than the trigger s19 $\oplus$ s23, and subtrigger s23 is a little bit more downscaled than subtrigger s19. The prescale for subtriggers s19 and s23 are close to one, whereas the prescale for subtrigger s15 is around 1.5. Subtriggers s19 $\oplus$ s23 will be used for this period.

In order to compare with the previous data taking period, figure 5.7 shows the integrated luminosity of the runs, the prescale factor of subtriggers s19 $\oplus$ s23as a function of the run period, and the distribution of theses prescale factors. For the majority of the runs the prescale is close to one, only subtrigger s23 has some runs with a prescale of 2 or 3.

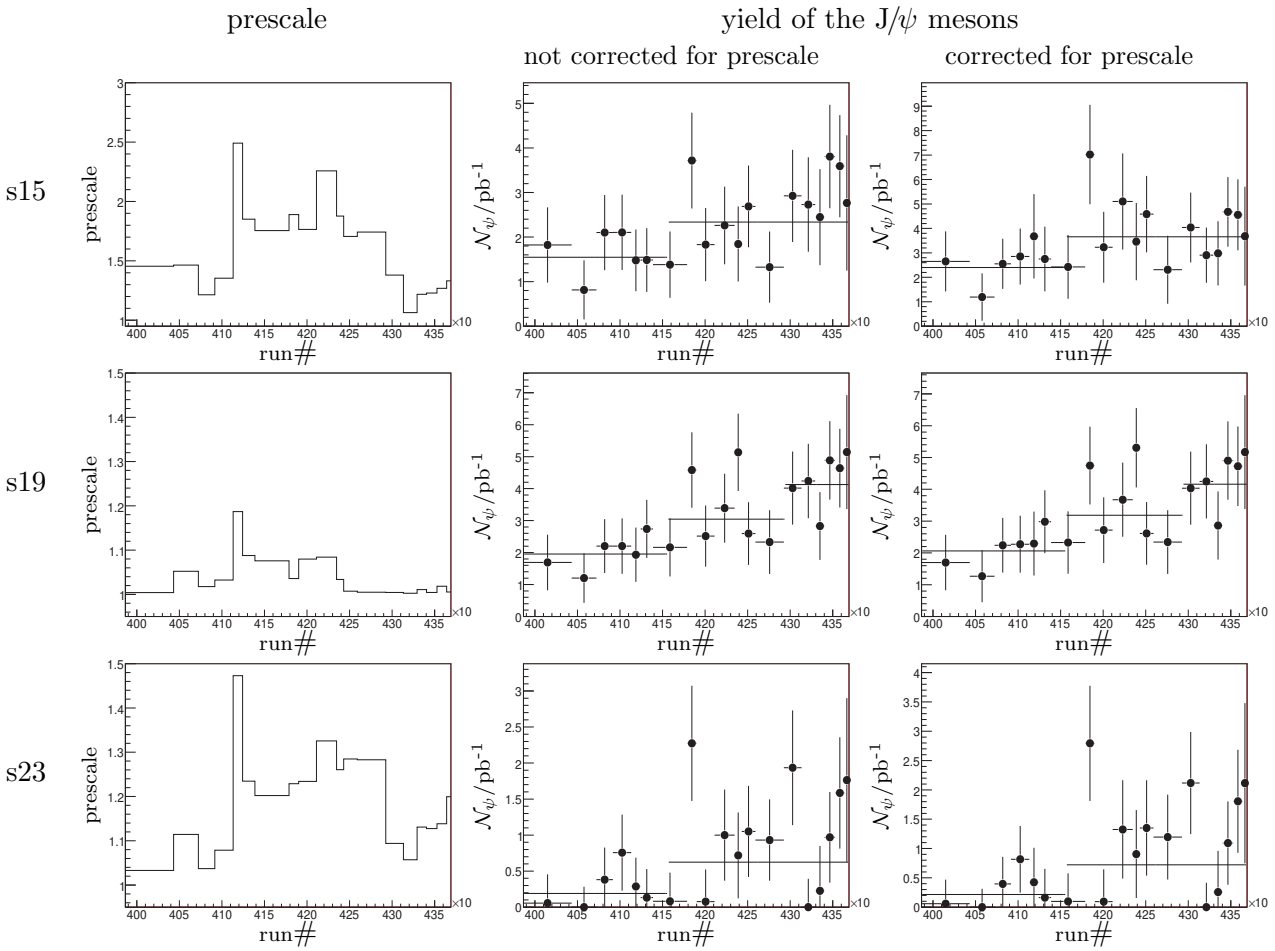

Figure 5.8: Prescale and number of J/ψ mesons per pb^{-1} for subtriggers s15, s19, and s23 for the **2004-2005** e$^-$ data taking period and the **low** z selection. Each data point corresponds to a run period with an integrated luminosity of approximately 5 pb^{-1}. For the first bin subtrigger s23 was not yet available. Subtrigger combinations are shown in figure 5.11.

[5] From February 2005, see at the beginning of section 5.1

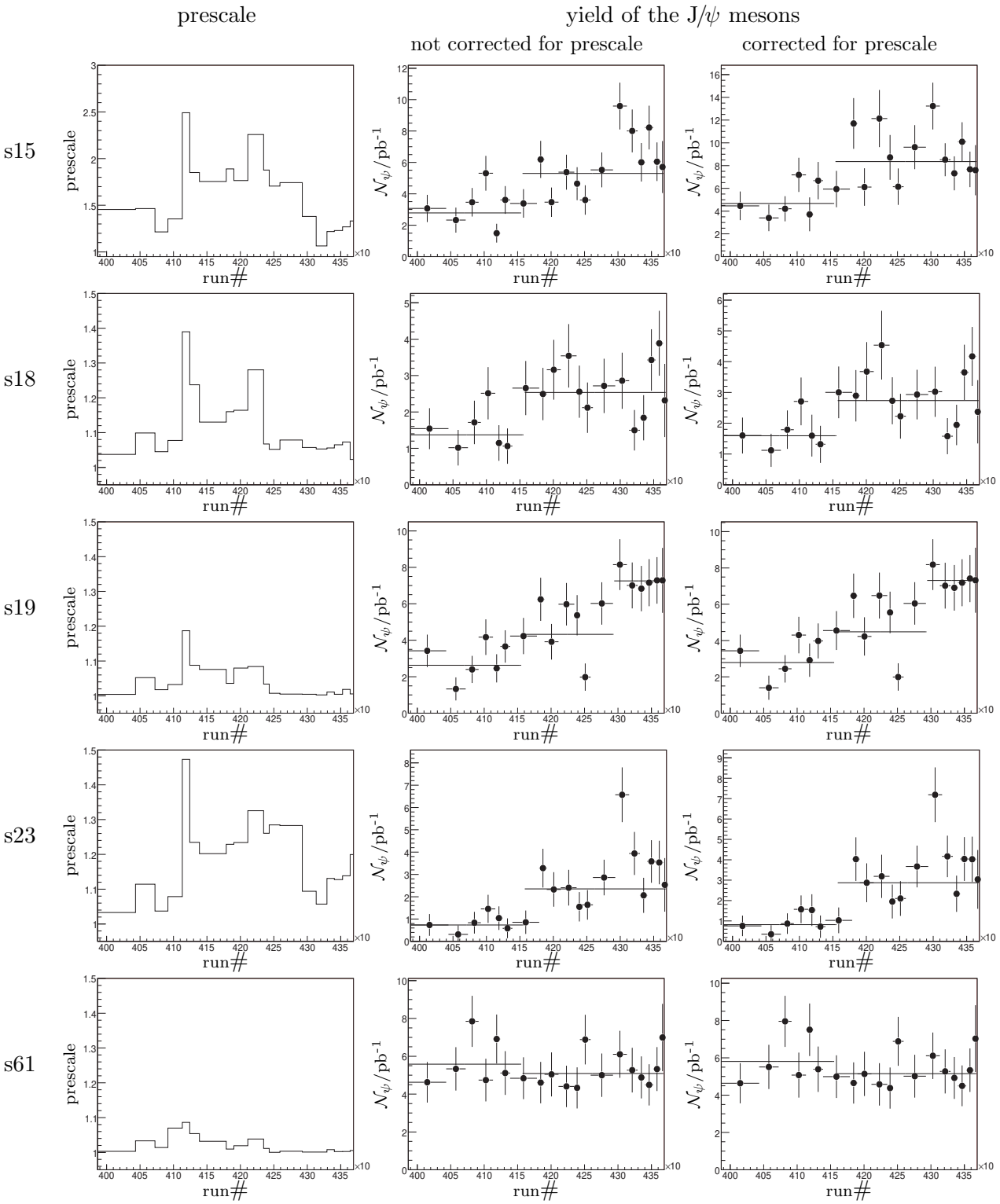

Figure 5.9: Prescale and number of J/ψ mesons per pb^{-1} for subtriggers s15, s18, s19, s23 and s61 for the **2004-2005** e$^-$ data taking period and the **medium** z selection. Each data point corresponds to a run period with an integrated luminosity of approximately 5 pb^{-1}. The third step for subtrigger s19 corresponds to run No. 429 402, see text for explanation. Subtrigger combinations are shown in figure 5.10.

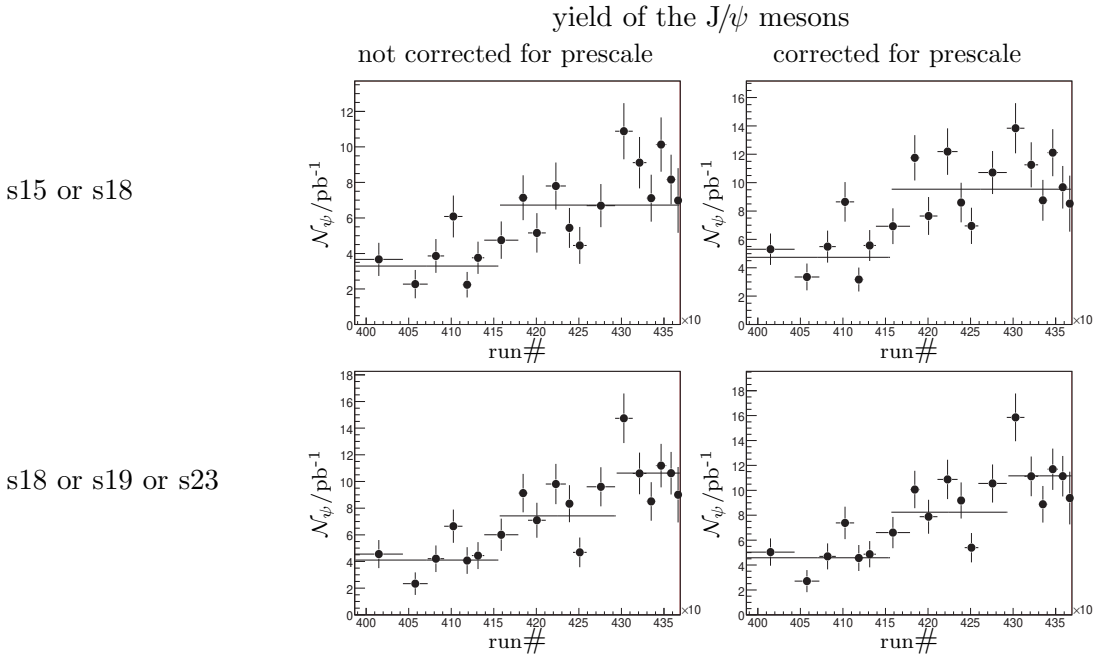

Figure 5.10: Number of J/ψ mesons per pb^{-1} for two subtrigger combinations during the **2004-2005** e$^-$ data taking period and for the **medium** z selection.

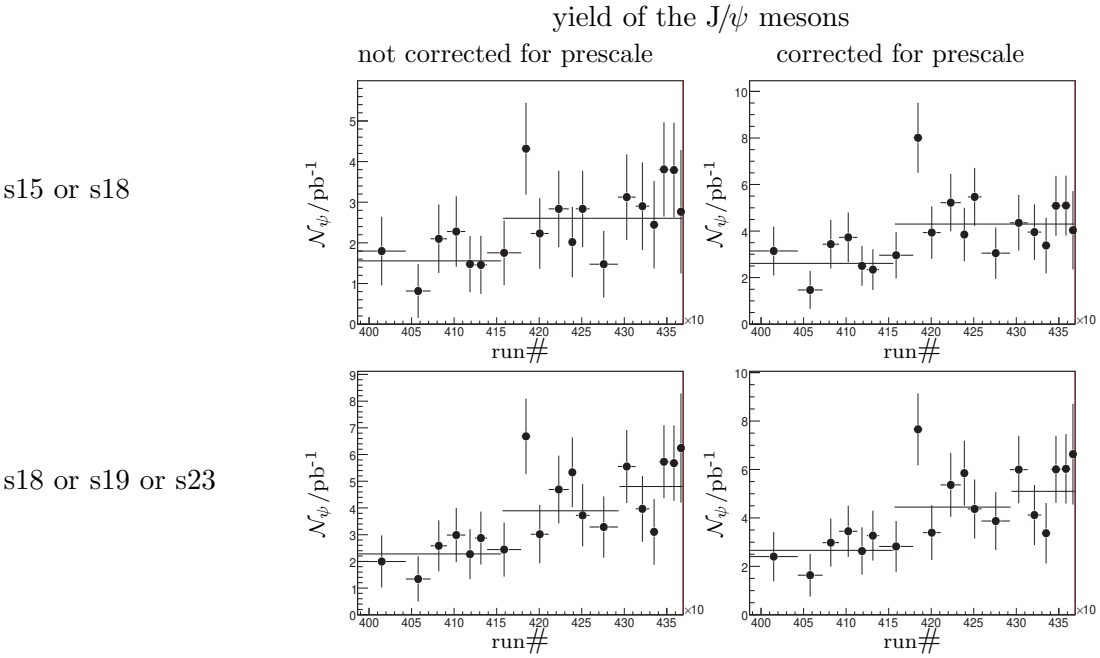

Figure 5.11: Number of J/ψ mesons per pb^{-1} for two subtrigger combinations during the **2004-2005** e$^-$ data taking period and for the **low** z selection.

Here the main points of the 2004-2005 e$^-$ data taking period will be outlined. Figure 5.9 shows the prescale and yield evolution in the periods that are discussed here.

- From run No. 401 617 (January 2005) the FTT trigger replaced the DC$r\phi$ trigger elements.
- Until run No. 415 620 (May 2005) a low voltage power supply of the iron muon trigger was faulty, causing a large inefficiency in a polar and azimuthal region of the instrumented iron detector (cf. figure 5.24 and figure 5.25). After the replacement of the power supply, the efficiency reached the expected value. This is clearly visible with an elastic J/ψ meson selection. Figure 5.12 shows the number of elastic J/ψ meson per pb^{-1} for subtriggers s18 and s61 for each data taking period. At the beginning of the 2004-2005 e$^-$ data taking period the yield of elastic J/ψ meson for subtrigger s18 is approximately half of the preceding data taking period. Then it reaches the same level and still continues to increase with the efforts to improve the efficiency of the instrumented iron detector by increasing the high voltage of the streamer tubes.
- From run No. 429 402 (September 2005), the multiplicity cut for tracks of P_t greater than 400 MeV was opened for subtrigger s19 (barrel), only one track instead of two was required. The previous requirement was responsible for an inefficiency for z greater than approximately 0.8 (cf. figure 5.18). It improves a little bit the yield.
- From run No. 431 583 (October 2005), the neural network for subtrigger s15 was adapted to the FTT and retrained.

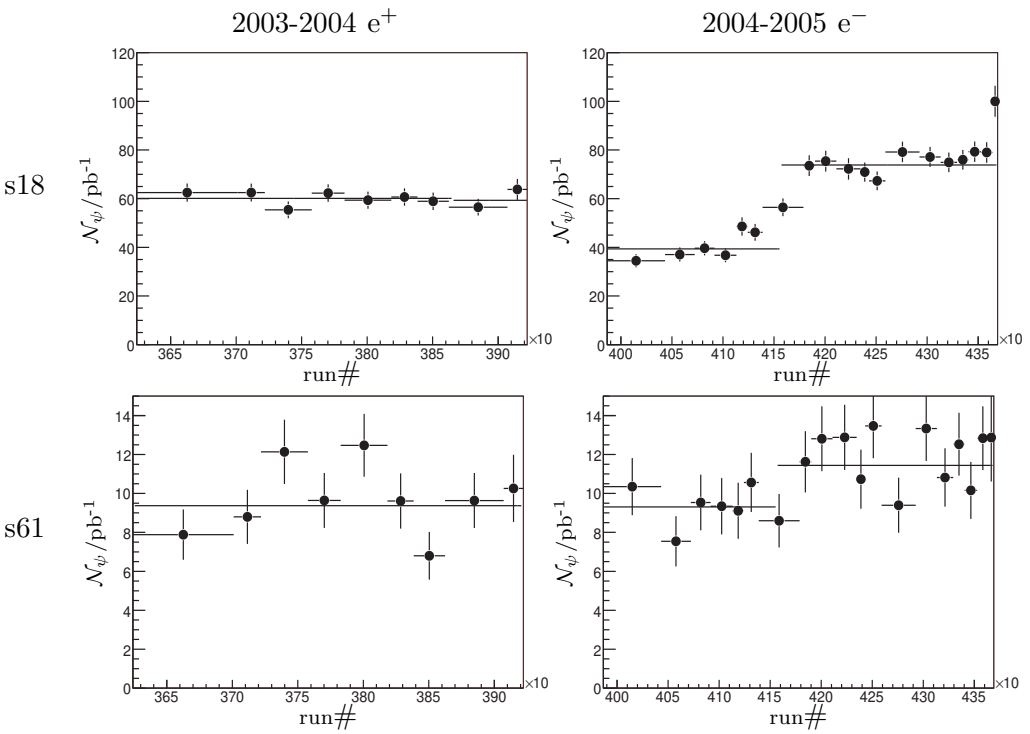

Figure 5.12: Number of elastic J/ψ meson per pb^{-1} for triggers s18, and s61 for each data taking periods.

The statistic for the 2004-2005 e^- data taking period suffers from the same inefficiency as the end of the 2003-2004 e^+ data taking period. But for the first half of this data taking period, it suffers from an additional sizeable inefficiency due to the malfunction of the iron muon trigger. The consequence is to split the data set in two periods:

run range	integrated luminosity		comment
from 396 667 to 415 620	32 747 nb^{-1}	35 %	not analysed due to muon trigger malfunction
from 415 620 to 436 893	59 671 nb^{-1}	65 %	analysed
total	92 418 nb^{-1}	↑	percent of the total integrated luminosity

These two effects together suppress definitely the hope to recover the data of the first half of the data taking period. Thus the first 32.7 pb^{-1} of integrated luminosity is lost. However the second half of the data taking period was only affected by the malfunction of the level 4 finder. Since the large amount of integrated luminosity of 60 pb^{-1} counterbalances a little bit this inefficiency, it will be possible to analyse this data taking period.

5.3 Subtrigger Yield

Figure 5.13 shows the number of entries per subtrigger for the data sample of this analysis. In order to have both photoproduction and DIS events, the photoproduction cut is omitted. The most active subtriggers are the previously introduced subtriggers s15, s18 and s19 $\oplus$ s23. SpaCal subtriggers s0, s3, s9 and especially s61 are also quite active for DIS events. This is true for the 2003-2004 e^+ data taking period, on the other hand the 2004-2005 e^- data taking period has to be interpreted as a higher luminosity period with a faulty level 4 finder. It explains why subtrigger s61 is so active by comparison to s15, s18, and s19 $\oplus$ s23.

Here some interesting properties of the subtriggers used for this analysis will be discussed. First the orthogonality of the subtrigger s19 $\oplus$ s23 will be proved, then the subtriggers choice will be confirmed, and finally the correlation between the elasticity z and the subtriggers will be shown. In the following, the background is not subtracted.

The following table demonstrates the orthogonality of subtrigger s19 and s23 during the 2004-2005 e^- data taking period. It gives the proportion of events matching the condition and the sum for each columns and line.

23 \ 19	off	on	
off	18.4 %	50.2 %	68.7 %
on	27.2 %	4.1 %	31.3 %
	45.7 %	54.3 %	

The overlap between s19 and s23 is of the order of a few percent. It is not surprising since the end-cap and barrel part of the instrumented iron detector have some overlap at their junctions.

The following table gives some impressions on the yield of subtrigger s15 versus subtrigger s19 $\oplus$ s23 for the 2003-2004 e^+ and 2004-2005 e^- data taking periods. These tables have the same structure as the previous one.

2003-2004 e^+

s19 \ s15	off	on	
off	7.4 %	49.9 %	57.3 %
on	7.2 %	35.5 %	42.7 %
	14.5 %	85.5 %	

2004-2005 e^-

s19 or s23 \ s15	off	on	
off	12.7 %	5.8 %	18.4 %
on	30.6 %	50.9 %	81.6 %
	43.3 %	56.7 %	

The comparison of the columns or rows of both tables, confirms that subtrigger s19 $\oplus$ s23 is more efficient than s15 for the 2004-2005 e^- data taking period, and subtrigger s15 is the most efficient for the 2003-2004 e^+ data taking period.

Figure 5.14 and figure 5.15 show the active subtriggers in elasticity bins for the 2004-2005 e^- data taking period and both analysis regions[6]. The rate of inelastic and elastic subtriggers are conter-balanced with the elasticity z. Low z events fire a lot of subtriggers above subtrigger s60 in addition to those fired by medium z events.

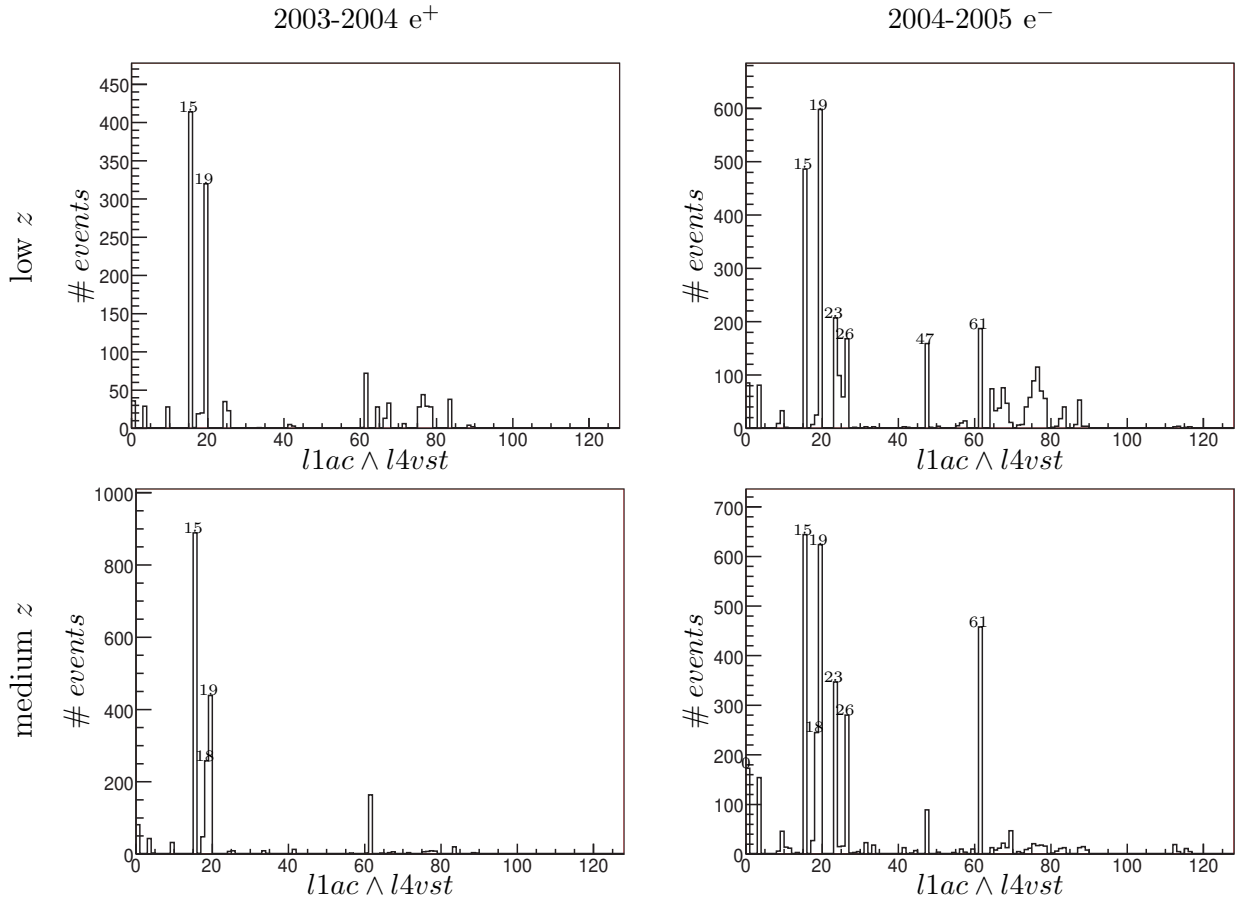

Figure 5.13: Number of entries per subtriggers. The data selection is given in table 4.6 for the **medium** z selection and in table 4.8 for the **low** z selection, but the cut on Q^2 (photoproduction) is omitted.

[6]The photoproduction cut was applied for these plots, contrary to the previous plots

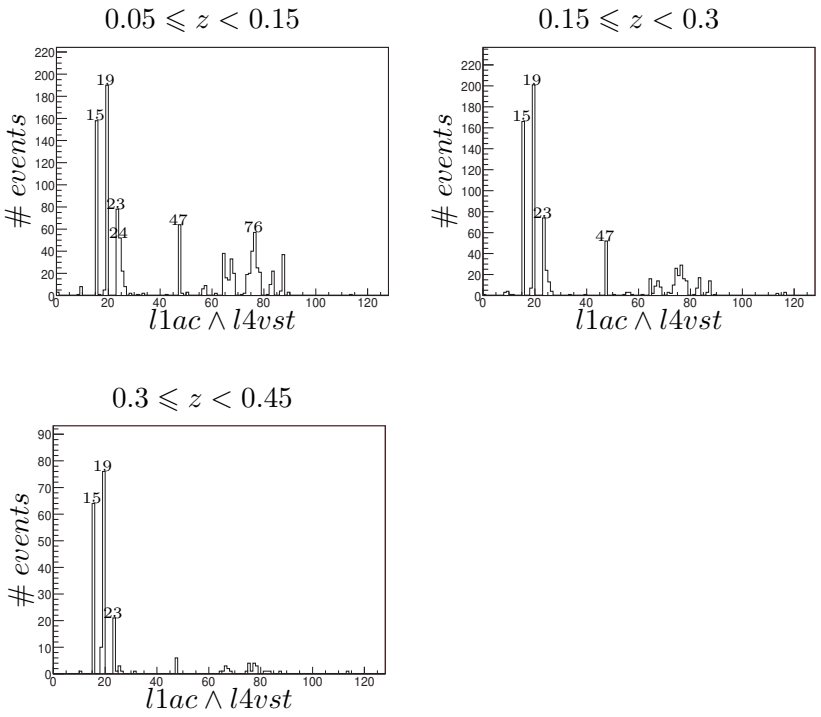

Figure 5.14: Number of entries per subtriggers in bin of z for the **low** z selection and the **2004-2005** e^- period.

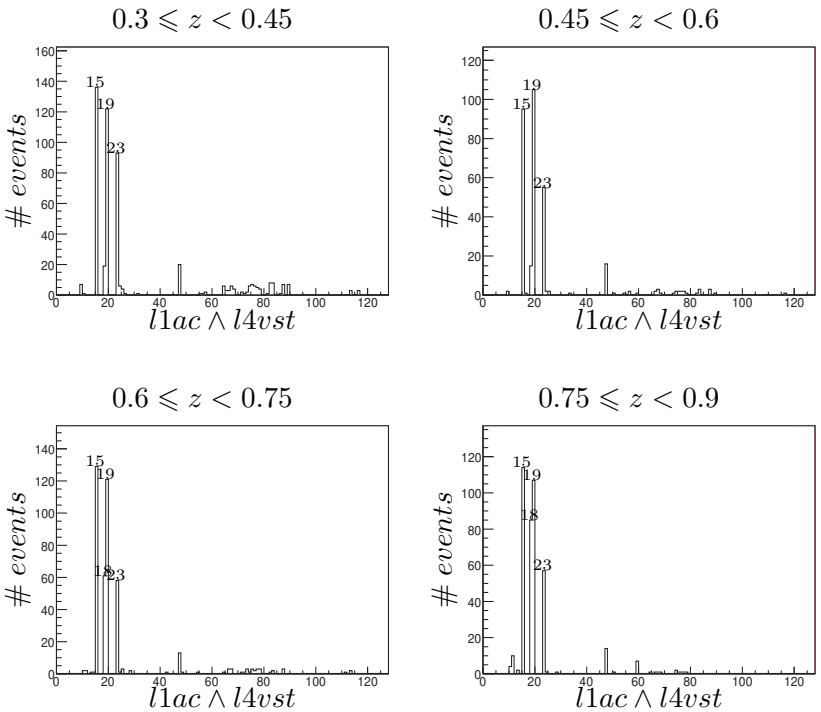

Figure 5.15: Number of entries per subtriggers in bin of z for the **medium** z selection and the **2004-2005** e^- period.

5.4 Trigger Efficiency

In this section the trigger efficiencies for the subtriggers used in this analysis will be discussed. Since the trigger system at H1 has four levels, the overall trigger efficiency corresponds to the product of the four trigger level efficiencies. Consequently each trigger level will be investigated separately. The subtriggers s15, s18, and s19 $\oplus$ s23 use only the first level for the data taking periods of this analysis [7]. Thus the second and the third level is transparent. At the fourth level, the "Heavy Flavour Closed" finder 16 is the relevant finder to save the events for this analysis. This finder is expected to have an efficiency close to 100 %. It will be verified for the 2003-2004 e^+ data taking period, but not for the 2004-2005 e^- data period, since it was faulty during this time. The efficiency of the first level will be discussed and then the efficiency of the fourth level.

5.4.1 Trigger Level One

The efficiency of a subtrigger depends on the efficiencies of the trigger elements of which it is composed. A subtrigger can be divided in two parts, the first to trigger the event, the second to veto the event under certain background conditions. The second part is not expected to suppress a sizeable amount of events, contrary to the first part, which is often inefficient. Consequently the first part is the most important to be studied.

trigger element	subtriggers				
	s15	s18	s19	s23	s61
CIP_mul < 11	×				
CIP_sig > 1			×	×	
Mu_Bar	×	×	×		
Mu_BOEC $\vee$ Mu_2_BIoOEC $\vee$ Mu_FOEC	×	×		×	
DCRPh_THig	×	×			×
FTT_mul_Tc > 1 ($P_t > 400\,\mathrm{MeV}$)	×		× [1]		
FTT_mul_Tc > 2			× [2]	×	
FTT_mul_Td > 0 ($P_t > 900\,\mathrm{MeV}$)	×	×	×		×

Table 5.3: Most important trigger elements. A cross indicates in which subtriggers they are used in. This table is only exhaustive for the **2003-2004** e^+ data taking period for subtrigger s15, and for the **2004-2005** e^- data taking period for subtriggers s19 $\oplus$ s23.

The complete subtrigger definitions are given in appendix A. Table 5.3 shows only the most important trigger elements and which subtriggers they are used in. The trigger elements are described in section 2.3.5.

These subtriggers (s15, s18, s19, and s23) are based on the CIP trigger system, a muon trigger, the DC$r\phi$ and then the FTT trigger. The information provided by this set of triggers includes the track multiplicity, the significance of the z vertex, the number of tracks in transverse momentum bins, and trigger signals from the instrumented iron detector.

[7] The level 2 neural network of the subtrigger s15 was not enabled during the data taking period used.

[1] After 22th September 2005 run No. 429 402

[2] Before 22th September 2005

The strategy to trigger inelastic or elastic J/ψ meson events decaying to muons is to require an iron track in the instrumented iron detector (Mu_Bar, Mu_FOEC, Mu_2_BIoOEC, Mu_BOEC), and at least a track with transverse momentum greater than 800 MeV (DCRPh_THig) in the CJC. Moreover a primary vertex around the nominal interaction point (CIP_sig) and some veto conditions as well as multiplicity conditions are required in order to suppress non-ep background. The new FTT trigger permits more possibilities to trigger tracks than the DC$r\phi$ trigger which was used previously. In particular the resolution and the granularity for the transverse momentum was improved.

Since subtrigger s23 is dedicated for the endcap regions of the instrumented iron detector, the transverse momentum threshold is lower than for subtrigger s19, 400 MeV (FTT_mul_Tc) instead of 900 MeV (FTT_mul_Td). Subtrigger s23 requires at least two tracks greater than 400 MeV, while subtrigger s19 requires at least one track greater than 900 MeV and at least another one greater than 400 MeV. In comparison, subtrigger s15 requires at least one track greater than 800 MeV in 2003-2004.

To be logged permanently an event has to be necessarily triggered by at least one subtrigger; mainly by subtriggers that contains the triggers elements of table 5.3. In order to have no bias for the determination of the efficiency, a subtrigger, which does not contain the studied trigger element has to be used, the so called *monitor trigger*. Then the sample used for the efficiency determination is independent of the status of the trigger element investigated. To choose the monitor trigger, the trigger yield distribution (cf. figure 5.13) gives an impression of the available statistics for a particular subtrigger, and table 5.3 permits to determine which subtrigger can be used. The available statistics is an important limitation to determine the efficiency with good accuracy, because these trigger elements are the most efficient to save the events of this analysis. The independence requirement implies in practice to use subtriggers based on SpaCal trigger elements, which are designed to trigger DIS events. This as two consequences, the first, is a lower statistics, which is correlated with the cross section for DIS events, the second is a different topology for the events, and thus different distributions for the variables. Subtrigger s61 is a possibility. Its statistics is approximately half of the statistics of this analysis. But for the trigger elements DCRPh_THig and FTT_mul_Td, only the subtrigger combination s0 $\vee$ s3 $\vee$ s9 can be used. Its statistics is approximately lower by a factor four. Due to the new optics for HERA II, the acceptance of these DIS subtriggers is reduced by the new acceptance of the SpaCal. Moreover the inner cells of the SpaCal trigger at right in the horizontal plane are excluded due to the higher rate of synchrotron radiation. For similar reason, the electron beam is shifted towards the ring centre, and thus still reduce the acceptance of the SpaCal. Since the cross section of DIS events is proportional to Q^{-4}, the statistics to cross check the trigger efficiency is lower for HERA II than for HERA I. For the 2003-2004 e^+ data taking period, the integrated luminosity does not permit to counter-balance the reduced yield. The accuracy of the cross check is thus worst.

The formula to compute the trigger element efficiency is:

$$\text{trigger element efficiency} \widehat{=} \frac{\text{selection cuts} \wedge \text{monitor trigger fired} \wedge \text{trigger element fired}}{\text{selection cuts} \wedge \text{monitor trigger fired}}$$

The selection cuts corresponds to those given in table 4.6 for the medium z selection and in table 4.8 for the low z selection respectively. When a DIS trigger monitor is used, the photoproduction cut is of course not imposed on the data selection.

5.4.1.1 Trigger Element Efficiency

In the following, the efficiency of the trigger elements shown in table 5.3 will be studied.

DC$r\phi$ and FTT trigger efficiency

The efficiency of the track trigger elements DC$r\phi$ and FTT mainly depends on the number of tracks in the event, which is approximated by the number of Lee West tracks N_{LW}.

The efficiency for the medium z selection will be presented firstly. Figure 5.16 shows the efficiency of the trigger element DCRPh_THig as a function of the transverse momentum squared of the J/ψ meson $P^2_{t,\psi}$, the photon-proton centre-of-mass energy $W_{\gamma p}$, the elasticity z and N_{LW}. These efficiencies are relatively good, of the order of 95 %. Data and simulation are compatible within the errors. The precision of the data is limited by the statistics of the trigger monitor combination s0 $\vee$ s3 $\vee$ s9. Only the 2003-2004 e^+ data taking periods is shown since the DC$r\phi$ trigger is replaced by the FTT for 2005.

Figure 5.18 shows the efficiency of the trigger element conditions FTT_mul_Tc > 1, FTT_mul_Tc > 2, and FTT_mul_Td > 0, as a function of $P^2_{t,\psi}$, $W_{\gamma p}$, z, and N_{LW}. Since the simulation of the FTT was not available during this thesis, only data will be shown. These efficiencies are also relatively good, of the order of 95 %, except for FTT_mul_Tc > 2, which shows an inefficiency for $z \gtrsim 0.75$, and decreasing with respect to the elasticity z. Since the elasticity is correlated with a low number of tracks, the same effect is observed in bins of N_{LW}. The efficiency in bins of $W_{\gamma p}$ shows an inefficiency at low $W_{\gamma p}$, where the muon tracks decayed from the J/ψ are predominately in the forward direction and thus with a low transverse momentum. The cut on FTT_mul_Tc was opened for subtrigger s19, the one dedicated for the barrel region of the instrumented iron detector, to one track instead of two at the end of September 2005 (run No. 429 402). What solved the inefficiency.

The efficiency for the low z selection are shown in figure 5.17 for the trigger element DCRPh_THig and in figure 5.19 for the FTT trigger elements respectively. These efficiencies are also relatively good, and any inefficiency is observed like for the medium z selection.

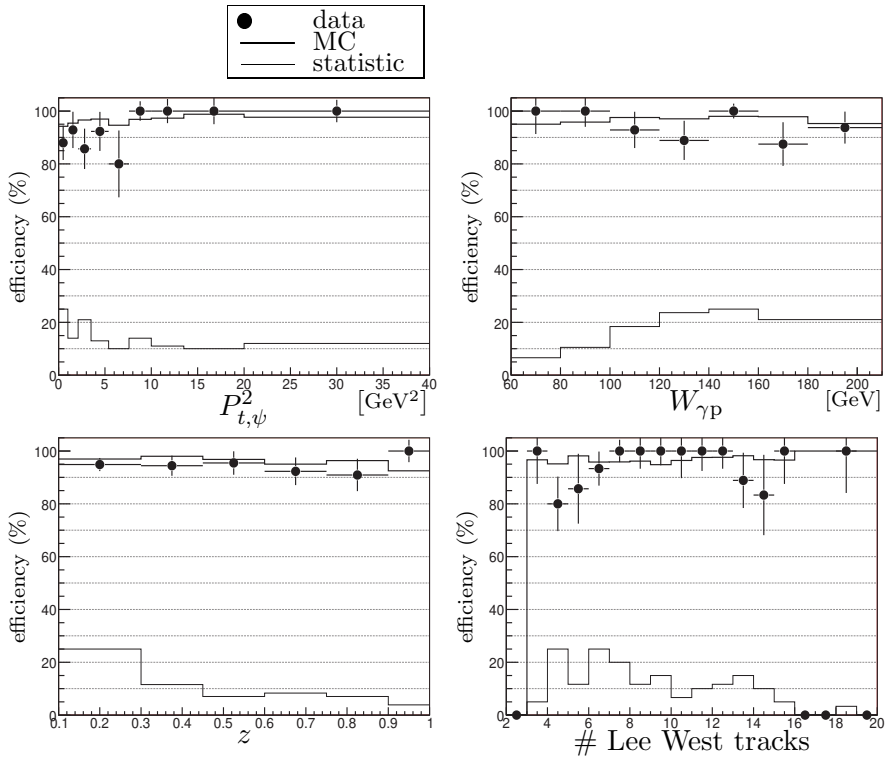

Figure 5.16: DCRPh_THig trigger efficiency as a function of $P^2_{t,\psi}$, $W_{\gamma p}$, z, and N_{LW} for the **2003-2004** e^+ period and the **medium** z selection. Trigger monitor is the subtrigger combination s0 $\vee$ s3 $\vee$ s9.

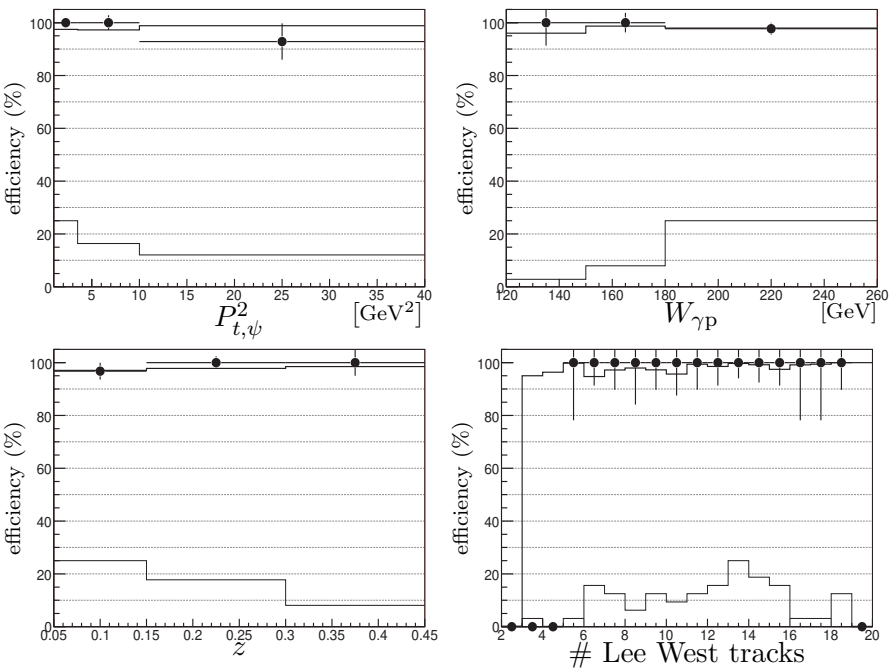

Figure 5.17: DCRPh_THig trigger efficiency as a function of $P^2_{t,\psi}$, $W_{\gamma p}$, z, and N_{LW} for the **2003-2004** e^+ period and the **low** z selection. Trigger monitor is the subtrigger combination s0 $\vee$ s3 $\vee$ s9.

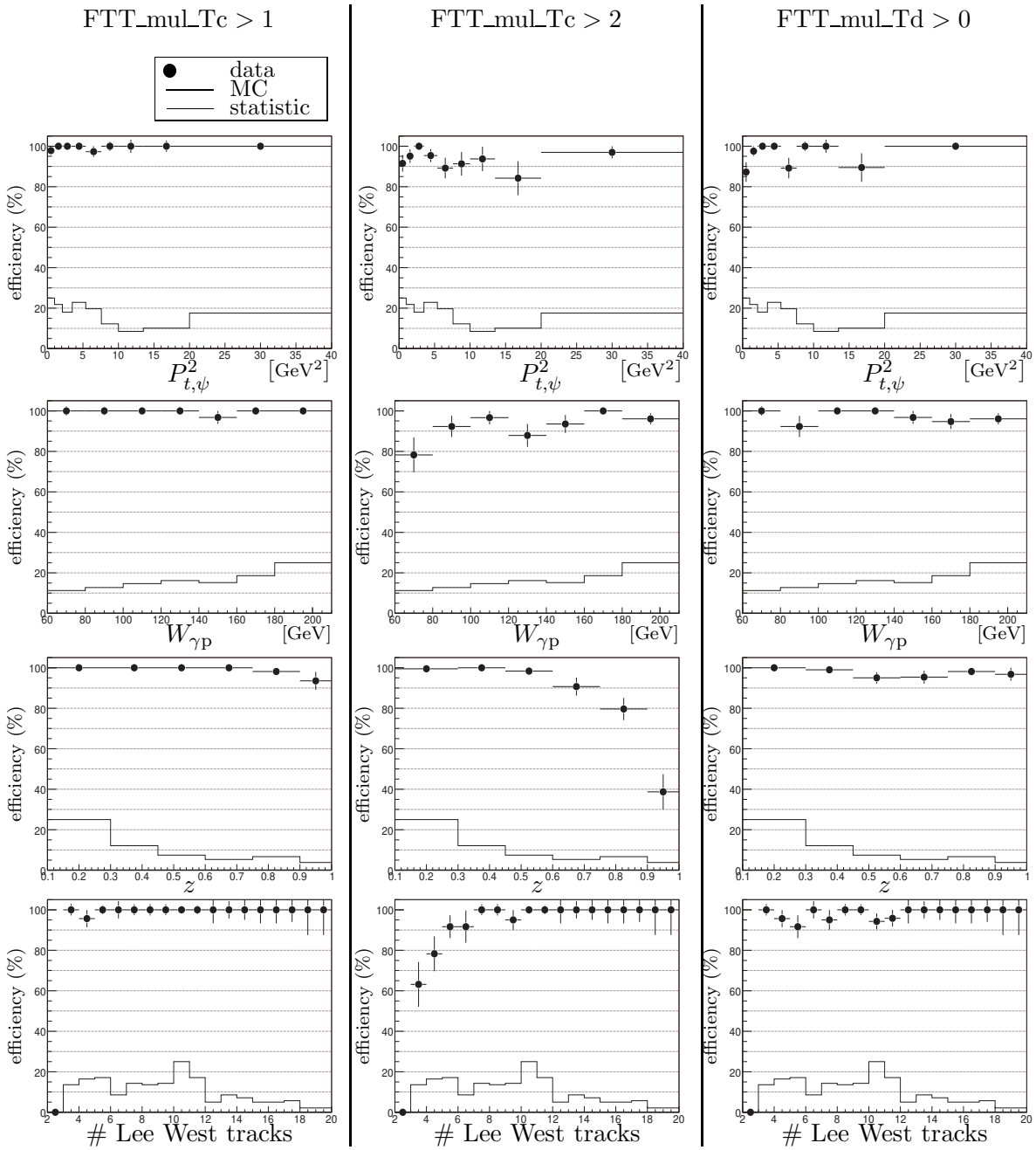

Figure 5.18: FTT trigger efficiency as a function of $P^2_{t,\psi}$, $W_{\gamma p}$, z, and N_{LW} for the **2004-2005** e^- period and the **medium** z selection. Trigger monitor is the subtrigger combination s0 $\vee$ s3 $\vee$ s9. Since the simulation of the FTT was not available during this thesis, only data is shown.

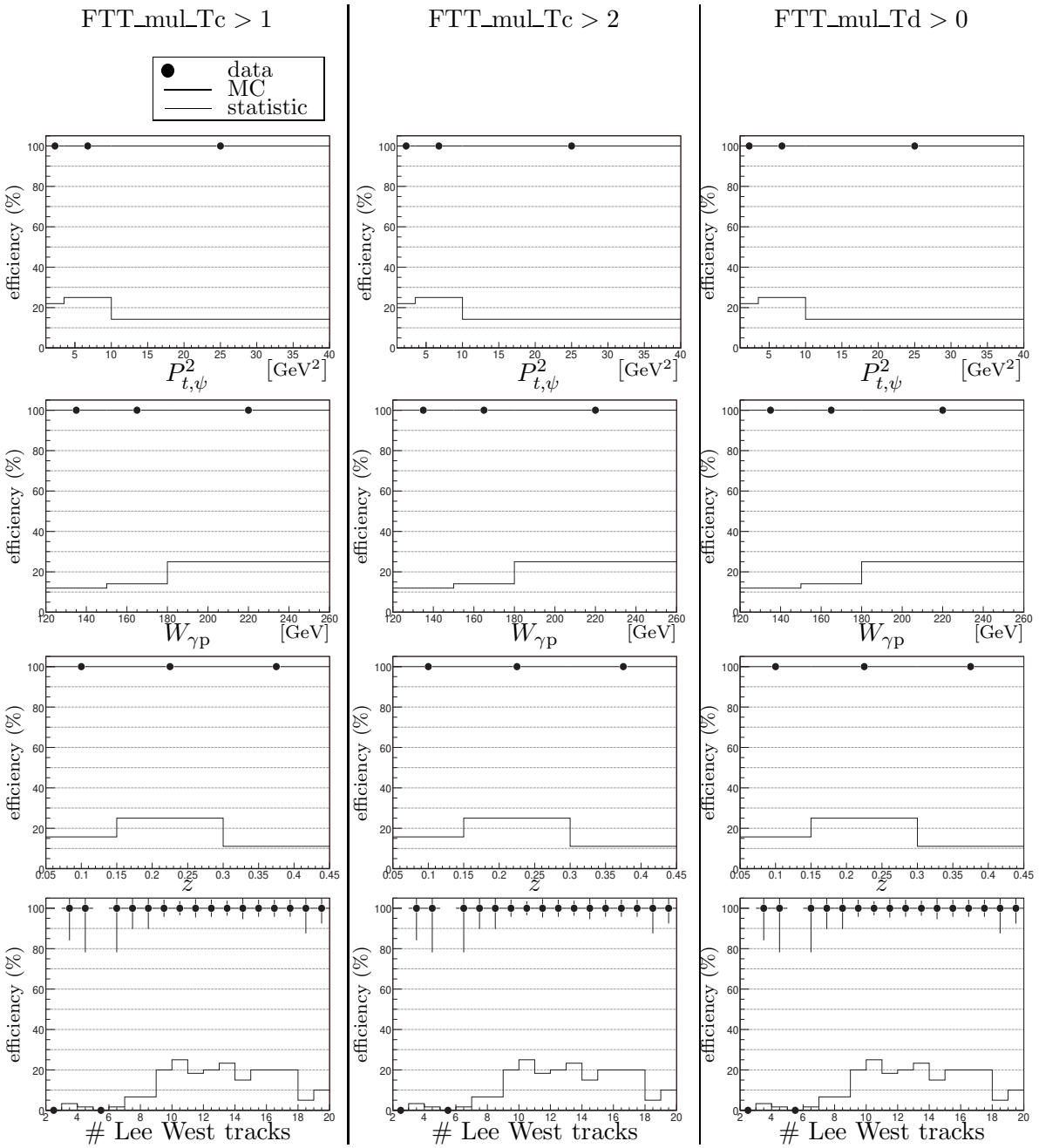

Figure 5.19: FTT trigger efficiency as a function of $P^2_{t,\psi}$, $W_{\gamma p}$, z, and N_{LW} for the **2004-2005** e^- period and the **low** z selection. Trigger monitor is the subtrigger combination s0 $\vee$ s3 $\vee$ s9. Since the simulation of the FTT was not available during this thesis, only data is shown.

CIP Trigger Efficiency

The efficiency as a function of $P^2_{t,\psi}$, $W_{\gamma p}$, z, and N_{LW} for the medium z selection is shown in figure 5.20 for the trigger element CIP_mul < 11 and in figure 5.21 for CIP_sig > 1, respectively. These efficiencies are relatively good, of the order of 95 %. Data and simulation are compatible within the errors. Figure 5.20 and 5.21 show the efficiencies for the low z selection. The same level of efficiency is observed as for the medium z selection.

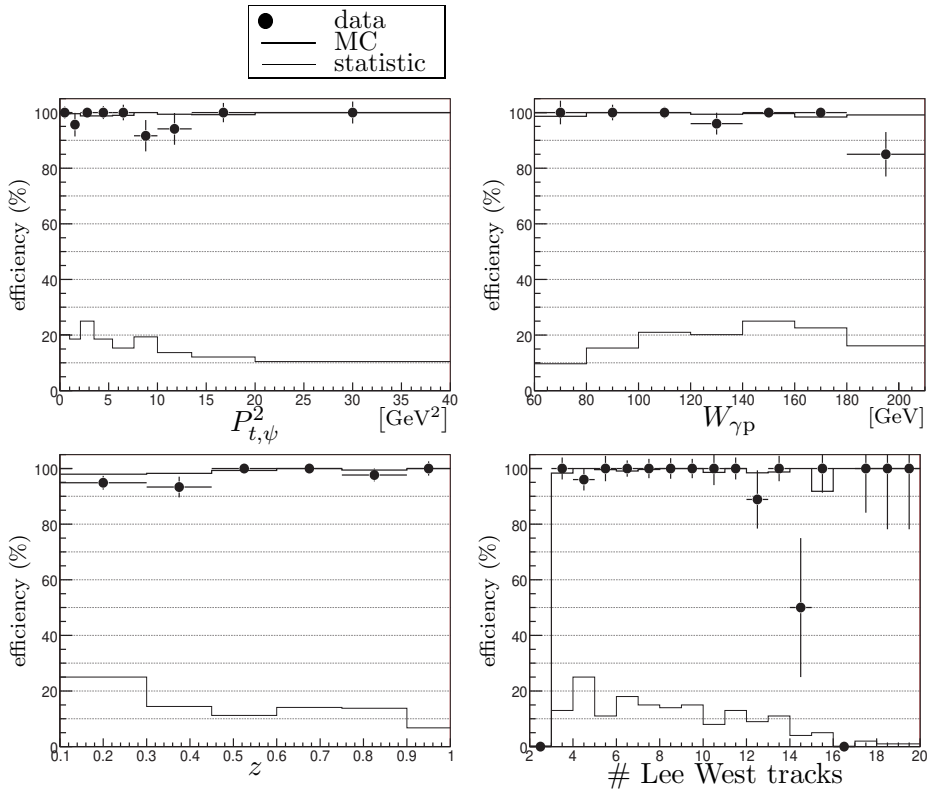

Figure 5.20: CIP_mul < 11 trigger efficiency for the **2003-2004** e^+ period and the **medium** z selection. Trigger monitor is subtrigger s61.

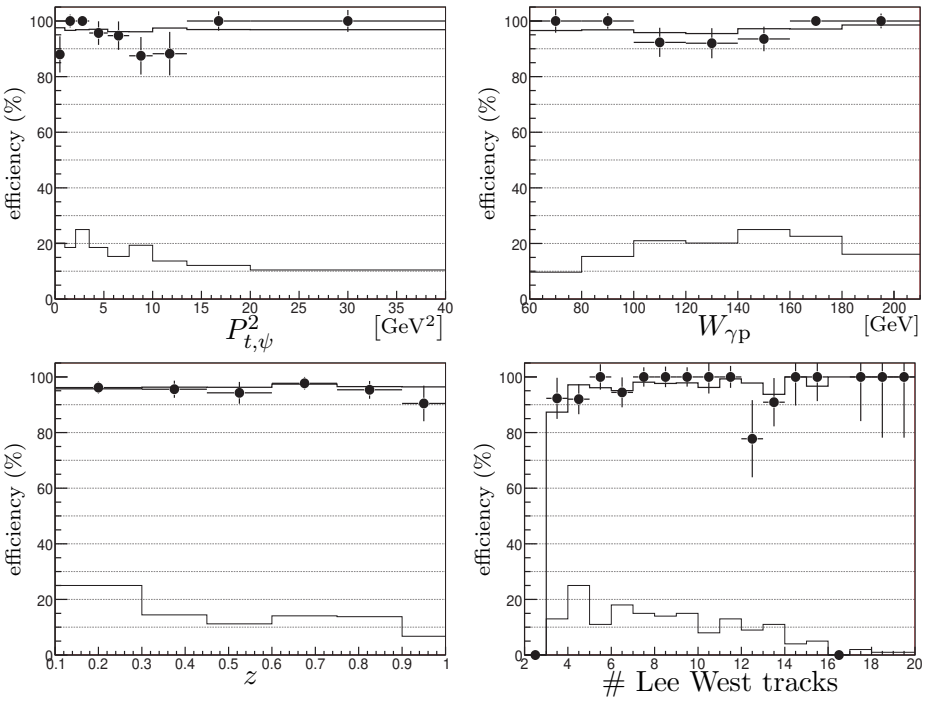

Figure 5.21: CIP_sig > 1 trigger efficiency for the **2003-2004** e^+ period and the **medium** z selection. Trigger monitor is subtrigger s61.

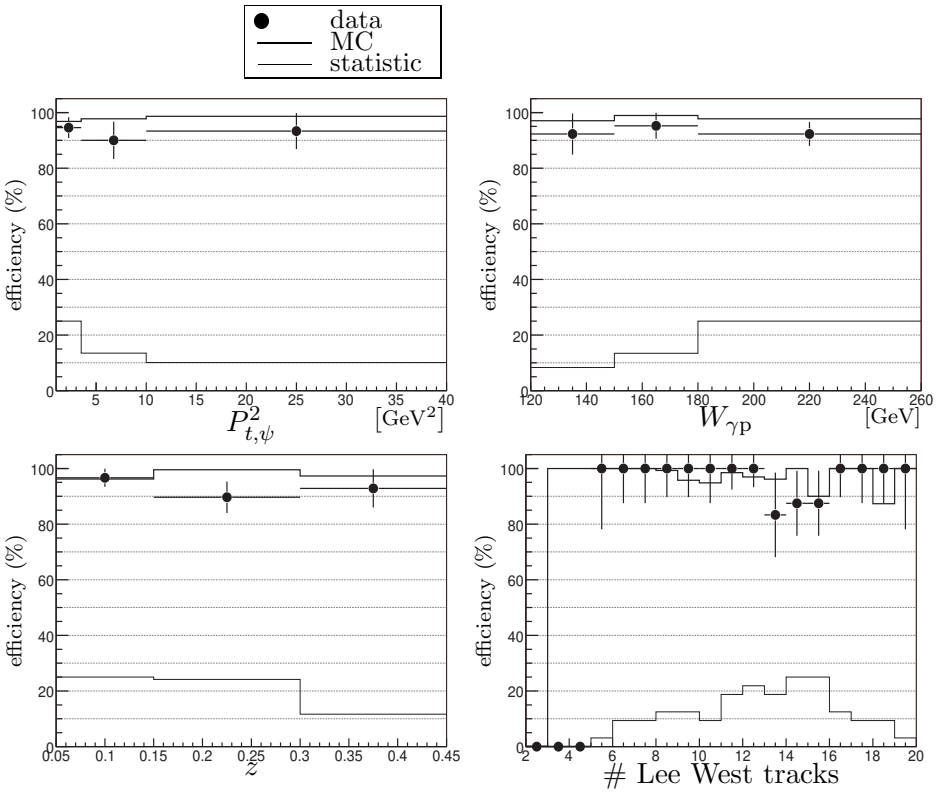

Figure 5.22: CIP_mul < 11 trigger efficiency for the **2003-2004** e^+ period and the **low** z selection. Trigger monitor is subtrigger s61.

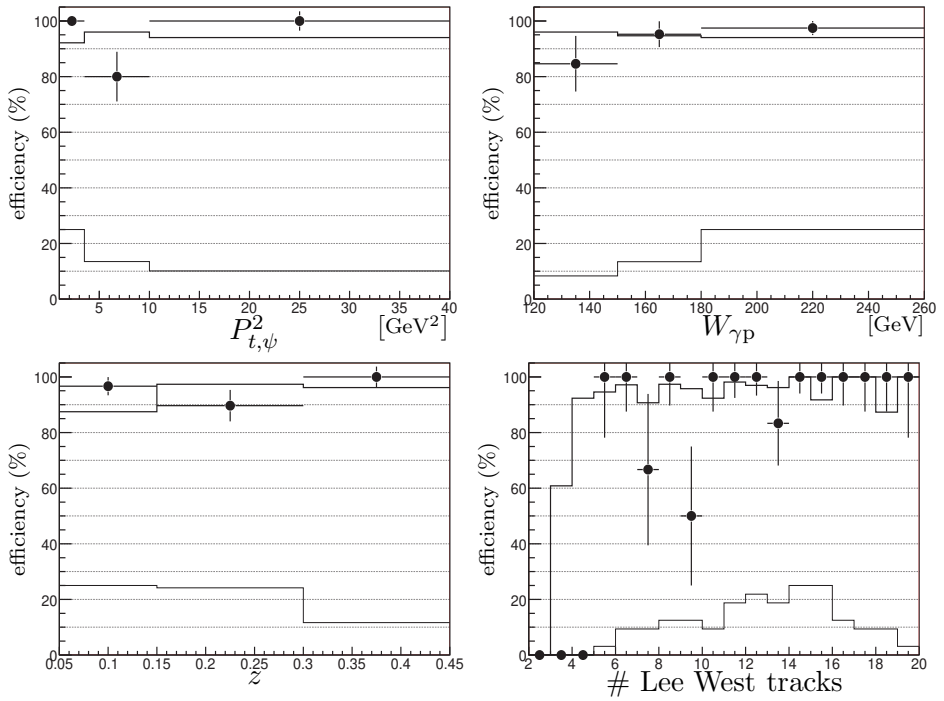

Figure 5.23: CIP_sig > 1 trigger efficiency for the **2003-2004** e^+ period and the **low** z selection. Trigger monitor is subtrigger s61.

Iron Trigger Efficiency

The trigger of the instrumented iron detector is the trigger element, which limits the efficiency of subtriggers s15, and s19 $\oplus$ s23, and consequently the available statistics. Thus it is important to study its efficiency.

In order to study the efficiency of the trigger elements of the instrumented iron detector, events containing exactly one track in the central muon detector are selected. The other track corresponds to a calorimeter muon. For HERA I, the independent subtriggers for this study were mainly SpaCal and electron tagger triggers as well as track based triggers for elastic J/ψ mesons production. For the 2003-2004 e^+ data taking period, the track based trigger is no more available. A replacement based on the FTT will be available only in 2005. Thus only the subtrigger s61 is available for the 2003-2004 e^+ data taking period, which reduces drastically the statistics. Since DIS trigger monitor is used, the photoproduction condition is omitted. The upper z cut and the requirement of at least three Lee West tracks are omitted since the data sample is not restricted to inelastic events. The cut on $W_{\gamma p}$ and $P^2_{t,\psi}$ are also omitted in order to improve the statistics. All other selection cuts are the same as in the analysis. The side band method (cf. section 7.2) is used to subtract the background, because this method is well suited for a data sample with low statistics.

Figure 5.24 shows the iron muon trigger efficiency in the polar θ and azimuthal ϕ space for the period where the iron trigger was faulty in 2005 (cf. section 5.2) and for the good period. The first is clearly sparse, while the second has still some holes, which can be interpreted as known dead regions. The same plot for the 2003-2004 e^+ data taking period is shown in figure 5.26. It is more sparse than the good period in 2005, probably due to the low statistics available and a tuning worst of the high voltage of the streamer tubes.

Figure 5.25 shows the iron trigger efficiency as a function of the polar angle θ and the transverse momentum P_t of the iron muon for the 2004-2005 e^- data taking period. The good and bad period is compared to the simulation. The ratio of the efficiencies between data and the simulation is also shown. The bad period shows clearly a 10 % to 20 % lower efficiency than the good period. The iron trigger efficiency for the 2003-2004 e^+ data taking period is shown in figure 5.27. Due to the low statistics available, it is difficult to interpret the efficiencies for data. Some bins are really poorly estimated, while some bins are compatible within the statistical errors with the simulation. However in the backward region the simulation is clearly too efficient. This effect is also clearly visible in control plots, where too many events in the simulation pass the selection in the backward region. Consequently the trigger efficiency is reweighted in the simulation for this region. For the 2003-2004 e^+ data taking period a correction factor of 0.46 is applied for $\theta > 140°$, and for the 2004-2005 e^- data taking period a correction factor of 1.10 is applied for $\theta < 30°$ and of 0.29 for $\theta > 150°$. The reweighting of the simulation affect only these bins in the polar angle θ distribution.

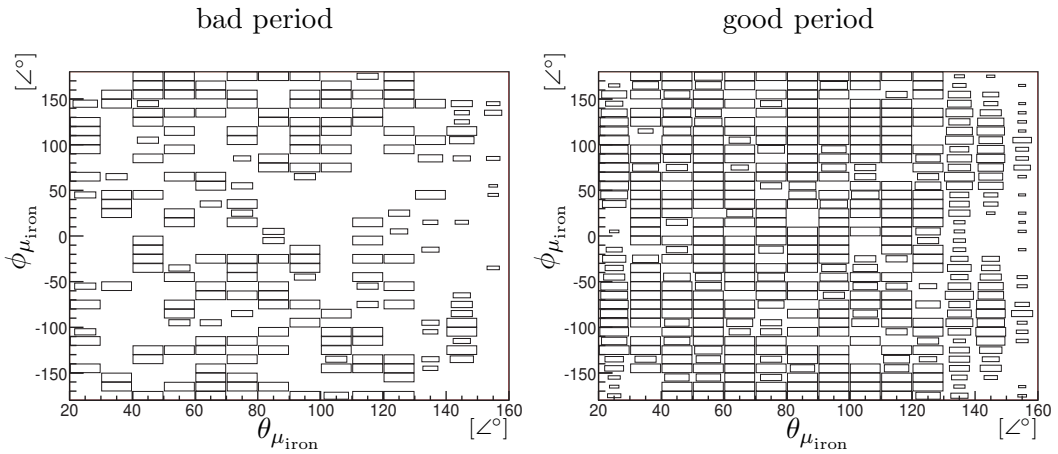

Figure 5.24: Iron muon trigger efficiency as a function of $\phi_{\mu_{\text{iron}}}$ and $\theta_{\mu_{\text{iron}}}$ for the **2004-2005** e^- data taking period. The size of the box is proportional to the efficiency.

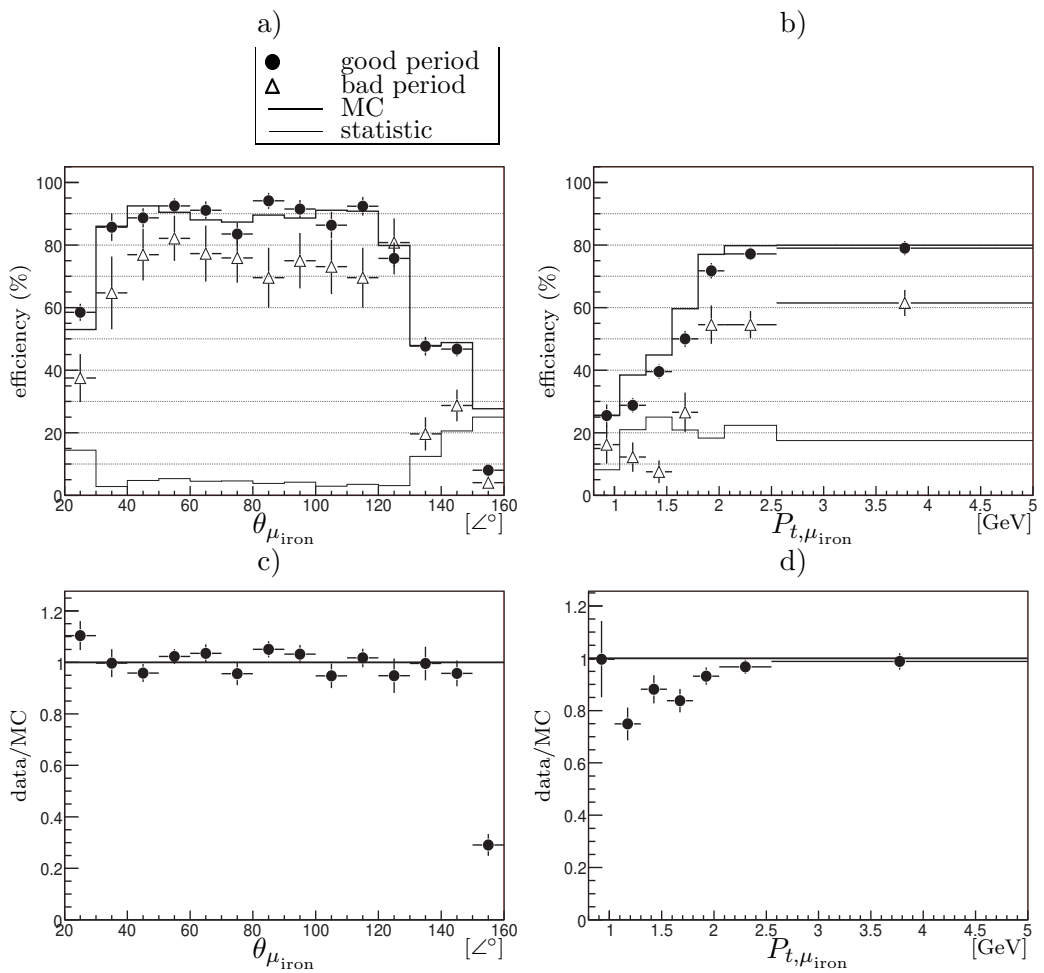

Figure 5.25: Iron muon trigger efficiency as a function of a) $\theta_{\mu_{\text{iron}}}$ and b) $P_{t,\mu_{\text{iron}}}$ for the **2004-2005** e^- data taking period. The ratio of the efficiencies between data and the simulation are shown in c) and d).

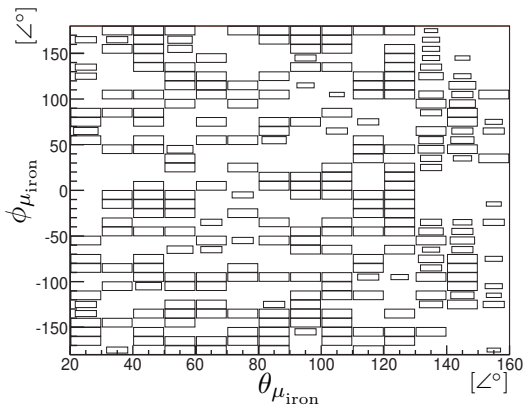

Figure 5.26: Iron muon trigger efficiency as a function of $\phi_{\mu_{\text{iron}}}$ and $\theta_{\mu_{\text{iron}}}$ for the **2003-2004** e^+ data taking period. The size of the box is proportional to the efficiency.

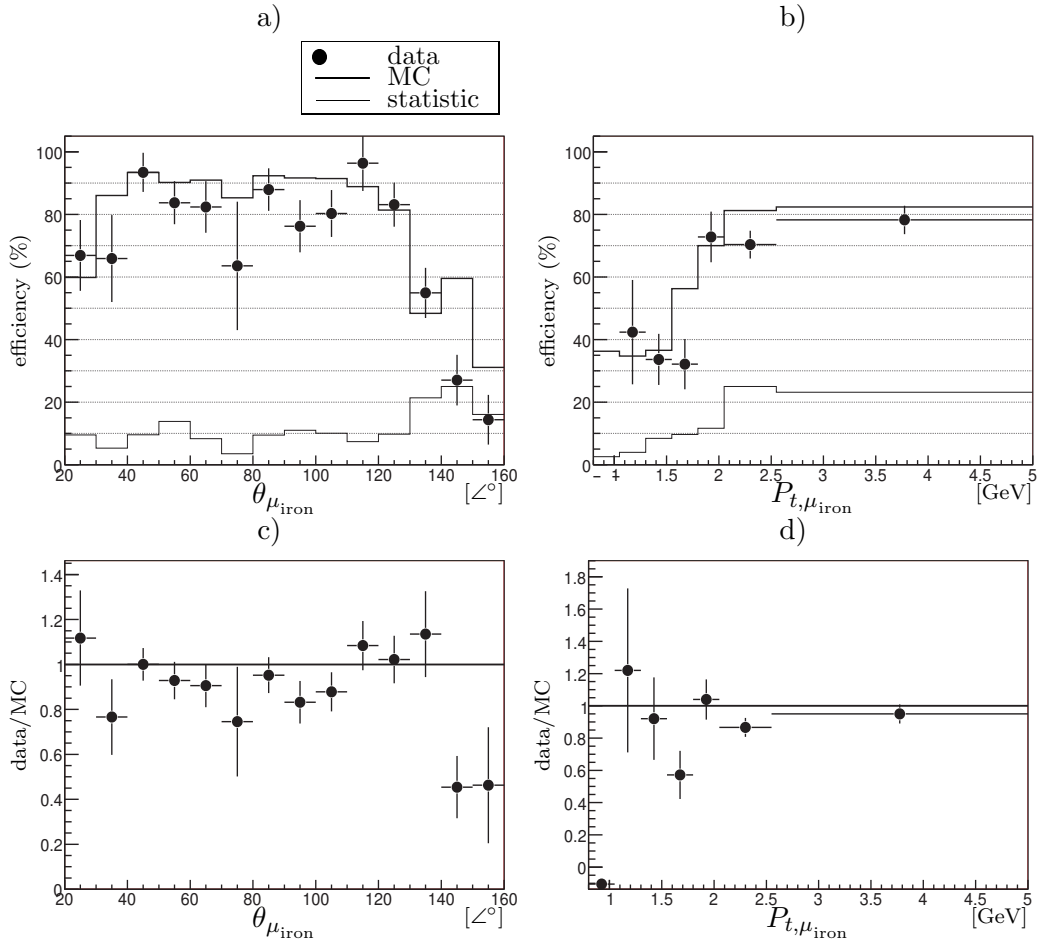

Figure 5.27: Iron muon trigger efficiency as a function of a) $\theta_{\mu_{\text{iron}}}$ and b) $P_{t,\mu_{\text{iron}}}$ for the **2003-2004** e^+ data taking period. The ratio of the efficiencies between data and the simulation are shown in c) and d).

5.4.1.2 Subtrigger Efficiency

There are several methods to determine the efficiency of the subtrigger combinations used for the analysis. A method using the simulation consists of comparing the efficiency of the trigger elements between data and the simulation, and then to compute a correction factor if they are too different. This method assumes the correction determined with the monitor trigger is the same as for the used subtriggers. In this way the reweighted Monte Carlo simulation should give the correct trigger efficiency. Indeed it is difficult to simulate correctly the trigger system.

A second method uses only data and is similar to the one for the determination of the trigger element efficiency. The formula is modified as:

$$\text{subtrigger efficiency} \mathrel{\widehat{=}} \frac{\text{selection cuts} \wedge \text{monitor fired} \wedge \text{raw subtrigger fired}}{\text{selection cuts} \wedge \text{monitor fired}}$$

However this method usually is limited by the available statistics for the monitor trigger and thus be quite inaccurate.

To determine the trigger efficiency the subtrigger monitor combination s0 $\vee$ s3 $\vee$ s9 is used in to order to be independent. The background is subtracted with a side band method because the statistics in the bins is too low to fit the distributions.

The trigger efficiency of the subtrigger combination s15 $\vee$ s18 for the medium z selection as a function of the observables used for the measurement of the cross section is shown in figure 5.28 for the 2003-2004 e^+ data taking periods. Data are compared to the simulation. Only bins with a low uncertainties are in agreement with the simulation. For many bins the statistics is not sufficient to study the efficiency. The yield of the trigger monitor is too low and is not counter-balanced by the integrated luminosity of the data taking period. Consequently the trigger efficiency could not be determined with the second method, and the simulated trigger efficiency will be used to determine the cross sections. The trigger efficiency is rising with respect to $P^2_{t,\psi}$ from 50 % to 0 %, while it decreases for $W_{\gamma p}$ and z from 80 % to 60 %.

Since the simulation of the FTT was not working during this thesis [8], a run dependent evaluation of the subtriggers with the simulated trigger elements was implemented in the analysis software. The trigger efficiency of the subtrigger combination s18 $\vee$ s19 $\vee$ s23 for the 2004-2005 e^- data taking period, where the FTT trigger elements conditions were removed of the definition of these subtriggers, is shown in figure 5.29. This trigger efficiency will be used to correct the cross sections. In order to verify the trigger efficiency of the FTT is close to 100 %, the trigger efficiency of the "removed part" is shown in figure 5.30. This assumption is trusted within the statistical uncertainties. The trigger efficiency has the same behaviour as the 2003-2004 e^+ data taking period. The inefficiency of the FTT trigger element FTT_mul_Tc previously discussed in section 5.4.1.1 is compensated by subtrigger s18.

The trigger efficiency of the subtrigger combination s15 $\vee$ s18 for the low z selection is shown in figure 5.31 for the 2003-2004 e^+ data taking period. The trigger efficiency of the subtrigger combination s18 $\vee$ s19 $\vee$ s23 for the 2004-2005 e^- data taking period, where the FTT trigger elements conditions were removed, is shown in figure 5.32, and the trigger efficiency of the "removed part" is shown in figure 5.33 in order to check it is of the order of 100 %. The trigger efficiency is approximately constant and of the order of 80 % for both data taking periods.

[8] The FTT trigger elements are set to false by default. Consequently all subtriggers which depend of them get the false value.

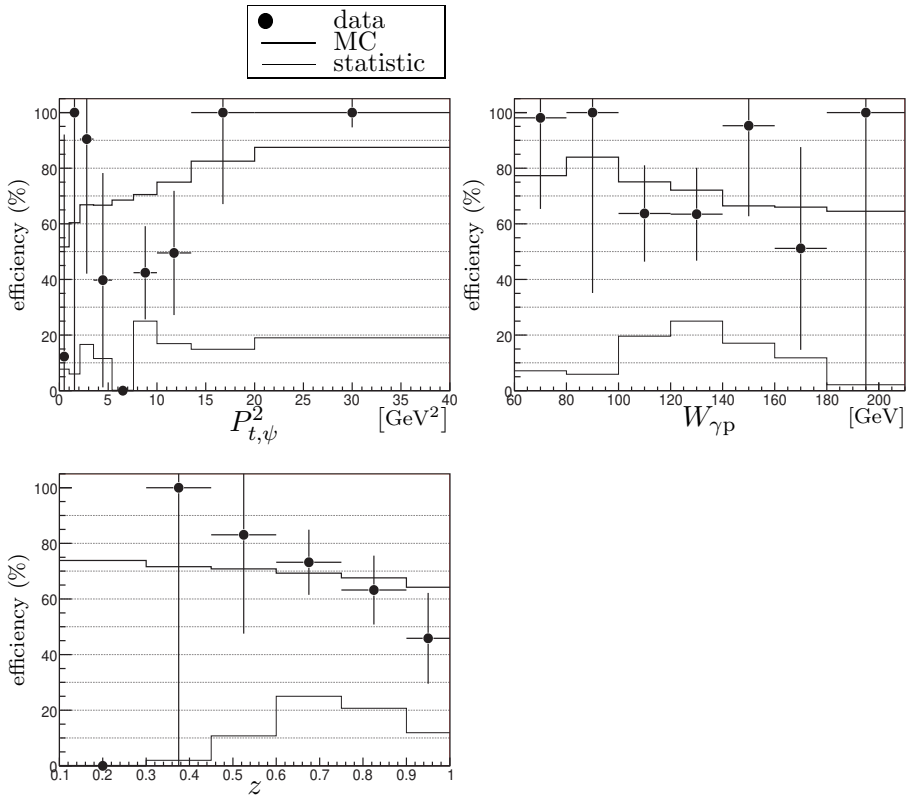

Figure 5.28: Trigger efficiency for the subtrigger combination s15 $\vee$ s18 as a function of $P^2_{t,\psi}$, $W_{\gamma p}$, and z for the **2003-2004** e^+ period and the **medium** z selection.

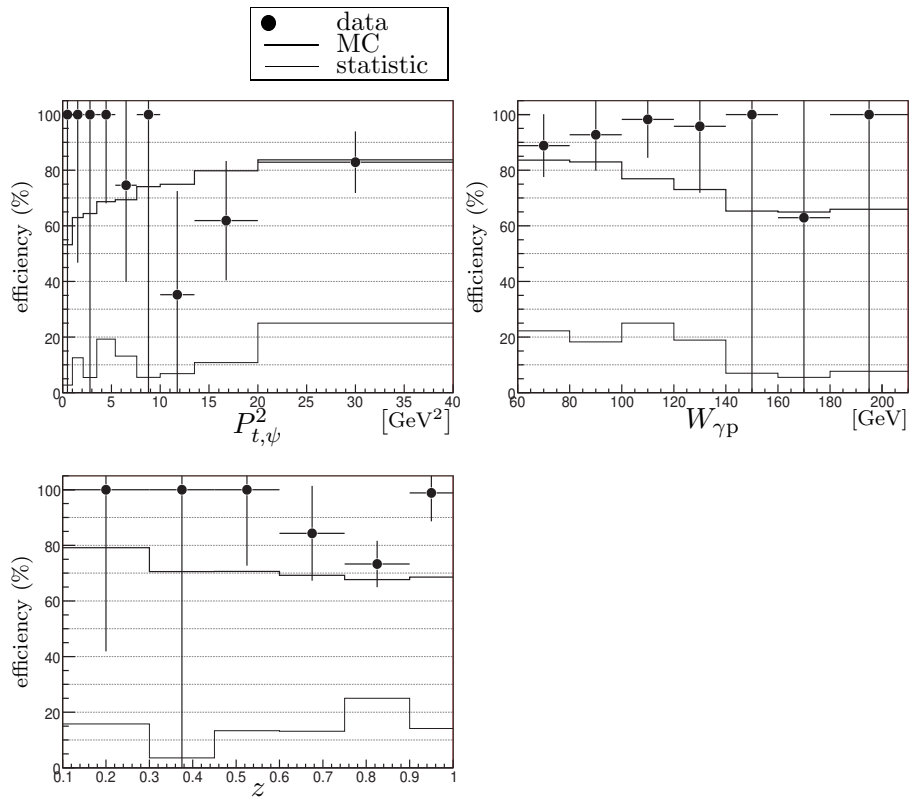

Figure 5.29: Trigger efficiency for the subtrigger combination s18 $\vee$ s19 $\vee$ s23, where the FTT trigger elements conditions were removed of the definition of these subtriggers, as a function of $P^2_{t,\psi}$, $W_{\gamma p}$, and z for the **2004-2005** e^- period and the **medium** z selection.

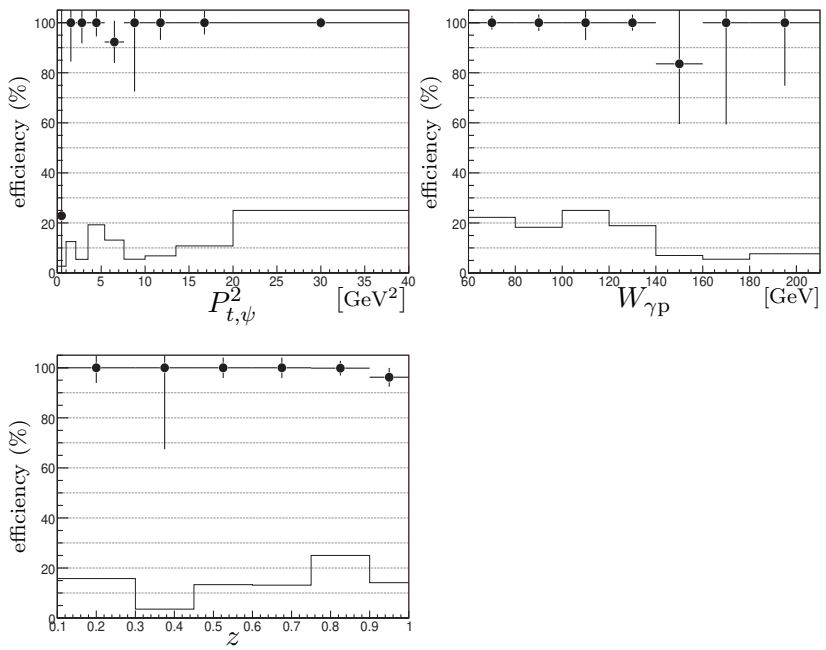

Figure 5.30: Trigger efficiency for the subtrigger combination s18 $\vee$ s19 $\vee$ s23 for the "removed part" as a function of $P^2_{t,\psi}$, $W_{\gamma p}$, and z for the **2004-2005** e^- period and the **medium** z selection.

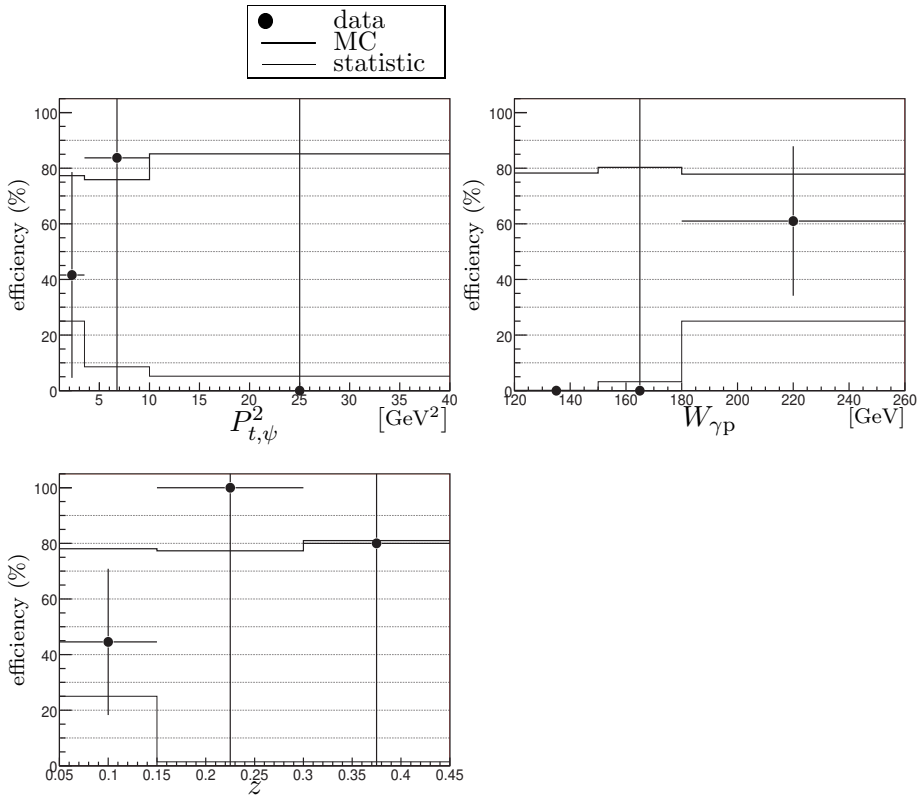

Figure 5.31: Trigger efficiency for for the subtrigger combination s15 $\vee$ s18 as a function of in $P^2_{t,\psi}$, $W_{\gamma p}$, and z for the **2003-2004** e^+ period and the **low** z selection.

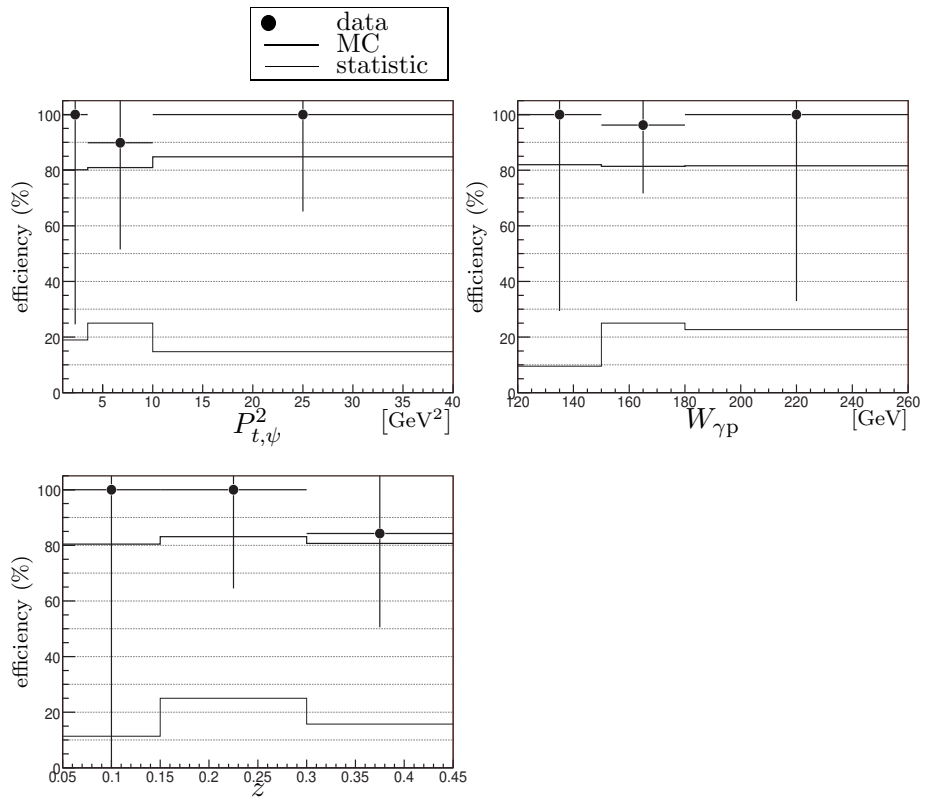

Figure 5.32: Trigger efficiency for the subtrigger combination s18 ∨ s19 ∨ s23, where the FTT trigger elements conditions were removed of the definition of these subtriggers, as a function of $P^2_{t,\psi}$, $W_{\gamma p}$, and z for the **2004-2005** e^- period and the **low** z selection.

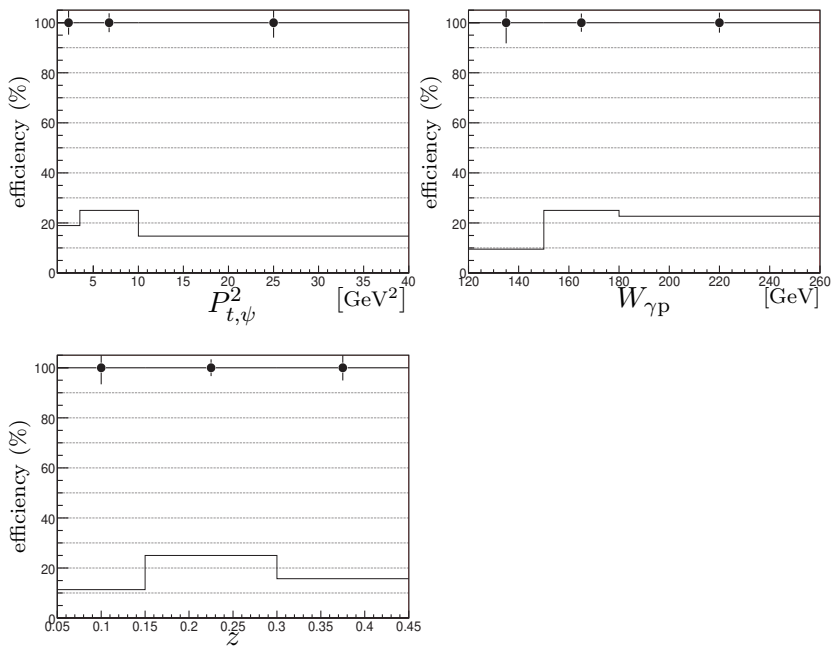

Figure 5.33: Trigger efficiency for the subtrigger combination s18 ∨ s19 ∨ s23 for the "removed part" as a function of $P^2_{t,\psi}$, $W_{\gamma p}$, and z for the **2004-2005** e^- period and the **low** z selection.

5.4.2 Trigger Level Four

The origin of the malfunction of the trigger level 4 from June 2004 to Avril 2006 will be presented. Then the impact and the treatment of it will be provided.

5.4.2.1 Origin of the Malfunction

In order to increase the specific luminosity for HERA II, two new magnets GO and GG were installed around the beam pipe in the iron instrumented detector. These magnets are switch on and off for every luminosity fill, which has for consequence to move the CST and prevented to perform the alignment in 2004. During HERA I and until June 2004 the online reconstruction software used the CST improved central fitted tracks for central, forward and combined tracks with lepton identification. It was decided to disable this in June 2004. From run No. 387 288 the software of the trigger level 4 was converted to use CJC only tracks. But this work was only partially done and introduced a malfunction in the software. The message [71] in the "L45 Trigger and Data-logging" mailing list announced the modification and strongly suggested to check if the finders were still working. This advertisement did not catch enough attention.

During the 2003-2004 e^+ data taking period the inelastic J/ψ meson yield corresponded to the one of HERA I. The "Heavy Flavour Closed" finder was verified successfully in January 2004 [72], but then it was not verified again until the discovery of the malfunction.

After the introduction of the malfunction many things contributed to hide the bug for a while. The activation of the level 2 neural network for subtrigger s15 at the same period, and then the unavailability of the FTT information for it, confused the situation of this subtrigger. During the first six months, the central muon trigger suffered from power supply problems causing bad efficiencies and thus affected the yield of subtriggers using it. The overlap of the other hard scales and finders permits to save part of the events, but prevented to have a yield quasi-null, which would be more explicit.

The malfunction could be detected quickly with the simulation, but the level 4 event rejection is not applied in Monte Carlo simulation. It could be also detected from the level 4 activity report [9]. The following rates show a drop of 17 % [10]:

luminosity fill	date	L4_EFS_HMASS [Hz]	L4_EFS_HMASS_Q2 [Hz]
3 377	12 May 2004	0.505	0.035
4 113	28 September 2005	0.177	0.017

In July 2005, the disastrous J/ψ meson yield was shown at the heavy flavour meeting [73]. A carefully analysis of these yield plots suggests something happened in June 2004. In particular, why the rate of inelastic J/ψ mesons triggered by the elastic subtrigger s18 suddenly drops and never reaches the previous rate (cf. figure 5.2). No suspicious action was done on the subtrigger s18 at this moment. Moreover despite continuous tuning of the subtriggers, the rate of 2004 could not be reached anymore. Finally, the bug was discovered on Easter Sunday in April 2006 from level 4 plots which were made in order to design level 3 based triggers for J/ψ mesons.

[9] See the url `https://www-h1.desy.de/itrigger/L4Farm/doc/fill_4113.html` and `https://www-h1.desy.de/itrigger/L4Farm/doc/fill_3377.html`

[10] The downscale of the rate of the "Heavy Flavour Closed" finder is normalised with the ratio of the rate for DIS events in order to be independent of the run condition.

5.4.2.2 Impact and Treatment of the Malfunction

Figure 5.35 shows for both analysis regions and data taking periods which hard scales or finders selected the events. The definition of the event classification bits is given in table 5.4. The level 4 weight of the selected events is given in table 5.6 for the 2004-2005 e^- data taking period. The loss is less for the low z selection of the order of 65 % instead of 80 % for the medium z selection, due to a better efficiency of finders like (7, 8, 9 and 15) for low z events.

Figure 5.34 shows the distributions of $P^2_{t,\psi}$, $W_{\gamma p}$, and z for the most active hard scales and finders for the medium z selection. For the low z selection the statistics is not sufficient to have significant plots. For finder 8 (High P_t central) the numbers of entries increase with respect to $P^2_{t,\psi}$. For the two other finders the distribution is approximately constant, but the numbers of entries is higher at low $P^2_{t,\psi}$ for finder 9 (High P_t forward). It is also visible in the $W_{\gamma p}$ distribution, but at the limit of the statistics for finder 8. There is small tendency to have more events at medium $W_{\gamma p}$ for finder 8, while for finder 9 there is more events a low $W_{\gamma p}$. For finders 8 and 9 the z distribution have approximately the standard shape. The "Heavy Flavour Closed" finder 16 finder was not completely inactive during this data taking period, since the sub-finder 2PRONG for elastic J/ψ mesons was still in order. The shape of the distributions of $W_{\gamma p}$ and z show the saved events have a low $W_{\gamma p}$ and a high z, which is typical of diffractive J/ψ mesons. Events only saved by this finder have to be excluded since they are dominantly resonant background at high elasticity.

The number of events compared to the weights for events classified as soft physics, and thus weighted by (20, 40, or 60), show clearly it is impossible to reverse the downscaling without spoiling the errors of the cross section by large statistical fluctuations. There is one order of magnitude between the weights and the full statistics, and the same order of magnitude between the weights and their corresponding number of events.

During this data taking period, the picture was absolutely different by comparison to the other periods. Events were saved when they matched the selections of the other finders or hard scales. It means the efficiency of the level 4 trigger depends of several observables, and the efficiency for the inelastic J/ψ mesons could be much lower than for the resonant background. The soft physics events are also excluded in addition to events only saved by finder 16.

Since the trigger level 4 is a software trigger, a high statistic Monte Carlo simulation could be used to determine its efficiency. But the simulation has to be done *run dependent*, which is not the default procedure. Moreover there are some subtleties due to the fact the selection was done online, and not offline as for the simulation.

Since the simulation of the trigger level 4 for the 2004-2005 e^- data taking period did not give a good description, the weights as functions of the observables used to measure the cross sections can be used to compute the efficiency of the trigger level 4 in order to downscale the simulation and to correct the cross sections. But the affectation of the weights is not a prefect random distribution. With such weights and statistics, the determination of the efficiency by this method cannot be accurate. The uncertainty is of the order of 10 %. Moreover the non-resonant background cannot be subtracted accurately for the same reasons.

The efficiencies of the trigger level 4 are shown in figure 5.36 for each selection. These plots reveal the efficiency depends on $P^2_{t,\psi}$, $W_{\gamma\mathrm{p}}$, and z. In particular for events with $P^2_{t,\psi} > 20\,\mathrm{GeV}^2$ the efficiency is 100 %. These events are saved dominantly by finders 8 (High P_t central). It is also visible with the efficiency as a function of the maximum transverse momentum P_t of the hadronic final state, which is rising with respect to P_t, especially at low z. For the low z selection, the efficiency is constant as a function of $P^2_{t,\psi}$, increases linearly with $W_{\gamma\mathrm{p}}$, and drops for the last bin of z. For the medium z selection, the efficiency is approximately constant as a function of $P^2_{t,\psi}$ and $W_{\gamma\mathrm{p}}$, and decreases linearly with respect to z, excepted for the bin $.75 \leqslant kz < .9$ which is higher.

For the 2003-2004 e^+ data taking period, all the weights of the selected events are found to be one (cf. table 5.5). Thus no correction has to be applied for this period, the level 4 is considered 100 % efficient.

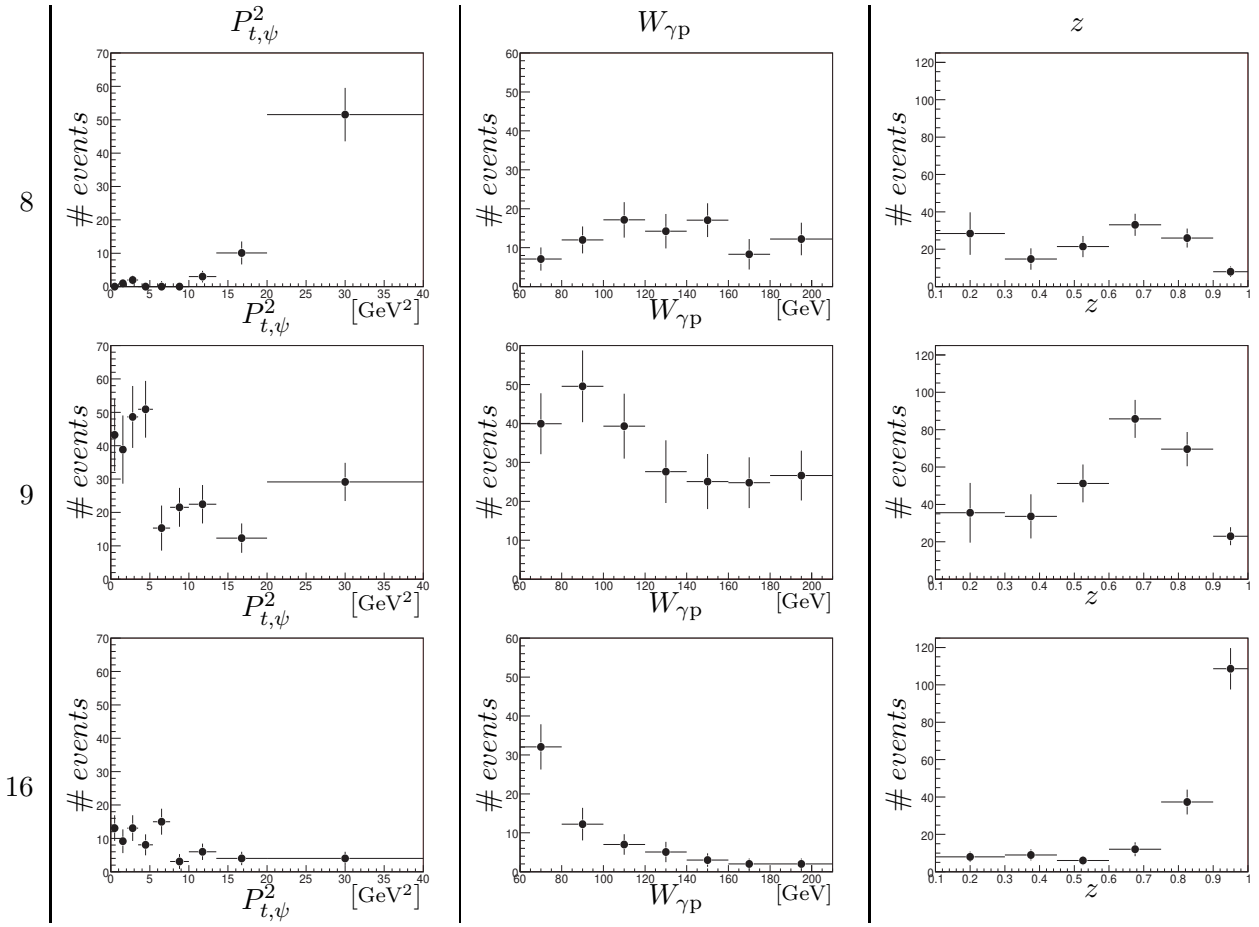

Figure 5.34: Distributions of $P^2_{t,\psi}$, $W_{\gamma\mathrm{p}}$ and z for events selected by finders (8, 9, 16) and the **medium** z selection during the **2004-2005** e^- data taking period. The non-resonant background is subtracted with the side-band method. Notice the last $P^2_{t,\psi}$ bin is larger than the others.

low z selection medium z selection

2003-2004 e^+ data taking period (Finder 16 in order)

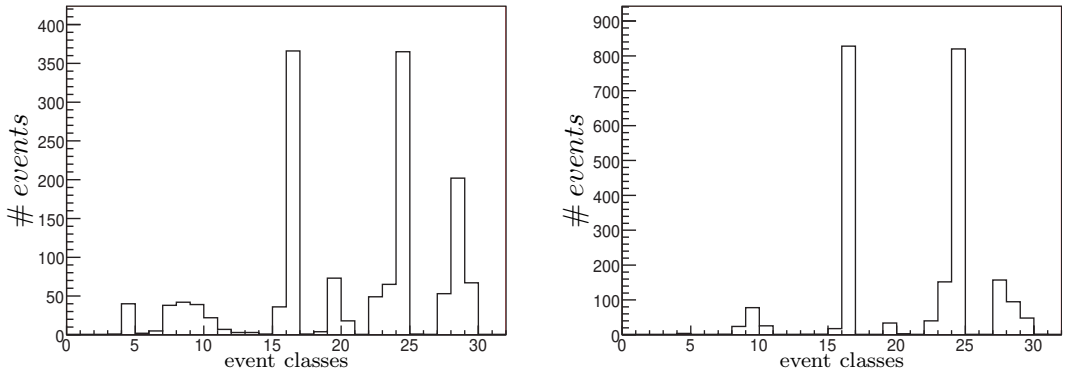

2004-2005 e^- data taking period (Finder 16 not in order)

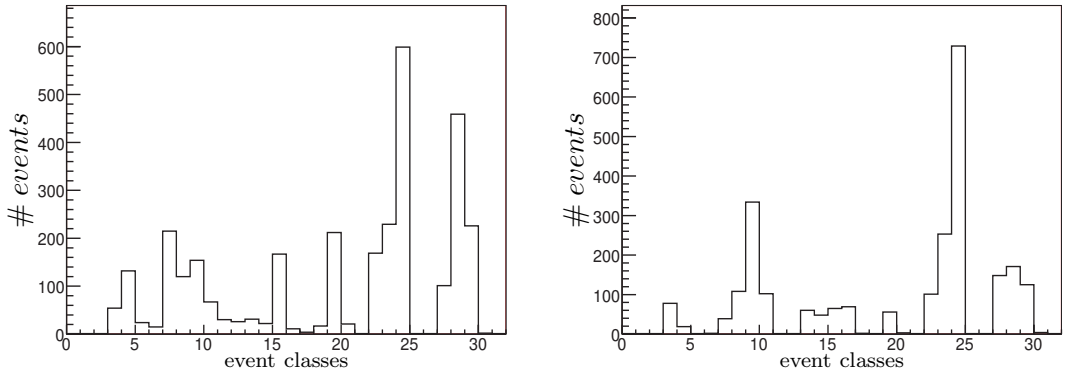

Figure 5.35: Event classes for each selection and data taking period.

bit	Physics class
0	Not classified junk
1	Pilot bunches
2	Lumi (DIS/BH overlap)
3	Soft physics (prescaled)

Hard Scale Physics	
4	High Q^2
5	ET_total
6	ET_miss
7	High_ET_jets
8	High_Pt_central
9	High_Pt_forward
10	High_Pt_muons
Exclusive Final States	
11	Multi-jets
12	Multi-particles
13	Diffraction
14	Leading baryons
15	Heavy flavour open
16	Heavy flavour closed
17	Photons (ISR, QEDC)
18	High-y DIS (FL)

Event Signatures	
19	Electron in LAr
20	Electron in Spacal
21	Electron in VLQ
22	Electron in E-taggers
23	Photon in Gamma-tagger
24	Muons
25	Hotline
26	Free quarks
27	Diffractive flag
28	Jets ($Et > 5\,\mathrm{GeV}$)
29	High $W^2_{\gamma\mathrm{p}}$
30	Cosmics

Table 5.4: Level 4 event classification bits

low z selection

L4 weight	number of entries	number of expected J/ψ	percent of saved events
1	395	395	100.0
10	0	0	0.0
20	0	0	0.0
40	0	0	0.0
60	0	0	0.0
sum	395	395	100.0 ± 0.0

medium z selection

L4 weight	number of entries	number of expected J/ψ	percent of saved events
1	851	851	100.0
10	0	0	0.0
20	0	0	0.0
40	0	0	0.0
60	0	0	0.0
sum	851	851	100.0 ± 0.0

Table 5.5: Level 4 weights and the corresponding number of entries for each selection for the **2003-2004** e^+ data taking period. The percentage of saved events is given, as well as the number of expected J/ψ mesons.

low z selection

L4 weight	number of entries	number of expected J/ψ	percent of saved events
1	627	627	100.0
10	4	40	10.0
20	4	80	5.0
40	1	40	2.5
60	19	1 140	1.7
sum	655	1 927	34.0 ± 4.6

medium z selection

L4 weight	number of entries	number of expected J/ψ	percent of saved events
1	689	689	100.0
10	0	0	0.0
20	10	200	5.0
40	4	160	2.5
60	50	3 000	1.7
sum	753	4 049	18.6 ± 1.9

Table 5.6: Level 4 weights and the corresponding number of entries for each selection for the **2004-2005** e^- data taking period. The percentage of saved events is given, as well as the number of expected J/ψ mesons.

low z selection

bit	4	5	6	7	8	9	10	11	12	13	14	15	16	17	18
4	40	2	2	19	16	4	6	6	1	1	0	6	36	0	0
5		2	1	2	1	0	1	2	0	0	0	0	1	0	0
6			5	5	4	0	2	2	0	0	0	1	3	0	0
7				38	16	3	7	6	1	0	0	7	33	0	0
8					42	5	22	4	0	0	0	7	38	0	0
9						39	1	2	0	0	0	5	38	0	0
10							22	2	0	0	0	3	22	0	0
11								7	0	0	0	1	5	0	0
12									3	0	0	3	3	0	0
13										3	0	0	3	0	0
14											1	1	1	0	0
15												36	32	0	0
16													366	1	4
17														1	1
18															4

medium z selection

bit	4	5	6	7	8	9	10	11	12	13	14	15	16	17	18
4	4	0	0	0	1	2	1	0	0	0	0	0	4	0	0
5		0	0	0	0	0	0	0	0	0	0	0	0	0	0
6			1	1	0	0	0	0	0	0	0	0	1	0	0
7				2	0	0	0	0	0	0	0	0	2	0	0
8					24	3	22	0	0	0	0	3	23	0	0
9						78	2	0	0	0	1	3	77	0	0
10							26	0	0	0	0	3	25	0	0
11								0	0	0	0	0	0	0	0
12									0	0	0	0	0	0	0
13										2	0	0	2	0	0
14											2	0	2	0	0
15												18	17	0	0
16													828	0	1
17														0	0
18															1

Table 5.7: Event classes matrix for the **2003-2004** e^+ data taking period. This matrix shows the overlaps between event classes. Numbers represent number of entries. Since the matrix is symmetrical only the upper part is shown. The diagonal gives the number of entries for each event classes.

low z selection

bit	4	5	6	7	8	9	10	11	12	13	14	15	16	17	18
4	132	12	8	78	45	22	21	22	9	7	4	32	0	0	1
5		24	3	24	7	0	5	11	1	0	0	5	0	0	0
6			15	15	7	2	4	2	1	0	0	3	0	0	0
7				215	61	22	29	27	13	5	7	52	0	0	1
8					120	9	64	17	6	0	2	21	1	0	1
9						154	2	3	2	2	4	20	1	0	3
10							67	9	5	0	1	11	1	0	0
11								30	4	1	1	7	0	0	4
12									26	4	0	16	0	0	2
13										31	2	10	2	0	3
14											22	7	0	0	0
15												167	0	0	1
16													11	1	1
17														4	1
18															17

medium z selection

bit	4	5	6	7	8	9	10	11	12	13	14	15	16	17	18
4	19	1	1	8	3	4	3	0	0	1	0	1	0	1	0
5		1	0	1	0	0	0	0	0	0	0	0	0	0	0
6			2	2	1	1	1	0	0	0	0	0	0	0	0
7				39	10	4	8	0	0	0	2	2	0	1	0
8					108	12	95	0	0	0	1	7	2	0	0
9						334	13	0	0	2	5	10	5	0	0
10							102	0	0	0	0	8	2	0	0
11								1	0	0	0	1	0	0	0
12									0	0	0	0	0	0	0
13										60	3	3	1	0	0
14											48	3	5	0	0
15												65	0	0	0
16													69	1	0
17														2	0
18															1

Table 5.8: Event classes matrix for the **2004-2005** e^- data taking period. This matrix shows the overlaps between event classes. Numbers represent number of entries. Since the matrix is symmetrical only the upper part is shown. The diagonal gives the number of entries for each event classes.

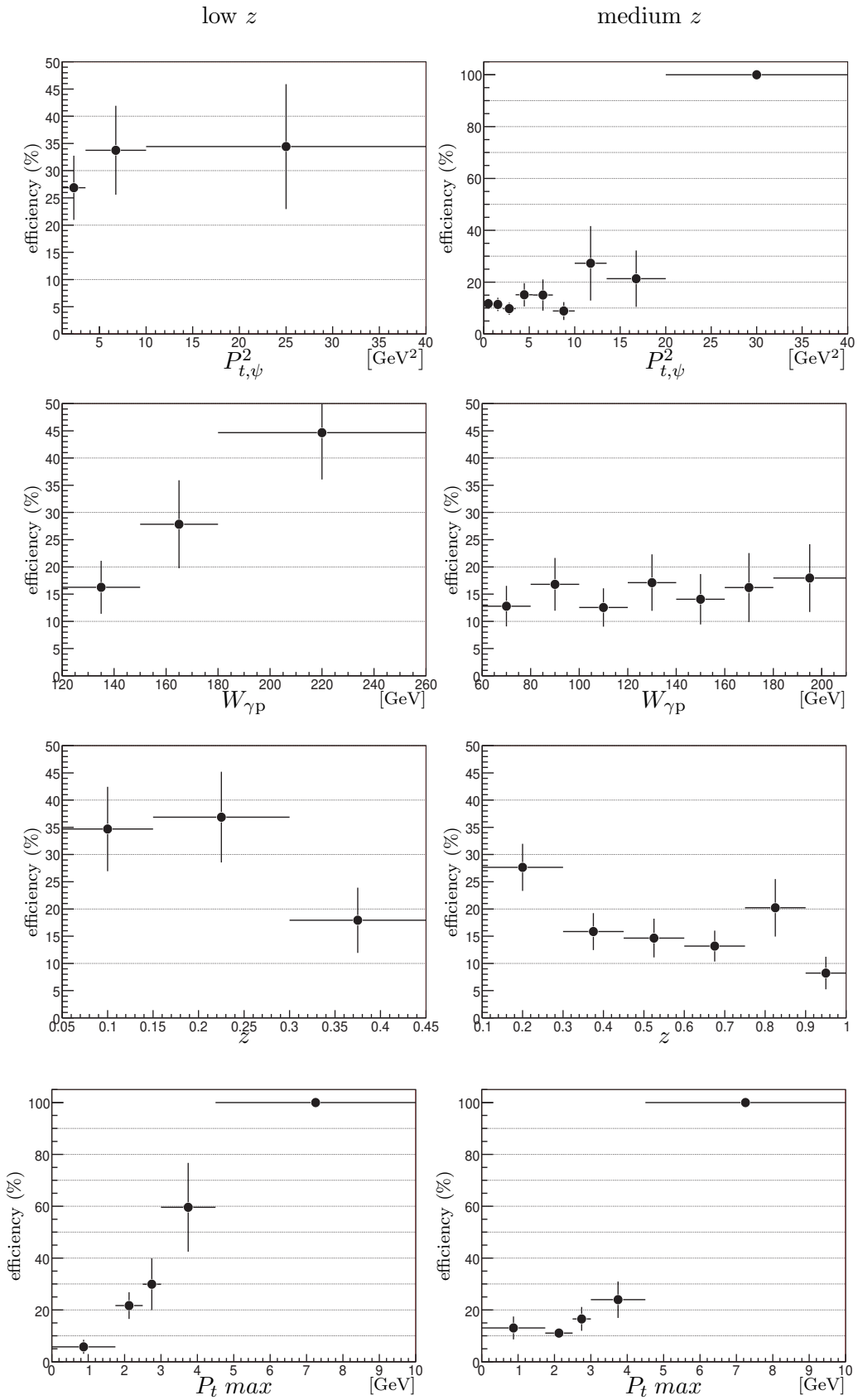

Figure 5.36: Level 4 efficiency as functions of $P^2_{t,\psi}$, $W_{\gamma p}$, z, and the P_t maximum for each selection. The efficiency as a function of $W_{\gamma p}$ for the medium z selection is approximately 14.6 %.

5.5 Event Weights

Since the level 1 subtriggers used in this analysis are downscaled (see prescale considerations in section 5.1 and in section 5.2), events have to be weighted to take into account the prescale factors. The method to compute the weights is described in the collaboration note [74]. A short summary will be presented in the following paragraph.

If we denote by

$$r_{ij} = \begin{cases} 1 & \text{if the raw subtrigger } i \text{ is set in the event } j, \\ 0 & \text{otherwise.} \end{cases}$$

the raw L1 bit of subtrigger i in event number j, and by d_{ik} the downscaling factor of the subtrigger i in run k, the probability that this subtrigger triggers the event in this run is

$$P_{ijk} = \frac{r_{ij}}{d_{ik}}$$

The probability that at least one of the N_{subtr} subtriggers triggers the event in run k is

$$P_{jk} = 1 - \prod_{i=1}^{N_{\text{subtr}}} (1 - P_{ijk})$$

The weight to be assigned to event j in run k is

$$w_{jk} = \frac{1}{P_{jk}}$$

In order to reduce the statistical error due to the variation of the downscaling factor from run to run, we use an averaged weight over the full run range:

$$w_j = \frac{\sum_{k=1}^{N_{\text{runs}}} L_k}{\sum_{k=1}^{N_{\text{runs}}} L_k P_{jk}}$$

where L_k is the integrated luminosity for run k. However this average has only sense on a run period with prescale factors of the same order of magnitude. The weights are determined for each combination of all used subtriggers. Table 5.9 lists the results for both data taking periods 2003-2004 e^+ and 2004-2005 e^-. The high event weights of the first part of the 2003-2004 e^+ data taking period are consistent with the previous prescale study.

2003-2004 e^+ data taking period

$362\,412 \leqslant$ run No. $\leqslant 364\,999$

s15	18	weight
off	on	1.17
on	off	1.27
on	on	1.15

$365\,000 \leqslant$ run No. $\leqslant 373\,658$

s15	18	weight
off	on	1.05
on	off	4.45
on	on	1.05

$374\,272 \leqslant$ run No. $\leqslant 392\,213$

s15	18	weight
off	on	1.01
on	off	1.18
on	on	1.01

2004-2005 e^- data taking period

$415\,905 \leqslant$ run No. $\leqslant 429\,402$

18	19	23	weight
off	off	on	1.25
off	on	off	1.04
off	on	on	1.03
on	off	off	1.12
on	off	on	1.07
on	on	off	1.03
on	on	on	1.02

$429\,402 \leqslant$ run No. $\leqslant 436\,893$

18	19	23	weight
off	off	on	1.12
off	on	off	1.01
off	on	on	1.01
on	off	off	1.06
on	off	on	1.03
on	on	off	1.00
on	on	on	1.00

Table 5.9: Event weights to correct for the prescale factors on the trigger level 1.

Chapter 6

Muon Identification Efficiency

Due to the nature of the interactions of muons with the detector, it is difficult to simulate correctly the response of the detector and it is known that some details of the simulation are not right. However the simulation can be corrected by a reweighting method, which compensates for the wrong description of the data by the simulation. Indeed the simulation has a tendency to overestimate the number of reconstructed muons in the calorimeter. Since the detection of the muons depends on the transverse momentum P_t and the polar angle θ, a correction factor can be determined in the (P_t, θ) space from the ratio of the efficiencies between data and the Monte Carlo simulation. Since muons can be detected in two detectors, the LAr calorimeter and the instrumented iron detector, the efficiencies are determined independently for both.

A data sample of elastic J/ψ mesons is used in order to benefit from its large statistics, and the fact that there are in principle only two muon tracks in the detector. The *elastic* tag of the J/ψ finder is required, as well as the tag *cosmic* to be false in order to suppress cosmic muons. At least two Lee West tracks are required. The same selection for muons than for the medium z selection is applied on the polar angle and the momentum. Also the same invariant mass window is used. The kinematic range of Q^2 is not restricted in order to have the largest statistics. Consequently the data set contains photoproduction and DIS events. Events are mainly triggered by subtrigger s18, track based subtriggers, and in lower proportion by subtrigger s61 (DIS events). Excepted for the iron muon identification efficiency where an independent trigger is mandatory (cf. section 6.2), any subtrigger is required. This selection is summarised in table 6.1.

preselection	
	elastic tag cosmic tag false #Lee West Tracks $\geqslant 2$
Acceptance cuts	
angular cut	$20^\circ \leqslant \theta_\mu \leqslant 160^\circ$
momentum cut	$P_\mu > 0.8\,\mathrm{GeV}$
Selection cuts	
Invariant mass window	$2.8 \leqslant M_{\mu\mu} \leqslant 3.4\,\mathrm{GeV}$

Table 6.1: Selection for the muon identification efficiency

In order to reduce the background and to tag the muonic decay of the J/ψ meson, a muon quality at least equal to a medium calorimeter quality (Quality$_\mu \geqslant 2$) is required for one of the tracks. The second track is expected to be a muon, and will be checked for the efficiency determination. This muon is called *test muon*. In order to have the highest statistic both tracks are studied successively per event.

Figure 6.1 shows the distribution of the momentum, the transverse momentum, the polar angle, and the azimuthal angle of the test muon. The cosmic rejection used here[1] is not sufficient to suppress all the cosmic muons. This is the reason why the distribution of the azimuthal angle is not flat.

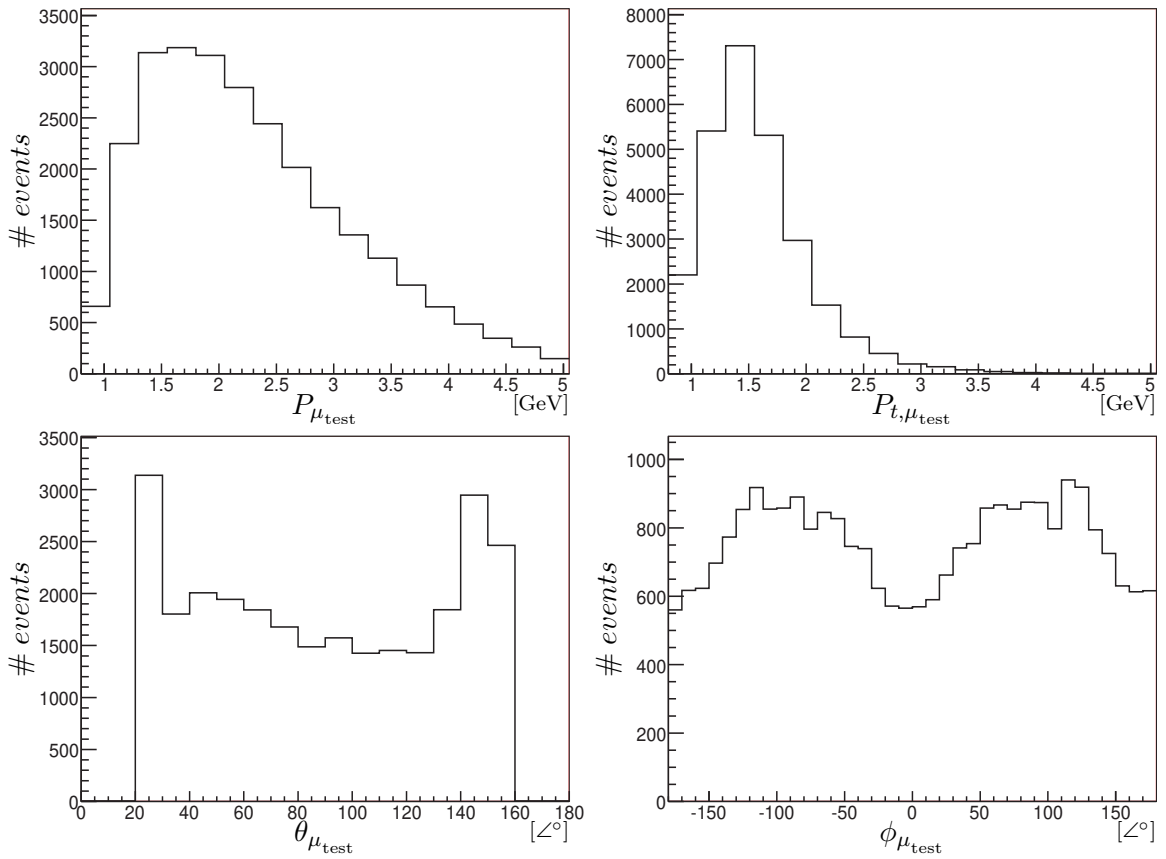

Figure 6.1: Distribution of the momentum, the transverse momentum, the polar angle, and the azimuthal angle of the test muon. Data are from the **2004-2005** e^- data taking period.

The muon identification efficiency will first be presented for the LAr calorimeter and then for the instrumented iron detector. Data from the 2004-2005 e^- data taking period are used. The reason to choose these data for the study is motivated in section 6.2.

[1] The H1OO version used for this thesis does not permit to apply a better rejection like in thesis [75].

6.1 LAr Muon Identification Efficiency

The LAr muon identification efficiency is defined by this formulae:

$$\text{denominator selection} = \text{selection cuts } \wedge \text{ Quality}_{\mu_{\text{tag}}} \geqslant 2 \tag{6.1}$$

$$\text{LAr efficiency} \mathrel{\widehat{=}} \frac{\text{denominator selection } \wedge \left(2 \leqslant \text{LAr Quality}_{\mu_{\text{test}}} \leqslant 3\right)}{\text{denominator selection}} \tag{6.2}$$

The quality of the test muon is tested if it corresponds to a medium or good calorimeter muon quality.

The efficiency is determined in the (P_t, θ) space. For this, the number of J/ψ mesons is extracted by a fit of the invariant mass distribution in each θ or P_t bin. The same method [2] as for the analysis is used with the exception that some bins require an exponential function to describe the background. The background subtraction is mandatory since the background biases the efficiency to lower values.

Figure 6.2 shows the distribution of the polar angle of the test muon in three P_t ranges. The data sample contains mainly J/ψ mesons produced via elastic and proton-dissociative diffraction, but also photon-gluon fusion events at high elasticity z. The DIFFVM Monte Carlo, as well as the EPJPSI Monte Carlo is used to compare data with the simulation. These two contributions are needed to fit the polar angle distribution in data. For $P_t \geqslant 1.2\,\text{GeV}$ events generated with DIFFVM contribute in the backward direction, while events generated with EPJPSI contribute in the forward direction. The relative normalisation is computed by solving the linear system of the number of events in a forward and backward window for data and both Monte Carlo simulations. For bins of θ, the relative normalisation is computed for each P_t range independently. For bins of P_t, the relative normalisation is computed with the full P_t range distribution. The normalised sum of the two contributions fit relatively well the data, excepted for the intermediate P_t range in the central region.

Figure 6.3 shows the LAr muon identification efficiency in bins of the polar angle θ for three P_t ranges and the ratio of these efficiencies between data and the Monte Carlo simulation. Figure 6.4 shows the LAr identification efficiency in transverse momentum P_t bins for three angular regions. As it was said in the introduction, the identification is overestimated in the simulation. For $P_t \leqslant 1.2$ a factor of approximately 0.8 is found between data and the simulation. And for $P_t > 1.2$ a factor of approximately 0.9, since the muons have more energy the efficiency of detection is better. As the LAr calorimeter does not extend to the backward region of the detector, the efficiency of detection falls at the transition to the BBE wheel, at approximately 130°. The correction of the simulation will be discussed in section 6.3.

[2] The method 2 described in section 7.2

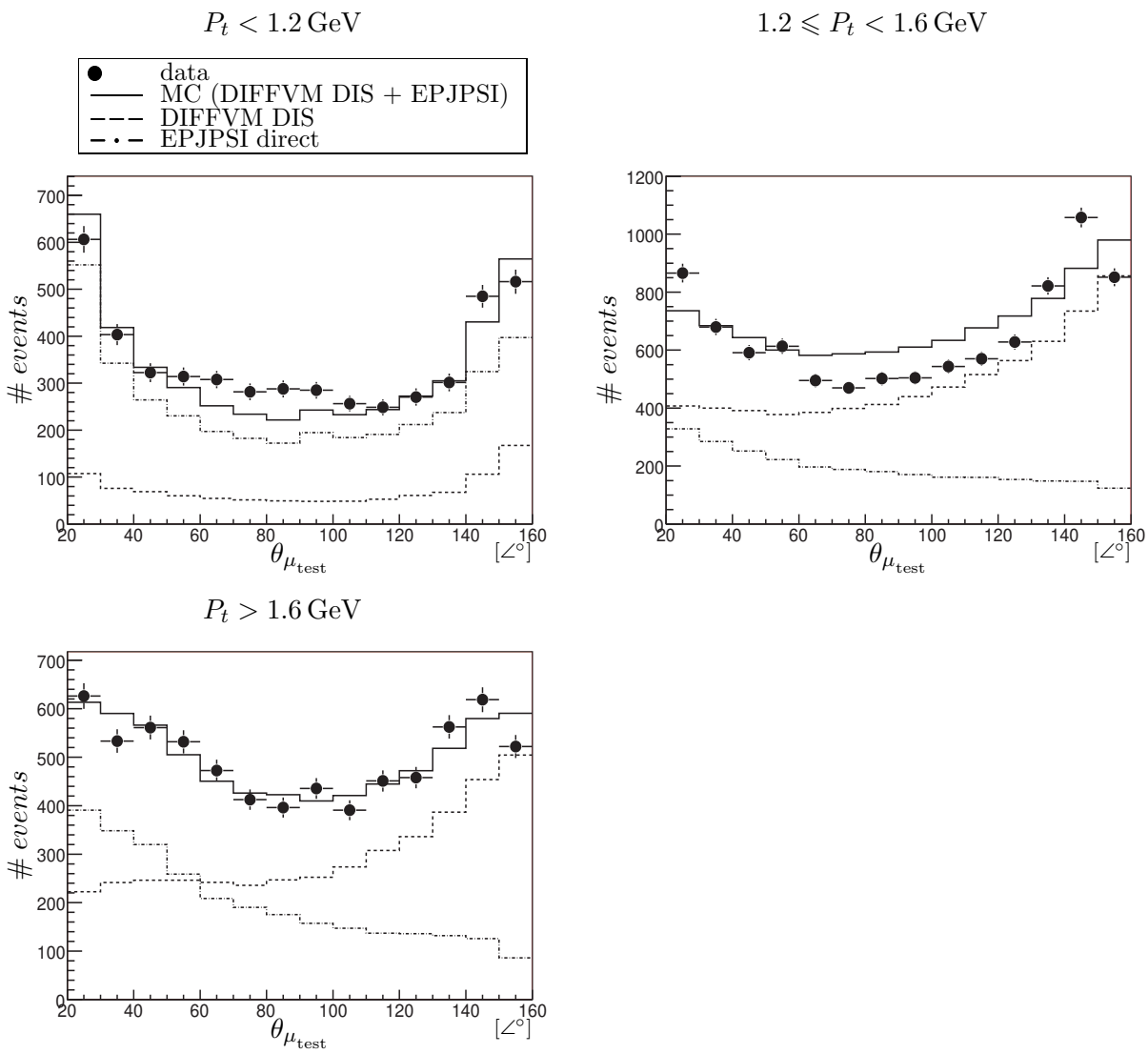

Figure 6.2: Distributions of the polar angle θ of the test muon for three P_t ranges. The contribution of the DIFFVM and EPJPSI Monte Carlo, and the normalised sum of these two contributions are shown.

6.2 Iron Muon Identification Efficiency

In order to have no bias, a trigger monitor without iron conditions has to be required. The same set of triggers as for the iron trigger efficiency is used (cf. section 5.4.1.1). Due to the absence of track based trigger this study cannot be achieved with the data of the 2003-2004 e^+ data taking period, the statistics being too low. This is the reason why data from the 2004-2005 e^- data taking period are used. The same two component simulation is used for the iron muon identification efficiency than for the calorimeter muon identification efficiency. The relative normalisation is computed in a similar way.

The identification efficiency for iron muon is defined by:

$$\text{denominator selection} = \text{selection cuts} \wedge \left(\text{Quality}_{\mu_{\text{tag}}} \geqslant 2 \ \vee \ 2 \leqslant \text{LAr Quality}_{\mu_{\text{test}}} \leqslant 3 \right) \tag{6.3}$$

$$\text{iron efficiency} \mathrel{\widehat{=}} \frac{\text{denominator selection} \ \wedge \ \text{Quality}_{\mu_{\text{test}}} \geqslant 10}{\text{denominator selection}} \tag{6.4}$$

A different selection for the denominator is used in order to not bias the efficiency. The muonic decay can be tagged by the tag muon or by a calorimeter quality for the test muon. The test muon is tested if it is an iron muon.

Figure 6.5 shows the iron muon identification efficiency in polar angle θ bins for three transverse momentum P_t ranges and the ratio of the efficiencies between data and the Monte Carlo simulation. The efficiency of detection is much lower in the forward and central regions than for the LAr detection efficiency, but the efficiency of detection is compensated in the backward direction due to the lack of material in this region. For $P_t > 1.6\,\text{GeV}$ the three data points around the vertical, $\theta = 90\,^\circ$, are approximately 10 % greater in the data than in the simulation. For these two regions the P_t distributions in the simulation do not describe the data, which contain much more events at high P_t. It is certainly due to a contribution of cosmic muons with a high momentum and a good efficiency of detection, which is not included in the simulation and thus bias the efficiency.

Figure 6.6 shows the iron muon identification efficiency in transverse momentum P_t bins for four angular regions. These plots explain why the efficiency of detection is low in the central region. It is nearly impossible to detect a muon in the instrumented iron detector with a transverse momentum less than approximately 1.8 GeV. This threshold effect is of course lower in the forward direction, and still lower in the backward direction due to the lack of material. Since the peak in the transverse momentum distribution of the muons of this data sample is approximately at 1.5 GeV, the majority of them cannot reach the instrumented iron detector. These plots do not show the discrepancies observed in bins of θ for $P_t > 1.6\,\text{GeV}$, and must be used to eventually correct the simulation.

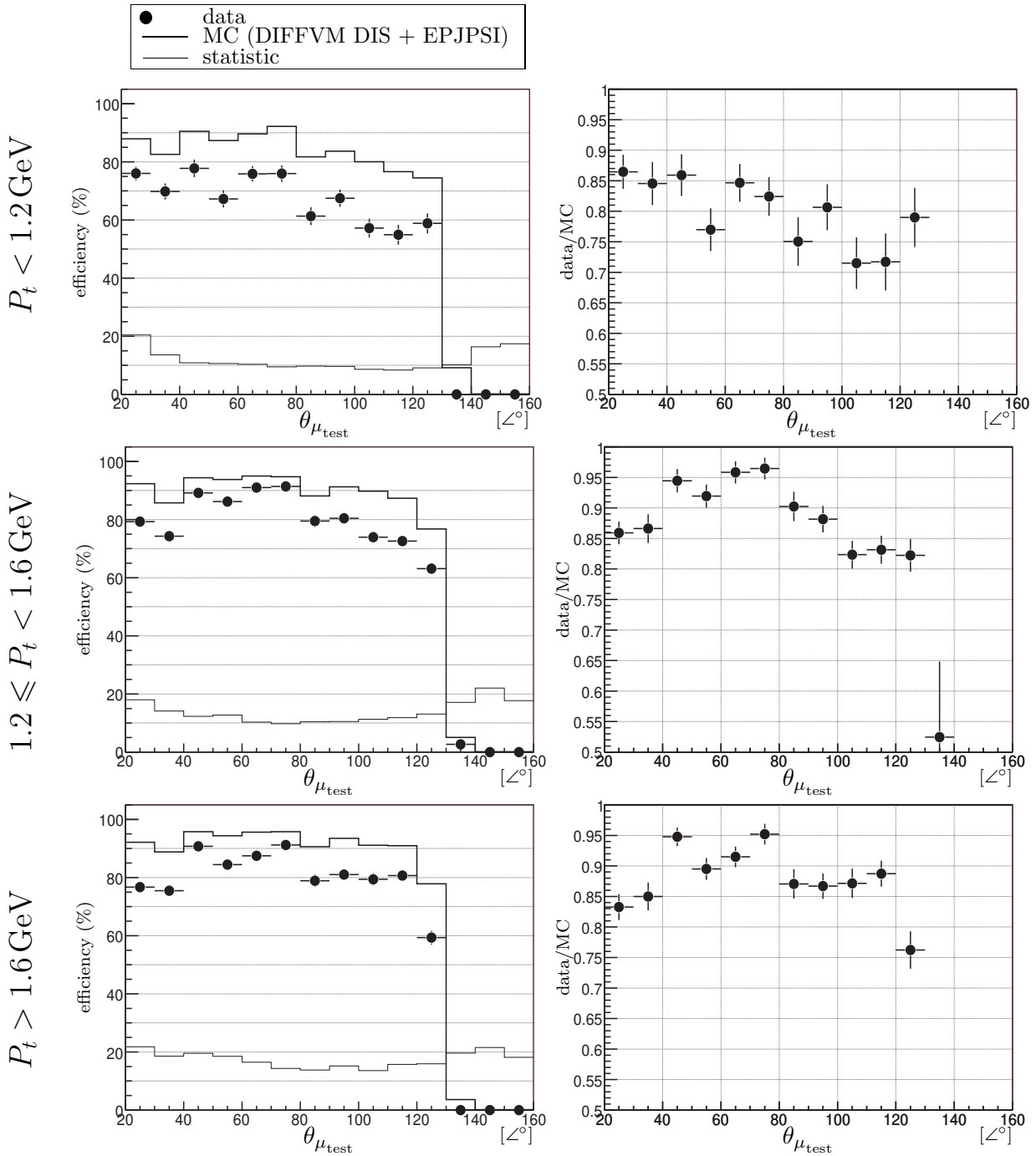

Figure 6.3: LAr muon identification efficiency in bins of polar angle θ for three P_t ranges. Data of the **2004-2005** e^- data taking period are compared with the simulation. The lower histogram shows the statistics. The ratio of the efficiencies between data and the Monte Carlo simulation are shown at right.

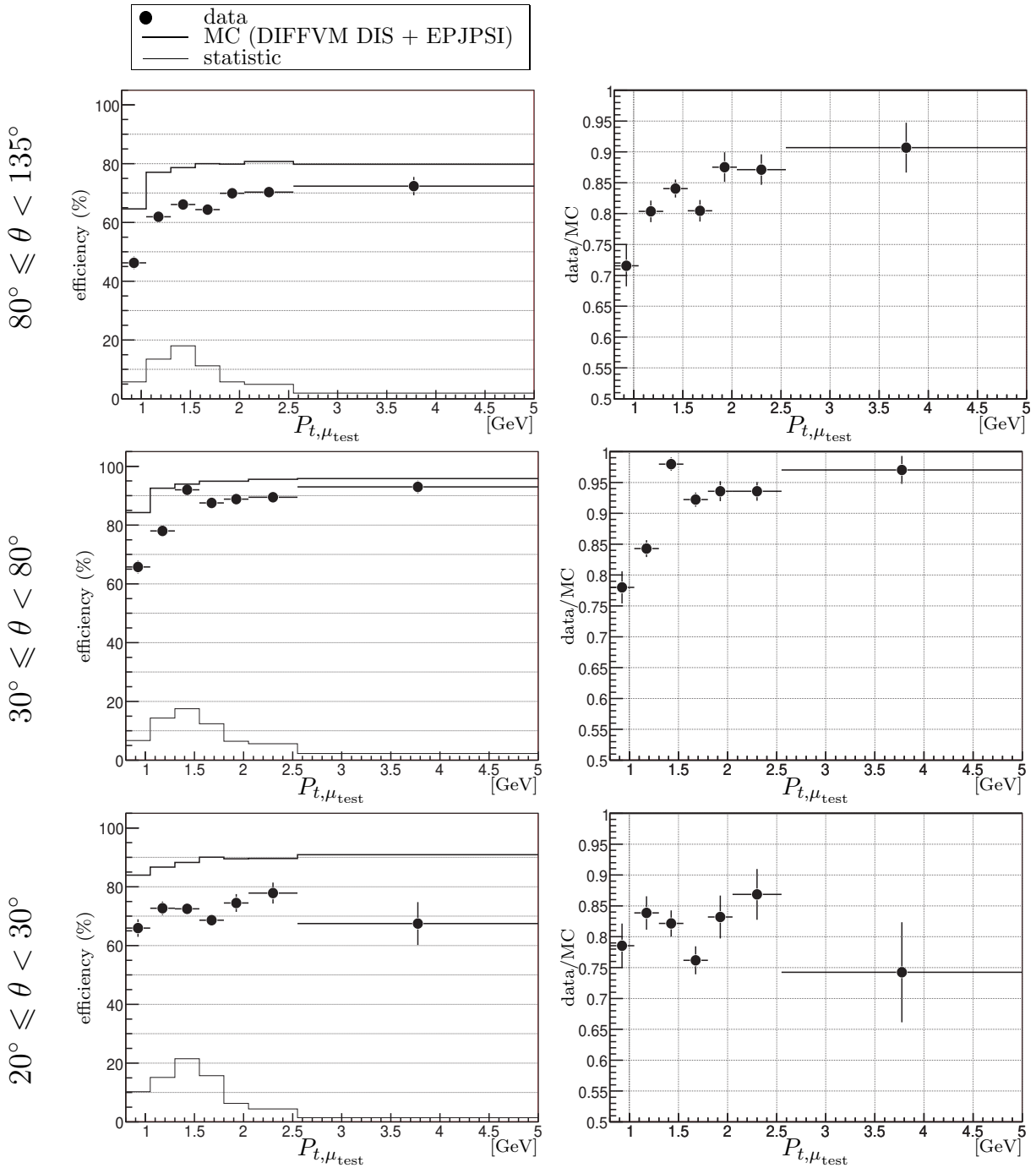

Figure 6.4: LAr muon identification efficiency in bins of transverse momentum P_t for three θ ranges. See figure 6.3 for explanation.

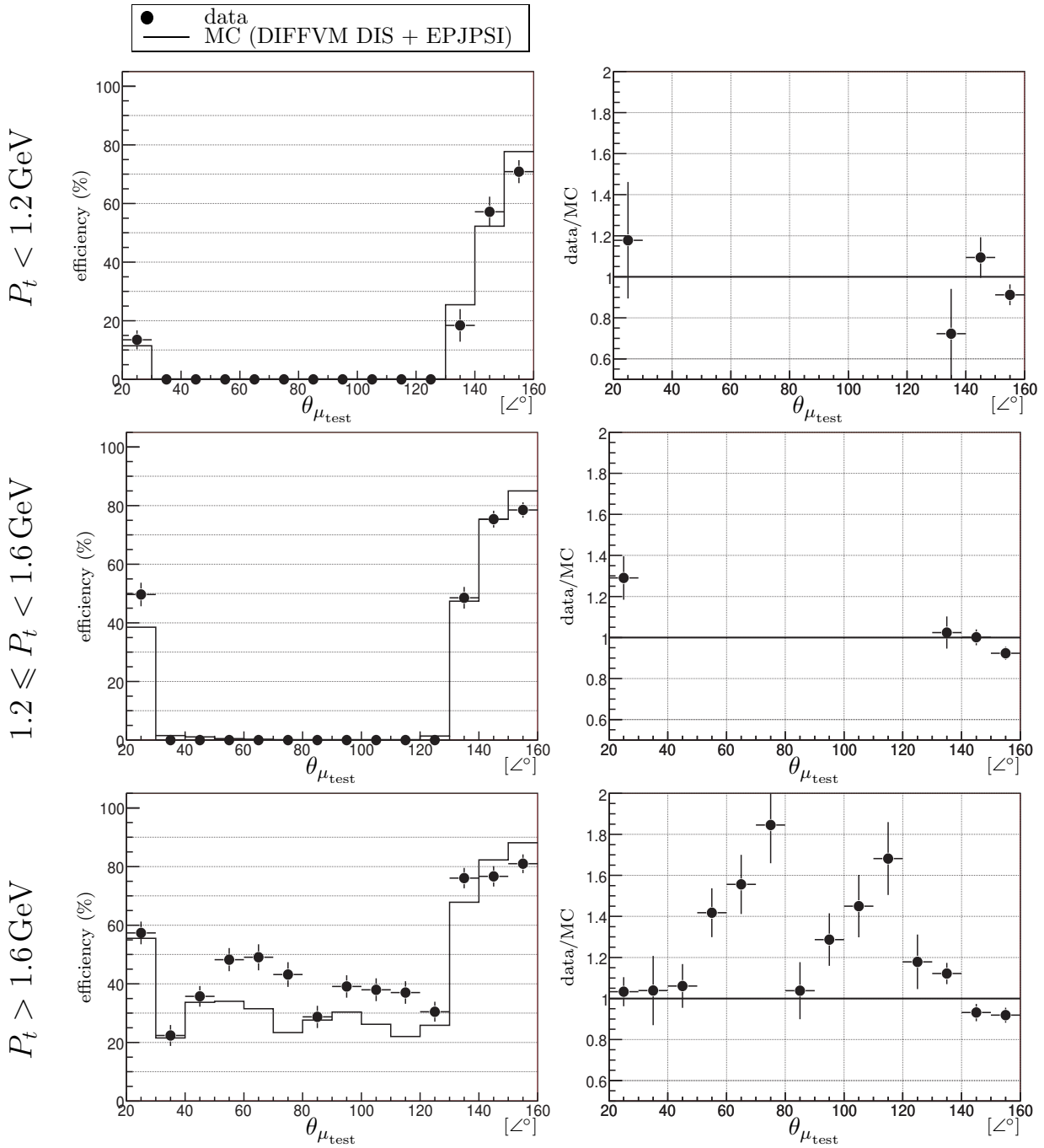

Figure 6.5: Iron muon identification efficiency in bins of polar angle θ for three P_t ranges. See figure 6.3 for explanation. The statistics is not shown in order to improve the visibility.

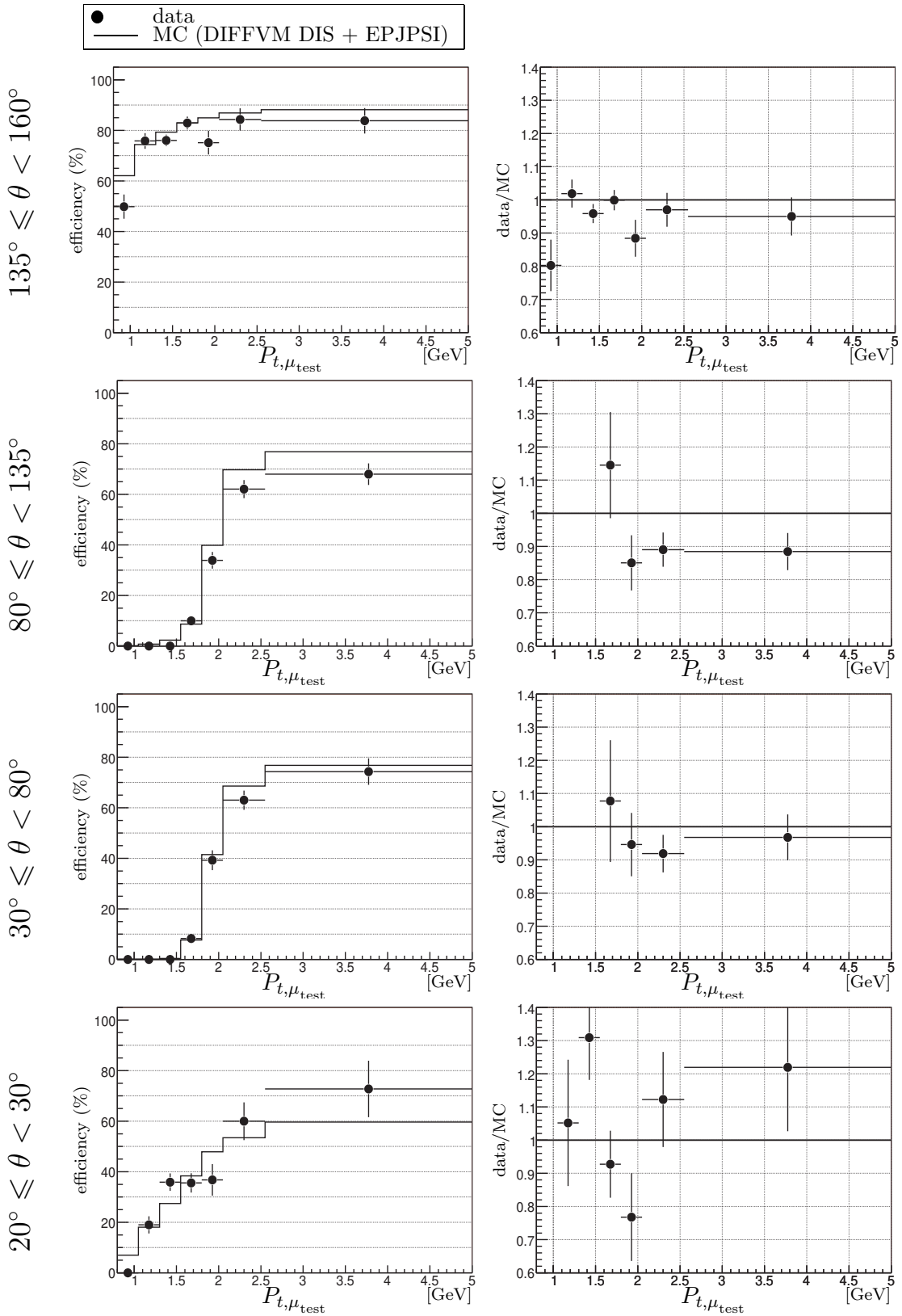

Figure 6.6: Iron muon identification efficiency in bins of transverse momentum P_t for four θ ranges. See figure 6.3 for explanation. The statistics is not shown in order to improve the visibility.

6.3 Muon identification Efficiency Reweighting

Since for the iron identification efficiency data and simulation are approximately compatible within the errors, only the LAr identification efficiency will be corrected for the 2003-2004 e^+ data taking period. This is also motivated by the fact, that it is impossible to study the iron identification efficiency for the 2003-2004 e^+ data taking period. Consequently the reweighting of the simulation is only determined with data from the 2004-2005 e^- data taking period and applied to both data taking periods. The purpose of this reweighting is to correct at the first order the Monte Carlo simulation, which is coherent with the low statistics available for this analysis. However following analyses should profit of the huge statistics of the full HERA II data taking period for the elastic J/ψ meson events to study more accurately the muon identification. The correction factors are set to one for polar angles greater than 130 °, where the LAr calorimeter stops to identify muons. For the 2004-2005 e^- data taking period the iron muon identification is also corrected in the simulation, using the ratio in bins of P_t of figure 6.6. A linear interpolation is used to compute the correction factor applied to events.

The result of the reweighting of the simulation for the LAr muon identification efficiency is shown in figure 6.7 and for the iron muon identification efficiency in figure 6.8, respectively. Now data and simulation are compatible within the errors. But for the LAr muon identification efficiency the first and the last bin of the central region have the tendency to be to too efficient in the simulation.

It is not possible to repeat the analysis without the requirement of identified muons in order to calculate the systematic error of the muon identification efficiency. Since only the LAr muon identification efficiency is corrected for the 2003-2004 e^+ data taking period, the systematic error for the iron muon identification efficiency is not determined. The analysis of the 2004-2005 e^-data being difficult, the systematic error for the iron muon identification efficiency are not considered. Therefore the remaining differences in the identification efficiency as a function of the polar angle are used to estimate the uncertainty. Since some statistical fluctuations are expected and should not be included in a systematic error, only half of the differences are used. The systematic error is calculated as a weighted quadratic average of half of the differences of the efficiency in the data and the simulation:

$$\text{systematic error} = \sqrt{\sum_{bins} N_i \left(\frac{\epsilon_{data,i} - \epsilon_{MC,i}}{2} \right)^2 / \sum_{bins} N_i},$$

where the weight N_i are the number of events in the polar angular distribution of the calorimeter muons for the corresponding transverse momentum range. The quadratic sum of the systematic errors of each ranges is used to obtain the total value. The systematic errors of the LAr muon identification are given for each analysis region in table 6.2.

low z	2.5 %
medium z	2.8 %

Table 6.2: Systematic errors of the LAr muon identification reweighting for each analysis region.

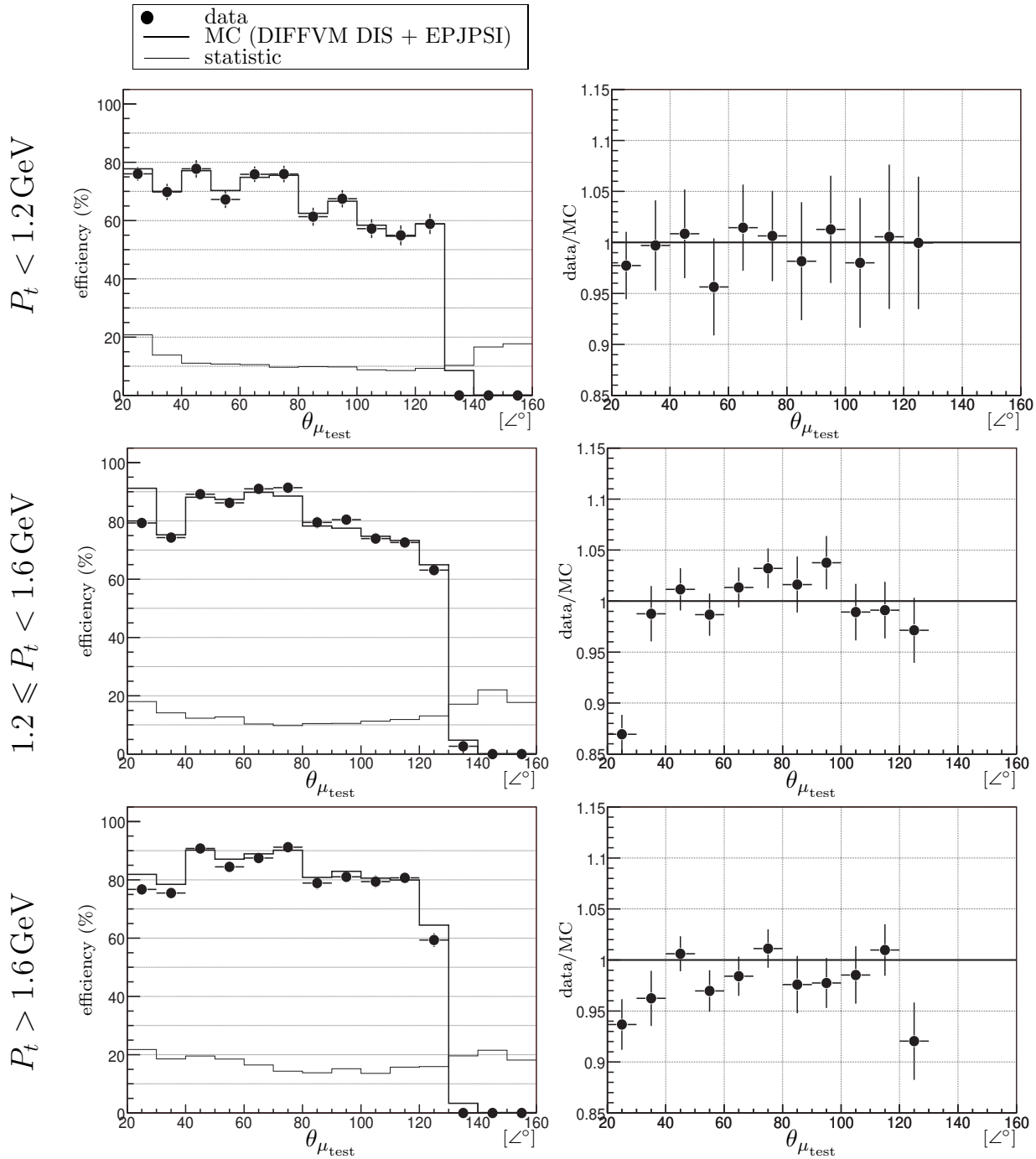

Figure 6.7: LAr muon identification efficiency in bins of polar angle θ after reweighting of the simulation. See figure 6.3 for explanation.

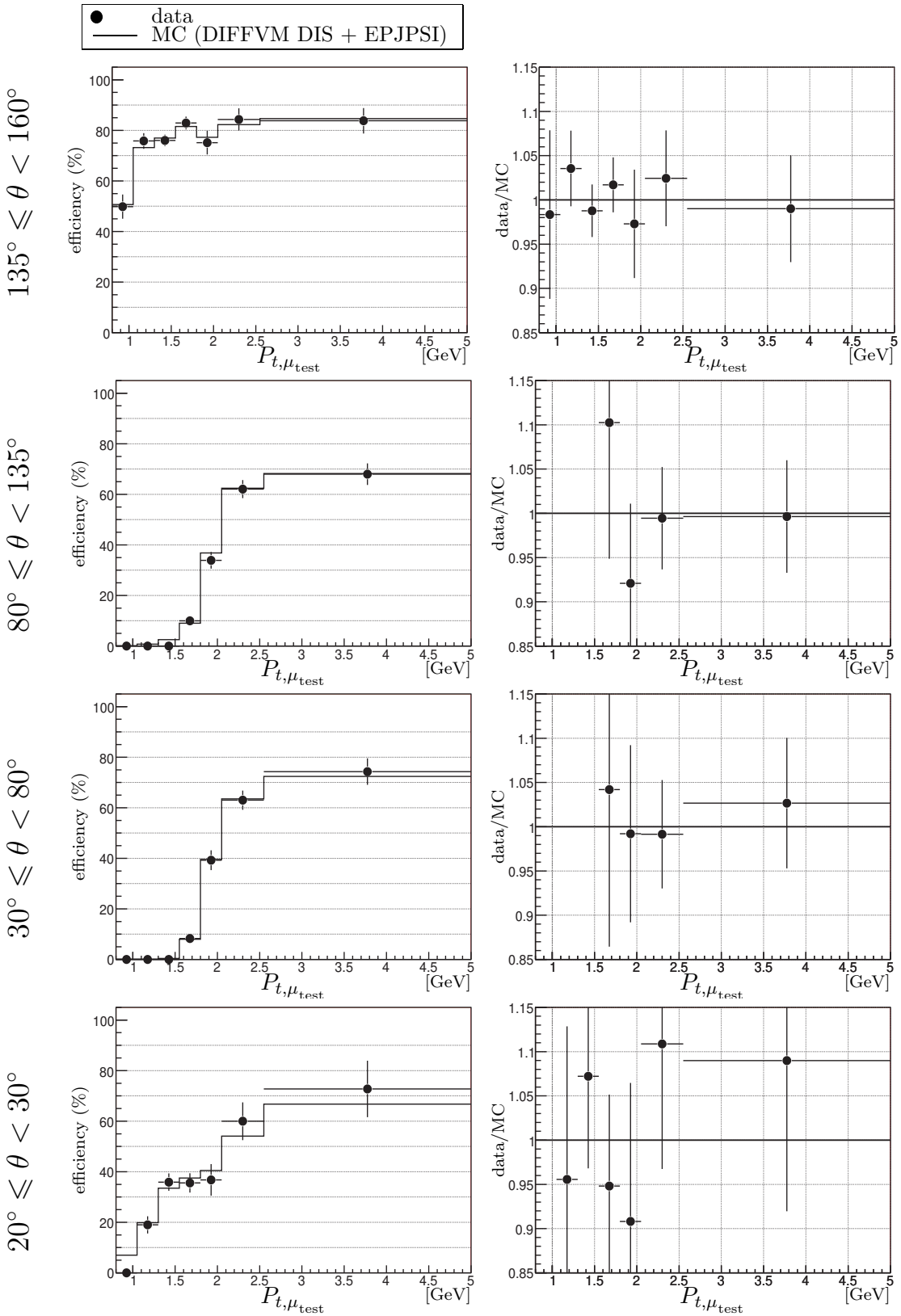

Figure 6.8: Iron muon identification efficiency in bins of transverse momentum P_t after reweighting of the simulation. See figure 6.3 for explanation. The statistics is not shown in order to improve the visibility.

Chapter 7

Cross Section Measurement

The results for the photoproduction of J/ψ mesons will be discussed in this chapter for the low and medium z selections. The first section will present the selected data sample. Then the determination of the number of J/ψ mesons and the method to subtract the non-resonant background will be described. Monte Carlo simulations of direct photon-gluon fusion (EPJPSI-direct) and resolved photon processes (EPJPSI-resolved) will be normalised and compared to the data. Then the systematic error will be determined, and finally the cross sections will be presented.

7.1 Selected Data Samples

The number of events which remain after applying the cuts described in chapter 4 are listed in table 7.2 for the low z selection and in table 7.3 for the medium z selection, respectively. The corresponding percentage of events which remain after the cuts, the number of non-resonant background events in the mass window, and the signal over background ratios are also given. The cut that reduces the number of events most is the muon quality requirement, but it improves at the same time the signal over background ratio. For the low z selection, the z cut restricts strongly the J/ψ meson statistics. Moreover the signal over background ratio is worse since the combinatorial background is higher at low elasticity. For the medium z analysis it is the inverse. The $P^2_{t,\psi}$ cut improves also the signal over background at medium z, but this is not the case at low z.

The invariant mass distribution of the muon pairs corresponding to the final selection (last row of the table) for each analysis region is shown in figure 7.1. Both analysis regions show a clear J/ψ meson signal. Of course, for the 2004-2005 e^- data taking periods the signal is strongly affected by the malfunction of the level 4 finder. The non-resonant background is relatively flat, especially at medium z. The invariant mass distribution is fit with a double Gaussian for the signal and a second degree polynomial for the non-resonant background.

The yields of inelastic J/ψ mesons computed from figure 7.1 using the method 2 (cf. section 7.2) are given in table 7.1. These values differ from the yields shown in chapter 5 due to the accuracy of their determination in luminosity bins.

Figure 7.3 and figure 7.2 show the percentage of remaining events for each cut of the selection in invariant mass bins at medium z and low z, respectively. The background is not subtracted here contrary to the signal over background ratio given in the tables. For both analysis regions, the muon quality requirement improves the signal. The cut on the elasticity z improves also the signal at medium z, while at low z it has the inverse effect.

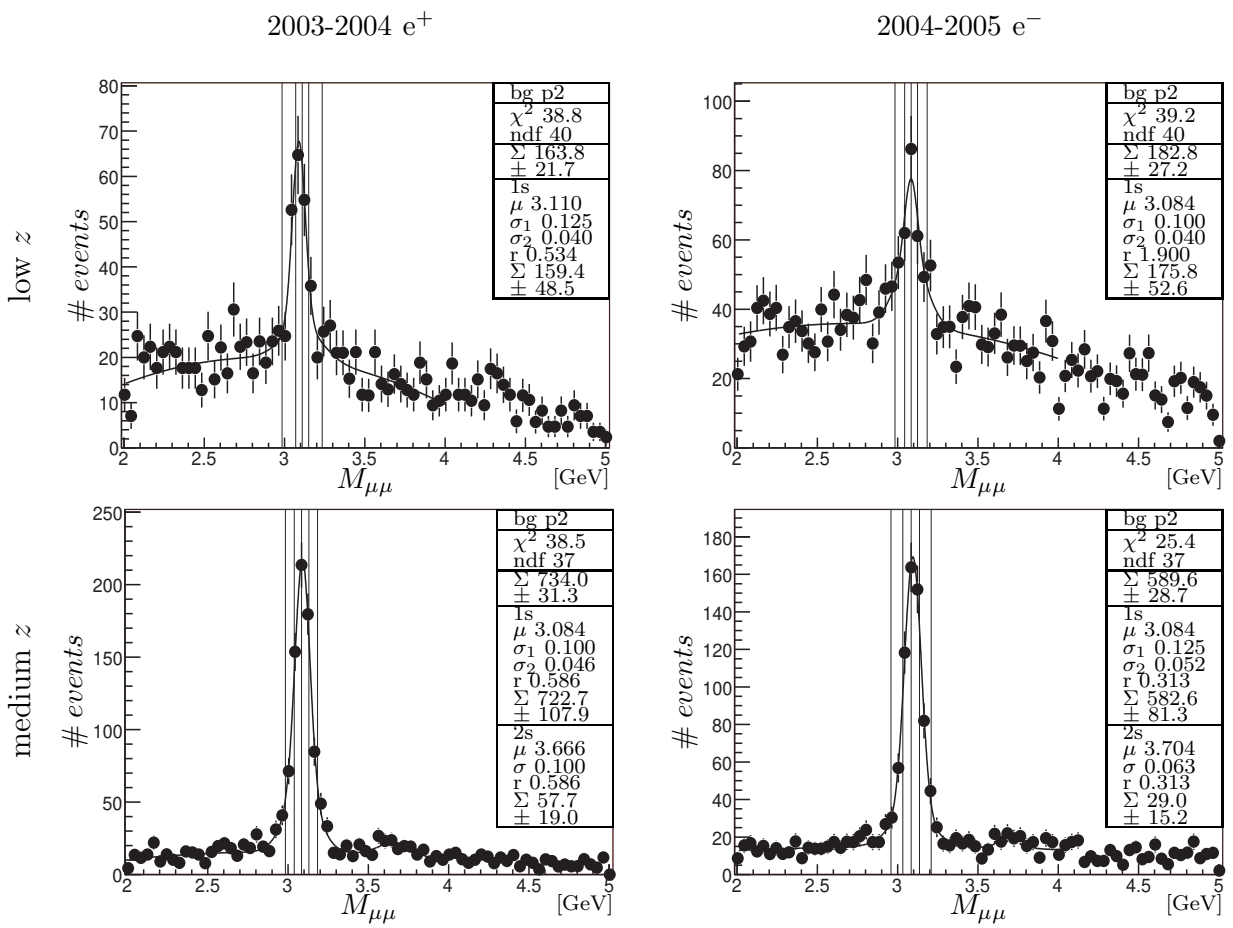

Figure 7.1: Invariant mass distributions of the muon pairs for each selection in the two data taking periods. The number of events are corrected for prescale. The invariant mass distribution is fit with a double Gaussian and a second degree polynomial for the non-resonant background. The parameters given in the box are explained in section 7.7.

data taking period	2003-2004 e^+	2004-2005 e^-
integrated luminosity [pb^{-1}]	23.5	60.1
number of J/ψ mesons per pb^{-1}		
low z	7 ± 0.9	3 ± 0.5
medium z	31 ± 1.3	10 ± 0.5

Table 7.1: Yield of the inelastic J/ψ mesons computed from figure 7.1

selection	2003-2004 e^+				2004-2005 e^-			
	inelastic J/ψ meson preselection							
	s15 or s18				s19 or s23 or s18			
	$\mathcal{N}_\psi$		bg	sg/bg	$\mathcal{N}_\psi$		bg	sg/bg
# J/ψ candidates	2 409		6 069	0.4	2 592		12 389	0.2
acceptance cut	1 673	69.4 %	3 183	0.5	1 507	58.1 %	6 152	0.2
μ quality cut	968	57.9 %	840	1.2	1 158	76.9 %	1 413	0.8
photoproduction	914	94.4 %	751	1.2	941	81.2 %	1 146	0.8
$.05 \leqslant z \leqslant .45$	259	28.4 %	584	0.4	266	28.3 %	945	0.3
$P^2_{t,\psi} > 1\,\mathrm{GeV}^2$	213	82.3 %	451	0.5	245	92.1 %	764	0.3
$120 \leqslant W_{\gamma\mathrm{p}} \leqslant 260\,\mathrm{GeV}$	159	74.9 %	328	0.5	181	74.0 %	601	0.3

Table 7.2: Number of selected events for each cut of the **low** z selection (cf. table 4.8). The J/ψ meson candidates are selected by the preselection described in section 4.1.4 and with the subtrigger combination used for each data taking periods. The number of events are corrected for prescale. The corresponding percentage of events which remain after the cut, the number of non-resonant background events in the mass window, and the signal over background ratio are also given.

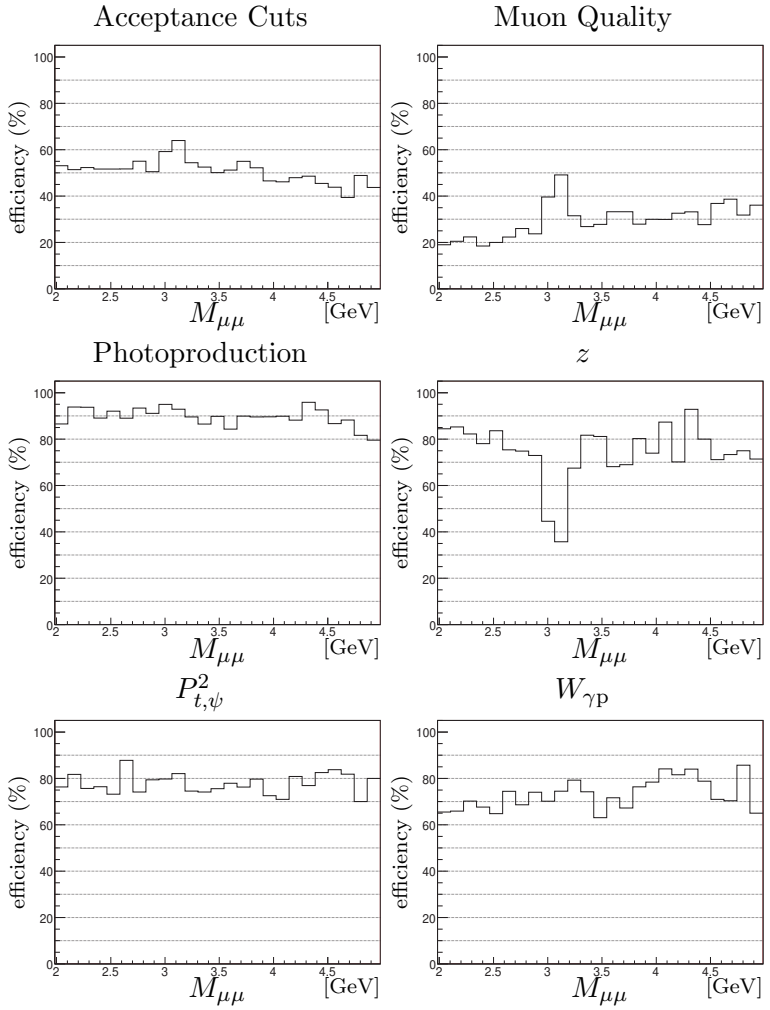

Figure 7.2: Efficiency of the selection cuts in invariant mass bins for the **low** z selection.

selection	2003-2004 e^+				2004-2005 e^-			
	inelastic J/ψ meson preselection							
	s15 or s18				s19 or s23 or s18			
	$\mathcal{N}_\psi$		bg	sg/bg	$\mathcal{N}_\psi$		bg	sg/bg
# J/ψ candidates	2 420		6 055	0.4	2 604		12 375	0.2
acceptance cut	2 341	96.7 %	5 315	0.4	2 302	88.4 %	10 266	0.2
μ quality cut	1 448	61.9 %	1 275	1.1	1 726	75.0 %	2 081	0.8
photoproduction	1 313	90.7 %	1 191	1.1	1 415	82.0 %	1 701	0.8
$0.45 \leqslant z \leqslant 0.9$	985	75.1 %	426	2.3	914	64.6 %	381	2.4
$P^2_{t,\psi} > 1\,\mathrm{GeV}^2$	791	80.3 %	271	2.9	675	73.8 %	281	2.4
$60 \leqslant W_{\gamma\mathrm{p}} \leqslant 240\,\mathrm{GeV}$	733	92.6 %	254	2.9	595	88.2 %	244	2.4

Table 7.3: Number of selected events for each cut of the **medium** z selection (cf. table 4.6). The J/ψ meson candidates are selected by the preselection described in section 4.1.4 and with the subtrigger combination of each data taking periods. See table above for comments.

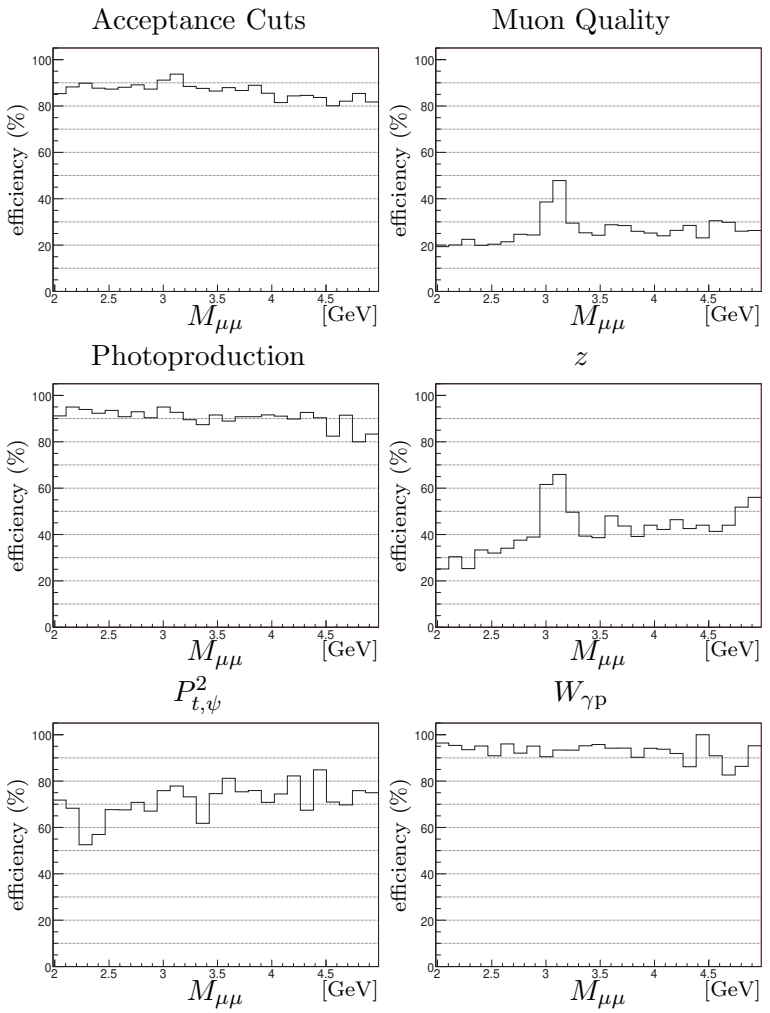

Figure 7.3: Efficiency of the selection cuts in invariant mass bins for the **medium** z selection.

7.2 Background Subtraction

At the end of the selection chain described in the previous chapter, a significant non-resonant background in the invariant mass distribution is still present. This background consists mainly of muon candidate pairs, where one or both particles are hadrons misidentified as muons. Events with two independent muons can also constitute a source of background. The amount and the shape of this background depends on the number of charged particles in the event, which is strongly correlated with the elasticity z, but also with the photon-proton centre-of-mass energy $W_{\gamma p}$.

Three approaches can be used to determine the number of J/ψ mesons:

- The first method (method 1) is to fit in each analysis bin the invariant mass distribution of the unlike-sign muon pairs with a function corresponding to a superposition of a Gaussian for the J/ψ signal and a polynomial function for the non-resonant background. Often a double Gaussian describes the signal better. However the real shape is still more complex, due to the momentum dependence of the tracker resolution. Despite a better description, a double Gaussian is more difficult to fit and produces instabilities. So to "help" the fit, the binning is centred on the average mass of the J/ψ meson, and the bin width is set to a value near the tracker resolution for the J/ψ meson, e.g. 0.04 GeV. This binning prevents an overshoot when the position of the Gaussian is between two bins. Like this the normalisation of the Gaussian is constrained by three data points near $\mu - \sigma$, μ and $\mu + \sigma$.

  The position and the width of the Gaussian are determined from a fit of the selected data sample. In order to have the highest statistics, the cuts on $P^2_{t,\psi}$ and $W_{\gamma p}$ are not applied for this fit. Due to the number of free parameters, the fit is unstable and can give different results for different selections and jobs. The data sample of the medium z selection and the 2003-2004 e^+ data taking period was used for this fit, because it has the largest statistics. Table 7.4 give the resulting parameters. These parameters was determined once and fixed afterwards.

Simple Gaussian	
μ	3.088 $\pm$ 0.002 GeV
σ	0.057 $\pm$ 0.003 GeV
Double Gaussian	
μ	3.087 $\pm$ 0.013 GeV
σ_1	0.100 $\pm$ 0.018 GeV
σ_2	0.046 $\pm$ 0.004 GeV
relative normalisation	0.557

Table 7.4: Position and width(s) of the Gaussian(s) used for the fit of the invariant mass distributions. The relative normalisation of the two components are given for the double Gaussian fit.

- For the second method (method 2) the number of J/ψ mesons is calculated by counting the number of the unlike-sign muon pairs in the mass window $2.8 \leqslant M_{\mu\mu} \leqslant 3.4$ GeV used for the selection and subtracting the non-resonant background obtained using the background fit described in the first method. This method is not as sensitive to the shape and the width of the peak as the number of events under the Gaussian obtained from the fit. The statistical error of the total number of muon pairs in the mass window is used as an estimator for the error of the number of J/ψ mesons.

- The side-band method is a third method to subtract the non-resonant background. The distribution corresponding to the selection for the J/ψ mesons is subtracted with the distribution for the background, i.e. the invariant mass cut is replaced by two invariant mass window framing the signal. The background distribution is scaled to the invariant mass window with the factor $w/(l-w)$, where w is the width of the invariant mass window used for the signal, and l is the width of the invariant mass window corresponding to the lower and upper mass cut used for the background distribution.

The method 1 and 2 are compared for each analysis region in figure 7.4 for the 2003-2004 e^+ data taking period, and in figure 7.5 for the 2004-2005 e^- data taking period, respectively. Numbers obtained directly from the first method are usually smaller than the ones obtained from the second method. As it was said previously there is no reason that a Gaussian describes the signal. However the differences are not larger than the statistical error. The second method is used to determine the number of J/ψ mesons in the analysis bins, since it is more robust

The signal over background ratio is shown in figure 7.6 for each analysis region. The amount of background is correlated with the combinatorial background, which depends on the number of tracks in the event and is thus correlated with the elasticity.

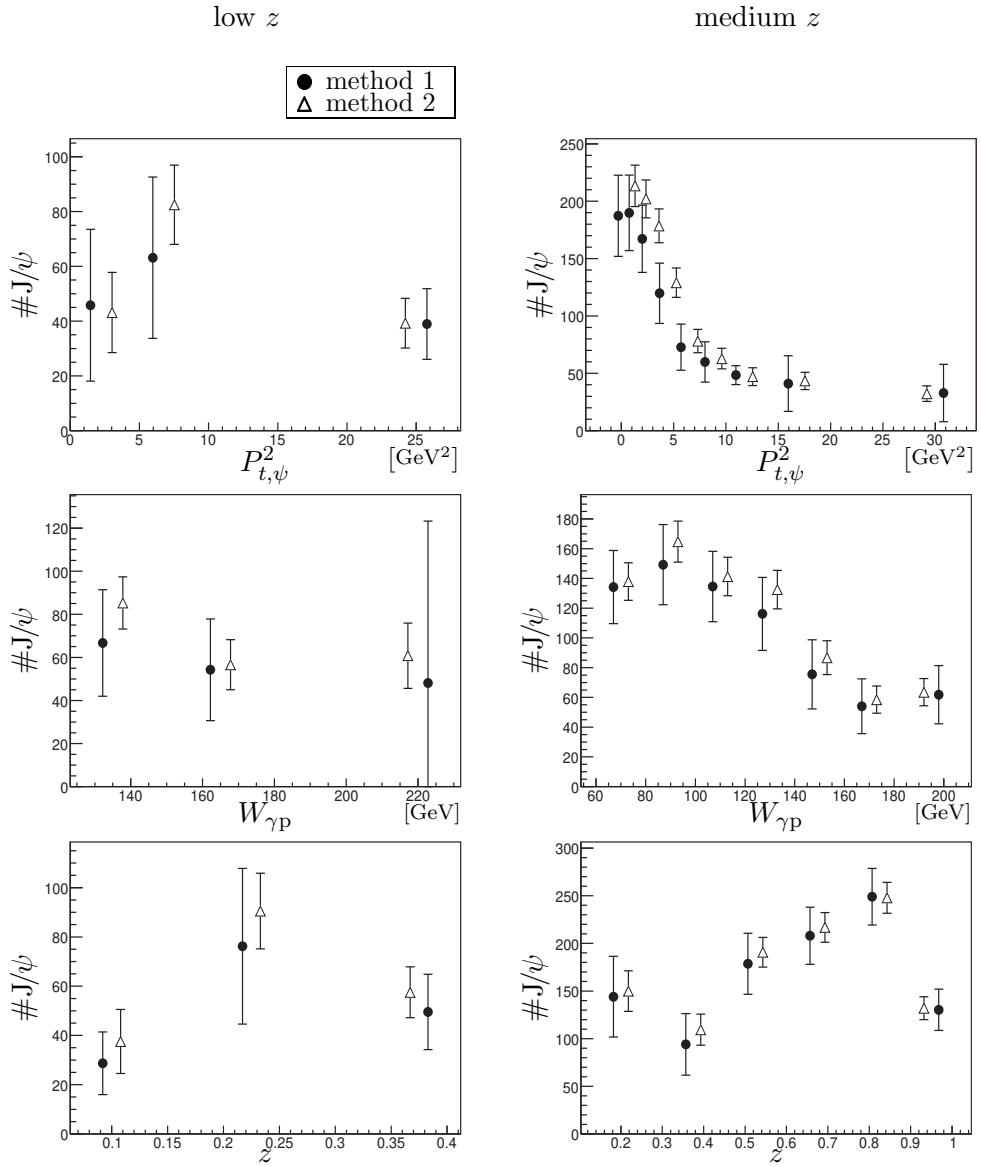

Figure 7.4: Comparison of the method 1 and 2 to determine the number of J/ψ mesons for each analysis region. The data points of the two methods are shifted to improve visibility, the order of the points for each period is conserved. Data are from the **2003-2004** e^+ data taking period.

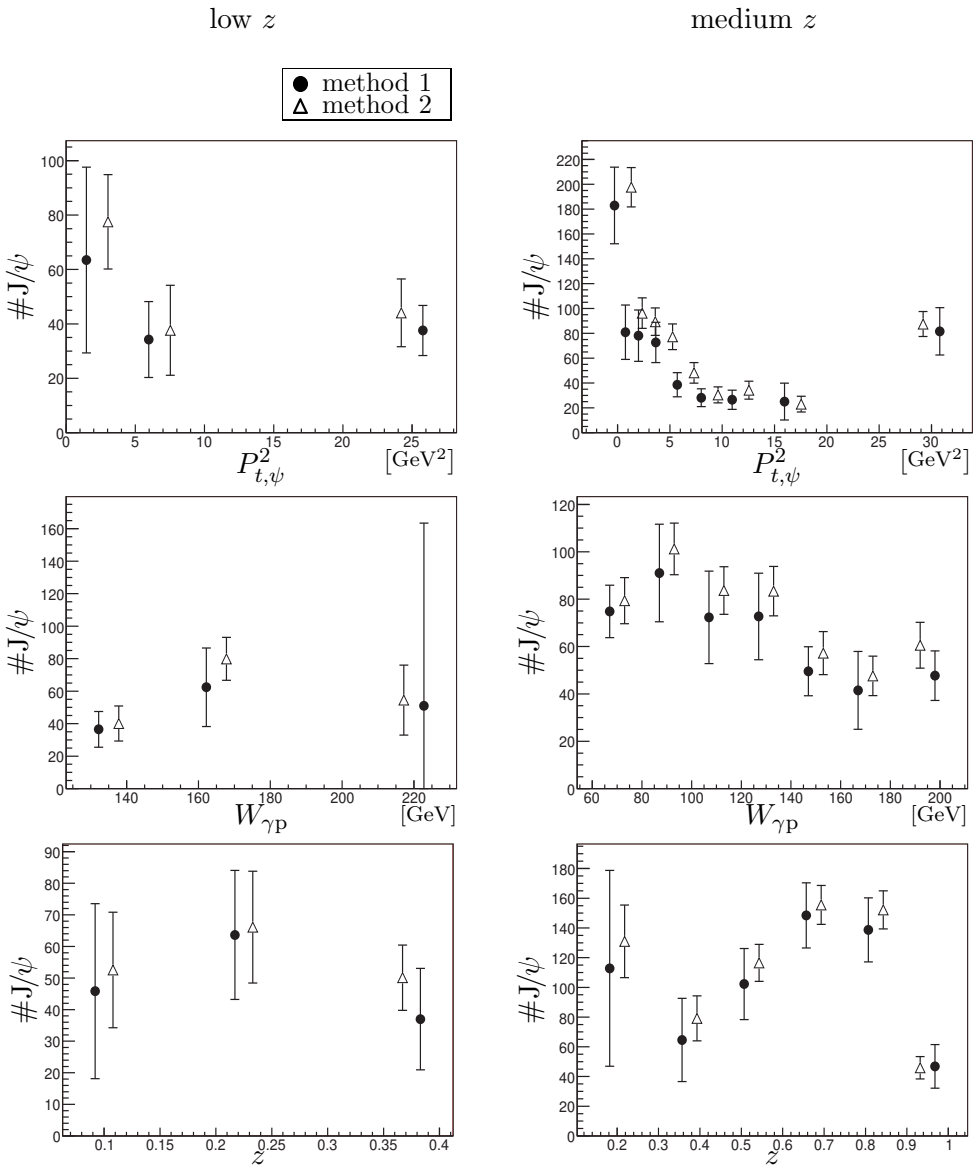

Figure 7.5: Comparison of the method 1 and 2 to determine the number of J/ψ mesons for each analysis region. The data points of the two methods are shifted to improve visibility. Data are from the **2004-2005** e^- data taking period.

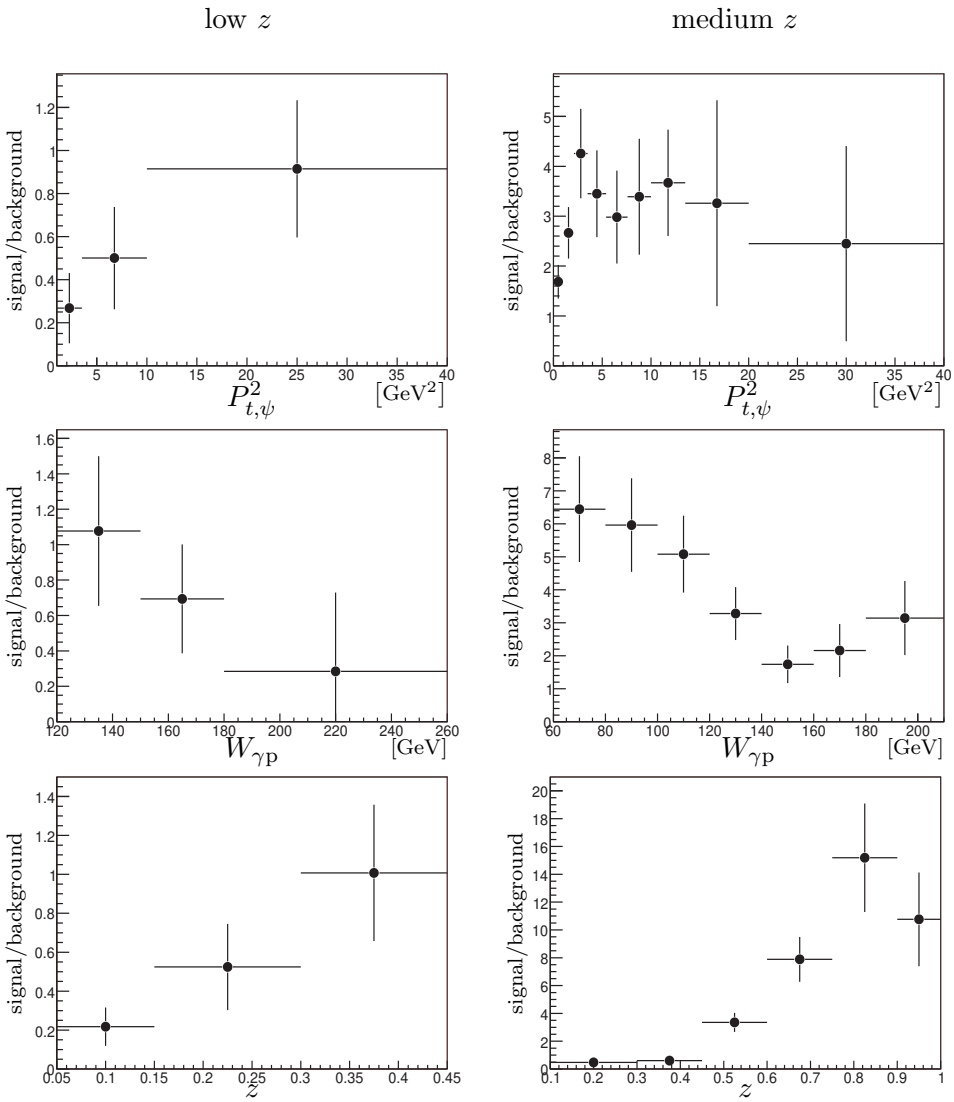

Figure 7.6: Signal over background for each analysis region. Data are from the **2003-2004** e^+ data taking period.

7.3 Comparison with the Simulation

In order to extract cross sections, the measured distributions have to be corrected for the acceptance and efficiency of the selection discussed in chapter 4. These efficiencies are determined from the simulation. Direct and resolved photon processes may contribute to the production of J/ψ mesons, which are simulated separately in the EPJPSI Monte Carlo program. The normalisation of the simulation of both contributions will be determined. The cross section predicted by the EPJPSI Monte Carlo program is only expected to describe correctly the shapes of the differential cross section (excepted for $P^2_{t,\psi}$). Data and this two component simulation will then be compared.

7.3.1 Reweighting of $P^2_{t,\psi}$

Figure 7.7 shows the distribution of the transverse momentum squared of the J/ψ meson $P^2_{t,\psi}$ for data compared with the EPJPSI Monte Carlo simulation for the medium z selection. The

normalisation of the two component simulation explained in the next section 7.3.2 was performed without the reweighting of $P^2_{t,\psi}$. The shape of the distribution in the simulation does not agree with the data, and the ratio of the number of events for data to the Monte Carlo simulation shows a clear tendency in figure 7.7 b). This is not surprising since the generator EPJPSI is a leading-order program and the $P^2_{t,\psi}$ spectrum is much harder in next-to-leading order calculations than in leading order [17]. The simulation is therefore reweighted by a second order polynomial as a function of $P^2_{t,\psi}$. Since the same effect is observed for the low z selection, the same reweighting is applied. All the distributions for the simulation shown in this thesis are reweighted. The reweighted simulation is compared to data in figure 7.9.

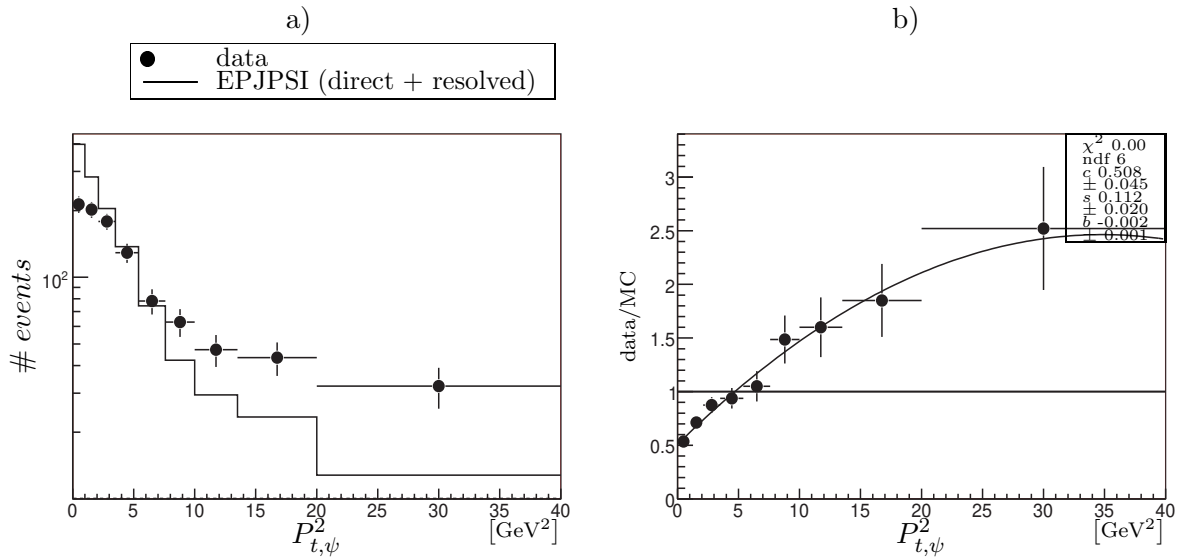

Figure 7.7: a) Distribution of $P^2_{t,\psi}$ for data compared with the EPJPSI Monte Carlo for the **medium** z selection. b) ratio between data and Monte Carlo fitted with a second order polynomial. See the text for a remark on the normalisation of the two component simulation used here.

7.3.2 Normalisation of the Simulations

The variable which allows the best distinction between direct and resolved photon processes is the elasticity z. Resolved photon processes are expected to contribute only below $z < 0.4$, while the direct photon process contribution dominates from medium to high z, and gives only a small contribution at low z. At very high z, background from diffractive J/ψ production is expected. This is nearly completely removed by the requirement of $z < 0.9$. J/ψ mesons originating from the decay of ψ(2S) mesons which are produced in elastic and proton dissociative processes are significantly reduced by the cut $P^2_{t,\psi} > 1\,\mathrm{GeV}^2$.

The following procedure is applied to determine the normalisation factors of the two component simulation:

- Firstly, we determine the "direct" normalisation factor f_{direct}. For $0.45 < z < 0.9$ we have the cross section equality

  $$\sigma_{data} = f_{direct} \times \sigma_{direct}$$

  Which gives the factor for the direct contribution

  $$f_{direct} = \frac{N_{data}}{L_{data}} \frac{L_{direct}}{N_{direct}}$$

Where N is the total number of events in the z range $0.45 < z < 0.9$, and L is the corresponding integrated luminosity.

- Then we determine the "resolved" normalisation factor $f_{resolved}$. For $0.05 < z < 0.45$ we have the cross section equality

$$\sigma_{data} = f_{direct} \times \sigma_{direct} + f_{resolved} \times \sigma_{resolved}$$

Which gives the factor for the resolved contribution

$$f_{resolved} = \left(\frac{N_{data}}{L_{data}} - f_{direct} \frac{N_{direct}}{L_{direct}} \right) \frac{L_{resolved}}{N_{resolved}}$$

Figure 7.8 shows the normalisation of the two component simulation. The simulation agrees relatively well with data for the medium z selection. Except for one bin, $0.3 \leqslant z < 0.45$, which is lower than the others in data. For the low z selection the sum of resolved and direct processes describes also relatively well the data. But a third contribution from B mesons may be sizeable. The normalisation factors are given in figure 7.8. The normalisation factors are determined with data of the 2003-2004 e^+ data taking period, and are used for both data taking period.

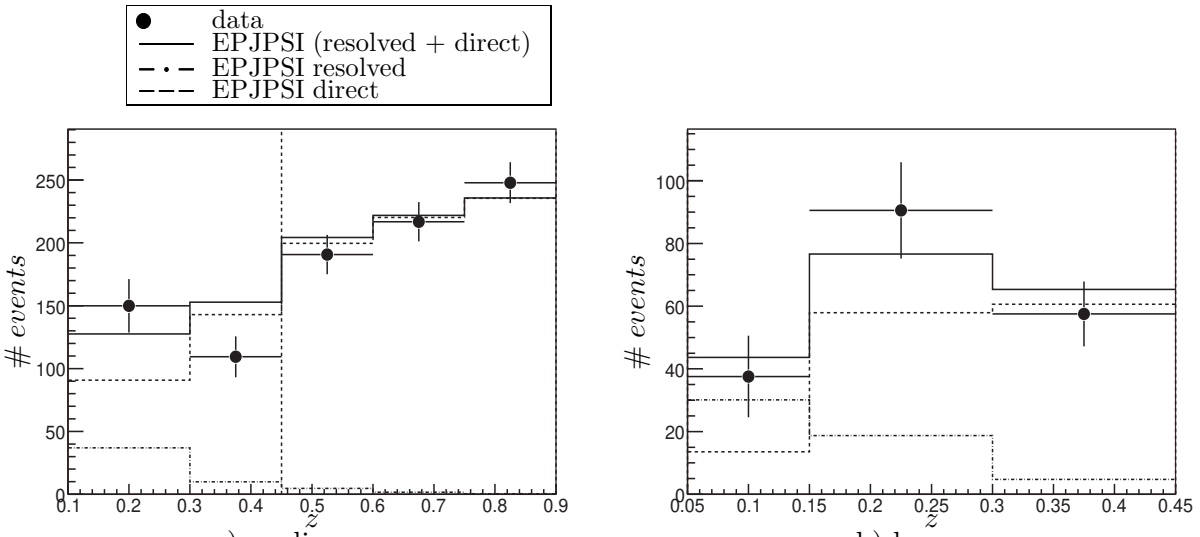

a) medium z b) low z

Normalisation factors	
EPJPSI direct	1.515
EPJPSI resolved	0.675

Figure 7.8: Normalisation of the two component simulation. a) at **medium** z and b) at **low** z. The normalisation factors are given in the table. Data are from the 2003-2004 e^+ data taking period.

7.3.3 Distributions of Observables

The distributions of several observables are compared between data of the 2003-2004 e^+ data taking period and the normalised two component simulation in figure 7.9 to 7.10 for the medium z selection and in figure 7.11 to 7.12 for the low z selection, respectively. The selection cuts are given in table 4.6 for the medium z selection and in table 4.8 for the low z selection, respectively.

The non-resonant background is subtracted by the same method as for the cross section measurement (method 2). The side-band method was used in previous analyses and was also tried because it is simple. But for this analysis the method 2 gives more stable results. The invariant mass distributions are shown in section 7.7 for $P^2_{t,\psi}$, $W_{\gamma \mathrm{p}}$ and z.

Data and the Monte Carlo simulation agree relatively well after the reweighting of the simulation in order to correct for the $P^2_{t,\psi}$ distribution, the muon identification and the iron trigger efficiency. For the medium z selection, the main discrepancy are found in the number of Lee West tracks and in the polar angular distribution of the iron muons. The excess of events in data for a number of Lee West tracks less than five are probably due to a contribution of $\psi(2\mathrm{S})$ mesons, which is not taken into account in the simulation. Since the iron muon efficiency could not be checked for the 2003-2004 e^+ data taking period (cf. chapter 6), we cannot know if the simulation need to be corrected and how to correct it. For the low z selection some bins are probably spoilt by statistical fluctuations due to the lower statistics.

The distributions of $P^2_{t,\psi}$, $W_{\gamma \mathrm{p}}$ and z for the 2004-2005 e^- data taking period is compared to the normalised two component simulation in figure 7.13 for the medium z selection and in figure 7.14 for the low z selection, respectively. The simulation is corrected for the malfunction of the trigger level 4 using the efficiencies determined in section 5.4.2 figure 5.36 from the level 4 weights. The band shows on the simulation the large uncertainty arising from the trigger level 4 efficiency determination, which is of the order of 10 %. The ratio between data and simulation is shown in the right column, a constant fit is used to compute the average. For the medium z selection it is evident the simulation is too much downscaled, even if some bins are compatible within the uncertainties. The same behaviour is observed if events with $P^2_{t,\psi} > 20\,\mathrm{GeV}^2$ are excluded of the selection. All the efficiencies will be corrected with the mean of the ratio between data and the simulation for the z distribution, approximately 1.244, excepted for $P^2_{t,\psi} > 10\,\mathrm{GeV}^2$ where the ratio are lower than one.

In order to compare the data with the simulation for the same observables as for the 2003-2004 e^+ data taking period, the trigger level 4 efficiency as a function of the elasticity z is used to reweight the simulation. The medium z selection is shown in figure 7.15 to 7.16 and the low z selection in figure 7.17 to 7.18, respectively. This procedure permits to describes relatively well the data for the medium z selection within the trigger level 4 uncertainties. The main discrepancies are due to the events with $P^2_{t,\psi} > 20\,\mathrm{GeV}^2$. In particular the reweighting is not correct for the last $P^2_{t,\psi}$ bin, which is due to the fact the efficiency here corresponds to an average and not to 100 %. For the low z selection the statistics is not sufficient to perform accurately this comparison between data and the simulation, many bins are probably spoilt by statistical fluctuations.

It was also tried to reweight the simulation using $W_{\gamma \mathrm{p}}$, but it did not give a good result. The trigger level 4 efficiency was also computed in the analysis bins using the efficiency as a function of the maximum transverse momentum P_t of the hadronic final state. The P_t distribution for each analysis bin was used to compute the average efficiency. This method gave too high efficiencies. One can also reweight the simulation taking into account the efficiency for $P^2_{t,\psi} > 20\,\mathrm{GeV}^2$ is 100 %, but in this case the trigger level 4 efficiency must be computed for events with $P^2_{t,\psi} < 20\,\mathrm{GeV}^2$.

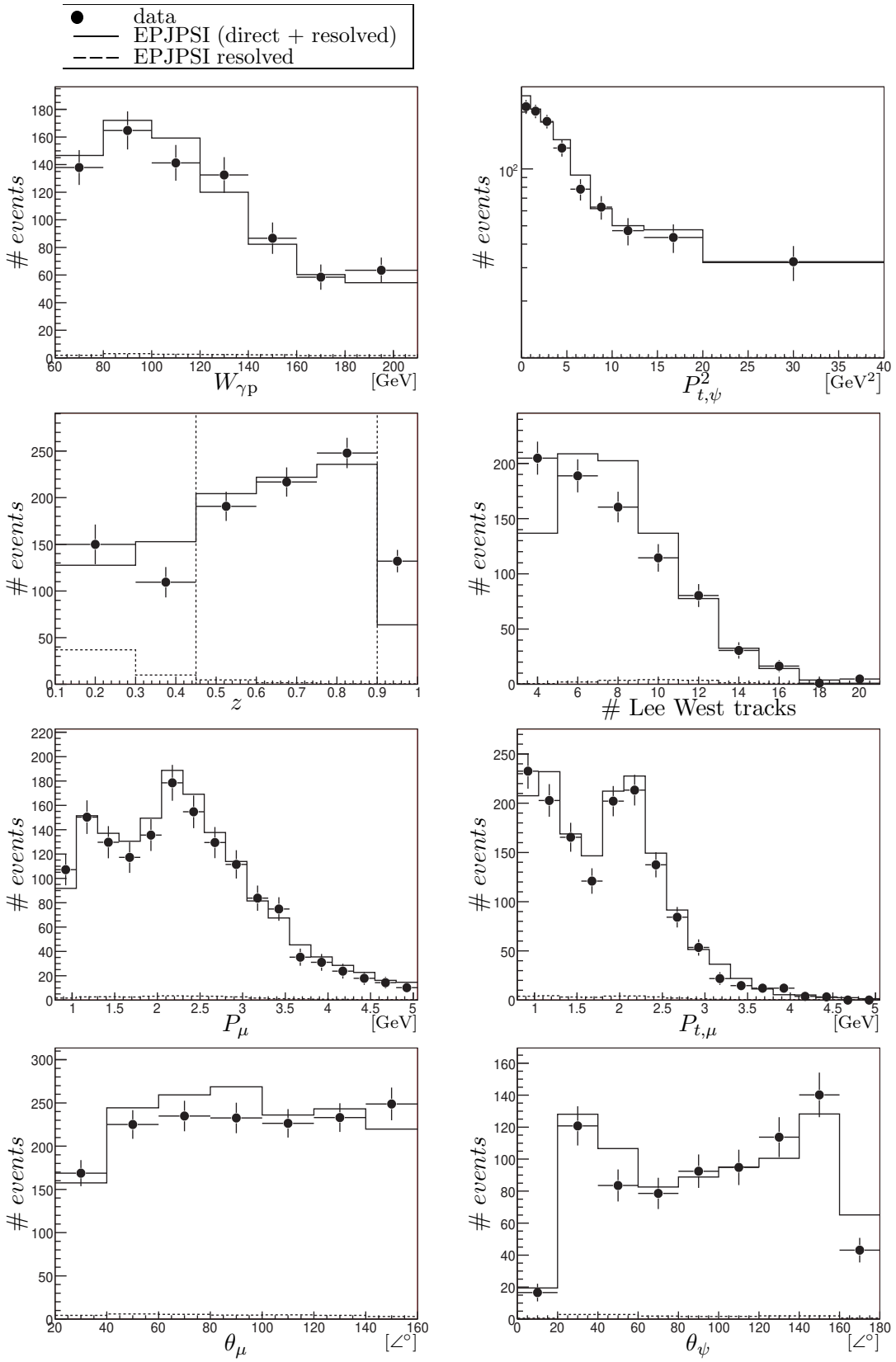

Figure 7.9: Comparison of **2003-2004** e^+ data and the normalised two component simulation for the **medium** z selection. Distributions of the photon-proton centre-of-mass energy $W_{\gamma p}$, the transverse momentum squared of the J/ψ meson $P^2_{t,\psi}$, the elasticity z, the number of Lee West tracks the momentum, the transverse momentum and the polar angle of the decay muons, and the polar angle of the J/ψ meson.

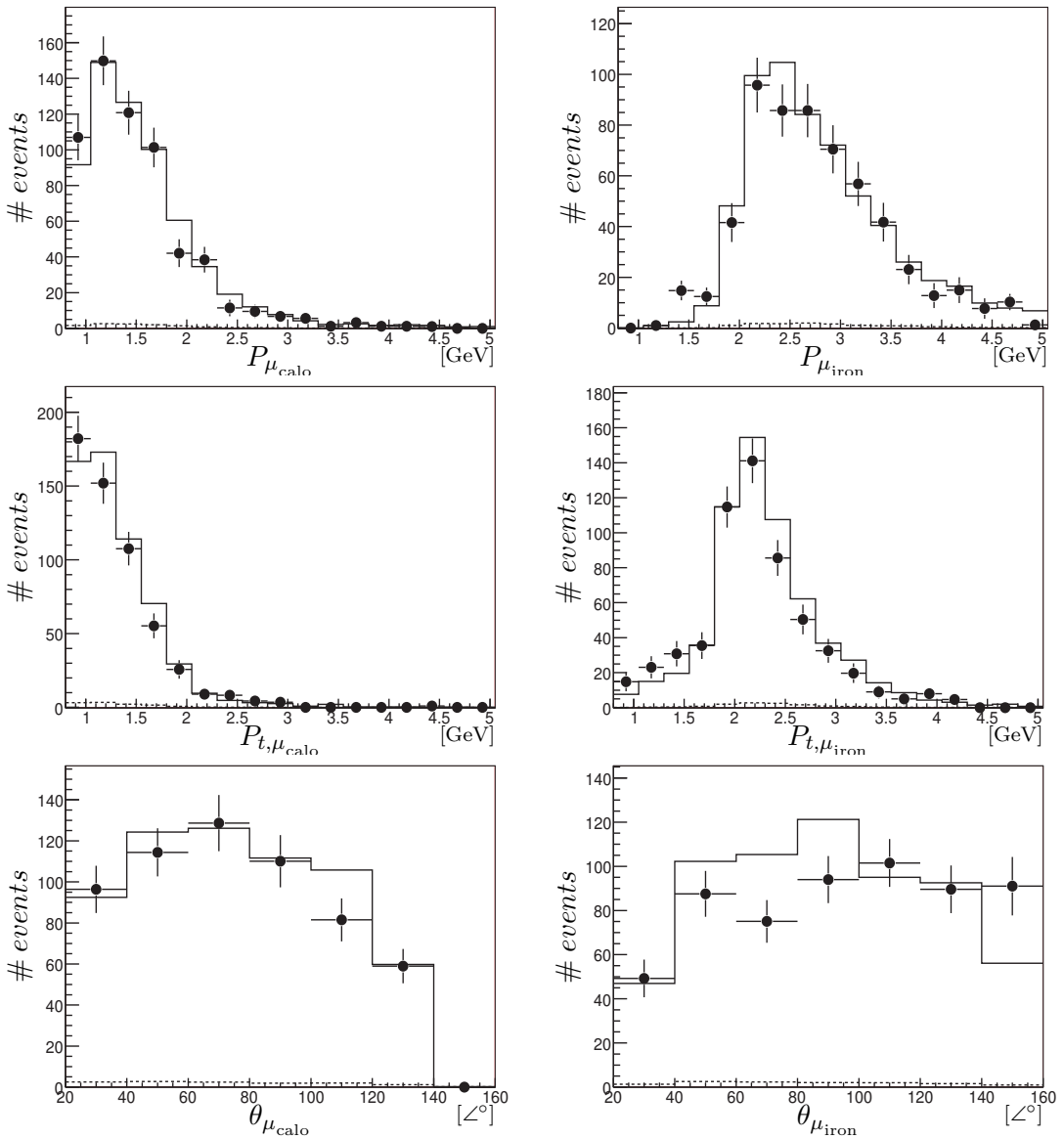

Figure 7.10: Continuation of figure 7.9. Distributions of the momentum, the transverse momentum and the polar angle of the calo and iron muon.

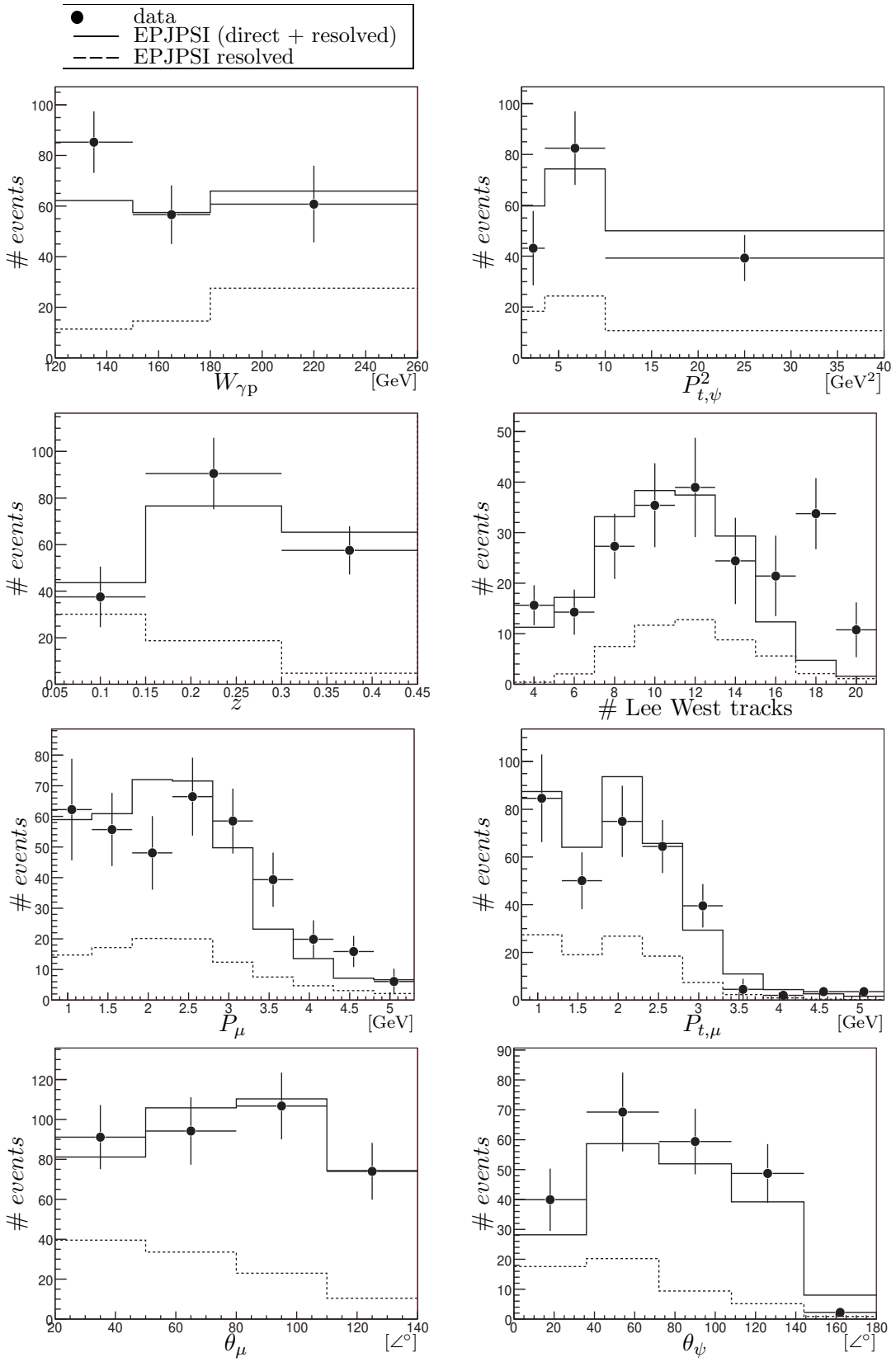

Figure 7.11: Comparison of **2003-2004** e^+ data and the normalised two component simulation for the **low** z selection. Distributions of the photon-proton centre-of-mass energy $W_{\gamma p}$, the transverse momentum squared of the J/ψ meson $P^2_{t,\psi}$, the elasticity z, the number of Lee West tracks the momentum, the transverse momentum and the polar angle of the decay muons, and the polar angle of the J/ψ meson.

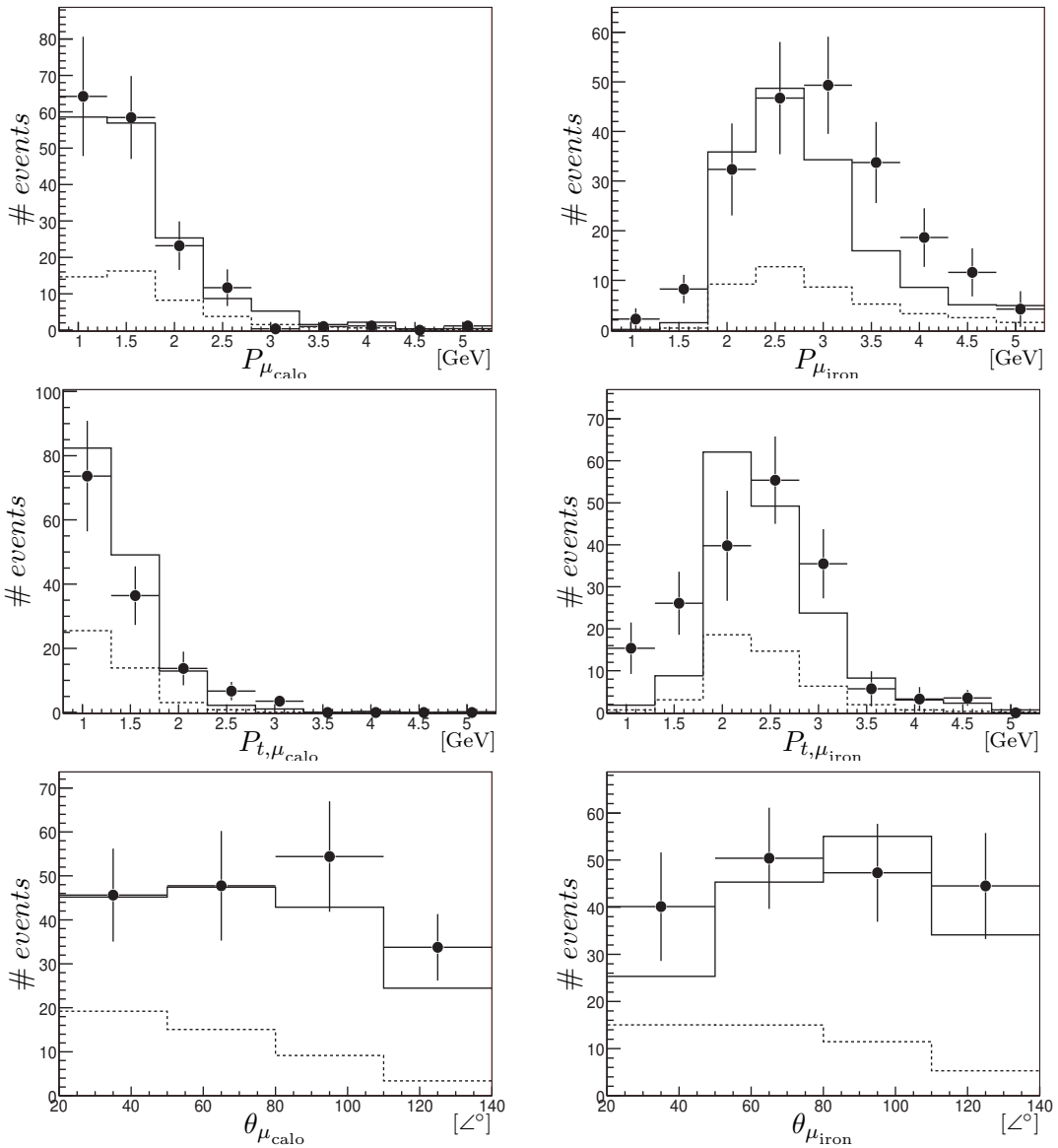

Figure 7.12: Continuation of figure 7.11. Distributions of the momentum, the transverse momentum and the polar angle of the calo and iron muon.

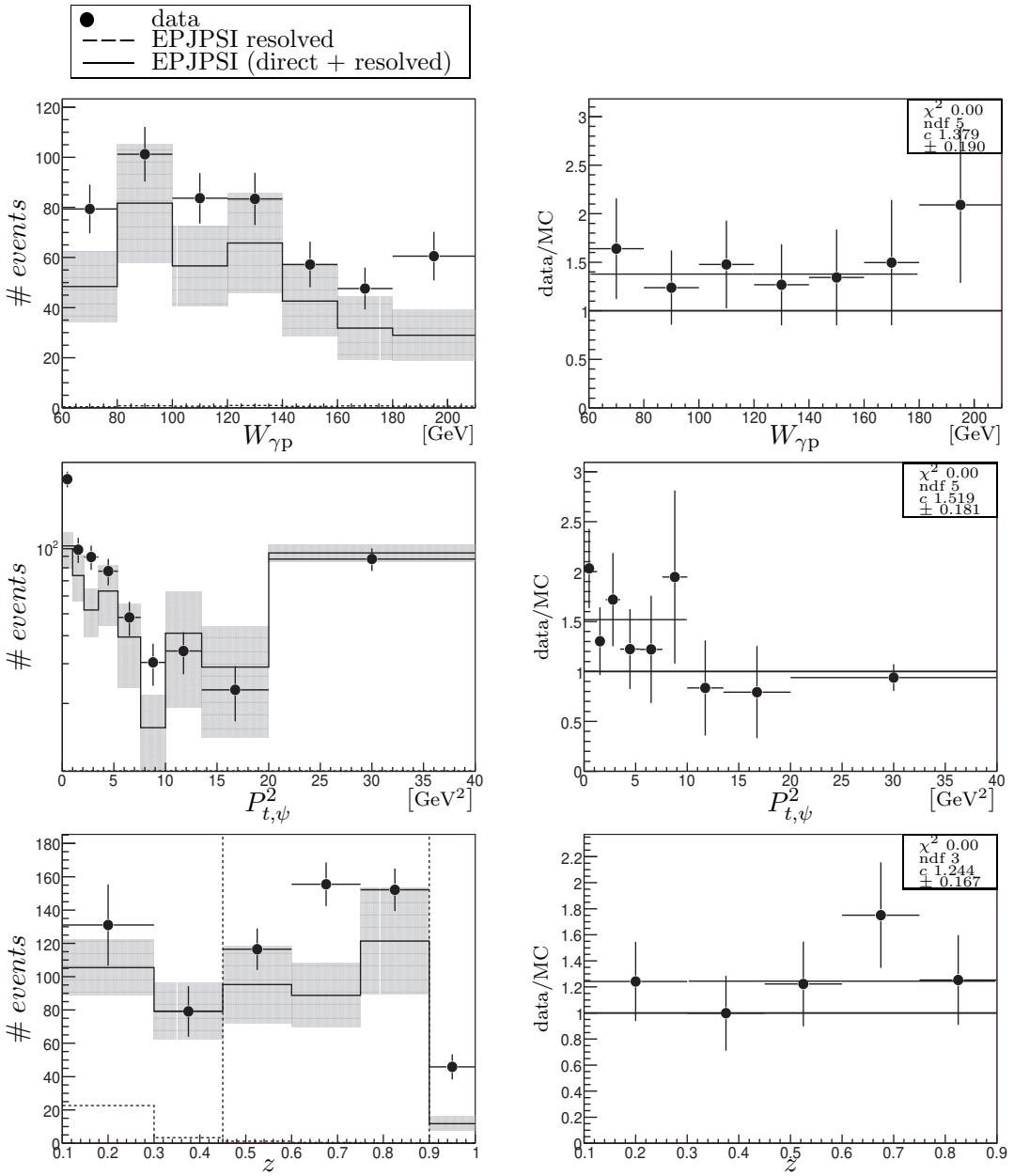

Figure 7.13: Comparison of **2004-2005** e^- data and the normalised two component simulation for the **medium** z selection. Distributions of the photon-proton centre-of-mass energy $W_{\gamma p}$, the transverse momentum squared of the J/ψ meson $P^2_{t,\psi}$ and the elasticity z. The band shows on the Monte Carlo simulation the uncertainty arising from the trigger level 4 efficiency determination. The ratio between data and simulation is shown in the right column. The parameters of the constant fit is given in the box.

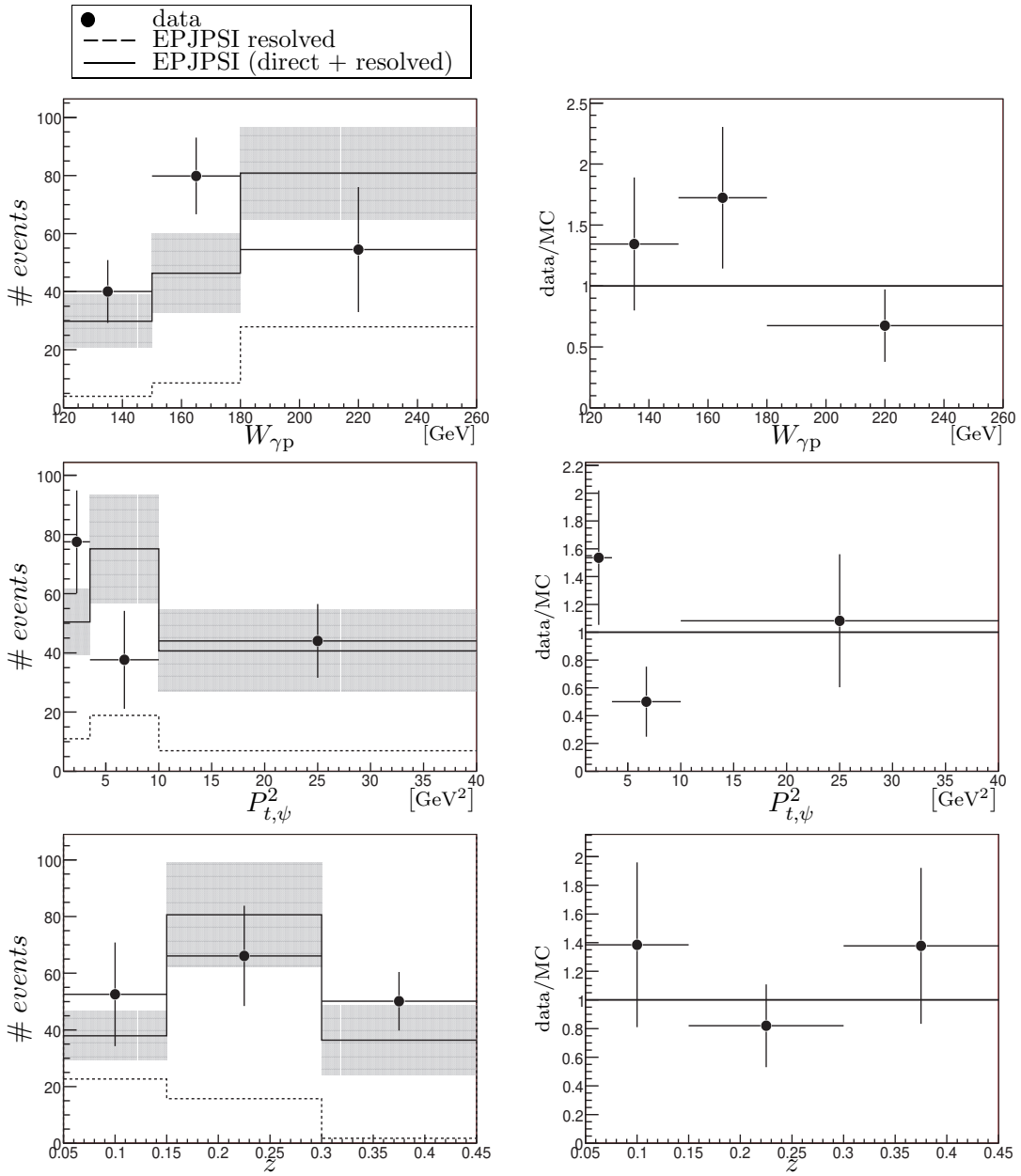

Figure 7.14: Comparison of **2004-2005** e^- data and the normalised two component simulation for the **low** z selection. Distributions of the photon-proton centre-of-mass energy $W_{\gamma p}$, the transverse momentum squared of the J/ψ meson $P^2_{t,\psi}$ and the elasticity z. The band shows on the Monte Carlo simulation the uncertainty arising from the trigger level 4 efficiency determination. The ratio between data and the simulation is shown in the right column.

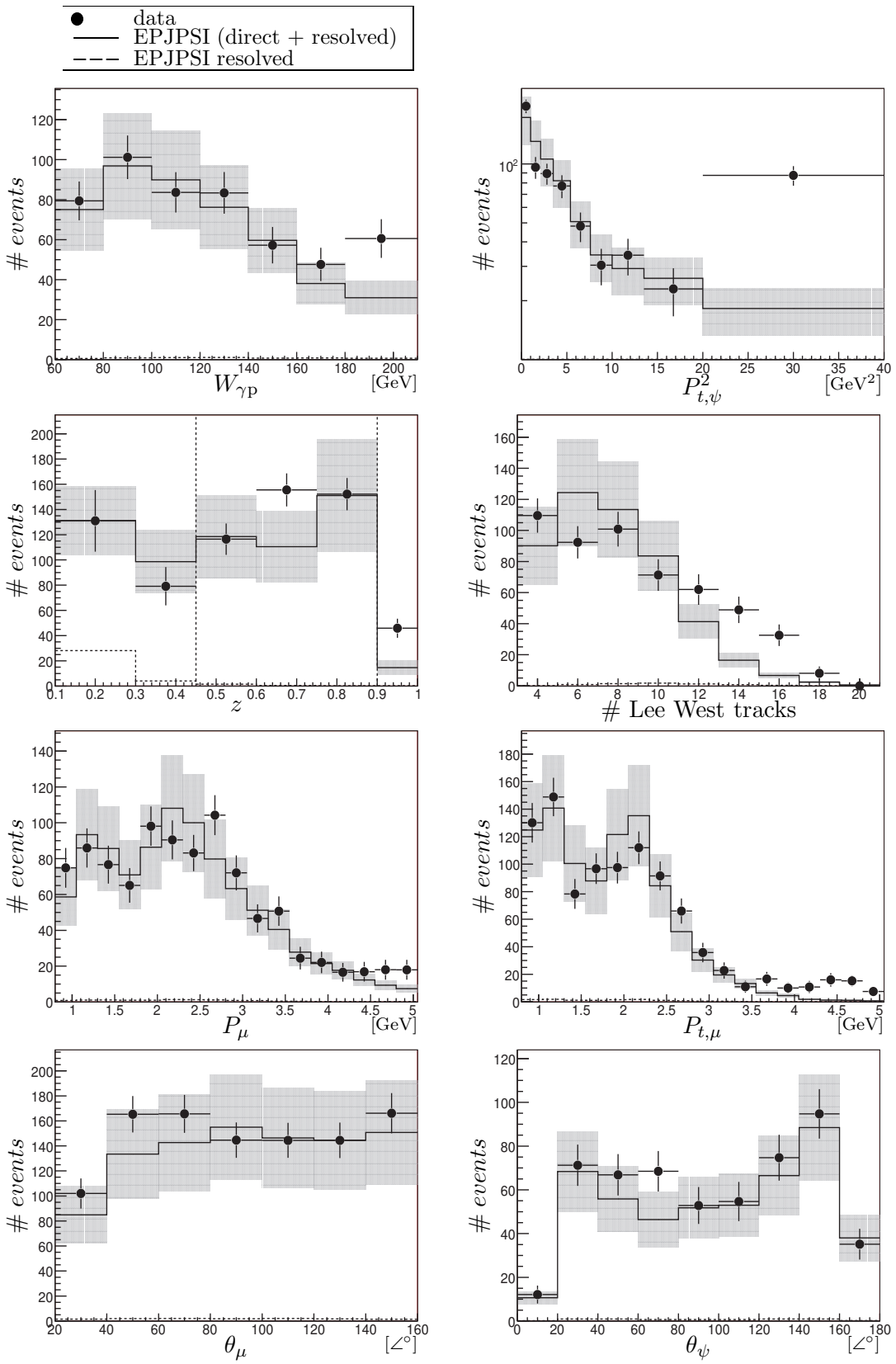

Figure 7.15: Comparison of **2004-2005** e^- data and the normalised two component simulation reweighted as a function z for the **medium** z selection. Distributions of the photon-proton centre-of-mass energy $W_{\gamma p}$, the transverse momentum squared of the J/ψ meson $P^2_{t,\psi}$, the momentum, the transverse momentum and the polar angle of the decay muons, the polar angle of the J/ψ meson, and the number of Lee West tracks. The discrepancy in the last $W_{\gamma p}$ and $P^2_{t,\psi}$ bin is due to the fact the reweighting is not correct for these particular bins.

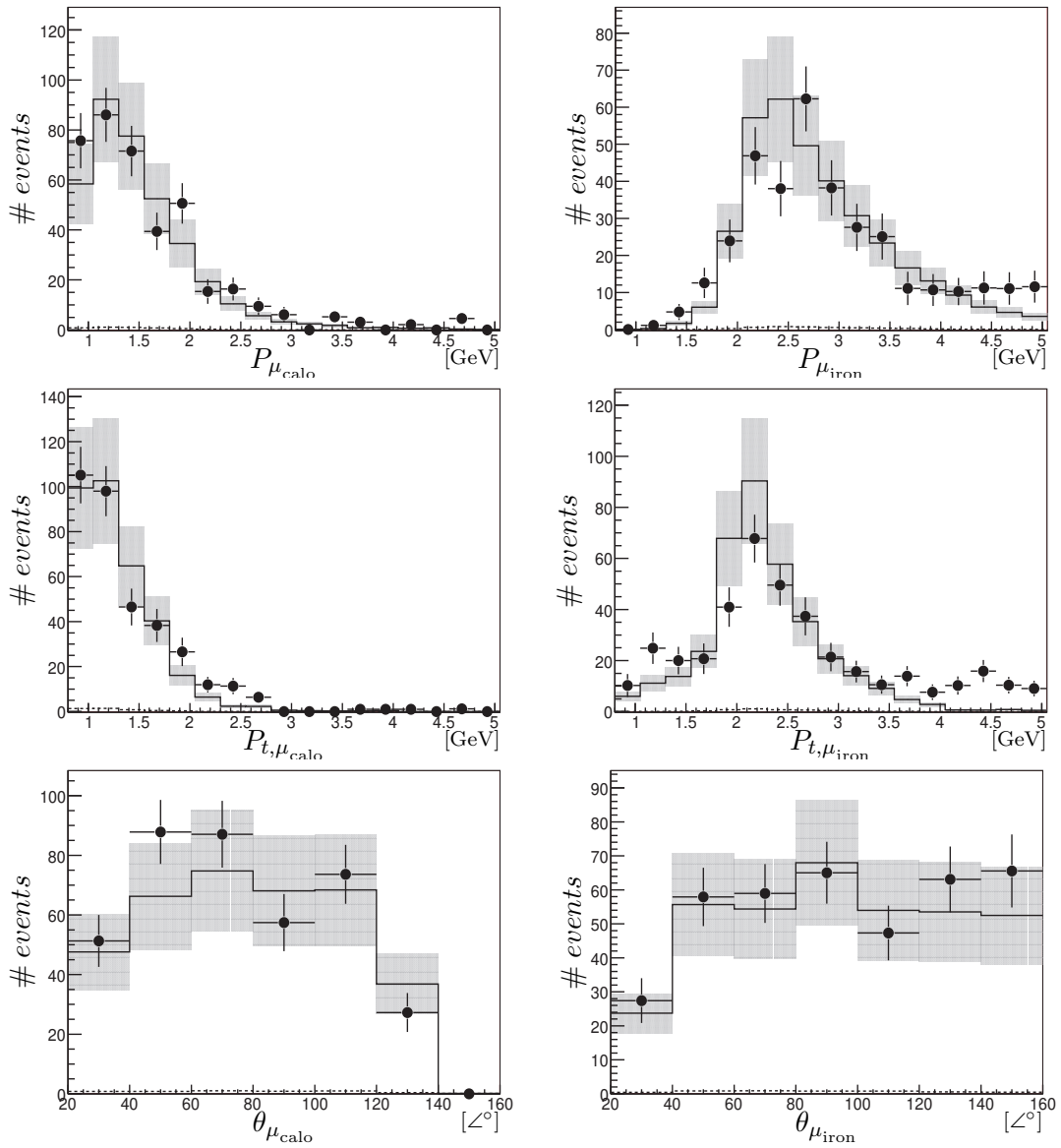

Figure 7.16: Continuation of figure 7.15. Distributions of the momentum, the transverse momentum and the polar angle of the calo and iron muon. The band shows on the Monte Carlo simulation the uncertainty arising from the trigger level 4 efficiency determination.

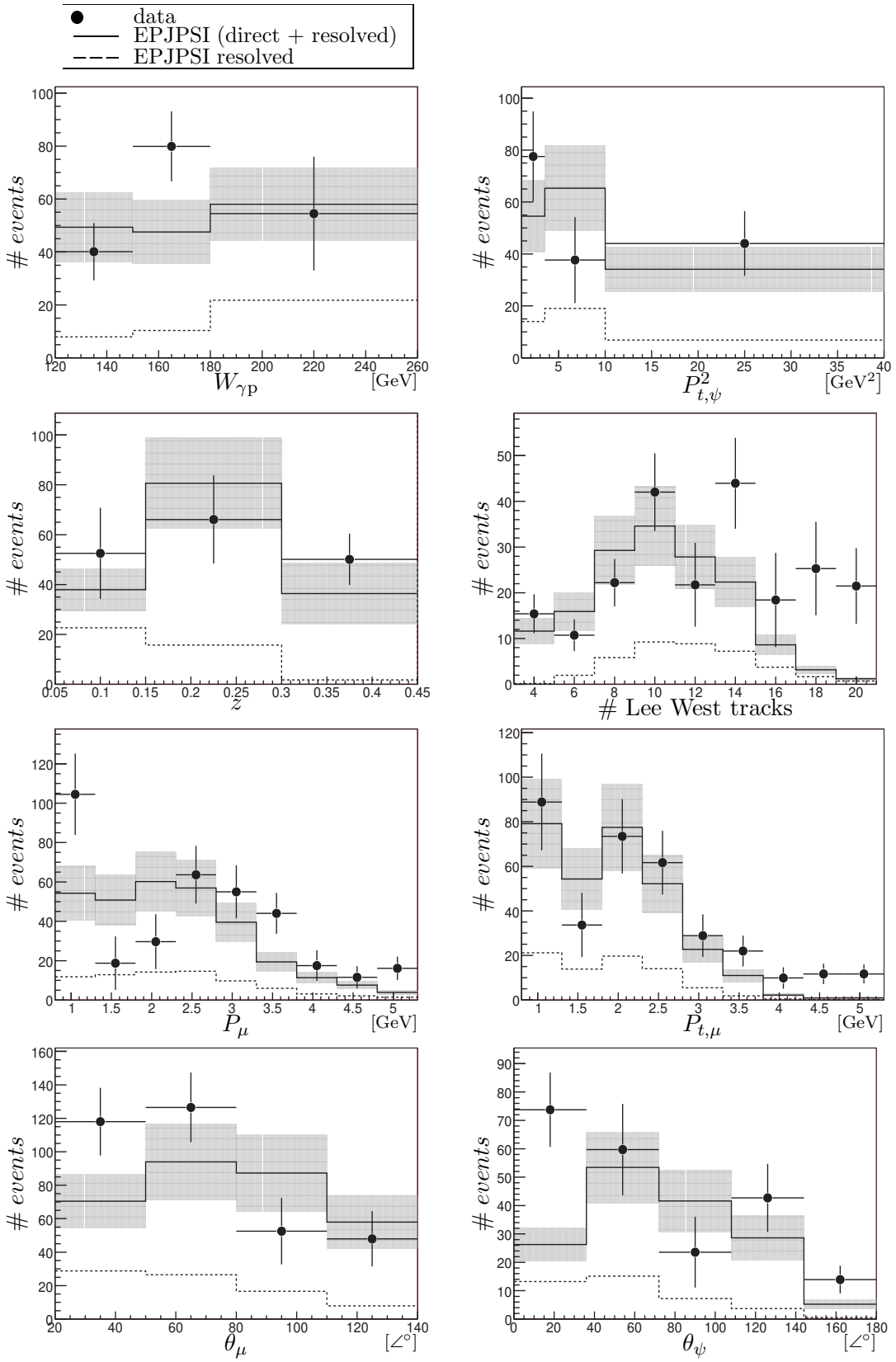

Figure 7.17: Comparison of **2004-2005** e^- data and the normalised two component simulation reweighted as a function z for the **low** z selection. Distributions of the photon-proton centre-of-mass energy $W_{\gamma p}$, the transverse momentum squared of the J/ψ meson $P^2_{t,\psi}$, the momentum, the transverse momentum and the polar angle of the decay muons, the polar angle of the J/ψ meson, and the number of Lee West tracks.

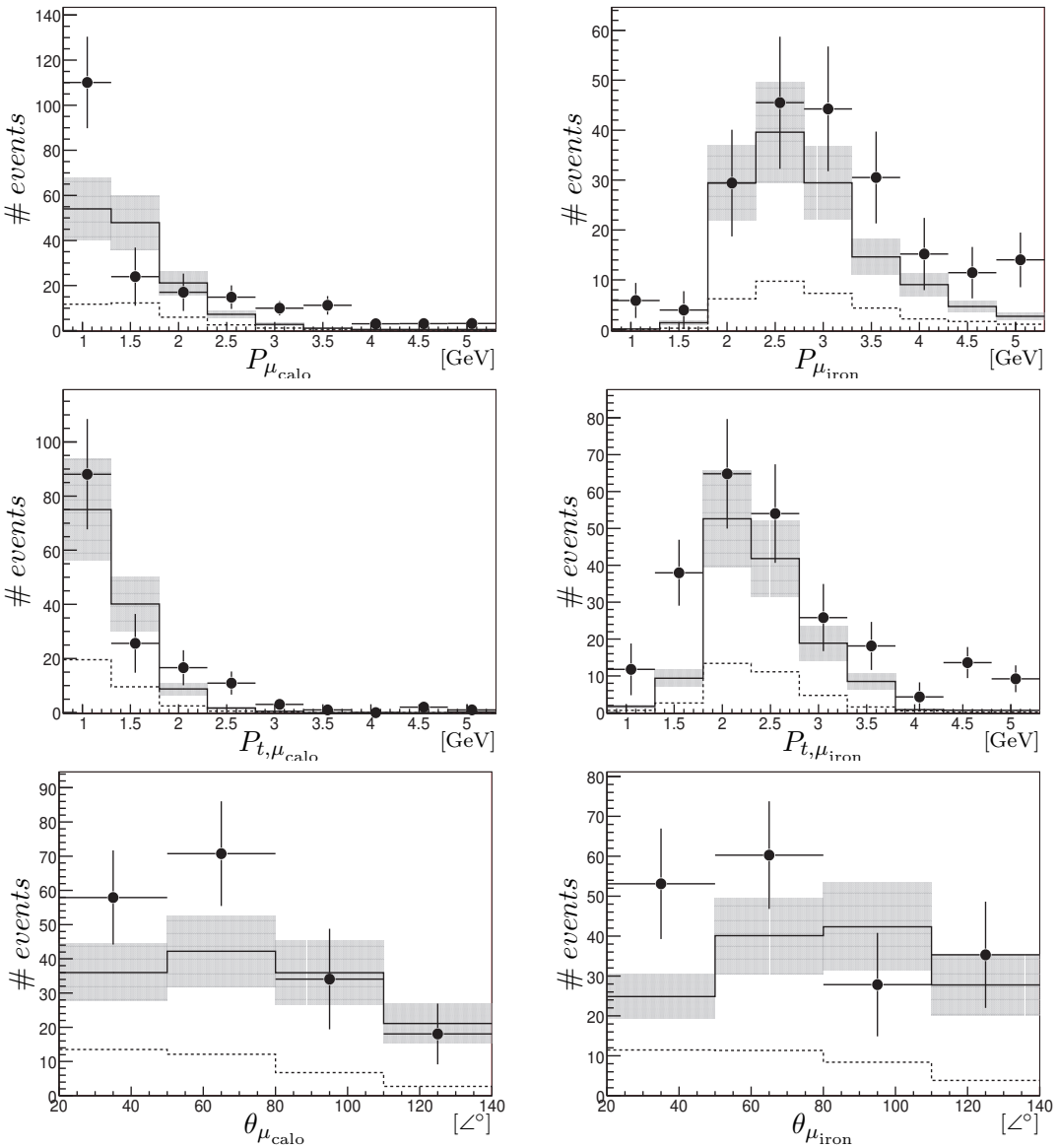

Figure 7.18: Continuation of figure 7.17. Distributions of the momentum, the transverse momentum and the polar angle of the calo and iron muon. The band shows on the Monte Carlo simulation the uncertainty arising from the trigger level 4 efficiency determination.

7.4 Systematic Errors

The systematic errors are listed in table 7.5 for the medium z selection and in table 7.6 for the low z selection, respectively. The sources of the systematic error will be discussed in the following.

source	amount in %	
track reconstruction	6.0	
muon identification	2.8	
L1 iron trigger efficiency	6.0	
parton density functions	2.0	
diffractive background	$P^2_{t,\psi} > 1\,\mathrm{GeV}^2$	$P^2_{t,\psi} < 1\,\mathrm{GeV}^2$
	2.0	28.0
luminosity	4.0	
branching ratio	1.7	
total	10.3	

Table 7.5: Systematic error for the **medium** z selection. The systematic error of 28 % for the diffractive background is only relevant for the lowest bin in the $P^2_{t,\psi}$ distribution. All other variables are studied in the kinematic range $P^2_{t,\psi} > 1\,\mathrm{GeV}^2$.

source	amount in %	
track reconstruction	6.0	
muon identification	2.5	
L1 iron trigger efficiency	6.0	
parton density functions	$W_{\gamma\mathrm{p}} > 150\,\mathrm{GeV}$	$W_{\gamma\mathrm{p}} < 150\,\mathrm{GeV}$
	5.0	10.0
background from B meson decays	−14.0	
luminosity	4.0	
branching ratio	1.7	
total	11.1 −17.8	

Table 7.6: Systematic error for the **low** z selection. The systematic error of 10 % for $W_{\gamma\mathrm{p}}$ refers to the lowest bin.

7.4.1 Track Reconstruction

The error of the track reconstruction efficiency is conservatively estimated to be 2 % per track as in previous analyses, resulting in an error of 6 % for at least three reconstructed tracks.

7.4.2 Muon Identification Efficiency

The muon identification efficiency is studied in chapter 6. Since the simulation has a tendency to be more efficient than the data, the simulation is reweighted in order to describe data. The reweighting and the resulting systematic errors are described in the section 6.3. The amount of the systematic error is given in the tables for each analysis region.

7.4.3 Iron Trigger Efficiency

The systematic error for the iron trigger efficiency is computed like for the muon identification efficiency by using the difference between the iron trigger efficiency of data and of the reweighted simulation (cf. section 5.4.1.1). A systematic error of 6 % is found between data and the reweighted simulation.

7.4.4 Proton Parton Density Function

The simulation of direct and resolved processes depends on the parton density function (PDF) and thus on the accuracy of its experimental determination. The influence of different parton density functions (MRS(A'), GRV98 LO, CTEQ5L and MRST LO) on the geometrical acceptance was studied in the previous analysis [36] with the direct photon-gluon fusion simulation. Nearly all deviations were found to be compatible with zero within the statistical error. A systematic error of 2 % is assigned to cover possible differences.

7.4.5 Photon Parton Density Fusion

In the simulation of the resolved processes the photon parton density function (PDF) enters in addition to the proton PDF. The photon PDF is not so well known as the proton PDF. The influence of different photon PDFs on the geometrical acceptance was studied in the previous analysis [36]. The biggest differences in the acceptance was found in the first $W_{\gamma p}$ bin, where an error of 10 % is assumed. For other observables, $P^2_{t,\psi}$, z, and in the higher $W_{\gamma p}$ region, the differences are covered by an error of 5 %.

7.4.6 Diffractive J/ψ and ψ(2S) Background

Diffractive processes of J/ψ and ψ(2S) mesons which have been produced elastically or with proton dissociation constitute a source of background. While only very few diffractively produced J/ψ mesons pass the selection, the cascade decay from diffractive production of the ψ(2S) mesons contributes significantly. A contribution of 28 % to the number of selected J/ψ mesons for the medium z selection at $P^2_{t,\psi} < 1\,\mathrm{GeV}^2$ is expected [36]. In order to be less sensitive to this source of background, the final analysis is carried out in the region $P^2_{t,\psi} > 1\,\mathrm{GeV}^2$, where this background is estimated to be only 2 %. The diffractive events are concentrated in the highest z bin. Therefore this contribution is taken into account in the systematic error only for the medium z selection. No correction is applied.

In the Colour Singlet Model the contribution from the cascade decay of inelastically produced ψ(2S) mesons is expected to be 15 %, which was confirmed experimentally [76]. Since this process is very difficult to distinguish from J/ψ production in photon-gluon fusion it is not corrected for.

7.4.7 Sources of Background for the Low z Selection

In addition to the decay via ψ(2S) mesons, production of J/ψ mesons via the decay of χ_c and B mesons are expected to contribute at low elasticity z.

The χ_c mesons are produced in resolved photon events via gluon-gluon fusion or in a quark-gluon interaction. The production of J/ψ mesons via the decay of χ_c mesons behaves similar as gluon-gluon fusion, but the cross section is predicted to be more than an order of magnitude smaller. A contribution of 7 % is expected [36]. The difference in the event topology between J/ψ mesons originating from χ_c decays and those formed in the gluon-gluon fusion process is the presence of an additional photon of low energy coming from the desexcitation of the charm bound state. The low

energy photon is very difficult to identify in the detector. Therefore no distinction between these processes is made and is not considered in the systematic error.

The dominant process for the production of B mesons is the direct photon-gluon fusion. An estimation of the contribution of this process was done with the EPJPSI Monte Carlo program in [36], which predicted that a fraction of 14 % of the J/ψ mesons results from the decay of B mesons in this analysis. The shapes of the distributions for J/ψ mesons originating from decay of B mesons differ from those of EPJPSI-direct and EPJPSI-resolved separately, but are in agreement with the shape of the sum of both simulations and with the data. This means that it cannot be excluded that the cross sections for direct photon-gluon fusion and gluon-gluon fusion with resolved photons are lower by a constant fraction and there is a third component, the decay of B mesons. Therefore the production of J/ψ mesons via the decay of B mesons is considered as a source of resonant background to the low z selection, and a fraction of 14 % is included in the systematic error.

7.4.8 Luminosity and Branching Ratio

The error of the luminosity measurement is not yet available officially. The unofficial value for 2004 and 2005 is approximately 4 %, and thus worse than for HERA I, which was 1.5 %. For the branching ratio and its error the Particle Data Group [3] value $\mathcal{B}\,(\mathrm{J}/\psi \longrightarrow \mu^-\mu^+) = 5.88 \pm 0.10\,\%$ is used. These errors affect only the normalisation.

7.5 Cross Sections as Functions of $W_{\gamma p}$, z, $P^2_{t,\psi}$

The differential electron-proton cross section in the kinematic range as a function of a variable x is calculated from the number of J/ψ mesons $\mathcal{N}_\psi$ [1] in a bin of x according to the formula:

$$\frac{d}{dx}\sigma_{\mathrm{ep}}(x) = \frac{\mathcal{N}_\psi(x)}{\delta x \cdot \epsilon_{\mathrm{total}} \cdot \mathcal{B} \cdot L},$$

The cross section is divided by the bin width δx in order to have a cross section as a function of x. The branching ratio $\mathcal{B}$ scales the integrated luminosity L of the analysed run period to the muonic decay of the J/ψ meson J/$\psi \longrightarrow \mu^-\mu^+$ [2]. The total efficiency $\epsilon_{\mathrm{total}}$ takes into account all efficiencies to correct the number of J/ψ mesons for the effect of the acceptance, the selection and the trigger. The bin centre is in principle determined with the method explained in section 7.5.3.

This formula depends on the probability of the beam electron to radiate a photon given by the photon flux $\mathcal{F}_\gamma$ (cf. section 7.5.2 for the definition). In order to have a cross section independent of the HERA beam kinematics, the following formula is used to obtain the photon-proton cross section:

$$\frac{d}{dx}\sigma_{\gamma\mathrm{p}} = \frac{1}{\mathcal{F}_\gamma}\frac{d}{dx}\sigma_{\mathrm{ep}},$$

All the numbers used to compute the cross sections are given in the tables of section 7.6.1 for the low z selection and in section 7.6.2 for the medium z selection, respectively.

[1] $\mathcal{N}_\psi$ is determined with the method 2, cf. section 7.2
[2] cf. section 7.4.8 for its value

7.5.1 Total Efficiency

The final correction to be applied to the number of J/ψ mesons in order to obtain the cross section is shown in the figure 7.19 for each analysis regions and data taking periods. The selection cuts are given in table 4.6 for the medium z selection and in table 4.8 for the low z selection, respectively. Both data taking periods have similar efficiencies (the malfunction of the trigger level 4 is not take into account here). The average total efficiency is of the order of 20 %, and the shape of the total efficiencies are similar to the product of the acceptances with the selection efficiencies. The total efficiency increases with $P^2_{t,\psi}$ up to 45 %. For the medium selection, the total efficiency as a function of $W_{\gamma\mathrm{p}}$ has a similar shape as for the acceptance, and drops at high elasticity z. For the low z selection, the last bin of $W_{\gamma\mathrm{p}}$ and z is lower.

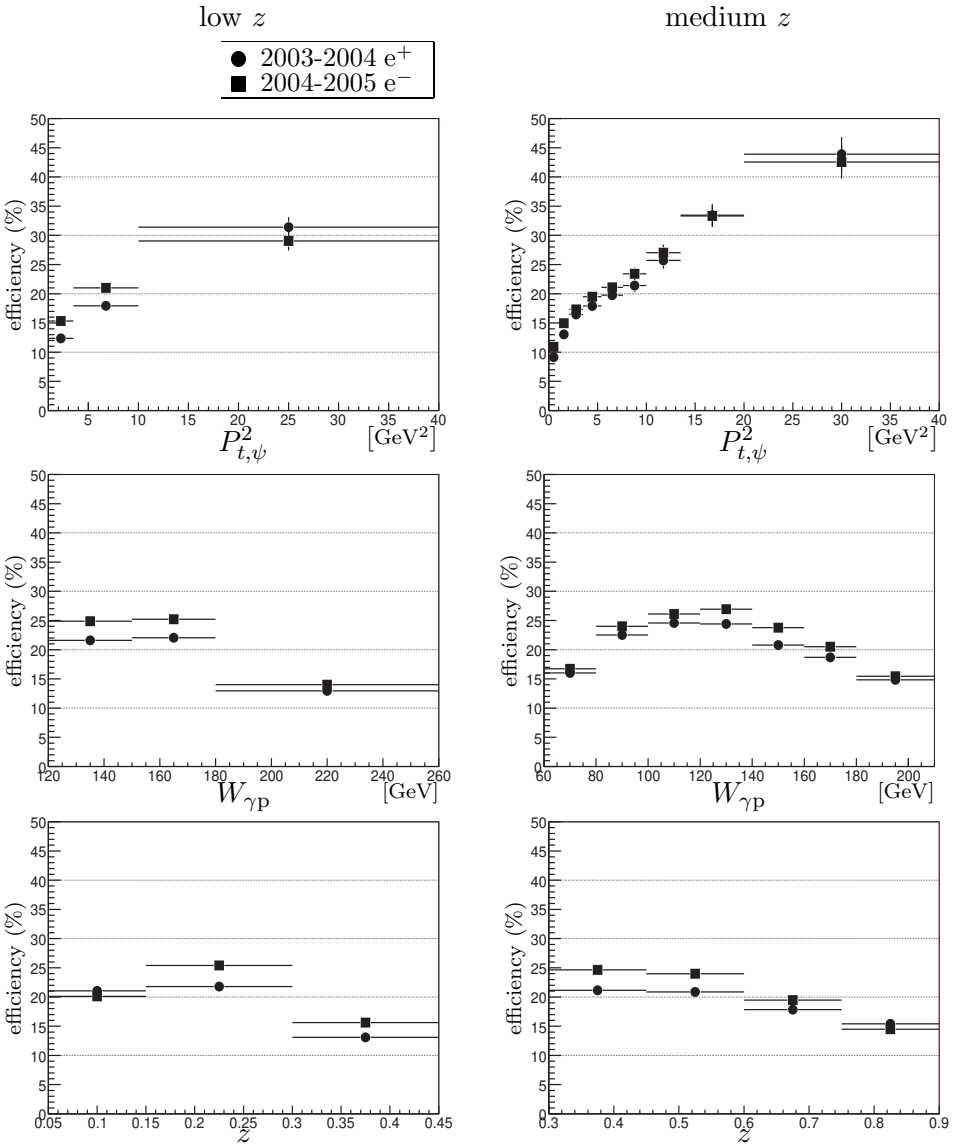

Figure 7.19: Total efficiency as a function of $P^2_{t,\psi}$, $W_{\gamma\mathrm{p}}$, and z for both data taking periods and analysis regions. The malfunction of the trigger level 4 is not take into account here.

7.5.2 Photon Flux

To leading order the electron-proton interaction can be described as arising from a photon-proton scattering interaction where the electron is the source of a photon flux (equivalent photon approximation [77, 78, 79]):

$$\sigma_{ep} = \int_{y_{min}}^{y_{max}} dy \int_{Q^2_{min}}^{Q^2_{max}} dQ^2 f_\gamma\left(y, Q^2\right) \sigma_{\gamma p}\left(y, Q^2\right), \tag{7.1}$$

where σ_{ep} denotes the electron-proton cross section and $\sigma_{\gamma p}$ the photon-proton cross section. The flux of transversely polarised photons $f_\gamma\left(y, Q^2\right)$ is given by:

$$f_\gamma\left(y, Q^2\right) = \frac{\alpha}{2\pi y Q^2}\left(1 + (1-y)^2 - 2m_e^2\frac{y^2}{Q^2}\right). \tag{7.2}$$

The integration limits on the virtuality are given by the kinematic minimum and the kinematic region used by this analysis:

$$Q^2_{min} = m_e^2\frac{y^2}{1-y} \quad \text{and} \tag{7.3}$$

$$Q^2_{max} = 2.5\,\text{GeV}^2. \tag{7.4}$$

For small Q^2 the dependence of the photon-proton cross section on y and Q^2 is much smaller than the dependence of the photon flux. Thus it is possible to treat $\sigma_{\gamma p}$ as a constant and bring it out of the integral. The photon-proton cross section can then be expressed with the integrated photon-proton flux $\mathcal{F}_\gamma$ as:

$$\sigma_{ep} = \frac{1}{\mathcal{F}_\gamma}\sigma_{\gamma p} \tag{7.5}$$

where

$$\mathcal{F}_\gamma = \int_{y_{min}}^{y_{max}} dy \int_{Q^2_{min}}^{Q^2_{max}} dQ^2 f_\gamma\left(y, Q^2\right) \tag{7.6}$$

After integration over Q^2, we obtain

$$\mathcal{F}_\gamma = \int_{y_{min}}^{y_{max}} \left\{\frac{\alpha}{2\pi}\left(2m_e^2 y\left(\frac{1}{Q^2_{min}} - \frac{1}{Q^2_{max}}\right) + \frac{1+(1-y)^2}{y}\ln\frac{Q^2_{max}}{Q^2_{min}}\right)\right\} dy \tag{7.7}$$

The following relation between Q^2, y, and $W_{\gamma p}$:

$$Q^2 = (s - m_p^2 - m_e^2)y - W^2 + m_p^2 \tag{7.8}$$

has to be respected during the integration.

The integral is computed with the Quadratic Adaptive algorithm using the Gauss-Kronrod rules from GSL/QUADPACK. It converges quickly with a higher precision than the cross section, and gives an estimation of the error. The photon flux $\mathcal{F}_\gamma$ as a function of photon-proton centre-of-mass energy $W_{\gamma p}$ is shown in figure 7.20 for each analysis region.

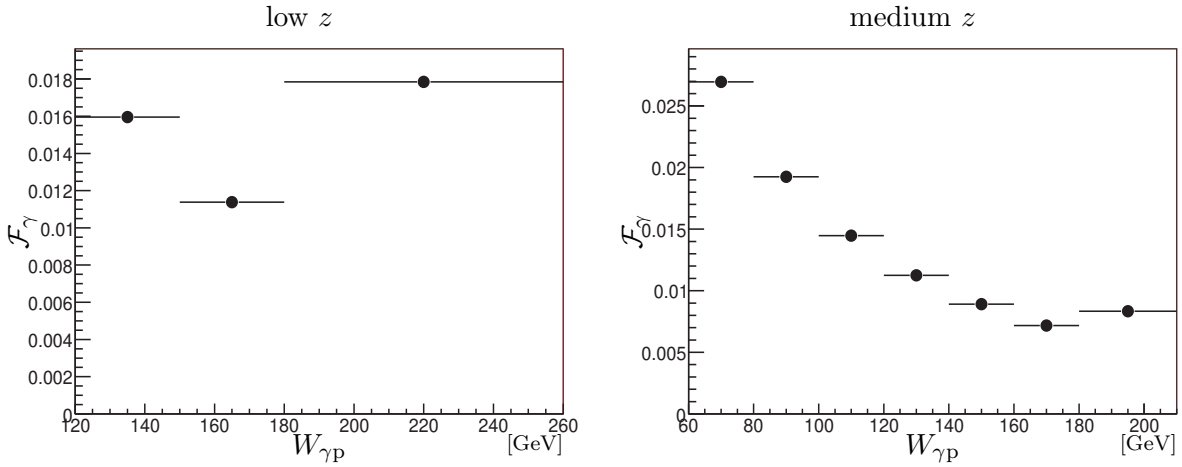

Figure 7.20: Photon flux $\mathcal{F}_\gamma$ as a function of $W_{\gamma p}$ for each analysis region.

7.5.3 Bin Centre Determination

In order to compare the measured cross sections with theoretical predictions corrected bin centres have to be determined.

If the cross section varies rapidly over a bin, the measured cross section will in principle not be equal to the expected value at the centre of the bin. This would only be the case for an infinitesimal bin or for a linear dependence. The treatment of $W_{\gamma p}$ is different from the other variables and is discussed first.

In the case of the photon-proton centre-of-mass energy $W_{\gamma p}$ the fact that the photon flux $\mathcal{F}_\gamma$ depends on y and therefore on $W_{\gamma p}$ has to be considered. For a bin $W_1 < W_{\gamma p} < W_2$ with a bin centre $\langle W_{\gamma p} \rangle$ the following equation is valid

$$\sigma\left(\langle W_{\gamma p} \rangle\right) = \int_{W_1}^{W_2} dW \mathcal{F}_\gamma(W)\sigma(W) / \int_{W_1}^{W_2} dW \mathcal{F}_\gamma(W)$$

In order to solve this equation an assumption on $\sigma(W_{\gamma p})$ has to be made. Data of preceding analysis was well fitted with a functional form $\sigma(W_{\gamma p}) \propto W_{\gamma p}^{\delta}$, where $\delta = 1.6$. The correction is always small, i.e. less than 1 GeV for a bin width of 20 GeV. The bin centres for the bins of $W_{\gamma p}$ are given in tables 7.12 and 7.13.

The photon flux depends only on $W_{\gamma p}$ and Q^2 and does not influence the bin centre of any other observable such as $P_{t,\psi}^2$ and z. Therefore the bin centre for any variable x can be determined using the following equation

$$\frac{d\sigma}{dx}\left(\langle x \rangle\right) = \frac{1}{x_2 - x_1} \int_{x_1}^{x_2} dx \frac{d\sigma}{dx}(x)$$

Again the functional form of $d\sigma/dx$ is needed to solve this equation. In the case of the elasticity z a linear function fits the data well, which means that no correction compared to the nominal bin centre is needed. One possibility for the bin centre correction in the transverse momentum squared $P_{t,\psi}^2$ of the J/ψ meson is to use the sum of two exponential functions.

7.5.4 Cross Sections for the Medium z Selection

The new results of HERA II will be compared with the previously published results of the H1 collaboration for HERA I [35]. The data were collected in the years 1996–2000 and correspond to a total integrated luminosity of $87.5 \pm 1.3\,\mathrm{pb}^{-1}$. The proton beam energy was 820 GeV before 1998 and 920 GeV since.

Cross sections are measured in the kinematic range given in the table 7.7. This analysis has a more extended Q^2 domain than for HERA I due to the new acceptance limit of the SpaCal calorimeter, $2.5\,\mathrm{GeV}^2$ instead of $1\,\mathrm{GeV}^2$ (cf. section 4.1). This new kinematic range increases the photon flux approximately by 5 %.

low z	medium z
HERA I $Q^2 < 1.0\,\mathrm{GeV}^2$ HERA II $Q^2 < 2.5\,\mathrm{GeV}^2$	
$0.05 \leqslant z \leqslant 0.45$	$0.3 \leqslant z \leqslant 0.9$
$P^2_{t,\psi} > 1\,\mathrm{GeV}^2$	
$120 \leqslant W_{\gamma p} \leqslant 260\,\mathrm{GeV}$	$60 \leqslant W_{\gamma p} \leqslant 240\,\mathrm{GeV}$

Table 7.7: Kinematic region for for each analysis region.

The selection for the HERA I analysis is given in table 7.8 and for this analysis in table 4.6. In order to suppress diffractive $\psi(2S)$ meson contributions, at least five tracks are required in the HERA I analysis, which is not done in this analysis due to the low statistics. Moreover the momentum cut for the decay muons is higher in order to have a better muon identification efficiency, 1.1 GeV instead of 0.8 GeV. But it does not affect the cross sections since it is corrected for.

Acceptance cuts	
angular cut	$20^\circ \leqslant \theta_\mu \leqslant 160^\circ$
momentum cut	$P_\mu > 1.1\,\mathrm{GeV}$
	$P_{\mu_{\mathrm{iron}}} > 1.8\,\mathrm{GeV}$
Selection cuts	
photoproduction medium elasticity	#Lee West Tracks $\geqslant 5$ no scattered electron in the main detector ($E_{cluster} < 8\,\mathrm{GeV}$), $Q^2 < 1\,\mathrm{GeV}^2$ $0.3 \leqslant z \leqslant 0.9$ $P^2_{t,\psi} > 1\,\mathrm{GeV}^2$ $60 \leqslant W_{\gamma p} \leqslant 240\,\mathrm{GeV}$

Table 7.8: Selection cuts for the **medium** z selection of the HERA I analysis

The total photoproduction cross section as a function of the photon-proton centre-of-mass energy $W_{\gamma p}$, the differential cross sections as functions of the transverse momentum squared of the J/ψ meson $P^2_{t,\psi}$ and the elasticity z, are shown in figure 7.21 for both data taking periods and the medium z selection. The ratio between this analysis and the HERA I analysis is also shown. Both analyses agree within the statistical errors at one or two standard deviations. The 2003-2004 e^+measurements have a tendency to be lower. Since the systematic error for the trigger efficiency determination is of the order of 10 % for these analyses, a perfect agreement is not expected. The agreement is also good in the last z bin, where resonant background is expected.

For the 2004-2005 e^- data taking period the uncertainties arising from the trigger level 4 efficiency determination is also shown in addition to the statistical uncertainties. All the measured data points are compatible if one take into account this additional uncertainty.

7.5.5 Cross Sections for the Low z Selection

The new results will be compared with the previous results of the HERA I analysis of H1 [35], see previous section for an introduction. The cross section is measured in the kinematic range given in table 7.7. The selection for the HERA I analysis is given in table 7.9, and for this analysis in table 4.8.

Acceptance cuts	
angular cut	$20^\circ \leqslant \theta_\mu \leqslant 140^\circ$
momentum cut	$P_\mu > 0.8\,\mathrm{GeV}$
	$P_{\mu_{\mathrm{iron}}} > 1.8\,\mathrm{GeV}$
Selection cuts	
photoproduction	#Lee West Tracks $\geqslant 5$
	no scattered electron in the main detector ($E_{cluster} < 8\,\mathrm{GeV}$), $Q^2 < 1\,\mathrm{GeV}^2$
low elasticity	$0.05 \leqslant z \leqslant 0.45$
	$P^2_{t,\psi} > 1\,\mathrm{GeV}^2$
	$120 \leqslant W_{\gamma\mathrm{p}} \leqslant 260\,\mathrm{GeV}$

Table 7.9: Selection cuts for the **low** z selection of the HERA I analysis

The total photoproduction cross section as a function of the photon-proton centre-of-mass energy $W_{\gamma\mathrm{p}}$, the differential cross sections as functions of the transverse momentum squared of the J/ψ meson $P^2_{t,\psi}$ and the elasticity z, are shown in figure 7.22 for both data taking period and the low z selection. The ratio between this analysis and the HERA I analysis is also shown. Like for the medium z selection, both analysis agree within the statistical errors at one or two standard deviations. Since at low z the statistics is lower, it is expected to have some deviations between the measurements due to the larger statistical uncertainties. Also the background subtraction is more difficult and the method used can bias to a lower or higher value the number of J/ψ mesons. It is clearly visible in figure 7.4, which compares the method 1 and 2.

Like for the medium z selection, all the measured data points of the 2004-2005 e^- data taking period are compatible if one take into account the uncertainty of the trigger level 4 efficiency.

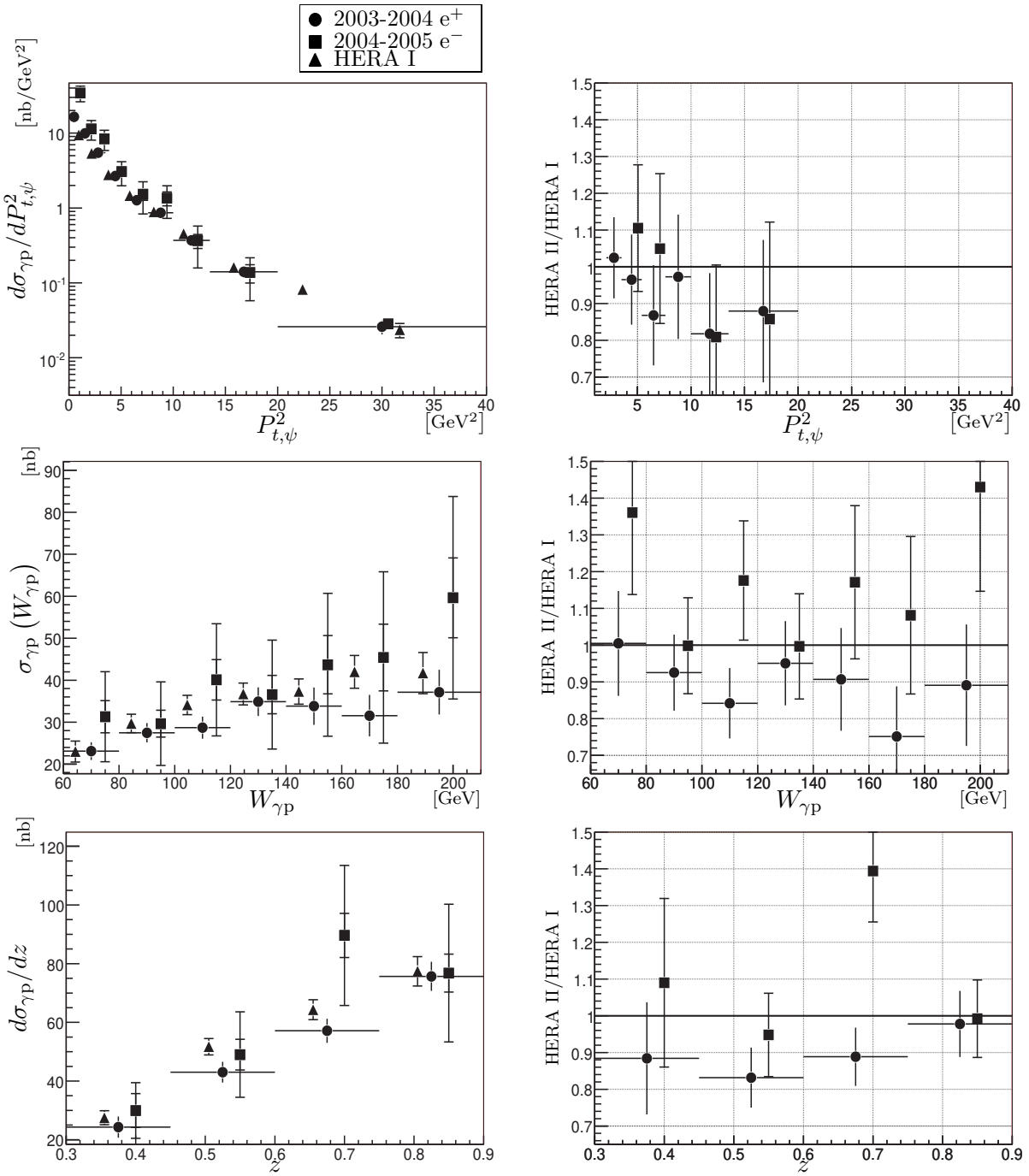

Figure 7.21: Total photoproduction cross section as a function of the photon-proton centre-of-mass energy $W_{\gamma p}$, differential cross sections as functions of the transverse momentum squared of the J/ψ meson $P^2_{t,\psi}$ and the elasticity z for both data taking period and the **medium** z selection. Data points are offset for visibility. The ratio between this analysis and the HERA I analysis is also shown. Since the upper bins of $P^2_{t,\psi}$ are not identical, the ratio is not shown for theses bins. The uncertainties arising from the trigger level 4 efficiency determination is also shown in addition to the statistical uncertainties for the 2004-2005 e$^-$ data taking period.

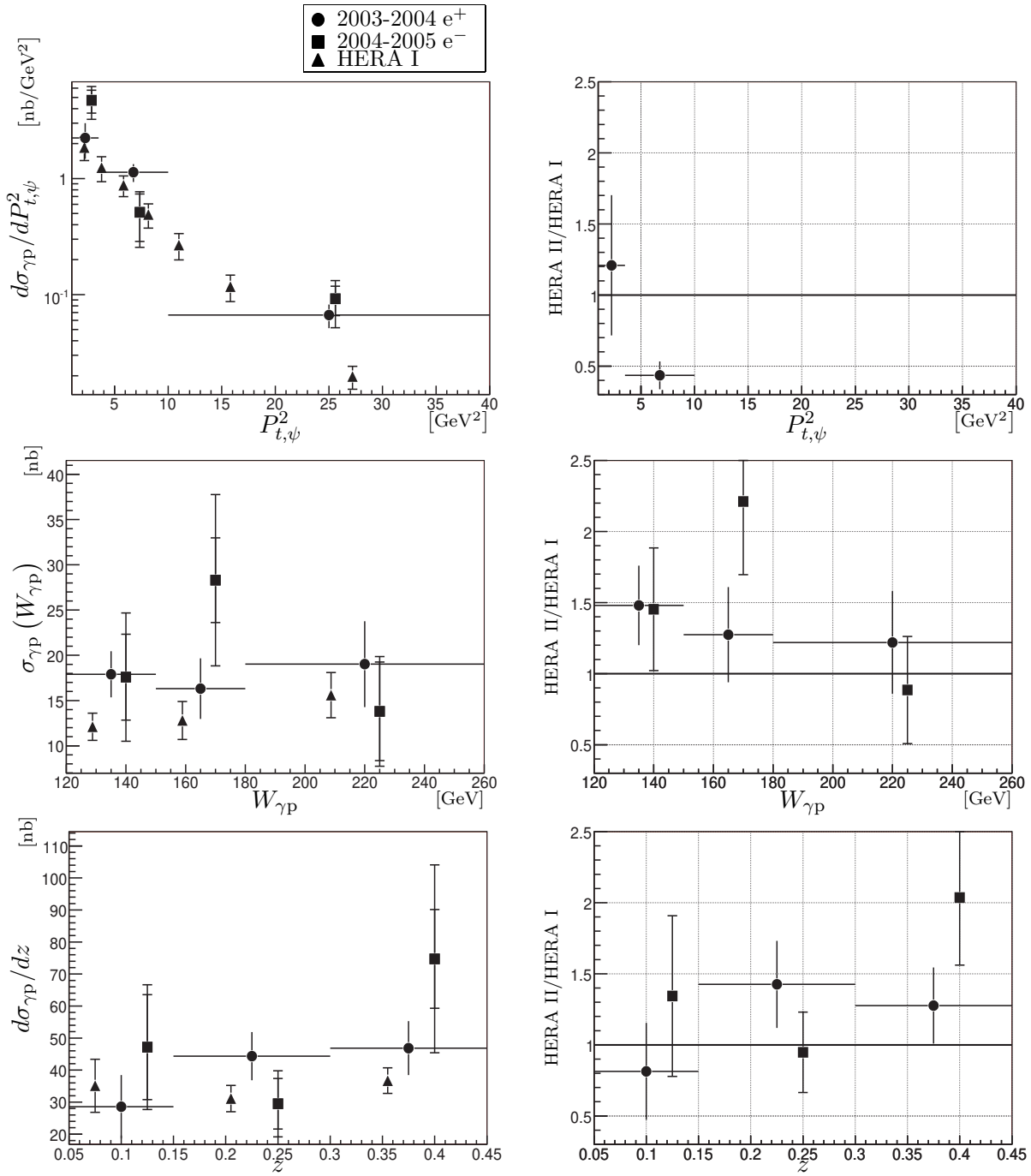

Figure 7.22: Total photoproduction cross section as a function of the photon-proton centre-of-mass energy $W_{\gamma p}$, differential cross sections as functions of the transverse momentum squared of the J/ψ meson $P^2_{t,\psi}$ and the elasticity z for both data taking period and the **low** z selection. Data points are offset for visibility. The ratio between this analysis and the HERA I analysis is also shown. Since the upper bins of $P^2_{t,\psi}$ are not identical, the ratio is not shown for theses bins. The uncertainties arising from the trigger level 4 efficiency determination is also shown in addition to the statistical uncertainties for the 2004-2005 e$^-$ data taking period.

7.6 Tables for the Cross Sections

In this section the tables containing all the numbers used to compute the cross sections are given. The notation used in the tables is:

- the integrated luminosity L
- the upper and lower values of the bin of x
- the bin width
- the bin center $\langle x \rangle$
- the number of J/ψ mesons $\mathcal{N}_\psi$ obtained with the method 2 (cf. section 7.2)
- the acceptance ϵ_{acc}
- the selection efficiency ϵ_{sel}
- the product of the acceptance and the selection efficiency $\epsilon_{acc \wedge sel}$
- the trigger efficiency ϵ_{trig}
- the trigger level 4 efficiency ϵ_{l4}, if it is different from 100 %
- the total efficiency ϵ_{total}
- the differential electron-proton cross section $d\sigma_{\mathrm{ep}}/dx$ or the electron-proton cross section $\sigma_{\mathrm{ep}}(x)$
- the photon flux $\mathcal{F}_\gamma$
- the differential photon-proton cross section $d\sigma_{\gamma\mathrm{p}}/dx$ or the photon-proton cross section $\sigma_{\gamma\mathrm{p}}(x)$

All efficiencies are given in percent.

7.6.1 Tables for the Low z Selection

$L = 23\,522.71\,\text{nb}^{-1}$											
z	bin width	$\langle z \rangle$	$\mathcal{N}_\psi$	ϵ_{acc}	ϵ_{sel}	$\epsilon_{acc \wedge sel}$	ϵ_{trig}	ϵ_{total}	$d\sigma_{\text{ep}}/dz$[nb]	$\mathcal{F}_\gamma$	$d\sigma_{\gamma\text{p}}/dz$[nb]
0.05 - 0.15	0.10	0.100	37.6 ± 13.0	54.4	49.6	27.0	78.1	21.1 ± 0.7	1.29 ± 0.45	0.0452	28.5 ± 9.9
0.15 - 0.3	0.15	0.225	90.5 ± 15.4	63.7	44.0	28.0	77.8	21.8 ± 0.8	2.00 ± 0.34	0.0452	44.3 ± 7.5
0.3 - 0.45	0.15	0.375	57.5 ± 10.3	40.9	39.5	16.2	81.0	13.1 ± 0.6	2.12 ± 0.38	0.0452	46.9 ± 8.4

$L = 23\,522.71\,\text{nb}^{-1}$											
$W_{\gamma\text{p}}$[GeV]	bin width	$\langle W_{\gamma\text{p}} \rangle$	$\mathcal{N}_\psi$	ϵ_{acc}	ϵ_{sel}	$\epsilon_{acc \wedge sel}$	ϵ_{trig}	ϵ_{total}	$\sigma_{\text{ep}}\left(W_{\gamma\text{p}}\right)$ [nb]	$\mathcal{F}_\gamma$	$\sigma_{\gamma\text{p}}\left(W_{\gamma\text{p}}\right)$ [nb]
120 - 150	30	134	85.3 ± 12.1	63.2	43.6	27.5	78.4	21.6 ± 0.9	0.286 ± 0.041	0.0159	17.9 ± 2.5
150 - 180	30	164	56.6 ± 11.6	60.1	45.5	27.4	80.6	22.1 ± 0.9	0.186 ± 0.038	0.0114	16.3 ± 3.3
180 - 260	80	216	60.8 ± 15.2	39.6	41.9	16.6	77.9	12.9 ± 0.5	0.339 ± 0.085	0.0178	19.0 ± 4.7

$L = 23\,522.71\,\text{nb}^{-1}$											
$P^2_{t,\psi}$[GeV^2]	bin width	$\left\langle P^2_{t,\psi} \right\rangle$	$\mathcal{N}_\psi$	ϵ_{acc}	ϵ_{sel}	$\epsilon_{acc \wedge sel}$	ϵ_{trig}	ϵ_{total}	$d\sigma_{\text{ep}}/dP^2_{t,\psi}$[nb/GeV^2]	$\mathcal{F}_\gamma$	$d\sigma_{\gamma\text{p}}/dP^2_{t,\psi}$[nb/GeV^2]
1 - 3.5	2.5	2.25	43.2 ± 14.6	47.5	33.5	15.9	77.7	12.4 ± 0.4	0.101 ± 0.034	0.0452	2.24 ± 0.76
3.5 - 10	6.5	6.75	82.5 ± 14.4	51.3	46.0	23.6	76.0	17.9 ± 0.6	0.0512 ± 0.0090	0.0452	1.13 ± 0.20
10 - 40	30	25.0	39.3 ± 9.0	59.1	62.3	36.8	85.2	31.4 ± 1.7	0.00301 ± 0.00069	0.0452	0.067 ± 0.015

Table 7.10: Overview of the numbers used to compute the cross section for the **2003-2004** e^+ data taking period and the **low** z section.

$L = 60\,132.50\,\text{nb}^{-1}$												
z	bin width	$\langle z \rangle$	$\mathcal{N}_\psi$	ϵ_{acc}	ϵ_{sel}	$\epsilon_{acc \wedge sel}$	ϵ_{trig}	ϵ_{l4}	ϵ_{total}	$d\sigma_{\text{ep}}/dz[\text{nb}]$	$\mathcal{F}_\gamma$	$d\sigma_{\gamma\text{p}}/dz[\text{nb}]$
0.05 - 0.15	0.10	0.100	52.5 ± 18.3	54.5	46.0	25.0	80.3	34.7 ± 7.7	7.0 ± 1.6	2.13 ± 0.74	0.0452	47 ± 16
0.15 - 0.3	0.15	0.225	66.1 ± 17.7	63.7	47.9	30.5	83.2	36.9 ± 8.3	9.4 ± 2.1	1.33 ± 0.36	0.0452	29.5 ± 7.9
0.3 - 0.45	0.15	0.375	50.1 ± 10.3	40.9	47.4	19.4	80.5	17.9 ± 6.0	2.8 ± 0.9	3.37 ± 0.70	0.0452	75 ± 15

$L = 60\,132.50\,\text{nb}^{-1}$												
$W_{\gamma\text{p}}[\text{GeV}]$	bin width	$\langle W_{\gamma\text{p}} \rangle$	$\mathcal{N}_\psi$	ϵ_{acc}	ϵ_{sel}	$\epsilon_{acc \wedge sel}$	ϵ_{trig}	ϵ_{l4}	ϵ_{total}	$\sigma_{\text{ep}}\left(W_{\gamma\text{p}}\right)[\text{nb}]$	$\mathcal{F}_\gamma$	$\sigma_{\gamma\text{p}}\left(W_{\gamma\text{p}}\right)[\text{nb}]$
120 - 150	30	134	40.1 ± 10.8	63.2	48.3	30.5	81.6	16.2 ± 4.9	4.0 ± 1.2	0.280 ± 0.076	0.0159	17.6 ± 4.7
150 - 180	30	164	79.9 ± 13.2	60.1	51.4	30.9	81.5	27.8 ± 8.1	7.0 ± 2.1	0.322 ± 0.053	0.0114	28.3 ± 4.7
180 - 260	80	216	54.5 ± 21.5	39.7	43.3	17.2	81.6	44.6 ± 8.6	6.3 ± 1.2	0.246 ± 0.097	0.0178	13.8 ± 5.4

$L = 60\,132.50\,\text{nb}^{-1}$												
$P^2_{t,\psi}[\text{GeV}^2]$	bin width	$\left\langle P^2_{t,\psi} \right\rangle$	$\mathcal{N}_\psi$	ϵ_{acc}	ϵ_{sel}	$\epsilon_{acc \wedge sel}$	ϵ_{trig}	ϵ_{l4}	ϵ_{total}	$d\sigma_{\text{ep}}/dP^2_{t,\psi}[\text{nb/GeV}^2]$	$\mathcal{F}_\gamma$	$d\sigma_{\gamma\text{p}}/dP^2_{t,\psi}[\text{nb/GeV}^2]$
1 - 3.5	2.5	2.25	77.5 ± 17.3	47.6	40.3	19.2	79.9	26.9 ± 5.9	4.1 ± 0.9	0.213 ± 0.048	0.0452	4.7 ± 1.1
3.5 - 10	6.5	6.75	37.7 ± 16.5	51.3	50.6	25.9	81.0	33.8 ± 8.2	7.1 ± 1.7	0.023 ± 0.010	0.0452	0.51 ± 0.22
10 - 40	30	25.0	44.0 ± 12.5	59.1	58.0	34.3	84.7	34.4 ± 11.5	10.0 ± 3.4	0.0042 ± 0.0012	0.0452	0.092 ± 0.026

Table 7.11: Overview of the numbers used to compute the cross section for the **2004-2005** e^- data taking period and the **low** z section.

7.6.2 Tables for the Medium z Selection

$L = 23\,522.71\ \text{nb}^{-1}$											
z	bin width	$\langle z \rangle$	$\mathcal{N}_\psi$	ϵ_{acc}	ϵ_{sel}	$\epsilon_{acc \wedge sel}$	ϵ_{trig}	ϵ_{total}	$d\sigma_{\text{ep}}/dz$[nb]	$\mathcal{F}_\gamma$	$d\sigma_{\gamma\text{p}}/dz$[nb]
0.1 - 0.3	0.20	0.200	149.9 ± 21.3	57.3	46.0	26.3	74.2	19.5 ± 0.5	2.77 ± 0.39	0.102	27.0 ± 3.8
0.3 - 0.45	0.15	0.375	109.4 ± 16.3	69.0	42.8	29.6	71.6	21.2 ± 0.6	2.49 ± 0.37	0.102	24.3 ± 3.6
0.45 - 0.6	0.15	0.525	190.7 ± 15.6	69.2	42.6	29.5	70.7	20.9 ± 0.6	4.41 ± 0.36	0.102	43.0 ± 3.5
0.6 - 0.75	0.15	0.675	216.8 ± 15.6	64.2	40.2	25.8	69.2	17.8 ± 0.5	5.86 ± 0.42	0.102	57.1 ± 4.1
0.75 - 0.9	0.15	0.825	247.9 ± 16.3	58.9	38.8	22.8	67.5	15.4 ± 0.4	7.76 ± 0.51	0.102	75.7 ± 5.0
0.9 - 1	0.10	0.950	132.0 ± 12.0	53.8	26.9	14.5	64.0	9.3 ± 0.4	10.30 ± 0.94	0.102	100.5 ± 9.1

$L = 23\,522.71\ \text{nb}^{-1}$											
$W_{\gamma\text{p}}$[GeV]	bin width	$\langle W_{\gamma\text{p}} \rangle$	$\mathcal{N}_\psi$	ϵ_{acc}	ϵ_{sel}	$\epsilon_{acc \wedge sel}$	ϵ_{trig}	ϵ_{total}	$\sigma_{\text{ep}}\left(W_{\gamma\text{p}}\right)$ [nb]	$\mathcal{F}_\gamma$	$\sigma_{\gamma\text{p}}\left(W_{\gamma\text{p}}\right)$ [nb]
60 - 80	20	69.5	137.9 ± 12.6	65.6	31.6	20.7	77.3	16.0 ± 0.7	0.623 ± 0.057	0.0269	23.1 ± 2.1
80 - 100	20	89.6	164.7 ± 13.8	83.5	32.2	26.9	83.9	22.5 ± 0.7	0.529 ± 0.044	0.0192	27.5 ± 2.3
100 - 120	20	110	141.3 ± 13.0	85.0	38.5	32.7	75.1	24.6 ± 0.8	0.416 ± 0.038	0.0145	28.7 ± 2.6
120 - 140	20	130	132.5 ± 13.0	78.0	43.4	33.8	72.1	24.4 ± 0.9	0.392 ± 0.038	0.0112	34.9 ± 3.4
140 - 160	20	150	86.7 ± 11.4	67.7	46.4	31.4	66.3	20.8 ± 0.8	0.301 ± 0.040	0.00892	33.8 ± 4.4
160 - 180	20	170	58.5 ± 9.1	56.4	50.3	28.4	65.8	18.7 ± 0.7	0.226 ± 0.035	0.00717	31.6 ± 4.9
180 - 210	30	194	63.5 ± 9.1	40.6	56.7	23.0	64.5	14.8 ± 0.6	0.309 ± 0.044	0.00833	37.1 ± 5.3

$L = 23\,522.71\ \text{nb}^{-1}$											
$P^2_{t,\psi}$[GeV^2]	bin width	$\left\langle P^2_{t,\psi} \right\rangle$	$\mathcal{N}_\psi$	ϵ_{acc}	ϵ_{sel}	$\epsilon_{acc \wedge sel}$	ϵ_{trig}	ϵ_{total}	$d\sigma_{\text{ep}}/dP^2_{t,\psi}$[nb/GeV^2]	$\mathcal{F}_\gamma$	$d\sigma_{\gamma\text{p}}/dP^2_{t,\psi}$[nb/GeV^2]
0 - 1	1.0	0.500	213.4 ± 18.0	62.4	28.3	17.7	51.7	9.1 ± 0.2	1.69 ± 0.14	0.102	16.5 ± 1.4
1 - 2.1	1.1	1.55	202.0 ± 16.5	62.4	34.6	21.6	60.3	13.0 ± 0.3	1.018 ± 0.083	0.102	9.93 ± 0.81
2.1 - 3.5	1.4	2.80	178.5 ± 14.8	63.1	38.9	24.5	67.1	16.4 ± 0.5	0.561 ± 0.046	0.102	5.47 ± 0.45
3.5 - 5.4	1.9	4.45	129.0 ± 12.8	65.0	41.4	27.0	66.5	17.9 ± 0.6	0.274 ± 0.027	0.102	2.67 ± 0.27
5.4 - 7.6	2.2	6.50	78.1 ± 10.1	65.2	44.4	28.9	68.4	19.8 ± 0.8	0.130 ± 0.017	0.102	1.27 ± 0.16
7.6 - 10	2.4	8.80	62.8 ± 9.0	64.6	46.8	30.3	70.7	21.4 ± 1.1	0.088 ± 0.013	0.102	0.86 ± 0.12
10 - 13.5	3.5	11.8	47.1 ± 7.8	66.7	51.6	34.4	74.7	25.7 ± 1.4	0.0379 ± 0.0062	0.102	0.369 ± 0.061
13.5 - 20	6.5	16.8	43.4 ± 7.5	70.2	57.8	40.6	82.5	33.5 ± 1.9	0.0144 ± 0.0025	0.102	0.141 ± 0.024
20 - 40	20	30.0	32.3 ± 6.8	74.6	67.2	50.2	87.5	43.9 ± 2.9	0.00266 ± 0.00056	0.102	0.0259 ± 0.0054

Table 7.12: Overview of the numbers used to compute the cross section for the **2003-2004** e^+ data taking period and the **medium** z section.

$L = 60\,132.50\,\text{nb}^{-1}$												
z	bin width	$\langle z \rangle$	$\mathcal{N}_\psi$	ϵ_{acc}	ϵ_{sel}	$\epsilon_{acc \wedge sel}$	ϵ_{trig}	ϵ_{l4}	ϵ_{total}	$d\sigma_{\text{ep}}/dz$[nb]	$\mathcal{F}_\gamma$	$d\sigma_{\gamma\text{p}}/dz$[nb]
0.1 - 0.3	0.20	0.200	131.0 ± 24.4	57.3	50.6	29.0	78.9	34.4 ± 7.1	7.9 ± 1.6	2.35 ± 0.44	0.102	22.9 ± 4.3
0.3 - 0.45	0.15	0.375	79.2 ± 15.2	69.0	50.7	35.0	70.5	19.7 ± 5.0	4.9 ± 1.2	3.07 ± 0.59	0.102	30.0 ± 5.7
0.45 - 0.6	0.15	0.525	116.5 ± 12.5	69.2	49.1	34.0	70.5	18.2 ± 5.1	4.4 ± 1.2	5.02 ± 0.54	0.102	49.0 ± 5.2
0.6 - 0.75	0.15	0.675	155.5 ± 13.1	64.1	43.9	28.1	69.2	16.4 ± 4.1	3.2 ± 0.8	9.19 ± 0.77	0.102	89.6 ± 7.5
0.75 - 0.9	0.15	0.825	152.2 ± 12.8	58.9	36.4	21.4	67.7	25.2 ± 7.4	3.6 ± 1.1	7.87 ± 0.66	0.102	76.8 ± 6.5
0.9 - 1	0.10	0.950	45.9 ± 7.5	53.9	22.0	11.9	68.4	10.2 ± 4.0	0.8 ± 0.3	15.6 ± 2.6	0.102	152 ± 25

$L = 60\,132.50\,\text{nb}^{-1}$												
$W_{\gamma\text{p}}$[GeV]	bin width	$\langle W_{\gamma\text{p}} \rangle$	$\mathcal{N}_\psi$	ϵ_{acc}	ϵ_{sel}	$\epsilon_{acc \wedge sel}$	ϵ_{trig}	ϵ_{l4}	ϵ_{total}	$\sigma_{\text{ep}}\left(W_{\gamma\text{p}}\right)$ [nb]	$\mathcal{F}_\gamma$	$\sigma_{\gamma\text{p}}\left(W_{\gamma\text{p}}\right)$ [nb]
60 - 80	20	69.5	79.4 ± 9.7	65.6	30.5	20.0	83.5	15.9 ± 5.1	2.7 ± 0.9	0.84 ± 0.10	0.0269	31.3 ± 3.8
80 - 100	20	89.6	101.2 ± 10.9	83.6	34.6	29.0	82.9	20.9 ± 6.6	5.0 ± 1.6	0.571 ± 0.061	0.0192	29.7 ± 3.2
100 - 120	20	110	83.7 ± 10.1	85.0	40.0	34.0	76.7	15.6 ± 4.9	4.1 ± 1.3	0.580 ± 0.070	0.0145	40.1 ± 4.8
120 - 140	20	130	83.4 ± 10.4	78.0	47.4	36.9	72.9	21.3 ± 7.1	5.7 ± 1.9	0.411 ± 0.051	0.0112	36.6 ± 4.6
140 - 160	20	150	57.2 ± 9.1	67.6	53.8	36.4	65.3	17.5 ± 6.2	4.2 ± 1.5	0.389 ± 0.062	0.00892	43.7 ± 6.9
160 - 180	20	170	47.6 ± 8.3	56.4	56.0	31.6	64.9	20.2 ± 8.3	4.1 ± 1.7	0.326 ± 0.057	0.00717	45.4 ± 8.0
180 - 210	30	194	60.5 ± 9.7	40.6	57.7	23.4	66.0	22.3 ± 8.3	3.4 ± 1.3	0.497 ± 0.079	0.00833	59.6 ± 9.5

$L = 60\,132.50\,\text{nb}^{-1}$												
$P^2_{t,\psi}$[GeV^2]	bin width	$\left\langle P^2_{t,\psi} \right\rangle$	$\mathcal{N}_\psi$	ϵ_{acc}	ϵ_{sel}	$\epsilon_{acc \wedge sel}$	ϵ_{trig}	ϵ_{l4}	ϵ_{total}	$d\sigma_{\text{ep}}/dP^2_{t,\psi}$[nb/GeV^2]	$\mathcal{F}_\gamma$	$d\sigma_{\gamma\text{p}}/dP^2_{t,\psi}$[nb/GeV^2]
0 - 1	1.0	0.500	197.6 ± 15.8	62.4	32.9	20.5	53.1	14.6 ± 3.2	1.6 ± 0.4	3.51 ± 0.28	0.102	34.3 ± 2.7
1 - 2.1	1.1	1.55	96.3 ± 12.3	62.4	38.1	23.8	62.9	14.2 ± 3.7	2.1 ± 0.6	1.17 ± 0.15	0.102	11.4 ± 1.4
2.1 - 3.5	1.4	2.80	89.4 ± 11.0	63.1	42.7	26.9	64.3	12.1 ± 3.3	2.1 ± 0.6	0.86 ± 0.11	0.102	8.4 ± 1.0
3.5 - 5.4	1.9	4.45	77.2 ± 10.4	65.1	43.4	28.2	69.0	18.8 ± 6.1	3.7 ± 1.2	0.314 ± 0.042	0.102	3.06 ± 0.41
5.4 - 7.6	2.2	6.50	48.2 ± 8.3	65.2	46.7	30.4	69.3	18.7 ± 7.9	3.9 ± 1.7	0.157 ± 0.027	0.102	1.53 ± 0.26
7.6 - 10	2.4	8.80	30.4 ± 6.4	64.6	49.0	31.7	73.9	11.0 ± 4.5	2.6 ± 1.1	0.139 ± 0.029	0.102	1.35 ± 0.29
10 - 13.5	3.5	11.8	34.2 ± 7.2	66.7	54.2	36.1	74.8	27.3 ± 14.4	7.4 ± 3.9	0.0375 ± 0.0079	0.102	0.366 ± 0.077
13.5 - 20	6.5	16.8	23.0 ± 6.3	70.1	59.9	42.0	79.2	21.3 ± 10.9	7.1 ± 3.6	0.0141 ± 0.0039	0.102	0.137 ± 0.038
20 - 40	20	30.0	87.5 ± 10.1	74.5	68.2	50.9	83.7	100.0 ± 0.0	42.6 ± 2.9	0.00291 ± 0.00033	0.102	0.0283 ± 0.0033

Table 7.13: Overview of the numbers used to compute the cross section for the **2004-2005** e^- data taking period and the **medium** z section.

7.7 Invariant Mass Distributions

In this section the mass distributions and the fits for each analysis bins are shown. A box gives the following information:

- the type of the function used to fit the background, denoted by "bg p(0,1,2)", where the number indicates the degree of the polynomial
- the χ^2 of the fit
- the number of degrees of freedom of the fit, denoted by "ndf"
- the number of J/ψ mesons and its error obtained with the method 2 (cf. section 7.2), denoted by "$\Sigma\pm$"
- the parameters of the function used to fit the J/ψ (method 1) denoted by "1s"
  - the position of the Gaussian, denoted by "μ"
  - the width(s) of the Gaussian, denoted by "σ"
  - the relative normalisation between the two Gaussians, denoted by "r"
  - the fitted number of J/ψ mesons and its error, denoted by "$\Sigma\pm$"

Vertical lines representing the width and the position of the Gaussian are also drawn on the plots.

7.7.1 Mass Distributions for the Low z Selection

7.7.1.1 2003-2004 e^+ Data Taking Period

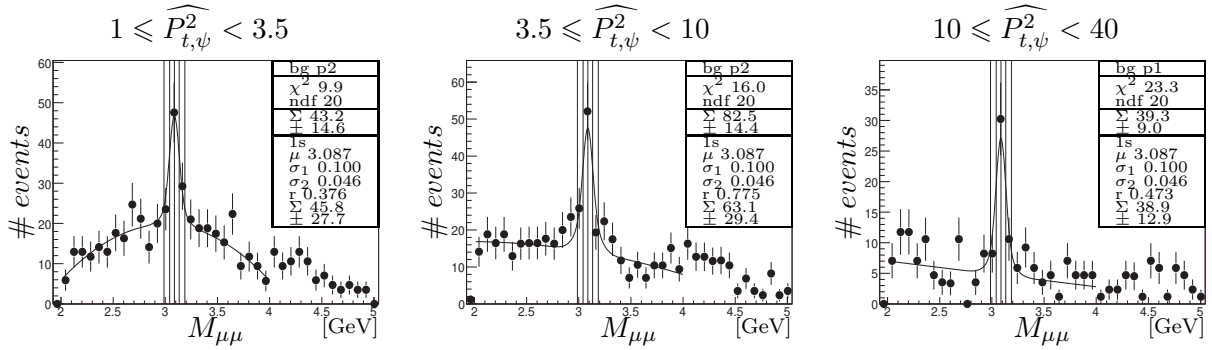

Figure 7.23: Invariant mass distribution in bins of $P^2_{t,\psi}$ for the **2003-2004** e^+ data taking period and the **low** z selection.

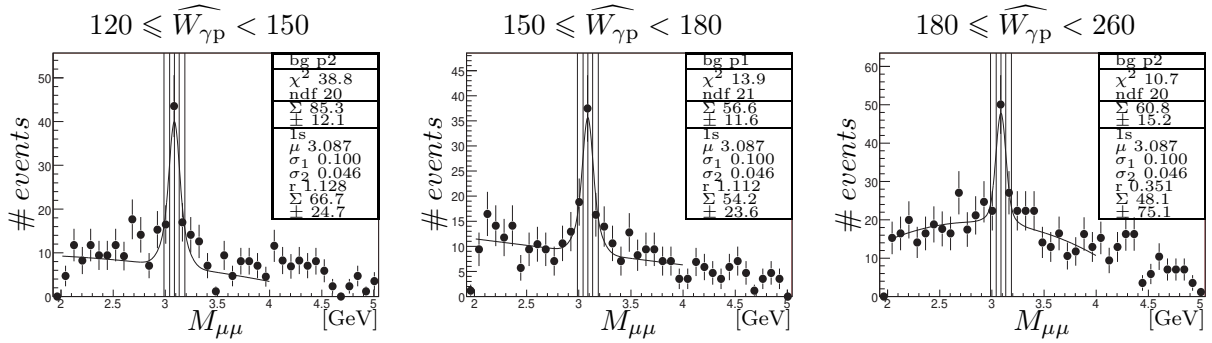

Figure 7.24: Invariant mass distribution in bins of $W_{\gamma p}$ for the **2003-2004** e^+ data taking period and the **low** z selection.

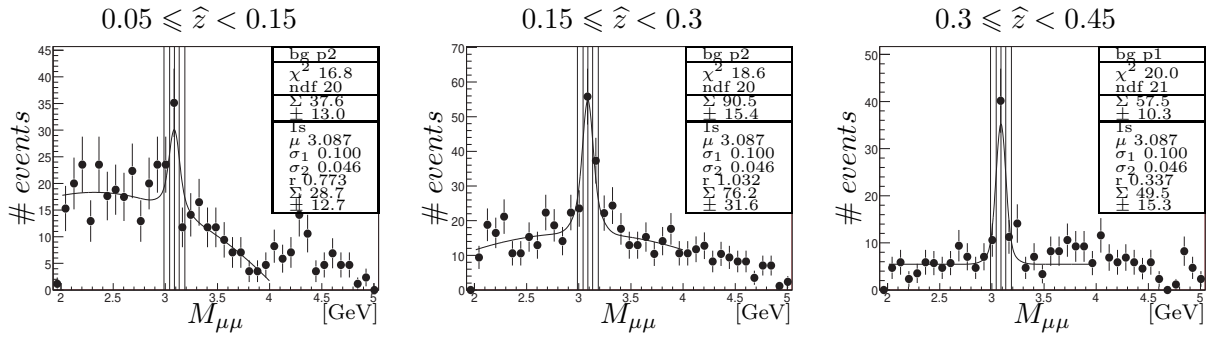

Figure 7.25: Invariant mass distribution in bins of z for the **2003-2004** e^+ data taking period and the **low** z selection.

7.7.1.2 2004-2005 e^- Data Taking Period

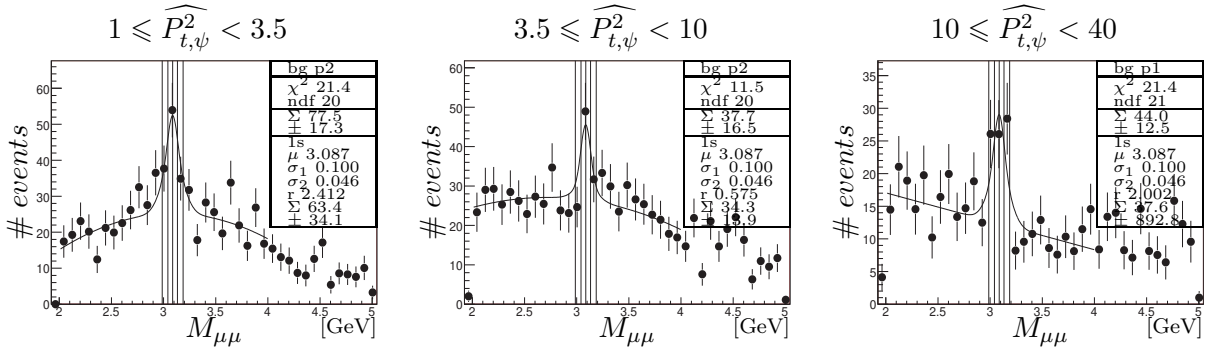

Figure 7.26: Invariant mass distribution in bins of $P^2_{t,\psi}$ for the **2004-2005** e^- data taking period and the **low** z selection.

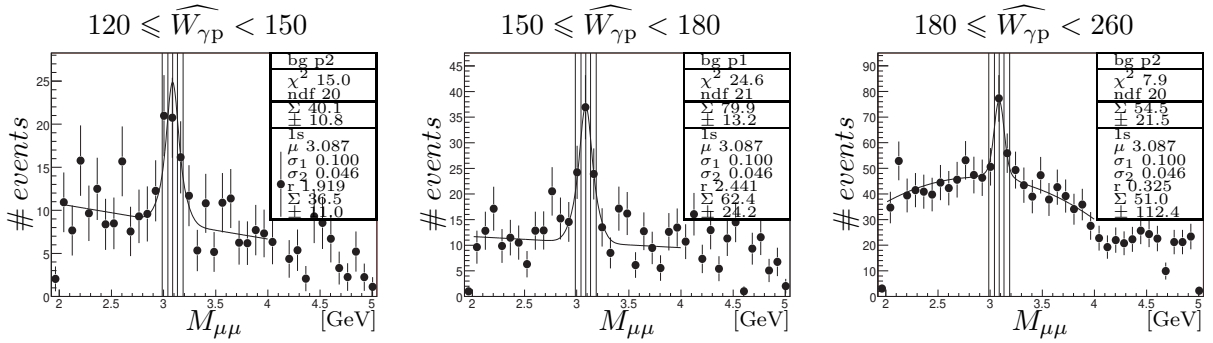

Figure 7.27: Invariant mass distribution in bins of $W_{\gamma p}$ for the **2004-2005** e^- data taking period and the **low** z selection.

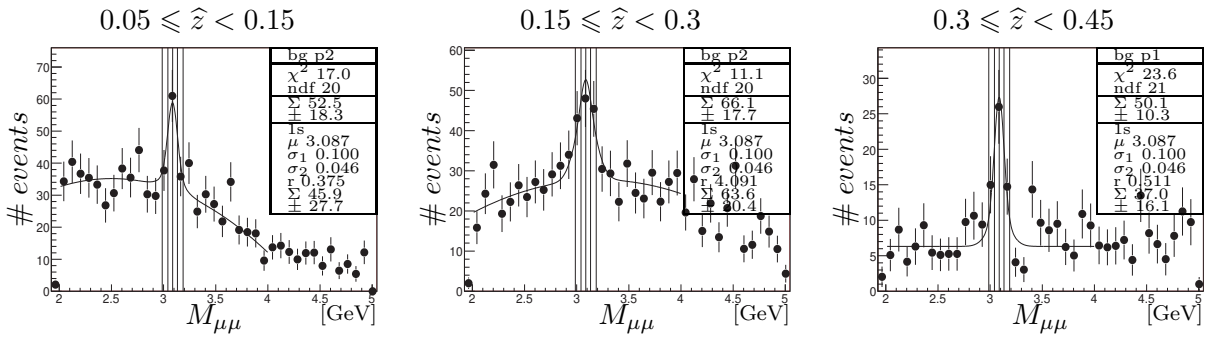

Figure 7.28: Invariant mass distribution in bins of z for the **2004-2005** e^- data taking period and the **low** z selection.

7.7.2 Mass Distributions for the Medium z Selection

7.7.2.1 2003-2004 e^+ Data Taking Period

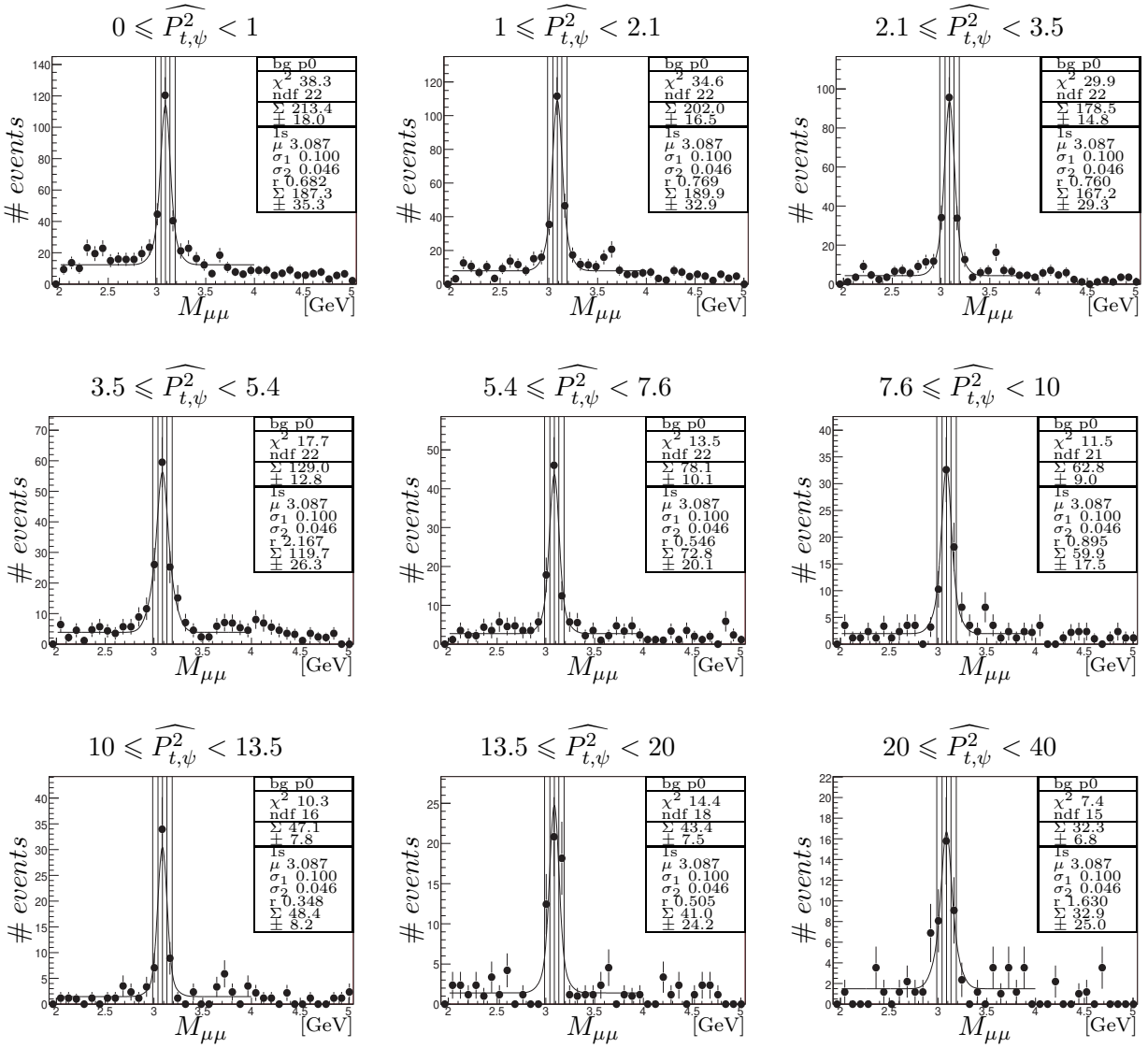

Figure 7.29: Invariant mass distribution in bins of $P^2_{t,\psi}$ for the **2003-2004** e^+ data taking period and the **medium** z selection.

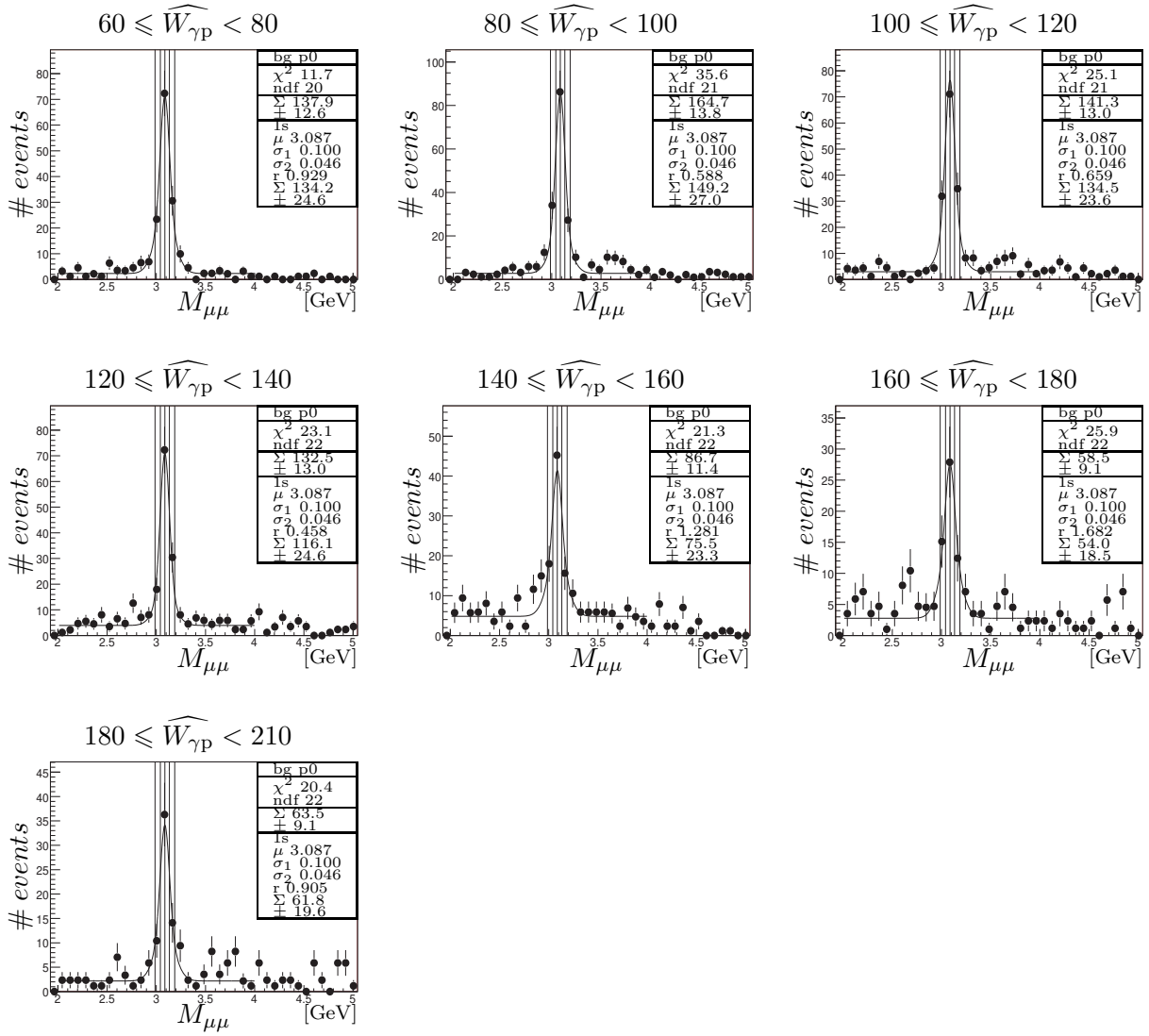

Figure 7.30: Invariant mass distribution in bins of $W_{\gamma p}$ for the **2003-2004** e^+ data taking period and the **medium** z selection.

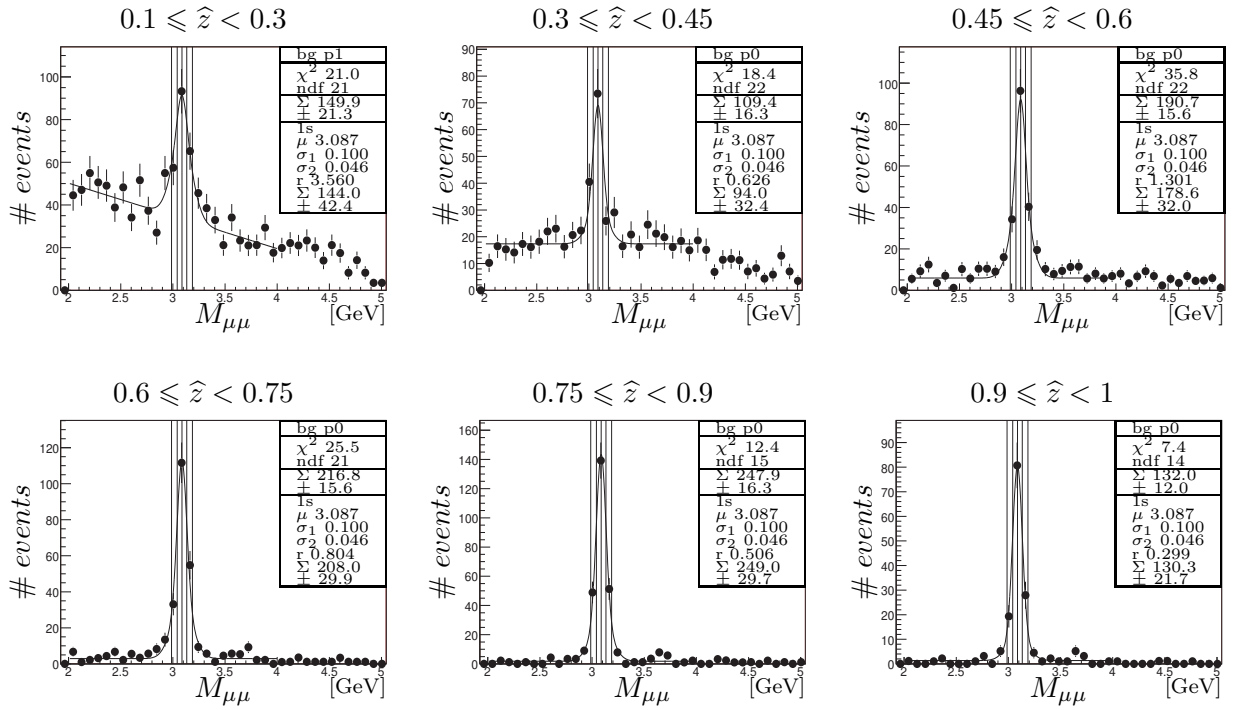

Figure 7.31: Invariant mass distribution in bins of z for the **2003-2004** e^+ data taking period and the **medium** z selection.

7.7.2.2 2004-2005 e^- Data Taking Period

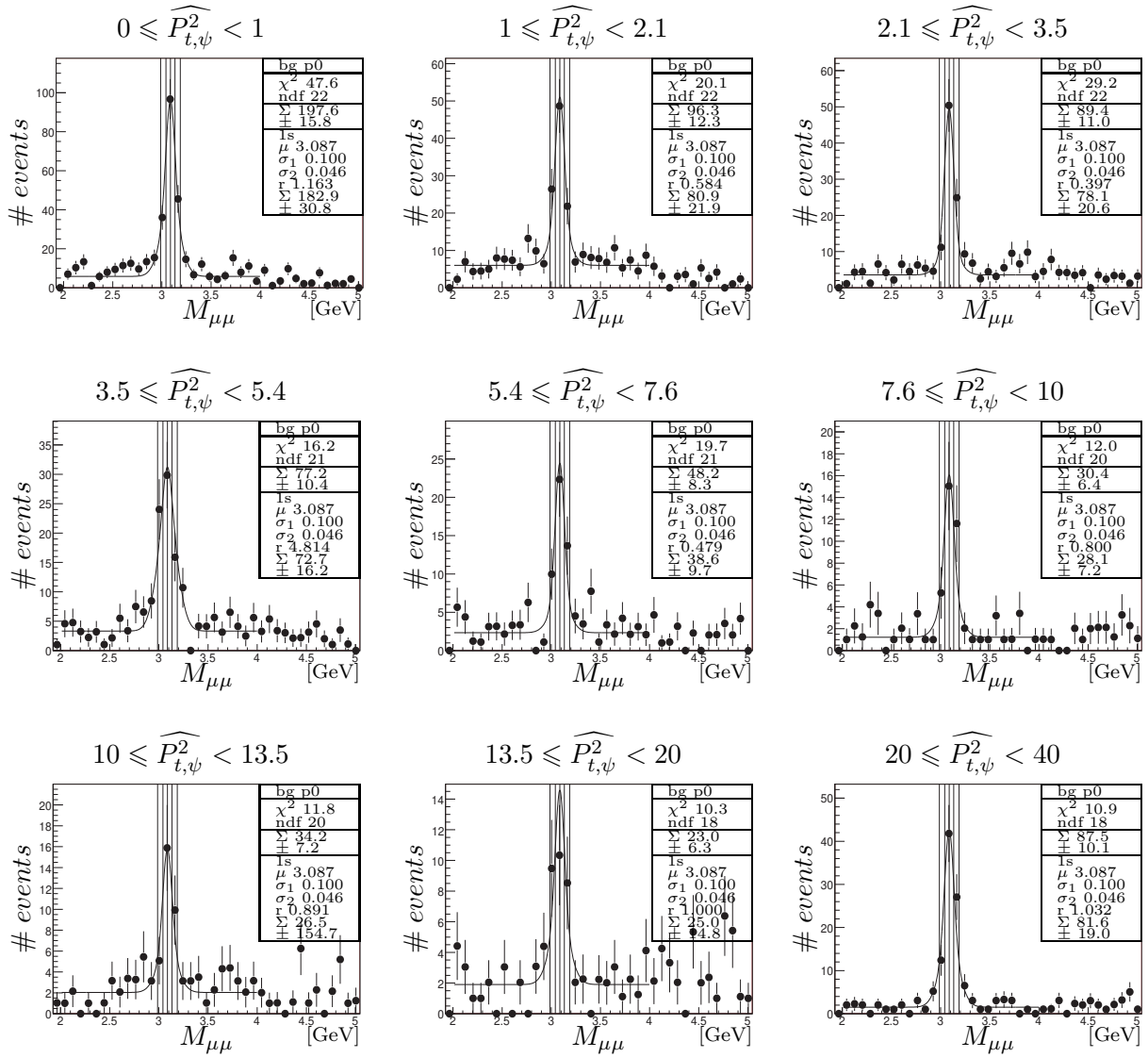

Figure 7.32: Invariant mass distribution in bins of $P^2_{t,\psi}$ for the **2004-2005** e^- data taking period and the **medium** z selection.

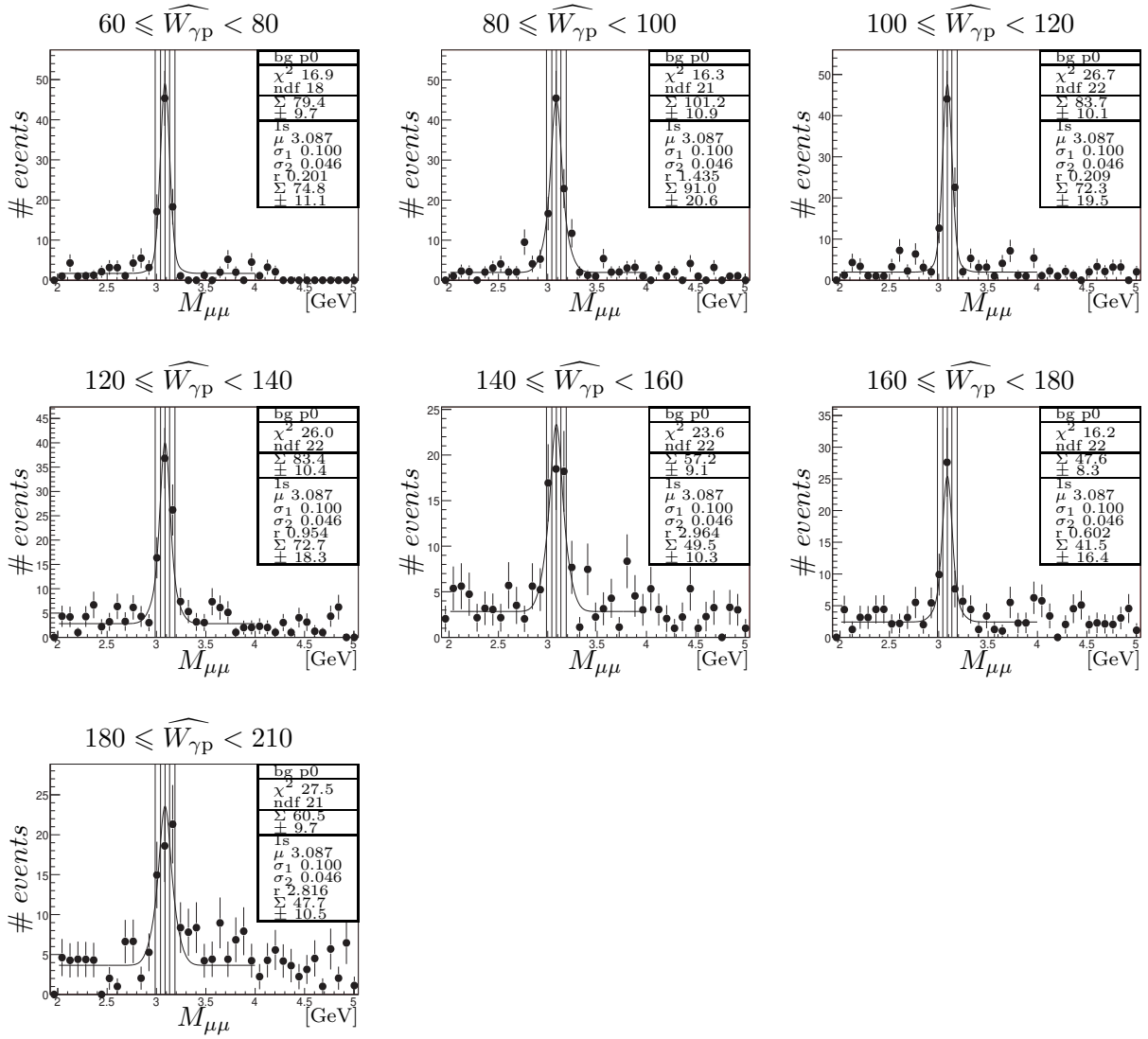

Figure 7.33: Invariant mass distribution in bins of $W_{\gamma p}$ for the **2004-2005** e^- data taking period and the **medium** z selection.

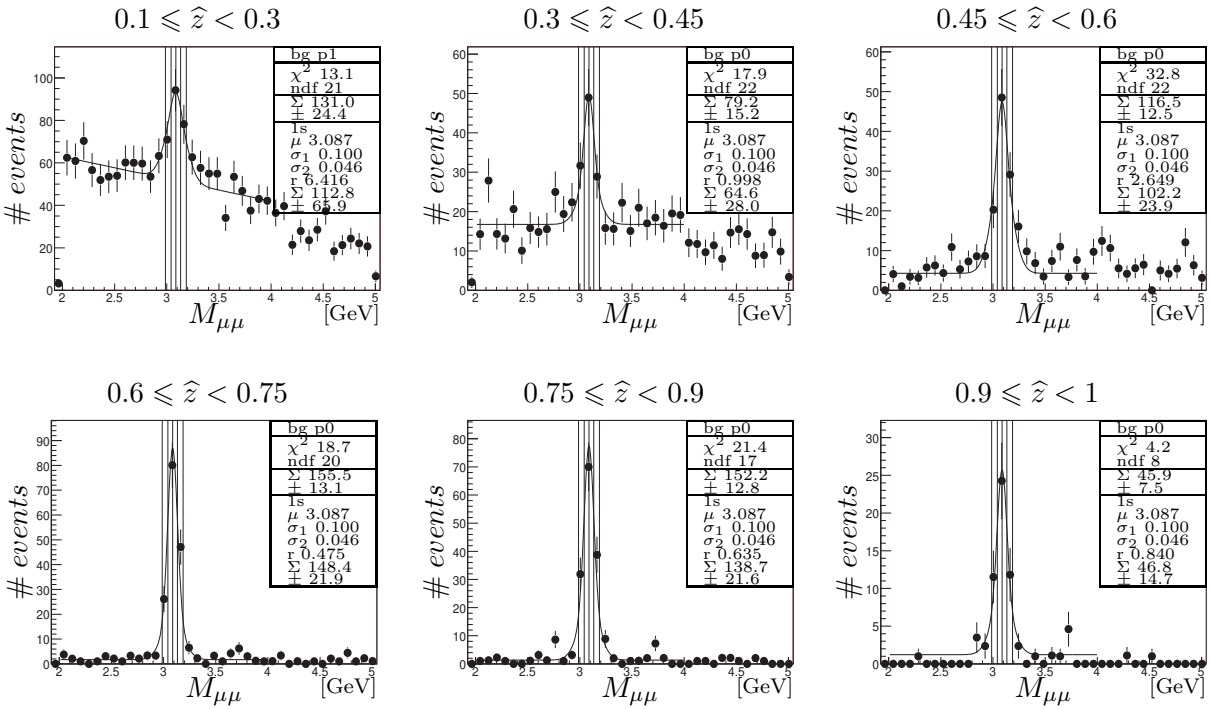

Figure 7.34: Invariant mass distribution in bins of z for the **2004-2005** e^- data taking period and the **medium** z selection.

Conclusions and Outlook

The first analysis of inelastic J/ψ mesons production in photoproduction ($Q^2 < 2.5\,\mathrm{GeV}^2$) of the H1 experiment for the second phase of HERA (HERA II) was presented. The analysis was carried out at low and medium elasticities. The muonic decay channel is used to select the J/ψ mesons.

The data was collected by the H1 detector during the period 2003–2005 and corresponds to an integrated luminosity of $133\,\mathrm{pb}^{-1}$. However only a subset of this data taking period could be analysed. At the start-up of HERA II the prescale of subtrigger s15 suffered from background and subtrigger s23 was falsely classified as monitor. Then a fault was introduced in the trigger level 4 software during the summer 2004 and was only discovered and solved in April 2006. This means that approximately 80 % of the triggered events at medium elasticities and 65 % at low elasticities were lost during this period. This malfunction has a severe cost for the HERA II data taking period for this channel, since the integrated luminosity of the affected period represents a large part of HERA II. Moreover during the first half of 2005 the muon trigger was affected by faulty power supplies. Consequently two good data taking periods were analysed: a first period with an integrated luminosity of $23\,\mathrm{pb}^{-1}$ collected in 2004, and a second period of $60\,\mathrm{pb}^{-1}$ collected during the second half of 2005, which is strongly affected by the malfunction of the trigger level 4.

The data could be described by a two component Monte Carlo simulation (EPJPSI) of direct photon-gluon fusion and gluon-gluon fusion with resolved photons, after reweighting the $P^2_{t,\psi}$ distribution. This simulation was used to correct the data for detector effects.

In the medium z range, the total photoproduction cross sections as a function of the photon-proton centre-of-mass energy $W_{\gamma\mathrm{p}}$, the differential cross sections as functions of the elasticity z and the transverse momentum squared of the J/ψ meson $P^2_{t,\psi}$ are extracted. The kinematic range is $0.3 \leqslant z \leqslant 0.9$, $60 \leqslant W_{\gamma\mathrm{p}} \leqslant 240\,\mathrm{GeV}$ and $P^2_{t,\psi} > 1\,\mathrm{GeV}^2$. The contribution from the decay of ψ(2S) mesons produced inelastically is included in the data. The results are found to be in agreement within the statistical errors at one or two standard deviations with previous H1 and ZEUS measurements for HERA I. The new measurements have a tendency to be lower for the 2003-2004 e^+ data taking periods. But the systematic error for the trigger efficiency determination is of the order of 10 % for these analyses, thus a perfect agreement is not expected.

The polarisation was studied but is not written in this thesis. Since the selection is harder the statistical uncertainties are larger and do not permit to have relevant plots to perform the study of the polarisation with a reasonable accuracy.

The total photoproduction cross section as a function of $W_{\gamma\mathrm{p}}$, the differential cross sections as functions of z and $P^2_{t,\psi}$ were also extracted in the low z range. The kinematic range is $0.05 \leqslant z \leqslant 0.45$, $120 \leqslant W_{\gamma\mathrm{p}} \leqslant 260\,\mathrm{GeV}$ and $P^2_{t,\psi} > 1\,\mathrm{GeV}^2$. The decay of ψ(2S) and χ_c mesons produced inelastically are included in the data. The results are also found to be in agreement within the statistical errors at one or two standard deviations with previous H1 measurements for HERA I. Since at low z the statistics is low it is difficult to determine accurately the number of J/ψ mesons. Moreover the ZEUS collaboration did not publish a low z analysis, thus a third analysis with different systematic uncertainties is not available to cross check the results. The analysis of the

data of the period 2006-2007, which should have the largest statistics of the H1 collaboration for the photoproduction of inelastic J/ψ mesons, should clarify this.

For this analysis, where the statistics is limited, the contribution of diffractive ψ(2S) mesons is included in the measurement contrary to the published HERA I analysis. Following HERA II analyses should suppress this resonant background by requiring at least five tracks instead of three.

The present analysis suffers from other difficulties in addition to those previously mentioned. The acceptance of the DIS subtriggers used as trigger monitor to determine efficiencies is reduced in comparison to HERA I due to the new acceptance limit of the SpaCal calorimeter and also due to the high synchrotron radiation of the electron beam for HERA II. Also the lack of track based subtriggers for the 2003-2004 e^+ data taking period does not permit to study the muon identification efficiency in the iron instrumented detector.

The malfunction of the trigger level 4 introduces an inefficiency, which has to be determined. Due to the large weights used to downscale events classified as soft physics, it was not possible to determine accurately the trigger level 4 efficiency. Moreover this malfunction produces side effects, since the algorithms which saved the data are not designed for inelastic J/ψ mesons but for other purposes.

In comparison to the published HERA I analysis the systematic errors are necessarily higher due to the previously mentioned difficulties. Also the statistical errors are higher for this analysis. For example the measured cross sections as a function of $W_{\gamma p}$ for the medium z selection have statistical errors greater than 20 % to 30 %.

The next analyses should try to extend the Lee West track selection to the new forward tracking system of the HERA II upgrade. This new detector could permit to extend the $W_{\gamma p}$ range if it has a better efficiency than the previous detector. The overall number of elastic J/ψ mesons recorded during HERA II, which is excellent and much higher than for HERA I, should permit to study the detector more accurately for the muon identification efficiency and the muon trigger efficiency. From a preliminary and fast analysis of the data taking period after the malfunction of the trigger level 4 was fixed, it was found that the order of the statistics available per analysis bin is of the order of the overall statistics of the present analysis, which means an improvement of the measurement can be expected.

Appendix A

Subtrigger Definitions

Tables A.5 to A.14 list the subtrigger changes for the HERA II data taking period. The definitions of the variables used in these tables are given in table A.3. Table A.2 gives the definitions of the trigger elements, and table A.1 the definition of the thresholds of the CIP_mul trigger element.

n	threshold
0	$= 0$
1	> 0
2	> 2
3	> 6
4	> 10
5	> 20
6	> 30
7	> 65
8	> 100
9	> 130
10	> 160
11	> 190

Table A.1: Definition of the thresholds of the CIP_mul trigger element

BToF_BG	Backward TOF background window (proton)
FIT_IA	Forward Interacting Timing hit in proton time window (proton)
FIT_BG	FIT background time window (electron)
PToF_IA	PLUG ToF background time window (e)
SPCLe_AToF_E_1	Etot ATOF above threshold 1 validated by ratio
SPCLe_IET_Cen_1	Level 1 of the central LIET bit
SPCLe_IET_Cen_2	Level 2 of the central LIET bit
SPCLe_IET_Cen_3	Level 3 of the central LIET bit
SPCLe_IET	the 2 bits of the GIET
SPCLe_ToF_E_1	Etot TOF above threshold 1 validated by ratio
SPCLe_ToF_E_2	Etot TOF above threshold 2 validated by ratio
SPCLh_AToF_E_1	Etot ATOF above threshold 1 validated by ratio
SPCLh_ToF_E_1	Etot TOF above threshold 1 validated by ratio
SPCLh_ToF_E_2	Etot TOF above threshold 2 validated by ratio
SToF_BG	SPACAL TOF background window (proton)
VETO_BG	Veto wall background window
zVtx_mul	coding number of entries in zVtx histogram
CIP_T0_nextbc	at least one track in next bunch crossing
CIP_T0	at least one central track
DCRPh_T0	at least one validated T0 mask fired
LAr_T0	digital T0
CIP_sig	Significance of central peak in zvtx histogram
CIP_mul	CIP multiplicity (number of tracks)
DCRPh_NH_many	at least 20 negative high momentum track candidates
DCRPh_NL_many	at least 20 negative low momentum track candidates
DCRPh_PH_many	at least 20 positive high momentum track candidates
DCRPh_PL_many	at least 20 positive low momentum track candidates
DCRPh_THig	at least x ($= 1$) $pt > 800\,\mathrm{MeV}$ masks (x programmable)
DCRPh_TNeg	at least x ($= 1$) negative masks (x programmable)
DCRPh_Tc	at least x ($= 3$) masks fired (x programmable)
FTT_mul_Ta	# of tracks above pt threshold 100 MeV
FTT_mul_Tb	# of tracks above pt threshold 160 MeV
FTT_mul_Tc	# of tracks above pt threshold 400 MeV
FTT_mul_Td	# of tracks above pt threshold 900 MeV
FTT_mul_Te	# of tracks above pt threshold 1 800 MeV
Mu_2_BIoOEC	$(\#\mu > 1$ in BIEC$) \vee (\#\mu > 1$ in BOEC$)$
Mu_BOEC	$\#\mu > 0$ in backward outer end-cap
Mu_Bar	$\#\mu > 0$ in barrel
Mu_FOEC	$\#\mu > 0$ in forward outer end-cap

Table A.2: Definitions of the trigger elements, as of June 2004

$$
\begin{aligned}
cip_a &\widehat{=} \neg(\text{CIP_mul} = 7 \wedge \text{CIP_sig} = 0)\\
cip_b &\widehat{=} \neg(\text{CIP_mul} > 7 \wedge \text{CIP_sig} = 0)\\
cip_c &\widehat{=} \text{CIP_sig} > 2 \wedge \text{CIP_mul} > 2\\
cip_d &\widehat{=} \text{CIP_sig} > 0 \wedge \text{CIP_mul} < 6\\
cip_mul_{11} &\widehat{=} \text{CIP_mul} < 11\\
cip_mul_{6} &\widehat{=} \text{CIP_mul} < 6\\
cip_sig_{0} &\widehat{=} \text{CIP_sig} > 0\\
cip_sig_{1} &\widehat{=} \text{CIP_sig} > 1\\
cip_t0 &\widehat{=} \text{CIP_T0}\\
dcrphi_a &\widehat{=} \text{DCRPh_THig}\\
dcrphi_b &\widehat{=} \text{DCRPh_Tc} \wedge \text{DCRPh_TNeg} \wedge dcrphi_a\\
dcrphi_many &\widehat{=} \neg(\text{DCRPh_NL_many} \wedge \text{DCRPh_NH_many} \wedge \text{DCRPh_PL_many} \wedge \text{DCRPh_PH_many})\\
fit &\widehat{=} \text{FIT_IA} \vee \neg\text{FIT_BG}\\
fit_ptof &\widehat{=} (fit) \wedge (ptof)\\
ftt_a_2 &\widehat{=} \text{FTT_mul_Ta} > 2\\
ftt_a_{l4} &\widehat{=} \text{FTT_mul_Ta} < 4\\
ftt_a_{l7} &\widehat{=} \text{FTT_mul_Ta} < 7\\
ftt_c_0 &\widehat{=} \text{FTT_mul_Tc} > 0\\
ftt_c_1 &\widehat{=} \text{FTT_mul_Tc} > 1\\
ftt_c_2 &\widehat{=} \text{FTT_mul_Tc} > 2\\
ftt_c_3 &\widehat{=} \text{FTT_mul_Tc} > 3\\
ftt_d_0 &\widehat{=} \text{FTT_mul_Td} > 0\\
ftt_d_1 &\widehat{=} \text{FTT_mul_Td} > 1\\
ftt_d_2 &\widehat{=} \text{FTT_mul_Td} > 2\\
ftt_qtot &\widehat{=} \text{FTT_Qtot} > 2 \wedge \text{FTT_Qtot} < 6
\end{aligned}
$$

Table A.3: Definition of the variables used in the next tables

$$
\begin{aligned}
ftt_qtot_back_to_back &\widehat{=} ftt_qtot \wedge \text{FTT_backtoback_2} \\
iron &\widehat{=} \text{Mu_Bar} \vee (iron_a) \\
iron_a &\widehat{=} \text{Mu_BOEC} \vee \text{Mu_2_BIoOEC} \vee \text{Mu_FOEC} \\
ptof &\widehat{=} \text{PToF_IA} \vee \neg\text{PToF_IA} \\
sbtof_bg &\widehat{=} \neg\text{BToF_BG} \wedge \neg\text{SToF_BG} \\
spcle_iet_0 &\widehat{=} \text{SPCLe_IET} > 0 \\
spcle_iet_1 &\widehat{=} \text{SPCLe_IET} > 1 \\
spcle_iet_2 &\widehat{=} \text{SPCLe_IET} > 2 \\
spclh_atof &\widehat{=} \neg\text{SPCLh_AToF_E_1} \wedge \neg\text{SPCLh_ToF_E_2} \\
spcl_a &\widehat{=} spcle_iet_2 \vee \text{SPCLe_IET_Cen_2} \\
spcl_b &\widehat{=} spcle_iet_2 \vee \text{SPCLe_IET_Cen_3} \\
t0_a &\widehat{=} \text{LAr_T0} \vee \text{DCRPh_T0} \\
t0_b &\widehat{=} \text{LAr_T0} \wedge \neg\text{CIP_T0_nextbc} \\
veto_a &\widehat{=} \neg\text{VETO_BG} \wedge sbtof_bg \\
veto_b &\widehat{=} \neg\text{SPCLh_AToF_E_1} \wedge veto_a \\
veto_c &\widehat{=} veto_b \wedge \neg\text{SPCLe_AToF_E_1} \\
veto_d &\widehat{=} veto_c \wedge fit \\
veto_e &\widehat{=} veto_d \wedge cip_t0 \\
veto_f &\widehat{=} dcrphi_many \wedge veto_a \\
vtx_mul_7 &\widehat{=} z\text{Vtx_mul} < 7
\end{aligned}
$$

Table A.4: Definition of the variables used in the next tables (continuation)

Run	Date	L1	L2
356304	14/10/03	$spcle_iet_2 \wedge veto_a \wedge fit_ptof$	
374272	11/03/04	$spcle_iet_1 \wedge veto_a \wedge fit_ptof$	(SPCL_R20) L2[22]
433029	14/10/05	$spcle_iet_1 \wedge veto_a \wedge fit_ptof$	
433739	20/10/05	$spcle_iet_1 \wedge veto_a \wedge fit_ptof$	(SPCL_R20) L2[22]

Table A.5: Subtrigger s0

Run	Date	L1	L2
335272	04/01/03	$spcle_iet_2 \wedge$ SPCLe_ToF_E_2 $\wedge spclh_atof \wedge veto_a$	(SPCL_R30) L2[17]
356304	14/10/03	$spcle_iet_2 \wedge$ SPCLe_ToF_E_2 $\wedge spclh_atof \wedge veto_a \wedge fit$	(SPCL_R30) L2[17]
374272	11/03/04	$spcle_iet_2 \wedge spclh_atof \wedge veto_a \wedge fit$	(SPCL_R30) L2[17]
433029	14/10/05	$spcle_iet_2 \wedge spclh_atof \wedge veto_a \wedge fit$	
433739	20/10/05	$spcle_iet_2 \wedge spclh_atof \wedge veto_a \wedge fit$	(SPCL_R30) L2[17]

Table A.6: Subtrigger s3

Run	Date	L1	L2
356331	14/10/03	$spcle_iet_1 \wedge spclh_atof \wedge veto_f \wedge fit_ptof$	(SPCL_R30) L2[22]
357230	17/10/03	$spcle_iet_1 \wedge spclh_atof \wedge cip_t0 \wedge veto_f \wedge fit_ptof$	(SPCL_R30) L2[22]
360628	04/11/03	$vtx_mul_7 \wedge spcle_iet_1 \wedge spclh_atof \wedge cip_t0 \wedge veto_f \wedge fit_ptof$	(SPCL_R30) L2[22]
361422	11/11/03	$spcle_iet_1 \wedge spclh_atof \wedge cip_t0 \wedge veto_f \wedge fit_ptof$	(SPCL_R30) L2[22]
362344	16/11/03	$spcle_iet_1 \wedge spclh_atof \wedge veto_f \wedge fit_ptof$	(SPCL_R30) L2[22]
362398	17/11/03	$spcle_iet_1 \wedge spclh_atof \wedge cip_t0 \wedge veto_f \wedge fit_ptof$	(SPCL_R30) L2[22]
374272	11/03/04	$spcle_iet_0 \wedge spclh_atof \wedge cip_t0 \wedge veto_f \wedge fit_ptof$	(SPCL_R30) L2[17]
401617	21/01/05	$spcle_iet_0 \wedge spclh_atof \wedge veto_a \wedge cip_t0 \wedge fit_ptof$	(SPCL_R30) L2[17]
421388	14/07/05	$spcle_iet_0 \wedge spclh_atof \wedge veto_a \wedge cip_t0 \wedge fit_ptof$	(SPCL_R40) L2[23]
433029	14/10/05	$spcle_iet_0 \wedge spclh_atof \wedge veto_a \wedge cip_t0 \wedge fit_ptof$	
433739	20/10/05	$spcle_iet_0 \wedge spclh_atof \wedge veto_a \wedge cip_t0 \wedge fit_ptof$	(SPCL_R40) L2[23]

Table A.7: Subtrigger s9

Run	Date	L1
335272	04/01/03	LAr_electron_1 $\wedge$ LAr_T0
387942	02/07/04	$spcl_b \wedge ftt_d_0 \wedge spclh_atof \wedge veto_f \wedge fit$
401617	21/01/05	$undefined$
412423	02/05/05	$cip_sig_1 \wedge cip_mul_6 \wedge$CIP_cosmic$\wedge ftt_a_{l4} \wedge ftt_d_2 \wedge ftt_qtot_back_to_back \wedge spclh_atof \wedge veto_a \wedge cip_t0$
412458	03/05/05	$cip_sig_1 \wedge cip_mul_6 \wedge$CIP_cosmic$\wedge ftt_a_{l4} \wedge ftt_d_1 \wedge ftt_qtot_back_to_back \wedge spclh_atof \wedge veto_a \wedge cip_t0$

Table A.8: Subtrigger s11

Run	Date	L1	L2
356331	14/10/03	$dcrphi_a \wedge iron \wedge veto_c \wedge fit$	
357230	17/10/03	$dcrphi_a \wedge iron \wedge veto_e$	
357477	19/10/03	$dcrphi_a \wedge iron \wedge veto_e$	(JPsi_mumu3) L2[5]
359905	30/10/03	$dcrphi_a \wedge iron \wedge veto_e \wedge cip_a$	
362344	16/11/03	$dcrphi_a \wedge iron \wedge veto_c \wedge fit \wedge cip_a$	
362399	17/11/03	$dcrphi_a \wedge iron \wedge veto_e \wedge cip_a$	
372718	21/02/04	$dcrphi_a \wedge iron \wedge veto_e \wedge cip_b$	
374272	11/03/04	$cip_mul_{11} \wedge dcrphi_a \wedge iron \wedge veto_e \wedge cip_b$	
386560	17/06/04	$cip_mul_{11} \wedge dcrphi_a \wedge iron \wedge veto_e \wedge cip_b$	(b4) L2[12]
387942	02/07/04	$cip_mul_{11} \wedge dcrphi_a \wedge iron \wedge veto_e \wedge cip_b$	(Inel_JPsi) L2[12]
401617	21/01/05	$cip_mul_{11} \wedge iron \wedge ftt_d_0 \wedge veto_e \wedge cip_b$	(Inel_JPsi) L2[12]
427872	10/09/05	$cip_mul_{11} \wedge cip_c \wedge iron \wedge ftt_a_2 \wedge ftt_c_1 \wedge ftt_d_0 \wedge veto_e \wedge cip_b$	(Inel_JPsi) L2[12]
431583	04/10/05	$cip_mul_{11} \wedge cip_c \wedge iron \wedge ftt_a_2 \wedge ftt_c_1 \wedge ftt_d_0 \wedge veto_e \wedge cip_b$	(JPsi_mumu) L2[4]
432138	09/10/05	$cip_mul_{11} \wedge cip_c \wedge iron \wedge ftt_a_2 \wedge ftt_c_1 \wedge ftt_d_0 \wedge veto_e \wedge cip_b$	(JPsi_mumu) L2[4]

Table A.9: Subtrigger s15

Run	Date	L1
361237	10/11/03	$cip_d \wedge dcrphi_a \wedge iron \wedge veto_e$
362344	16/11/03	$cip_d \wedge dcrphi_a \wedge iron \wedge veto_c \wedge fit$
362398	17/11/03	$cip_d \wedge dcrphi_a \wedge iron \wedge veto_e$
401617	21/01/05	$cip_d \wedge iron \wedge ftt_d_0 \wedge veto_e$
427872	10/09/05	$cip_d \wedge iron \wedge ftt_a_{l7} \wedge ftt_d_0 \wedge veto_e$

Table A.10: Subtrigger s18

Run	Date	L1
356331	14/10/03	$dcrphi_b \wedge$ Mu_Bar $\wedge veto_c \wedge fit$
357230	17/10/03	$dcrphi_b \wedge$ Mu_Bar $\wedge veto_e$
359724	30/10/03	$dcrphi_b \wedge$ Mu_Bar $\wedge veto_e \wedge cip_a$
362344	16/11/03	$dcrphi_b \wedge$ Mu_Bar $\wedge veto_c \wedge fit \wedge cip_a$
362399	17/11/03	$dcrphi_b \wedge$ Mu_Bar $\wedge veto_e \wedge cip_a$
372718	21/02/04	$dcrphi_b \wedge$ Mu_Bar $\wedge veto_e \wedge cip_b$
401627	21/01/05	Mu_Bar $\wedge ftt_c_2 \wedge ftt_d_0 \wedge veto_e \wedge cip_b$
427872	10/09/05	$cip_sig_1 \wedge$ Mu_Bar $\wedge ftt_c_2 \wedge ftt_d_0 \wedge veto_e \wedge cip_b$
429402	22/09/05	$cip_sig_1 \wedge$ Mu_Bar $\wedge ftt_c_1 \wedge ftt_d_0 \wedge veto_e \wedge cip_b$

Table A.11: Subtrigger s19

Run	Date	L1
369461	19/01/04	$dcrphi_b \wedge iron_a \wedge veto_e \wedge cip_a$
372718	21/02/04	$dcrphi_b \wedge iron_a \wedge veto_e \wedge cip_b$
401627	21/01/05	$iron_a \wedge ftt_c_2 \wedge veto_e \wedge cip_b$
427872	10/09/05	$cip_sig_1 \wedge iron_a \wedge ftt_c_2 \wedge veto_e \wedge cip_b$

Table A.12: Subtrigger s23

Run	Date	L1
335272	04/01/03	DCRPh_T0 $\wedge$ LU_ET_40
358242	22/10/03	$dcrphi_a \wedge spcl_b \wedge spclh_atof \wedge veto_f \wedge fit$
374272	11/03/04	$(dcrphi_a \wedge (spcle_iet_1 \vee$ SPCLe_IET_Cen_2$)) \wedge spclh_atof \wedge veto_f \wedge (fit)$
401617	21/01/05	$undefined$
430276	27/09/05	$cip_d \wedge ftt_c_1 \wedge ftt_a_{l4} \wedge ftt_qtot \wedge sbtof_bg \wedge cip_t0 \wedge fit$
431583	04/10/05	$cip_d \wedge ftt_c_0 \wedge ftt_a_{l4} \wedge ftt_qtot \wedge sbtof_bg \wedge cip_t0 \wedge fit$
432014	07/10/05	$cip_sig_1 \wedge cip_mul_6 \wedge ftt_a_{l4} \wedge ftt_d_0 \wedge sbtof_bg \wedge cip_t0 \wedge fit$
433022	14/10/05	$cip_sig_1 \wedge cip_mul_6 \wedge ftt_a_{l4} \wedge ftt_d_0 \wedge sbtof_bg \wedge cip_t0 \wedge fit$

Table A.13: Subtrigger s59

Run	Date	L1
356331	14/10/03	$dcrphi_a \wedge spcl_a \wedge spclh_atof \wedge veto_f \wedge fit$
357230	17/10/03	$dcrphi_a \wedge spcl_b \wedge spclh_atof \wedge cip_t0 \wedge veto_f \wedge fit$
357485	19/10/03	$cip_sig_0 \wedge dcrphi_a \wedge spcl_b \wedge spclh_atof \wedge cip_t0 \wedge veto_f \wedge fit$
358897	24/10/03	$dcrphi_a \wedge spcl_b \wedge spclh_atof \wedge veto_f \wedge fit$
401627	21/01/05	$spcl_b \wedge ftt_c_1 \wedge spclh_atof \wedge veto_a \wedge fit$
405720	28/02/05	$spcl_b \wedge ftt_d_0 \wedge spclh_atof \wedge veto_a \wedge fit$

Table A.14: Subtrigger s61

Bibliography

[1] J.J. Aubert et al. Experimental observation of a heavy particle J. *Physical Review Letters*, 33:1404, 1974.

[2] J.-E. Augustin et al. Discovery of a narrow resonance in e^+e^- annihilation. *Physical Review Letters*, 33:1406, 1974.

[3] Particle Data Group. Particle physics booklet, July 2004.

[4] P. Joos et al. ρ production by virtual photons. *Nuclear Physics B*, 113:53–92, October 1976.

[5] M. Beneke, M. Krämer, and M. Vänttinen. Inelastic photoproduction of polarized J/ψ. *Physical Review D*, 57(7):4258–4274, April 1998.

[6] Jean-Philippe Lansberg. J/ψ, ψ(2S) and Υ production at hadron colliders: a review, February 2006. hep-ph/0602091.

[7] Harald Fritzsch. Producing heavy quark flavors in hadronic collisions — A test of quantum chromodynamics. *Physics Letters B*, 67(2):217–221, 1977.

[8] M. Glück, J. F. Owens, and E. Reya. Gluon contribution to hadronic J/ψ production. *Physical Review D*, 17(9):2324–2331, May 1978.

[9] Francis Halzen. CVC for gluons and hadroproduction of quark flavours. *Physics Letters B*, 69(1):105–108, July 1977.

[10] E. M. Gregores J. F. Amundson, O. J. P. Éboli and F. Halzen. Colorless states in perturbative QCD: Charmonium and rapidity gaps. *Physics Letters B*, 372(1–2):127–132, April 1996.

[11] E. M. Gregores J. F. Amundson, O. J. P. Éboli and F. Halzen. Quantitative tests of color evaporation: Charmonium production. *Physics Letters B*, 390(1-4):323–328, January 1997.

[12] Chao-Hsi Chang. Hadronic production of J/ψ associated with a gluon. *Nuclear Physics B*, 172:425–434, 1980.

[13] R. Baier and R. Rückl. Hadronic production of J/ψ and Υ: Transverse momentum distributions. *Physics Letters B*, 102(5):364–370, June 1981.

[14] R. Baier and R. Rückl. On inelastic leptoproduction of heavy quarkonium states. *Nuclear Physics B*, 201(1):1–15, June 1982.

[15] Edmond L. Berger and D. Jones. Inelastic photoproduction of J/ψ and Υ by gluons. *Physics Review D*, 23(7):1521–1530, April 1981.

[16] John C. Collins, Davison E. Soper, and George Sterman. Factorization of hard processes in QCD. *Advanced Series on Directions in High Energy Physics*, 5:1, 1988.

[17] Michael Krämer. QCD corrections to inelastic J/ψ photoproduction. *Nuclear Physics B*, 459(1–2):3–50, January 1996. DESY 95-155 and hep-ph/9508409.

[18] E. Braaten, S. Fleming, and T. C. Yuan. Production of heavy quarkonium in high energy colliders. *Annual Review of Nuclear and Particle Science*, 46:197, 1996.

[19] L. Frankfurt, W. Koepf, and M. Strikman. Diffractive heavy quarkonium photo– and electroproduction in QCD. *Physical Review D*, 57:512, 1998.

[20] Martin Beneke and Michael Krämer. Direct J/ψ and ψ(2S) polarization and cross sections at the Fermilab Tevatron. *Physical Review D*, 55(9):5269–5272, May 1997.

[21] C. Albajar et al. J/ψ and ψ(2S) production at the CERN p$\overline{\text{p}}$ collider. *Physics Letters B*, 256(1):112–120, February 1991.

[22] Daniel M. Kaplan. Charmonium production in Fermilab E789. *International Journal of Modern Physics A*, 12(22):3827–3836, 1997.

[23] Geoffrey T. Bodwin, Eric Braaten, and G. Peter Lepage. Rigorous QCD predictions for decays of p-wave quarkonia. *Physical Review D*, 46(5):1914–1918, September 1992.

[24] Geoffrey T. Bodwin, Eric Braaten, and G. Peter Lepage. Rigorous QCD analysis of inclusive annihilation and production of heavy quarkonium. *Physical Review D*, 51(3):1125–1171, February 1995. Erratum ibid. D55 (1997) 5853.

[25] Eric Braaten and Yu-Qi Chen. Helicity decomposition for inclusive J/ψ production. *Physical Review D*, 54(5):3216–3227, September 1996.

[26] W. E. Caswell and G. P. Lepage. Effective lagrangians for bound state problems in QED, QCD, and other field theories. *Physics Letters B*, 167(4):437–442, February 1986.

[27] Michael Krämer. Quarkonium production at high-energy colliders. *Progress in Particle and Nuclear Physics*, 47:141, 2001.

[28] Bernd A. Kniehl and Gustav Krämer. TEVATRON-HERA colour-octet charmonium anomaly versus higher-order QCD effects. *European Physical Journal C*, 6:493, 1999.

[29] Miguel A. Sanchis-Lozano and Beatriz Cano-Coloma. Charmonia production in hadron colliders and the extraction of colour-octet matrix elements. *Nuclear Physics B*, 508:753, 1997.

[30] M. Beneke, G. A. Schuler, and S. Wolf. Quarkonium momentum distributions in photoproduction and B decay. *Physical Review D*, 62:034004, 2000.

[31] K. Sridhar, A. D. Martin, and W. J. Stirling. J/ψ production at the Tevatron and HERA: the effect of k_t smearing. *Physics Letters B*, 438:211, 1998.

[32] T. Affolder et al. Measurement of J/ψ and ψ(2S) polarization in p$\overline{\text{p}}$ collisions at $\sqrt{s} = 1.8\,\text{TeV}$. *Physical Review Letters*, 85:2886, 2000.

[33] M. J. Kim. Quarkonia production and polarization at CDF. slides of the talk, June 2006. 4th Workshop on Quarkonium at Brookhaven.

[34] C. Adloff et al. H1 Collaboration. Inelastic photoproduction of J/ψ mesons at HERA. *European Physical Journal C*, 25:25, 2002.

[35] C. Adloff et al. H1 Collaboration. Inelastic leptoproduction of J/ψ mesons at HERA. *European Physical Journal C*, 25:41, 2002.

[36] Katja Krüger. *Photoproduction of J/ψ mesons at medium and low elasticities at HERA*. PhD thesis, University of Hamburg, June 2001. DESY-THESIS-2001-025.

[37] S. MOHRDIECK. *Inelastische J/ψ-Erzeugung in Elektro-produktion am H1-Experiment bei HERA*. PhD thesis, University of Hamburg, 2000.

[38] ZEUS collaboration. Measurement of J/ψ helicity distributions in inelastic photoproduction at HERA. Moscow, July 2006. XXXIII International Conference on High Energy Physics.

[39] A. Donnachie and P. V. Landshoff. Soft interactions, 1997.

[40] H1 Collaboration. Elastic photoproduction of ρ mesons at HERA. *Nuclear Physics B*, 463(1):3–29, March 1996.

[41] ZEUS Collaboration. Elastic and proton-dissociative ρ photoproduction at HERA. *European Physical Journal C*, 2:247–267, 1998.

[42] ZEUS Collaboration. Measurement of elastic ϕ photoproduction at HERA. *Physics Letters B*, 377(4):235–355, June 1996.

[43] H1 Collaboration. Elastic photoproduction of J/ψ and Υ mesons at HERA. *Physics Letters B*, 483(1):23–35, June 2000.

[44] ZEUS Collaboration. Measurement of elastic J/ψ photoproduction at HERA. *Zeitschrift für Physik C*, 75(2):215–228, June 1997.

[45] see url `http://www-h1.desy.de/h1det/lumi/`.

[46] G. Hoffstaetter. Future possibilities for HERA. Vienna, June 2000. EPAC 2000.

[47] Background working group. H1-10/02-606. Technical report, H1, 2004.

[48] Background working group. H1-01/03-607. Technical report, H1, 2003.

[49] H1 Collaboration. The H1 detector at HERA. *Nuclear Instruments and Methods in Physics Research Section A*, 386:310–347, February 1997.

[50] Petra Merkel. *HMASS finder on L4 for 1999 e^+ running*, July 1999.

[51] Joachim Meyer. *Guide to simulation program H1SIM*, 1991. H1 internal software manual.

[52] M. Hansroul R. Brun, R. Hagelberg and J.C. Lassalle. *GEANT – Detector description and simulation tool*. CERN, 1978. CERN program library long writeup W5013, CERN-DD-78-2-REV.

[53] Hannes Jung. Monte carlo generator EPJPSI for J/ψ mesons in high energy γp, ep, μ^-p, p$\overline{\text{p}}$ and pp collisions. In G. Ingelman Eds. W. Buchmüller, editor, *Proceedings Physics at HERA*, page 1488, 1991. `http://www-h1.desy.de/~jung/epjpsi.html`.

[54] H. Plothow-Besch. *CERN Program Library Long Writeup W5051*, chapter PDFLIB: proton, pion and photon parton density functions, parton density functions of the nucleus, and α_s calculations, Users's manual, version 8.04, page 2901. Int. J. Mod. Phys. A, 2000.

[55] H. Plothow-Besch. The parton distribution function library. *International Journal of Modern Physics A*, 10(20–21):2901–2920, 1995.

[56] H. L. Lai, J. Huston, S. Kuhlmann, J. Morfin, F. Olness, J. F. Owens, J. Pumplin, and W. K. Tung. Global QCD analysis of parton structure of the nucleon: CTEQ5 parton distributions. *European Physical Journal C*, 12:375–392, 2000. hep-ph/9903282.

[57] M. Glück, E. Reya, and A. Vogt. Parton structure of the photon beyond the leading order. *Physical Review D*, 45(11):3986–3994, June 1992.

[58] M. Glück, E. Reya, and A. Vogt. Photonic parton distributions. *Physical Review D*, 46(5):1973–1979, Sep 1992.

[59] T. Sjöstrand. PYTHIA 5.7 and JETSET 7.4: Physics and manual. hep-ph/9508391, 1995.

[60] H. Jung, D. Krücker, C. Greub, and D. Wyler. Relativistic corrections to photoproduction of J/ψ. *Zeitschrift für Physik C*, 60(4):721–729, December 1993.

[61] Benno List. Diffraktive J/ψ-Produktion in Elektron-Proton-Stößen am Speicherring HERA. Diploma thesis, Berlin, 1993.

[62] Matti Peez, Benjamin Portheault, and Emmanuel Sauvan. An energy flow algorithm for hadronic reconstruction in OO: Hadroo2. H1 internal note, H1, 2005. H1-01/05-616.

[63] The H1OO Group. *The H1OO physics analysis project*. H1 collaboration, September 2004. outdated.

[64] The H1OO Group. The H1OO code.

[65] Lee West. *How to use the heavy flavour working group track, muon and electron selection code*. H1 collaboration, 2000. H1 internal software manual.

[66] *Proceedings of the workshop: Study for an* e^-p *facility in Europe*, 1979. DESY-79-048.

[67] The H1OO Group. *The H1OO user guide*. H1 collaboration, May 2005.

[68] G. SCHMIDT. *Untersuchung der diffraktiven Photoproduktion von J/ψ-Mesonen im H1-Detektor bei HERA*. PhD thesis, University of Hamburg, August 1997.

[69] H1 hypernews `http://www-h1.desy.de/icgi-hypernews/get/Detector/Trigger/481/3/1/1/1.html`.

[70] Laforge Bertrand and Schoeffel Laurent. Elements of statistical methods in high energy physics analyses. Technical report, H1, 1997. H1-08/97-528.

[71] H1 hypernews `http://www-h1.desy.de/icgi-hypernews/get/Detector/L45/151.html`.

[72] Mária Martišíková. Checks of heavy flavour level four finders. talk at heavy flavour meeting `http://www-h1.desy.de/h1/iww/iwork/ihq/minutes/agenda040127.html`, January 27 2004.

[73] Fabrice Salvaire. Analysis status report. talk at heavy flavour meeting `http://www-h1.desy.de/h1/iww/iwork/ihq/minutes/agenda050712.html`, July 12 2005.

[74] S. Egli et al. Calculating event weight in case of downscaling on trigger levels 1-4. H1 internal note, H1, April 1997. H1-04/97-517.

[75] Phillip Fleischmann. *Elastic* J/ψ *Production at HERA*. PhD thesis, University of Hamburg, May 2004. DESY-THESIS-2004-013.

[76] C. Adloff et al. H1 Collaboration. contributed paper 157aj. In *Proceedings of the International Europhysics Conference on High Energy Physics (EPS-HEP99)*, Tampere, Finland, 1999.

[77] C.F. von Weizsäcker. *Z. Phys.*, 88:612, 1934.

[78] E.J. Williams. *Phys. Rev.*, 45:729, 1934.

[79] V.M. Budnev. *Phys. Rep.*, 15:181, 1975.

[80] Andreas Meyer. L4 filter and HQ trigger news. talk at heavy flavour meeting `http://www-h1.desy.de/h1/iww/iwork/ihq/minutes/agenda060502.html`, May 2 2006.

[81] H1 Collaboration. Luminosity measurement in the H1 experiment at HERA. pages 17–26, Warsaw, 1996. In Proceedings of the XXVIII International Conference on High Energy Physics.

[82] W. J. Stirling A. D. Martin and R. G. Roberts. Pinning down the glue in the proton. *Physics Letters B*, 354(1–2):155–162, 1995.

[83] Geoffrey T. Bodwin, Eric Braaten, and G. Peter Lepage. Erratum: Rigorous QCD analysis of inclusive annihilation and production of heavy quarkonium [phys. rev. d 51, 1125 (1995)]. *Physical Review D*, 55(9):5853–5854, May 1997.

[84] W.-M. Yao et al. Review of Particle Physics. *Journal of Physics G*, 33:1, 2006.